
Dissertation

submitted to the
Combined Faculties for the Natural Sciences and for Mathematics
of the Ruperto-Carola University of Heidelberg (Germany)
for the degree of

Doctor of Natural Sciences

presented by

Diplom-Physicist

Rainer Johannes Klement

born in Bad Kissingen (Germany)

Oral examination: October 29, 2008

Stellar Phase-Space Structure and Dynamics in the Solar Neighbourhood

**Referees: Prof. Dr. Hans-Walter Rix
Prof. Dr. Burkhard Fuchs**

Abstract:

This PhD thesis describes the search for, and analysis of, substructure in the phase-space distribution of stars within 1-2 kpc of the Sun. Such substructure, caused by stellar streams, is an important diagnostic of stellar dynamics and hierarchical formation of the Galaxy. While possibly phase-mixed, stellar streams remain detectable as coherent features in the space of integrals of motion. We develop new search techniques in phase- and [Fe/H]-space to derive "effective" integrals of motion that are most suitable for a comparison with the observables. We apply our method to two new data sets which contain radial velocity- and proper motion estimates: the first RAVE public data release and a sample of metal-poor ($[Fe/H] < -0.5$) stars from the seventh SDSS data release, where [Fe/H]-estimates exist. To convert proper motions to velocities, we obtain distances to all stars from two different photometric parallax relations, one calibrated on *Hipparcos* stars for RAVE stars and one derived by Ivezić et al. (2008) for SDSS stars. From comparisons of the latter to cluster fiducial sequences from the literature we obtain a systematic relative distance error of $< 5\%$. Based on these 6D data, we identify significant "phase-space overdensities" of stars on similar orbits, of which some are already known, but at least five are described here for the first time. These kinematical detections are corroborated by analyzing their clustering in [Fe/H]-space.

This thesis also outlines a preparatory study in the context of GAIA to measure the local gravitational potential on kpc scale.

Zusammenfassung:

Diese Doktorarbeit behandelt die Suche und Analyse von Feinstruktur in der Phasenraumverteilung der Sterne, welche sich innerhalb von 1-2 kpc um die Sonne befinden. Diese Feinstruktur, hervorgerufen durch Sternenströme, ist ein wichtiges diagnostisches Werkzeug auf den Gebieten der Stelldynamik und der hierarchischen Entstehung der Milchstraße. Sternenströme bleiben im Raum der Bewegungsintegrale als koherente Strukturen erkennbar, während sie im Phasenraum möglicherweise schon vermischt sind. Wir entwickeln neue Suchmethoden im Phasen- und [Fe/H]-Raum, um „effektive“ Bewegungsintegrale herzuleiten, welche sich sehr gut für einen Vergleich mit den Beobachtungsgrößen eignen. Wir erproben unsere Methode an zwei neuen Datensätzen, die Radialgeschwindigkeiten und Eigenbewegungen beinhalten: der ersten Datenveröffentlichung von RAVE sowie einem Sample metallarmer ($[Fe/H] < -0.5$) Sterne aus der siebten Datenveröffentlichung von SDSS, welche auch [Fe/H]-Bestimmungen enthält. Um Eigenbewegungen in Geschwindigkeiten umzurechnen, leiten wir Entfernungen zu allen Sternen aus zwei verschiedenen photometrischen Parallaxen-Beziehungen ab, einer für die RAVE Sterne, die wir an *Hipparcos* Sternen geeicht haben, und einer, die von Ivezić et al. (2008) für SDSS Sterne hergeleitet wurde. Für letztere erhalten wir durch Vergleich zu Sternhaufen-Hauptreihen aus der Literatur einen systematischen Entfernungsfehler $< 5\%$. Basierend auf diesen 6D Daten identifizieren wir signifikante „Überdichten“ im Phasenraum, welche Sternen auf ähnlichen Orbits entsprechen und von denen ein Teil schon bekannt ist, aber mindestens fünf hier zum ersten mal beschrieben werden. Diese kinematischen Entdeckungen werden durch die Analyse ihres Clusterings im [Fe/H]-Raum untermauert.

Diese Arbeit fasst außerdem eine vorbereitende Studie zusammen, welche im Kontext von GAIA das lokale Gravitationspotential im kpc-Bereich bestimmen soll.

*Meinen Eltern, Elfi und Horst,
meinen Brüdern, Ulrich und Andreas,
und
Sina Fuhrmann
gewidmet*

Contents

I	Introduction	7
1	An Introduction to Stellar Streams	9
1.1	The Formation of the Milky Way	10
1.1.1	Formation of the Galaxy in a Cosmological Context	10
1.1.2	Tidal Streams as Relics from the Formation of the Milky Way	12
1.1.3	Dynamical Streams in the Disk	14
1.1.4	The Goals of this Thesis	15
2	The Sloan Digital Sky Survey	17
3	The Radial Velocity Experiment	21
4	The Orbits of Stars	23
4.1	General Aspects and Definitions	23
4.1.1	The Gravitational Potential	23
4.1.2	The Distribution Function	24
4.1.3	The Collisionless Boltzmann Equations	25
4.1.4	Integrals of Motion	27
4.2	Coordinates and Velocities	28
4.2.1	Definitions	28
4.2.2	Transforming Coordinates and Velocities	32
4.3	Orbits in Spherical Potentials	34
4.4	Orbits in Axisymmetric Potentials	36
4.4.1	The Meridional Plane	36
4.4.2	The Epicycle Approximation	38
4.4.3	The Keplerian Approximation	39
4.4.4	The Third Integral And Surfaces Of Section	41
4.5	Summary	44
II	Searching for Stellar Streams	47
5	Search Strategies	49
5.1	Stellar Streams in Configuration Space	49
5.1.1	The Global Morphology of Stellar Streams	51
5.2	Stellar Streams in Velocity Space	54
5.2.1	The Velocity Distribution of Tidal Streams	55
5.2.2	The Velocity Distribution of Young Moving Groups	57

5.2.3	The Velocity Distribution of Dynamical Streams	58
5.2.4	Conclusions	58
5.3	Stellar Streams in Integrals of Motion Space	59
5.3.1	The Classical Integrals of Motion (E, L_z, L)	59
5.3.2	Alternate Ways to Define a Nearby Stellar Orbit	60
5.3.3	Conclusions	62
6	Identifying Streams in the RAVE DR1	69
6.1	The Data	69
6.1.1	Estimation of Distances using a Photometric Parallax Relation	69
6.1.2	Deriving the velocities	75
6.2	Search strategy for streams	77
6.3	Results and Discussion	77
6.4	The Wavelet Transform	78
6.5	Subtracting a Smooth Velocity Distribution	80
6.6	Significance of the Streams	83
6.7	Streams in the Geneva-Copenhagen survey	87
6.8	Searching for Stellar Streams in (U, V, W) and (L_z, L_\perp) space	88
6.8.1	Analyzing the RAVE Data in (U, V, W) -Space	89
6.8.2	Analyzing the RAVE Data in (L_z, L_\perp) -Space	91
6.9	Conclusions	94
7	Halo Streams in SDSS DR7	97
7.1	The Data	97
7.1.1	Distance Estimates	98
7.1.2	A Metal-Poor Sample within 2 kpc	109
7.2	Search Strategy for Streams	110
7.3	Placing Solar Neighborhood Streams in the $(V_{az}, V_{\Delta E})$ -Plane	113
7.4	The Effects of Systematic Distance Errors	117
7.5	Estimating the Significance of Overdensities	117
7.6	The Results: Stellar Halo Streams	118
7.6.1	Substructure in the Thick Disk	118
7.6.2	Confirming the Discovery of the RAVE DR1 Stream	122
7.6.3	A New Stream Candidate	125
7.6.4	Two Related Streams?	126
7.6.5	The Helmi Stream	131
7.6.6	More Substructure at Very Low Metallicities	131
7.7	Conclusions	138
III	The Local Gravitational Potential	141
8	Introduction to the K_z-force problem	143
9	A New Method to Determine the K_z Force Law	145
9.1	Description of the Method	145
9.2	Validity of the New Method	148
9.2.1	The Disk Models	148

9.2.2	Direct Comparison of the Analytical and Orbital densities	149
9.2.3	Least Squares Fitting in a Grid of Parameter Space	152
9.2.4	Least Squares Fitting Using a Levenberg-Marquart Algorithm . . .	154
9.3	Approximation of the True K_z -force by a Higher-Parameter Spline Function	156
9.3.1	The Fourth-order Spline Function	156
9.4	Conclusions	158

IV Summary and Outlook **161**

A Bibliography **167**

List of Figures

4.1	The Equatorial coordinate system	29
4.2	The Galactic coordinate system	30
4.3	Galactocentric and heliocentric coordinates	31
4.4	Effective potential	38
4.5	Comparison between J_z and E_z along stellar orbits	43
4.6	R vs. J_z part I	44
4.7	R vs. J_z part II	45
5.1	Adopted Milky Way potential	51
5.2	Orbital evolution of 200 stream stars from models 1 and 2	52
5.3	Orbital evolution of 200 stream stars from different variations of model 3	53
5.4	Orbital evolution of 200 stream stars from models 3a and 4	54
5.5	Velocity distribution of stars from model 3e	64
5.6	Velocity distribution of stars from model 2	65
5.7	$(V_{az}, V_{\Delta E})$ -distribution of stars from models 2 and 3e	66
5.8	ν -distributions of stars from models 2 and 3e	67
6.1	Sky coverage of the RAVE DR1	70
6.2	$(V_T - H)$ vs. M_{V_T} photometric parallax relation calibrated on <i>Hipparcos</i> stars	71
6.3	$(B1 - H)$ vs. M_{V_T} photometric parallax relation calibrated on <i>Hipparcos</i> stars	72
6.4	Intrinsic scatter of the photometric parallax relations	73
6.5	M_{V_T} -distribution of RAVE stars	74
6.6	Distribution of velocity errors (σ_U, σ_V)	76
6.7	Distribution in $\sqrt{U^2 + 2V^2}$ vs. V	78
6.8	Wavelet transform of our RAVE sample in $\sqrt{U^2 + 2V^2}$ vs. V	80
6.9	Velocity distributions of the RAVE sample and one Monte Carlo realization	81
6.10	Wavelet transform of one particular Monte Carlo sample	82
6.11	Mean wavelet transform of all Monte Carlo samples	83
6.12	Standard deviation of all Monte Carlo samples	84
6.13	Significance map of the RAVE phase space overdensities	85
6.14	CMD for stars in the newly discovered feature	86
6.15	Wavelet transform of the Geneva-Copenhagen sample	87
6.16	Scatter and contour plots of the (U, V, W) -distribution of our RAVE sample	89
6.17	Significance map of the (U, V, W) -distribution of our RAVE sample	90
6.18	Scatter and contour plots of the (L_z, L_\perp) -distribution of our RAVE sample	91

6.19	Significance map of the (L_z, L_\perp) -distribution of our RAVE sample	92
6.20	Significance map of the (L_z, L_\perp) -distribution of our RAVE sample with individual stream stars overplotted	93
7.1	Sky coverage of our sample of SEGUE stars	98
7.2	$\log g$ -distribution of the SEGUE sample	99
7.3	Comparison of the Ivezic et al. (2008) photometric parallax relation to fiducial sequences of NGC5053, M92, M15 and NGC5466	101
7.4	Comparison of the Ivezic et al. (2008) photometric parallax relation to fiducial sequences of M53, NGC4147, M2 and M3	102
7.5	Comparison of the Ivezic et al. (2008) photometric parallax relation to fiducial sequences of M13, Pal5, M5 and M71	103
7.6	Comparison of the Ivezic et al. (2008) photometric parallax relation to fiducial sequences of NGC2420, M67 and NGC6791	104
7.7	Histogram of systematic distance errors for eleven clusters with $-2.0 < [\text{Fe}/\text{H}] < -0.3$	105
7.8	$g - i$ -color distribution for stars with flag='nnnn', $\log g \geq 3.5$, $d \leq 2$ kpc, $\sigma_d/d \leq 15\%$, and $[\text{Fe}/\text{H}] \leq -0.5$	106
7.9	Distribution of velocity errors $(\sigma_U, \sigma_V, \sigma_W)$ for stars with flag='nnnn', $\log g \geq 3.5$, $d \leq 2$ kpc and $\frac{\sigma_d}{d} \leq 15\%$	108
7.10	$[\text{Fe}/\text{H}]$ versus v_ϕ , v_R and W	109
7.11	Histograms of $g - r$, $g - i$, d and $[\text{Fe}/\text{H}]$ for the final sample	111
7.12	Wavelet transform of the $(V_{\text{az}}, V_{\Delta E})$ -distribution across twelve ν -bins for sub-sample s1	112
7.13	Wavelet transform of the $(V_{\text{az}}, V_{\Delta E})$ -distribution across twelve ν -bins for sub-sample s2	113
7.14	Wavelet transform of the $(V_{\text{az}}, V_{\Delta E})$ -distribution across twelve ν -bins for sub-sample s3	114
7.15	Wavelet transform of the $(V_{\text{az}}, V_{\Delta E})$ -distribution across twelve ν -bins for sub-sample s4	115
7.16	Effect of the systematic distance error on the $(V_{\text{az}}, V_{\Delta E})$ -distribution	117
7.17	Significance map for sub-sample s1	119
7.18	Significance map for sub-sample s2	120
7.19	Significance map for sub-sample s3	121
7.20	Significance map for sub-sample s4	121
7.21	'R1' and 'R2': ν -distributions	123
7.22	'R1' and 'R2': $[\text{Fe}/\text{H}]$ -distributions	123
7.23	'R2': (L_z, L_\perp) -distribution	124
7.24	'R2': (U, V, W) -distribution	125
7.25	'C1': (L_z, L_\perp) -, $[\text{Fe}/\text{H}]$ - and (U, V, W) -distributions	128
7.26	ν -distribution of stars in s2 with the same $(V_{\text{az}}, V_{\Delta E})$ as the overdensity 'S3'	129
7.27	'C2' and 'S3': (L_z, L_\perp) -, $[\text{Fe}/\text{H}]$ - and (U, V, W) -distributions	130
7.28	'H99': Density distribution in $[\text{Fe}/\text{H}]$ vs. ν	132
7.29	'H99': (L_z, L_\perp) -, $[\text{Fe}/\text{H}]$ - and (U, V, W) -distributions	134
7.30	'C3': (L_z, L_\perp) -, $[\text{Fe}/\text{H}]$ - and (U, V, W) -distributions	135
7.31	'C4': Density distribution in $[\text{Fe}/\text{H}]$ vs. ν	136
7.32	'C4': (L_z, L_\perp) -, $[\text{Fe}/\text{H}]$ - and (U, V, W) -distributions	137

9.1	Density distribution ρ_{obs} of 10^5 stars in the isothermal and Camm's disk .	149
9.2	Initial velocity distribution at the midplane for stars in the isothermal and Camm's disk	149
9.3	Energy conservation during integration	150
9.4	Comparison between orbital and analytical densities if the test potential is equal to the set-up potential	151
9.5	Effect of changing the seed for the set-up on the orbital density	152
9.6	Comparison between orbital and analytical densities if the test potential is not equal to the set-up potential	153
9.7	Contours of the $10^4\chi^2$ -values given in Table 9.2.3	154
9.8	Best-fit $K_z(z)$ - and $\rho(z)$ -curves compared to the true ones	156
9.9	Best-fit of a four-parameter spline function to the data points taken from Flynn and Fuchs (1994)	157
9.10	K_z -force of the isothermal disk, and the input and output spline functions of the Levenberg-Marquart routine.	158

List of Tables

5.1	Model parameters	52
7.1	Velocities and derived effective integrals of motion for already known solar neighborhood streams.	116
9.1	Isothermal disk: $10^4 \chi^2$ -values for different combinations of z_{fit} and k_{fit} . .	154
9.2	Results of testing the self-consistency of the isothermal disk and Camm's disk models, respectively.	155

Part I

Introduction and General Aspects

Chapter 1

An Introduction to Stellar Streams

According to current ideas about the cosmogony of galaxies these were assembled through hierarchical merging, which should result in a richly structured phase-space distribution of dark matter and stars. Direct empirical evidence for such events has been sought among the stellar populations of the Milky Way with large scale surveys. Ongoing satellite accretion events have been discovered in several instances. A prominent example is the Sagittarius galaxy (Ibata et al., 1994) with its associated tidal stream which wraps around the Galaxy nearly perpendicular to the galactic plane (Ibata et al., 2001; Majewski et al., 2003; Belokurov et al., 2006). Numerical simulations have shown that such debris streams can survive as coherent spatial structures over gigayears (Helmi et al., 2003; Peñarrubia et al., 2005; Law et al., 2005).

Star streams, i.e. groups of stars on essentially the same orbits in the galactic potential, have also been detected as overdensities in the phase space distribution of stars in the Solar neighbourhood. The concept of "moving groups" originates from the work of Eggen (Eggen, 1996, and references therein). Some of the moving groups are associated with young open clusters and can be naturally explained as clouds of former cluster members, now unbound and drifting away from their origin; these moving groups only reflect the nature of star formation, not necessarily that of hierarchical galaxy formation.

However, data from the last decade seem to support the concept of cold¹ star streams in the Solar neighbourhood, consisting of old stars (5-10 Gyrs) (e.g. Helmi et al., 1999). These mainly belong to the stellar halo, and – as relics from the formation of the Milky Way – are essential tracers for carrying out "Milky Way archaeology"; but moving groups of old stars are also observed in the velocity distribution of thin disk stars in the Solar vicinity. These moving groups are very probably not related to tidal debris streams, but originated from dynamical effects within the disk itself like resonances with the inner bar of the Milky Way (Dehnen, 2000) or with spiral density waves (Quillen and Minchev, 2005).

With the advent of large sky surveys like the Radial Velocity Experiment (RAVE, Steinmetz et al., 2006) or the Sloan Digital Sky Survey (SDSS, York et al., 2000) new large data samples of stars in the Milky Way with kinematics have become available, which are ideally suited for phase-space studies. In this thesis we report on the results of such studies that we conducted with RAVE and SDSS data with the aim of identifying stellar streams in the Solar neighborhood. This is the subject of Part II, where we describe

¹By "cold" we mean clustered in phase-space compared to the background population.

the data, our search strategies and stream detections. In Part III we develop a new method to use the kinematics of stars to constrain the local gravitational potential. This method is validated on theoretical disk models with the goal of applying it to large data sets like RAVE and GAIA (Lindgren and Perryman, 1996).

1.1 The Formation of the Milky Way

1.1.1 Formation of the Galaxy in a Cosmological Context

The Milky Way has its name from the faint band of light that can be observed in clear nights arching across the sky from horizon to horizon. Although Galileo Galilei (1564-1642) recognized this band to consist of a huge number of stars, it was not until the 20th century that astronomers were able to deduce the distribution of those stars with any accuracy and to figure out that they belong to only one of the stellar components out of at least four that we nowadays associate with the Milky Way galaxy: the thin disk, thick disk, halo and bulge. We classify the Milky Way as a SBbc spiral galaxy in the Hubble sequence, thereby downgrading it to only one out of billions of spiral galaxies that have a bar in their center. And still, the Milky Way is unique to us in the sense that it is the only galaxy that we can study directly from within in 3D or 6D.

Not until the past two decades have we begun to understand the composition of our Galaxy in a universal context of galaxy formation and evolution, thanks to great progress in both observations and theoretical work. Historically, there have been two different toy models for the early formation of the Milky Way's stellar halo. Eggen et al. (1962) found strong correlations between the metallicity and eccentricity of stars in the Solar neighborhood. To explain the highly eccentric orbits of the oldest stars, they argued that at the time of formation of these stars, the Galaxy could not have been in dynamical equilibrium, but in a state of rapid gravitational collapse ($\sim 10^8$ yr) from a larger homogenous spheroid, the "protogalaxy". After the Galaxy reached dynamical equilibrium and became rotationally supported, further star formation would have taken place in a metal-enriched disk, thereby explaining the disk-like orbits of the metal-rich stars. This scenario is called a **monolithic collapse**. Although the correlation between eccentricity and metallicity found by Eggen et al. (1962) is empirically correct for samples including both disk and halo stars, many authors later questioned its validity for a pure halo sample and it was definitively discarded from a kinematically unbiased sample of 1203 metal-poor stars (Chiba and Beers, 2000, hereafter CB00, and references therein). However, early simulations from Larson (1974) were able to reproduce the properties of elliptical galaxies by simulating the collapse of a spherical protogalaxy made up of stars and gas. A basic result was that the model galaxies exhibit an abundance gradient with metal-poor stars being very rare in the inner regions.

In the simplest scenario of a **monolithic collapse**, the halo has grown from the isolated and uniform collapse of dark matter particles, which build up its halo, together with baryonic matter, which has radiated away energy and therefore settled into the center of the dark matter halo, eventually forming a disk. There have been two different models of how galaxy formation proceeded.

The monolithic collapse of a uniform protogalaxy into the Milky Way's halo through rapid collapse was questioned by Searle and Zinn (1978), who found no abundance gradient, but a substantial spread in ages in the distribution of globular clusters in the outer

halo. They concluded that, although the lack of an abundance gradient would still be consistent with cluster formation during the rapid free-falling phase of a galactic collapse, it would not be possible to bring both the abundance and age distributions in concordance with the monolithic collapse model. Therefore, Searle and Zinn (1978) proposed a slow ($\sim 10^8$ yr) and more chaotic process in which the Milky Way was gradually built through the merging of several small protogalactic "fragments". This is called a **bottom-up scenario**, since galaxies are generally formed through the amalgamation of smaller fragments. However, CB00 found that the density distribution of the halo changes from highly flattened in the inner parts to nearly spherical in the outer parts with no discrete boundary. Also they found a continuous negative rotational velocity gradient with height above the Galactic plane, both results that are hard to arrange with the original Searle and Zinn (1978) scenario, because chaotic merging would not produce such kinematic and spatial structures.

Therefore both simplistic models cannot fully explain the distribution, kinematics and abundances of halo stars in the Milky Way. However, the stellar halo only accounts for 1% of all stars in the Milky Way, and a more general approach towards understanding the formation of the Milky Way, and disk galaxies in general, is needed. Such an approach has to take into account cosmological principles and the nature and properties of dark matter. Dark matter is the dominant form of matter in the Universe and it should play the key role in galaxy formation through gravitational collapse (Press and Schechter, 1974; White and Rees, 1978). Numerical and semi-analytic models show that, if the random velocities of the dark matter particles are small compared to the speed of light (cold dark matter or CDM), present day galaxies can be formed through gravitational collapse of the small density fluctuations which were present in the early Universe after the big bang. While the average density of the cosmic matter declined as the Universe expanded, some density enhancements of sufficient size became more pronounced, because of their own gravitational attraction. These protosystems drew in more matter from surrounding regions and subsequently merged to larger and larger structures, increasing further the lumpiness of the once highly (but not perfectly) uniform distribution of matter. The "trunks" of such "merger trees" in the **hierarchical scenario** are the present day galaxies (e.g. Katz, 1992; Cole et al., 1994; Mo et al., 1998; Steinmetz and Navarro, 1999; Bekki and Chiba, 2001; Steinmetz and Navarro, 2002). Although these simulations lack high enough resolution to study the detailed spatial and kinematic distribution of stars, they qualitatively can explain the formation and properties of different galactic components. CDM has become part of the cosmological standard model, the power law- Λ CDM model, which is able to describe the power spectrum of the Cosmic Microwave Background (Spergel et al., 2003, 2007), the large scale distribution of galaxies (Springel et al., 2005), observations of supernovae (Riess et al., 1998; Perlmutter et al., 1999) and observations of the baryon fraction of clusters (White et al., 1993). In this model the Universe is spatially flat, isotropic and homogeneous, contains radiation, baryonic matter and non-baryonic CDM, and is dominated by dark energy in form of a cosmological constant Λ . Tiny, nearly scale-invariant adiabatic Gaussian fluctuations that are still imprinted in the power-law power spectrum of the Cosmic Microwave Background gave rise to the dark matter halos with their galaxies and the large scale structures we observe today. Recent simulations of galaxy formation in the Λ CDM cosmology were able to build Milky Way-like spiral galaxies including thin disk, thick disk, bulge and halo (Abadi et al., 2003a,b; Brook et al., 2004b). A basic result of these simulations is that the thick disk was built from accreted gas during an early

phase of hierarchical merging, while the thin disk formed in the quiescent phase after the major merging processes ceased. As another example, Samland (2004) simulated the baryonic growth of a Milky Way-like galaxy in a Λ CDM cosmology using a complex chemodynamical model. In this simulation the inner stellar halo and a protobulge formed first through collapse of a baryonic protogalactic cloud inside the dark matter halo during redshift $z = 10$ to $z = 2$. At $z = 2$ the stellar feedback in form of supernovae that resulted from the increasing star formation slows the collapse down into a quasi-static contraction. The thick disk forms and supernovae drive metal-enriched gas from the bulge into the disk. At redshifts between $z = 1$ and $z = 0.5$ the thin disk forms from pre-enriched gas as the star formation moves more and more radially outwards. During the following 'quiescent' evolution phase, when the galaxy has achieved its final shape, star formation slows down, but can be triggered locally by earlier expelled gas that is re-captured from the still growing dark halo. In this scenario the Galaxy grows continuously through accretion without any major mergers. Another interesting outcome of that particular simulation is the trend that more metal-poor stars move on more eccentric orbits with lower rotation speeds around the Galactic center, but with a large scatter, so that there also exist metal-poor stars on nearly circular orbits. This would naturally explain the existence of a metal-weak thick disk (Morrison et al., 1990; Beers and Sommer-Larsen, 1995; Chiba and Beers, 2000; Arifanto et al., 2005).

Recently, Veltz et al. (2008) have used star counts and kinematics of RAVE data to claim the existence of a sharp spatial transition between the thin and thick disk and a gap between their vertical velocity dispersions. These observations would be consistent with the Λ CDM scenarios described above, but discard models where the thick disk built through continuous heating of the thin disk (by molecular clouds or spiral arms²).

Two main problems relating CDM structure growth have resulted from the analysis of such simulations, namely that CDM produces too many dark matter halos and hence too many satellite galaxies (Moore et al., 1999), and that the halo cores are too cuspy (Dalcanton and Hogan, 2001). An alternative for CDM exists in the form of warm dark matter (WDM), which has high enough thermal velocities to inhibit the dark halo formation below a certain scale that depends on the exact velocities of the WDM particles. WDM halos have far less substructure and less concentrated cores than their CDM counterparts, which would naturally solve the two main problems associated with the CDM cosmology (Bode et al., 2001). The large scale distribution of galaxies comes out to be the same in CDM and WDM simulations (Gao and Theuns, 2007). On the other hand, observations from the *Wilkinson Microwave Anisotropy Probe* rule out the contribution of WDM to galaxy formation (Spergel et al., 2003). Therefore, the issues of satellite-halo numbers and dark matter density cusps remain.

1.1.2 Tidal Streams as Relics from the Formation of the Milky Way

We have seen that the amount of substructure as well as the chemical, dynamical and spatial properties of the different Milky Way components provide important clues to the question how the Milky Way formed. Hierarchical merging would result in a richly structured phase-space distribution of dark matter and stars (e.g. Bullock and Johnston, 2005).

²We also note the simulations by Sellwood and Binney (2002), showing that the dominant effect of spiral arms is to cause radial migration without heating.

As a satellite gets 'captured'³ by the Milky Way, it is subject to a tidal field that may vary in space and time. Baryonic and non-baryonic matter gets stripped from the satellite and forms two distinct tidal tails or streams, respectively – a **leading tail** ahead of the satellite and a **trailing tail** behind it (e.g. Choi et al., 2007; Warnick et al., 2008). Tidal streams connected with ongoing satellite accretion events have been discovered in several instances. A prominent example is the Sagittarius galaxy (Ibata et al., 1994) with its associated tidal stream which wraps around the Galaxy nearly perpendicular to the galactic plane (Ibata et al. (2001), Majewski et al. (2003), Belokurov et al. (2006)). Similarly the Monoceros stream at low galactic latitudes (Yanny et al., 2003; Ibata et al., 2003) or the recently discovered Orphan stream (Belokurov et al., 2006) are interpreted as tidal debris from the Canis Major and Ursa Major II dwarf galaxies, respectively (Peñarrubia et al., 2005; Fellhauer et al., 2007). Numerical simulations have shown that such debris streams can survive as coherent structures over gigayears (Helmi et al., 2003; Peñarrubia et al., 2005; Law et al., 2005).

Constraints on the Milky Way's potential and Properties of the Progenitor

If such tidal streams result from the Milky Way's formation, we can ask two questions: can the observations of tidal streams constrain the Milky Way's gravitational potential, that is, the distribution of dark and luminous matter in the Milky Way? And: can tidal streams reveal properties of their progenitor? The first question has been addressed using simulations of satellite disruption in a fixed Milky Way potential by Johnston et al. (1999), who showed that observational data, even without known distances, could be used to constrain the circular velocity and flattening of the dark halo. Many attempts have been made to use the Sagittarius tidal tails to constrain the flattening of the halo. Ibata et al. (2001) and Majewski et al. (2003) argued that the distribution of Sagittarius debris along a great circle implies that the halo is nearly spherical. Later, Helmi (2004a) disagreed, arguing that the Sagittarius trailing tail was dynamically too young to constrain the shape of the dark halo. However, when new data of the leading, slightly older tail became available, Helmi (2004b) used N-body Sagittarius disruption studies to claim that the halo is prolate. Recently, SDSS data revealed the continuation of the Sagittarius stream towards the North Galactic Cap and a bifurcation of the distribution of the debris (Belokurov et al., 2006). This bifurcation was successfully modeled by Fellhauer et al. (2006) as the projection of the old trailing and young leading tidal tails within a spherical halo potential.

According to Johnston et al. (1996), a spherical potential implies that satellite debris remains aligned along great circles over the lifetime of the Galaxy. Helmi and White (1999) pointed out that this could only be the case for late accretion events in the outer halo; they performed simulations of disrupting satellites crossing the Solar neighborhood and showed that the debris loses its spatial coherence completely over a Hubble time. Instead, the stream stars stay clumped in velocity space, resembling classical moving groups that have been known to exist in the velocity distribution of nearby stars for some time (Proctor, 1869; Lindblad, 1925; Eggen, 1996, and references therein). This has been confirmed with different data sets and stellar halo streams have been identified in the kinematic distribution of Solar neighborhood stars (Helmi et al., 1999; Chiba and Beers, 2000; Navarro et al., 2004; Arifanto and Fuchs, 2006; Helmi et al., 2006; Dettbarn et al.,

³By 'captured' we mean it enters the virial radius of the Milky Way; see, however the discussion of this definition in Diemand et al. (2007).

2007). Tidal streams also conserve the so-called integrals of motion of their progenitor, energy and angular momentum, allowing their recovery even if the halo has undergone complete mixing (Helmi and de Zeeuw, 2000). Trying to confine Milky Way streams into a small range of energies could yield a best-fit to the gravitational potential.

Peñarrubia et al. (2006) addressed the question whether observations of tidal streams could also constrain the past evolution of the host halo's potential in a Λ CDM cosmological context. They found that present-day stream properties can only give informations about the present gravitational potential. The most recent cosmological studies of subhalo disruption, however, seem to question even this result. For example, Choi et al. (2007) found that the leading and trailing X-points, the points where the attractive forces of the host halo and the satellite are equal, lie at different distances from the satellite center, leading to a different morphology of leading and trailing tail. Also, the escaped ejecta in the leading (trailing) tail continue to be decelerated (accelerated) by the satellite's gravity, displacing their orbits from the original progenitor's orbit. These effects have been found to depend on the masses of the satellite and host proportional to $(M_s/M_h)^{1/3}$, therefore requiring modelling over a wide range of masses. But still, the leading and trailing stream particles are clustered in $(E - L_z)$ space, albeit at different energies; this would, in principal, still allow to derive a model of the potential which leads to the strongest clustering for observed stream stars.

Another study was conducted by Warnick et al. (2008), who simulated the accretion of subhalos onto "live" host halos with a wide range of masses which underwent a steady hierarchical evolution. They found very little correlations between the properties of the ejecta and the host halo's potential, at most a trend of increasing differences between leading and trailing tail masses with increasing host halo mass. But they confirmed the findings of Johnston (1998) that the leading and trailing tails can be separated by means of their energy, which again would give an observer the opportunity to constrain the gravitational potential. It should be noted that these authors did not specifically look at the phase-space and integrals-of-motion space distribution of stream particles. On the other hand, they find correlations between the spread of stream particles about the best-fit debris plane and the infall mass of the progenitor subhalo, allowing to reconstruct the infall mass from the spread of tidal debris in space. They also find the spread in radial velocities of the debris particles to be related with the infall eccentricity of the progenitor. So, even in such "realistic" simulations, where the conditions of the host halo like the amount of substructure and shape of the potential are undergoing steady changes, there exist correlations between properties of the progenitor and its tidal debris, which can be constrained by observations.

1.1.3 Dynamical Streams in the Disk

Besides the moving groups that are relics from the formation of the Milky Way and exhibit the properties of their progenitor systems, there exist many groups of stars that share the same kinematics. The concept of moving groups in the Solar neighborhood goes back to the work of Eggen (1996, and references within), who connected them to certain open clusters. He worked on the hypothesis that moving groups originate from the dispersion of stellar clusters over several Galactic rotations. Once dispersed, the stars from such a cluster would "remember" their common origin and keep moving on similar orbits as a "supercluster". While this scenario seems to be valid for some stellar streams (e.g. the

HR1614 De Silva et al., 2007), the chemical and chronological properties of the largest moving groups are incompatible with it. For example, Chereul and Grenon (2001) reported an age range of 0.5 Gyr to more than 2-3 Gyr for the Hyades supercluster and a rather large velocity dispersion, which they identified with the presence of several sub-groups. Such sub-groups have also been found by Dehnen (1998), who used sub-samples of young and old stars based on their spectral types. He discovered an asymmetric drift relation for the moving groups in the sense that those only present in red samples (old stars) have larger radial velocity components and lag with respect to the Local Standard of Rest⁴ than those containing also blue stars. In other words, old moving groups move on more eccentric orbits. To explain this observation, Dehnen (1998) proposed that these streams consist of stars that have been trapped onto nearly resonant orbits that oscillate about their parent resonant orbits, while the latter slowly change their eccentricity along with the non-axisymmetric potential. Therewith he picked up suggestions already made by Mayor (1972) and Kalnajs (1991). The latter tried to explain the bimodal velocity distribution of the Sirius (moving radially inwards) and Hyades (moving radially outwards) streams by putting the Sun at the position of the outer Lindblad resonance (OLR) of the Galactic bar. However, Famaey et al. (2005) later pointed out that these streams are better explained as stars on horseshoe orbits that cross-cocotate in the rest frame of spiral density waves (for more informations see Sellwood and Binney, 2002). They further argued that the clusters of coeval stars that have traditionally been connected to these streams would have been picked up by the spiral waves along with field stars of different ages, therefore just moving in these kinematic groups by chance. De Simone et al. (2004) also found that spiral waves can produce kinematic structures similar to those observed in the Solar neighborhood, although they attributed this more to disk heating rather than radial migration.

Dehnen (2000) and Fux (2001) later used the position of the Hercules stream, which is lagging the Local Standard of Rest with $\sim 50 \text{ km s}^{-1}$, to constrain the inclination angle and position of the OLR of the Galactic bar. Similarly, Quillen and Minchev (2005) found that placing the Sun near the 4:1 inner Lindblad resonance with a two-armed spiral density wave could account for the position of the Hyades and Coma Berenices moving groups in velocity space. Very recently, simulations of the birth and evolution of disk stars in a Milky Way potential including an axisymmetric component of the disk, the bulge and halo, spiral arms and a bar were able to reproduce the shape of the Hercules, Coma Berenices, Hyades and Sirius moving groups in velocity space (Antoja et al. 2008, in press). These examples show that the velocity distribution as well as the age and chemical composition of dynamical streams in the Solar neighborhood can be used as tracers of the Galactic potential.

1.1.4 The Goals of this Thesis

We have seen that hierarchical Λ CDM formation predicts substructure even in localized small volumes. Further, the dynamics of nearby stars seem to be strongly influenced by large-scale features of the Milky Way, such as the central bar or spiral arms. Therefore, our primary goal is to find substructure in the Solar neighborhood. Surveys like the *Hipparcos* mission (Perryman et al., 1997) or the Geneva-Copenhagen Survey (Nordstrom et al.,

⁴The Local Standard of Rest is the circular velocity of a perfectly circular orbit at the Solar position; for more informations see Section 4.2.1

2004) have in this context contributed significantly to our current understanding of origin and evolution of the Milky Way. Currently, however, the Sloan Digital Sky Survey (SDSS Stoughton et al., 2002) and the Radial Velocity Experiment (RAVE Steinmetz et al., 2006), which have collected and will collect spectra of some 240,000 and one million stars, respectively, promise the most extensive database both qualitatively and quantitatively collected to date. In addition, GAIA, the successor of the *Hipparcos* satellite, is expected to measure positions, parallaxes and annual proper motions of many millions of stars with an accuracy of $10 \mu\text{as}$ or better and also radial velocities for up to 100 million stars until 2018. Given the already available data, and in prospect of such upcoming datasets, it is time to develop new tools for finding and analyzing substructure in the Solar neighborhood. By applying these tools to the new data sets, we hope to increase the number of currently known stellar streams.

In addition, these data will allow the dynamical determination of the local gravitational potential, and hence the amount of visible and dark matter in the disk with unprecedented accuracy. Therefore, we set out to develop a new method for determining the vertical disk potential using the vertical positions and velocities of disk stars. The method is principally extendable to constrain also the radial dependency of the disk's potential.

This thesis is structured as follows: After an introduction to the SDSS and RAVE surveys in Chapter 2 and 3, we will shortly describe mathematical tools needed as the groundwork for the following chapters of this thesis. In Part II, we present search strategies and results of kinematic stream searches in the Solar neighborhood, using data from the first RAVE public data release, as well as from the seventh SDSS data release. These include the detection of already known stellar streams and of previously unknown features, which we interpret as tidal debris from past accretion events. Finally, Part III describes first tests of a new method to constrain the vertical component of the local gravitational disk potential.

Chapter 2

The Sloan Digital Sky Survey

The SDSS is an imaging and spectroscopic survey which began routine operations in April 2000 and lasted through June 2008. Recently, the SDSS finished imaging the North Galactic Cap, covering about one quarter of the Celestial Sphere (9583 deg²) and collecting images of 285 million objects. Originally, the northern part of the survey was complemented by a smaller area (~ 225 deg²), but deeper survey in the Southern Galactic hemisphere (Stoughton et al., 2002; Abazajian et al., 2003, 2004, 2005; Adelman-McCarthy et al., 2006, 2007, 2008). The SDSS uses a dedicated 2.5 m telescope located at the Apache Point Observatory in New Mexico. The telescope is equipped with an imaging camera and a pair of spectrographs. The imaging camera (Gunn et al., 1998) contains an imaging array of 30 4-megapixel CCDs and astrometric arrays which measure fluxes for calibration with standard astrometric catalog stars. The flux densities of observed objects are measured almost simultaneously in the five bands [u, g, r, i, z] with effective wavelenghts of [3540, 4760, 6280, 7690, 9250] (Fukugita et al., 1996; Gunn et al., 1998; Hogg et al., 2001). The camera sweeps the sky in great circles (drift scan mode) and a point on the sky passes the filters in the order of r, i, u, z, g . The brightness limit where the imaging camera saturates is at $g \sim 14$ mag. The completeness at this magnitude is $\sim 99.3\%$ for point sources (Ivezic et al., 2001); it drops to 95% at magnitudes of [22.1, 22.4, 22.1, 21.2, 20.3]¹. The SDSS photometry is accurate to 0.02 mag rms at the bright end² with well controlled tails of the error distribution (Ivezic et al., 2003). Astrometric positions are accurate to about 0.1" per coordinate for sources brighter than $r \sim 20.5$ mag (Pier et al., 2003) and the morphological information from the images allows point source-galaxy separation to $r \sim 21.5$ mag (Lupton et al., 2002).

Originally, funding was provided for five years of operations, that is, through summer 2005 (SDSS-I). Thanks to further financial support from the National Science Foundation, the Alfred P. Sloan Foundation and the member institutes, an extended phase of operations could be started for another three years (SDSS-II). The SDSS-II contains three surveys: *Legacy* had the goal to complete the imaging and spectroscopy of a contiguous ~ 7700 deg² region in the North Galactic Cap. *Supernovae* repeatedly imaged a ~ 300 deg² equatorial stripe in the Southern Galactic Cap to search for supernovae in the redshift

¹These values have been derived by comparing multiple scans of the same area obtained during the commissioning year with typical seeing of $1.5'' \pm 0.1''$.

²This value is determined using repeated observations of 3,000,000 point sources over time spans ranging from 3 hours to 3 years.

range $0.05 < z < 0.35$ with the goal to measure the redshift-distance relation. Finally, *SEGUE* (Sloan Extension for Galactic Understanding and Exploration) has imaged an additional 3500 deg^2 and obtained $\sim 240,000$ spectra.

The goal of *SEGUE*, the part of SDSS-II most relevant for this thesis, is to trace all stellar components of the Milky Way Galaxy. Therefore the imaging is not aimed to cover a contiguous area, but designed to sample the large-scale structure of the Milky Way. The 2.5° wide imaging stripes are separated by gaps of no more than $10'$ at high Galactic latitude ($|b| > 30^\circ$) and no more than $20'$ at low Galactic latitude ($|b| < 30^\circ$). Because the photometric pipeline is not designed for crowded fields, photometry at the lowest Galactic latitudes is not reliable (if the density of objects exceeds ~ 5000 per $10' \times 13'$ field, roughly 10 times the number density of objects at high latitude). The targets of *SEGUE* are selected using color-color and color-magnitude cuts designed to sample at varying densities across the main sequence from $g - r = 0.75$ (K dwarfs at $T_{\text{eff}} < 5000\text{K}$) through the turn-off. The main sequence targets are complemented by metal-poor turn-off stars, white dwarfs, distant BHB stars (e.g. Sirko et al., 2004) and halo red giants. Distances probed by these target selections range from 0.5 to 100 kpc from the Sun. The spectroscopic selection also includes some interesting targets like cool white dwarfs and high proper motion stars.


The proper motions come from a combination of the SDSS and a recalibrated version of the USNO-B catalog (Munn et al., 2004). Statistical errors in the USNO-B proper motions have been reduced by 20%-30% and recently a systematic error in the right ascension proper motions has been removed, improving the proper motion accuracy to a few mas yr^{-1} (Munn et al. 2008, internal SDSS memorandum). The proper motions are complemented by radial velocity estimates based on $\sim 250,000$ medium resolution ($R = 2000$) spectra of stars in the magnitude range $14.0 \leq g \leq 20.5$. The spectroscopic pipeline provides two radial velocity estimates. One is based on a cross-correlation of the observed spectra with a variety of templates in Fourier space to determine absorption-line redshifts (Stoughton et al., 2002). The other comes from a χ^2 fit of the spectra to external templates (both SDSS derived stellar templates and templates from the high-resolution ELODIE library, Prugniel and Soubiran, 2001). Usually, the adopted radial velocity value comes from matching with the ELODIE template, because these are the most reliable results when repeated observations are undertaken. Typical errors range from 5 km s^{-1} to $\sim 10 \text{ km s}^{-1}$, with a systematic error being fixed recently (Adelman-McCarthy et al., 2007).

The full potential of *SEGUE* for tracing the stellar populations of the Milky Way is utilized with the determination of effective temperatures T_{eff} , surface gravities $\log g$ (with g in units of cm s^{-2}) and metallicities $[\text{Fe}/\text{H}]$ from the spectra. These values are obtained from the *SEGUE* Stellar Parameter Pipeline (SSPP, Lee et al., 2007a) which measures 77 atomic and molecular line indices for each object. A total of eleven various techniques is used to estimate the atmospheric parameters and the adopted values are chosen using a decision tree based on the colors of the stars and the S/N of the spectra. More details on the different techniques can be found in Lee et al. (2007a, and references therein). The use of multiple approaches allows for an empirical determination of the internal errors for each derived parameter, based on the range of the reported values from each method. Typical internal errors for T_{eff} , $\log g$ and $[\text{Fe}/\text{H}]$ are smaller than 75 K, 0.2 dex and 0.1 dex, respectively. A comparison with an analysis of high-resolution spectra for over 150 SDSS-I/*SEGUE* stars suggests that the SSPP is able to estimate T_{eff} , $\log g$ and $[\text{Fe}/\text{H}]$

to an external uncertainty (random plus systematic errors) of 117 K, 0.26 dex, and 0.22 dex, respectively, in the temperature range $4500 \text{ K} \leq T_{\text{eff}} \leq 7,500 \text{ K}$ (Allende Prieto et al., 2007). An analysis of likely member stars in a handful of Galactic open and globular clusters indicates that the SSPP slightly over-estimates $[\text{Fe}/\text{H}]$ (by on the order of 0.15 dex) for stars with $[\text{Fe}/\text{H}] < -2.0$, and underestimates $[\text{Fe}/\text{H}]$ for stars with near solar metallicities by ~ 0.3 dex (Lee et al., 2007b). Determinations of T_{eff} and $\log g$ exhibit no obvious offsets relative to expectations.

Chapter 3

The Radial Velocity Experiment

 RAVE¹ is a large international collaboration (PI: Matthias Steinmetz) aimed at revolutionizing our understanding of the formation of the different Milky Way components (disk, bulge and halo). Science goals include the search for unique chemical and kinematic signatures of stellar streams in the halo, outer bulge and thick disk due to satellite accretion, the dynamical influence of the local spiral arms and inner bar, and the first non-local measurement of surface density in the disk. A key aspect of the RAVE survey is the determination of radial velocities and chemical signatures like $[\alpha/\text{Fe}]$ and $[\text{Fe}/\text{H}]$ for the brightest 50 million stars in the Galaxy down to a completeness limit of $V = 16$ mag (Steinmetz, 2003). The survey is conducted using the Six Degree Field (6dF) multiobject spectrograph at the 1.2m UK-Schmidt Telescope at the Anglo-Australian Observatory. The RAVE program started in 2003, obtaining medium-resolution spectra (median $R = 7500$) in the Ca-triplet region ($8410\text{-}8795 \text{ \AA}$), which has almost no atmospheric absorption line features and is also favoured by the GAIA instrument definition team. Over this wavelength range the CCD used with the 6dF spectrograph has a quantum efficiency of 40%-30% (Steinmetz et al., 2006). This range contains many metal lines dominated by CaII, FeI, TiI, Cn, MgI, SiI, CrI, NiI, MnI, SI and TiO, allowing the determination of $[\alpha/\text{Fe}]$ abundance ratios to better than 0.15 dex and $[\text{Fe}/\text{H}]$ to similar precision.

The program is planned to run until 2010. The main data product will be a Southern hemisphere survey of at least one million stars including 0.7 million thin disk main sequence stars, 250,000 thick disk stars, 100,000 bulge and halo stars, and a further 50,000 giant stars including some out to 10 kpc from the Sun. In 2006, the first data release (DR1) has been published (Steinmetz et al.), containing radial velocities for 24,748 individual stars which cover $\sim 4760 \text{ deg}^2$ of the sky (see Figure 6.1 in Section 6.1 for a map of the sky coverage). These stars were observed during the first year between 2003 April 11 and 2004 April 3 and selected from the Tycho-2 catalog of the 2.5 million brightest stars (Høg et al., 2000) and the SuperCOSMOS Sky Survey (SSS, Hambly et al., 2001) over the magnitude range $9 < I < 12$. Both Tycho-2 and SSS are astrometric surveys with faint and bright end respectively at $I \sim 11$.² To achieve better photometric accuracy, the targets have been cross-matched with optical and near-infrared catalogs (USNO-B, DENIS and 2MASS). 69.1% of the proper motions come from the Starnet 2.0 catalog,

¹Homepage: <http://www.rave-survey.aip.de>

²For Tycho-2, this is only a pseudo- I , calculated from the Tycho-2 magnitudes V_T and B_T .


which is currently being compiled at the Astronomisches Rechen-Institut Heidelberg, and combines the former Starnet catalog (Röser, 1996) with new proper motion estimates from Tycho-2, UCAC-2 and 2MASS. The mean proper motion error in the DR1 is 2.6 mas yr^{-1} in each coordinate for proper motions taken from Starnet 2.0. Another 29.3% of the stars have proper motions from the SSS, and a minor fraction from either Tycho-2 or an auxiliary catalog combined from 2MASS and the Guide Star Catalog 1.2 (Morrison et al., 2001).

Radial velocities are calculated from a cross-correlation technique which compares a given spectrum to a library of theoretical spectra containing 62,659 synthetic spectra in the RAVE/GAIA resolution (Zwitter et al., 2004). The spectra corresponding to DR1 are contaminated by second-order light, because no blue-blocking filter (Schott OG531) has been used during the first year. Therefore a second library of synthetic spectra from Munari et al. (2005) is used, which covers a bluer wavelength range and is degraded to RAVE's spectral resolution. The effect of second-order light on the radial velocities, however, is negligible, because the strong absorption lines in the first-order spectra, which are used in the cross-correlation to determine the wavelength shift, are not affected. The internal errors of the radial velocities are better than 3 km s^{-1} for 80% of the RAVE measurements with a mean error of 2.3 km s^{-1} . The zero-point calibration is accurate to better than 2 km s^{-1} for 97% of the targets.

Recently, the second data release (DR2, Zwitter et al., 2008) became public, containing 51,829 radial velocities for 49,327 stars. The second-order spectra have now been blocked by a blue light blocking filter (Schott OG531), which allows the estimation of stellar parameters. DR2 contains stellar parameter estimates from 22,407 spectra of 21,121 individual stars. From comparison with external data sets, the estimates of errors of the stellar parameters for a spectrum with an average signal-to-noise ratio of ~ 40 are 400 K in temperature, 0.5 dex in gravity, and 0.2 dex in metallicity, slightly worse than for SEGUE stars (Chapter 2). The release of DR2 was not in time for the studies conducted in this thesis, but we are planning to use its data for future studies.

Chapter 4

Mathematical Tools: The Orbits of Stars

he stellar body of our Milky Way Galaxy consists of about 100 billion stars that move on individual orbits that give rise to its overall structure and shape. Despite this vast number of stars, the Galaxy is a collisionless system: each star only knows about the overall potential, not the other stars. The Solar neighbourhood, a region of roughly 1-2 kpc around the Sun¹, is dominated by the Milky Way's disk population of stars; these stars have a common clockwise sense of rotation about the Galactic center, but their rotational, radial and vertical velocity components depend on their age, chemical composition, origin and possible moving group membership as well as the local gravitational potential. The Solar neighbourhood is also visited by halo stars which – as a population – have no definite sense of rotation. If the Galaxy were old enough the phase-space distribution of stars would be fully "phase-mixed"; however we observe it to be richly sub-structured, because phase-space substructure is conserved. To understand these sub-structures from a theoretical point of view one needs to know the basic mathematical principles behind the orbits of stars.

This chapter serves as an introduction to the fields of stellar dynamics and potential theory. It provides the essential mathematical concepts that will be needed for the remainder of this thesis. Some topics that follow are just briefly outlined; more informations will be found in the cited works.

In addition, we present in Section 4.4.4 our own studies on an effective third integral of the stellar orbits, which lays the theoretical groundwork for the use of larger samples in future studies of the vertical gravitational potential.

4.1 General Aspects and Definitions

4.1.1 The Gravitational Potential

The orbit of a star depends on the gravitational potential created by all other gravitating matter around the star, and hence the orbits of stars can be used to get information about the gravitational potential and the mass density distribution of their host galaxy.

¹this definition of the Solar neighbourhood is chosen for our applications; much more often it is quite a bit smaller (50-100 pc).

Newton's law of gravity tells us that a star of mass m_1 at position \mathbf{r}_1 is attracted by another star of mass m_2 at position \mathbf{r}_2 with the force

$$\mathbf{F}(\mathbf{r}_1) = m_1 \frac{d^2 \mathbf{r}_1}{dt^2} = -\frac{Gm_1 m_2}{|\mathbf{r}_1 - \mathbf{r}_2|^3} (\mathbf{r}_1 - \mathbf{r}_2) \quad (4.1)$$

(G is Newton's gravitational constant).

In a cluster of N stars with masses m_α ($\alpha = 1, 2, \dots, N$) at positions \mathbf{r}_i the force acting on the star α is the sum of the forces from every other star:

$$\mathbf{F}_i(\mathbf{r}_i) = m_i \frac{d^2 \mathbf{r}_i}{dt^2} = -\sum_{\substack{j \\ i \neq j}} \frac{Gm_i m_j}{|\mathbf{r}_i - \mathbf{r}_j|^3} (\mathbf{r}_i - \mathbf{r}_j) \quad (4.2)$$

In the case of a continuous distribution of stars the summation is replaced by the integration over the whole volume. If we allow the mass density to vary with time and define the gravitational potential as

$$\Phi(\mathbf{r}, t) = -G \int \frac{\rho(\mathbf{r}', t)}{|\mathbf{r} - \mathbf{r}'|} d^3 \mathbf{r}', \quad (4.3)$$

we get for the force per unit mass at position \mathbf{r} at any time t

$$\mathbf{F}(\mathbf{r}, t) = -\nabla \Phi(\mathbf{r}, t) = G \int \frac{\rho(\mathbf{r}', t)(\mathbf{r} - \mathbf{r}')}{|\mathbf{r} - \mathbf{r}'|^3} d^3 \mathbf{r}'. \quad (4.4)$$

Note that the mass distribution $\rho(\mathbf{r}, t)$ can change with time as all the matter particles move with respect to each other.

Applying ∇^2 to both sides of (4.3) and using the *divergence theorem* (e.g. BT 1987), one obtains the **Poisson equation**:

$$\nabla^2 \Phi = 4\pi G \rho. \quad (4.5)$$

The Poisson equation is used in most cases to calculate the potential of a given mass density distribution.

The form of the potential and its geometrical properties confine the orbit that is allowed for a star. For example, the potential can be static and radially symmetric, i.e. $\Phi(\mathbf{r}, t) = \Phi(r)$ and this will confine the orbit to a plane called the orbital plane (see below). In the following, the potential is always assumed to be static.

4.1.2 The Distribution Function

Similar to the atoms of a gas, the motion of the stars of a stellar system such as a galaxy can be described statistically in the 6-dimensional **phase-space** (\mathbf{q}, \mathbf{p}) , where $\mathbf{q} = (q_1, q_2, q_3)$ are the n **generalized coordinates** and $\mathbf{p} = (p_1, p_2, p_3)$ their **conjugate momenta**.² Each star of a stellar system defines through its generalized coordinates \mathbf{q} and conjugate momenta \mathbf{p} a representative point in phase-space. Its orbit is then described by the evolution of the representative point under the **canonical equations of motion**

$$\dot{q}_i = \frac{\partial H}{\partial p_i}, \quad \dot{p}_i = -\frac{\partial H}{\partial q_i} \quad (i = 1, 2, 3), \quad (4.6)$$

²In the general case, a system may have n generalised coordinates $\mathbf{q} = (q_1, q_2, \dots, q_n)$ and conjugate momenta $\mathbf{p} = (p_1, p_2, \dots, p_n)$, so the phase-space (\mathbf{q}, \mathbf{p}) has $2n$ dimensions.

where $H = H(\mathbf{p}, \mathbf{q}, t)$ is the Hamiltonian function.

However, when describing a stellar system statistically, we are not so much interested in the particular orbit of a specific star, but in the density of representative points in a particular region of phase-space and their average movement. Therefore we introduce the **distribution function** $f(\mathbf{q}, \mathbf{p}, t)$ as the density of representative points in phase-space, so that $f(\mathbf{q}, \mathbf{p}, t)d^3\mathbf{q}d^3\mathbf{p}$ is the number of stars that at time t have generalised coordinates between \mathbf{q} and $\mathbf{q} + d\mathbf{q}$ and conjugate momenta between \mathbf{p} and $\mathbf{p} + d\mathbf{p}$. For stellar systems that are in equilibrium, the time-dependence of the distribution function vanishes.

The distribution function is the most important quantity in the field of Galactic Dynamics. If $f(\mathbf{q}, \mathbf{p}, t)$ is known for a stellar system, it is possible to derive all kinds of observable photometric and kinematical data from it. Furthermore, f contains information about the dynamical properties of the system that cannot be directly observed. For example, the spatial number density of the system $\rho(\mathbf{r}, t)$ is obtained by integration of the distribution function over velocities,

$$\nu(\mathbf{r}, t) = \int_{-\infty}^{+\infty} f(\mathbf{r}, \mathbf{v}, t) d^3\mathbf{v}. \quad (4.7)$$

In turn, $\nu(\mathbf{r}, t)$ can be used to get the gravitational potential via Poisson's equation (4.5).

The surface mass density $\Sigma(\mathbf{R}, t)$, e.g. of the Milky Way disk, where $\mathbf{R} = (x, y)$, is given through

$$\Sigma(\mathbf{R}, t) = \int_{-\infty}^{+\infty} \int_{-\infty}^{+\infty} f(\mathbf{r}, \mathbf{v}, t) dz d^3\mathbf{v} \quad (4.8)$$

Practically, it is not possible to measure the distribution function $f(\mathbf{r}, \mathbf{v}, t)$ at any phase-space point (\mathbf{r}, \mathbf{v}) . What is rather measured is the so-called **coarse-grained distribution function** $|f|$, which is an average value of f in a finite phase-space cell centered at (\mathbf{r}, \mathbf{v}) .

4.1.3 The Collisionless Boltzmann Equations

As the representative points of stars of a stellar system move smoothly with time, their density $f(\mathbf{q}, \mathbf{p}, t)$ obeys **Liouville's theorem**

$$\frac{df}{dt} = 0 \quad (4.9)$$

which states that *the distribution function is constant along any trajectory in phase-space*. In other words, the number density of stars in any infinitesimally small phase-space element $d^3q d^3p$ is conserved during the evolution of the stellar system. equation (4.9) can be re-written by using

$$\frac{d}{dt} = \frac{\partial}{\partial t} + \sum_{i=1}^3 \left(\dot{p}_i \frac{\partial}{\partial p_i} + \dot{q}_i \frac{\partial}{\partial q_i} \right) \quad (4.10)$$

together with the canonical equations of motion (4.6) as

$$\frac{\partial f}{\partial t} + \sum_{i=1}^3 \left(\frac{\partial H}{\partial p_i} \frac{\partial f}{\partial q_i} - \frac{\partial H}{\partial q_i} \frac{\partial f}{\partial p_i} \right) = 0. \quad (4.11)$$

We will apply Liouville's theorem to a **collisionless** system of stars; this is a system in which encounters between stars can be ignored so that every star moves under the mean gravitational potential $\Phi(\mathbf{r}, t)$ of the system, where $\mathbf{r} = (x_1, x_2, x_3)$ is the position vector of a star with respect to the center. In general, galaxies and star clusters are collisionless systems. In this case the Hamiltonian for a star of mass m is given by

$$H = \frac{\mathbf{p}^2}{2m} + \Phi(\mathbf{r}, t). \quad (4.12)$$

$\mathbf{p} = m\mathbf{v}$ with $\mathbf{v} = \dot{\mathbf{r}}$ is the classical linear momentum. Therefore one can also consider (\mathbf{r}, \mathbf{v}) as the "phase-space", and the phase-space density f becomes a function of \mathbf{r} and \mathbf{v} . From equation (4.12) together with (4.6) follows

$$\begin{aligned} \frac{\partial H}{\partial p_i} &= \frac{p_i}{m} = v_i \\ \frac{\partial H}{\partial x_i} &= \frac{\partial \Phi}{\partial x_i}, \end{aligned} \quad (4.13)$$

so Liouville's theorem (equation 4.11) now takes the form

$$\frac{\partial f}{\partial t} + \sum_{i=1}^3 \left(v_i \frac{\partial f}{\partial x_i} - \frac{\partial \Phi}{\partial x_i} \frac{\partial f}{\partial v_i} \right) = 0, \quad (4.14a)$$

or

$$\frac{\partial f}{\partial t} + \mathbf{v} \cdot \nabla f - \nabla \Phi \cdot \frac{\partial f}{\partial \mathbf{v}} = 0. \quad (4.14b)$$

Equations (4.14) are called the **collisionless Boltzmann equations**; they are the fundamental equations of stellar dynamics. The collisionless Boltzmann equations can be regarded either as linear homogenous partial differential equations for f or as linear non-homogenous partial differential equations for Φ . Finding a solution can be either accomplished by knowing the potential Φ and solving for f or vice versa. Generally, the collisionless Boltzmann equations cannot be solved, because they involve seven independent variables. Instead, numerical solutions using N -body simulations must be sought. However, in the next section it is shown that solutions can be obtained if the potential is static and has some kind of symmetry.

Phase-Mixing

A sub-population of stars with small initial displacements and velocity dispersions will have slightly different orbital frequencies. Its representative points that evolve under the canonical equations of motion (4.6) will disperse in phase-space, leading to a distortion of the initial phase-space volume. Thereby the phase-space density f around any point in phase-space remains constant according to the collisionless Boltzmann equations. This behaviour, however, is of little use for an observer, because he will always measure the coarse-grained density $|f|$. Initially $f = |f|$, but as the system evolves, the phase-space regions with high density stretch out and get thinner; the coarse-grained density decreases with time until a final equilibrium state is achieved. In practise this means that in an observational volume the stellar density of the sub-population decreases and its velocity dispersion increases with time.

4.1.4 Integrals of Motion

Constants of motion are functions $C(\mathbf{r}, \mathbf{v}, t)$ of the phase-space coordinates (\mathbf{r}, \mathbf{v}) and time t , which are constant along any stellar orbit:

$$C(\mathbf{r}(t), \mathbf{v}(t), t) = \text{const.} \quad (4.15)$$

Their value depends on the specific orbit, but is constant along that orbit. This is true for every orbit.

An **integral of motion** $I(\mathbf{r}, \mathbf{v})$ is a function of the phase-space coordinates alone, that is constant along any stellar trajectory in phase-space. It does not depend on time:

$$I(\mathbf{r}(t), \mathbf{v}(t)) = \text{const.} \quad (4.16)$$

So every integral of motion is also a constant of motion, while the reverse is not true. Examples for integrals of motion are the energy E in a static potential or the z-component of angular momentum L_z in an axisymmetric potential. Integrals of motion allow the identification of stellar streams even if their stars are dispersed in configuration space (see also Section 6.2).

Each integral of motion defines a hypersurface in phase-space through equation (4.16). If the phase-space has $2n$ dimensions there must exist $2n - 1$ independent integrals of motion, so the trajectory is the intersection of the $2n - 1$ trajectories (Ollongren, 1962; Henon and Heiles, 1964). But integrals of motion can be either **isolating** or **non-isolating**. A non-isolating integral of motion is infinitely many-valued, i.e. the corresponding hypersurface consists of an infinity of sheets which fill the phase-space densely. Practically, these integrals give no information and are equivalent to no conditions at all. Non-isolating integrals play no role in Galactic dynamics. On the other hand, isolating integrals have the property of isolating points on a star's trajectory from neighbouring points in phase-space.

Regular orbits are those that have as many isolating integrals as spatial dimensions n . A regular orbit can formally be decomposed into n independent periodic oscillations (Binney and Tremaine, 1987). Orbits with less isolating integrals than spatial dimensions are called **irregular** orbits.

It is worth to investigate the content of equation (4.16) in more detail. If it is rewritten as

$$\frac{d}{dt}I(\mathbf{r}(t), \mathbf{v}(t)) = 0, \quad (4.17)$$

then

$$\frac{dI}{dt} = \nabla I \frac{d\mathbf{r}}{dt} + \frac{\partial I}{\partial \mathbf{v}} \frac{d\mathbf{v}}{dt} = 0, \quad (4.18a)$$

or

$$v \cdot \nabla I - \nabla \Phi \cdot \frac{\partial I}{\partial \mathbf{v}} = 0. \quad (4.18b)$$

A comparison with equations (4.14) shows that the condition that I is an integral of motion is equivalent to the condition that I is a steady-state solution to the collisionless

Boltzmann equations. Furthermore, if $f(I_1, I_2, \dots, I_n)$ is any function of n integrals of motion, then f also satisfies the collisionless Boltzmann equations, because

$$\frac{d}{dt}f(I_1(\mathbf{r}, \mathbf{v}), \dots, I_n(\mathbf{r}, \mathbf{v})) = \sum_{m=1}^n \frac{\partial f}{\partial I_m} \frac{dI_m}{dt} = 0. \quad (4.19)$$

So any function of the integrals of motion yields a solution to the (stationary) collisionless Boltzmann equation. This statement is sometimes referred to as the **Jeans theorem** (Binney and Tremaine, 1987, Sect. 4.4). Note that the function which solves the Boltzmann equation can be a function of up to any number of integrals that the potential admits. However, because the non-isolating integrals have no influence on the density distribution, the distribution function is a function of the isolating integrals only.

4.2 Coordinate systems and velocities

In studying the Milky Way's overall structure by observations from Earth, different coordinate systems prove useful for different aspects. These will be described in the following sections.

4.2.1 Definitions

Coordinates

The **Equatorial coordinate system** (α, δ) , which is closely related to the Earth's latitude-longitude system, does not participate in Earth's rotation. Figure 4.1 shows how the coordinates and reference points are defined. The projection of the Earth's equator onto the celestial sphere is called the **celestial equator**. Similarly, projecting the geographic poles onto the celestial sphere defines the north and south **celestial poles**. The point where the Sun crosses the celestial equator in spring is called the **vernal equinox**. The **declination** δ is the equivalent of geographical latitude and measured in degrees north or south of the celestial equator. The analog to longitude is the **right ascension** α which is measured in hours eastward along the celestial equator starting from the vernal equinox to the intersection with the great circle that passes through the observed object and the north celestial pole.

Because the Equatorial coordinate system is based on the celestial equator and the vernal equinox, the right ascension and declination of an object are independent of the geographical latitude and longitude of the observer and the annual motion of the Earth around the Sun. However, when studying the kinematics of stars in the Solar neighbourhood, it is more beneficial to define a coordinate system which reflects the symmetry of the underlying gravitational potential. Such a symmetry is naturally introduced by the existence of the Galactic disk. The Sun is located almost in the middle of the disk, called the **Galactic midplane**, approximately 8 kpc from the Galactic center (Reid, 1993); its offset is only about 24 pc above the plane (Jurč et al., 2008). The intersection of the celestial sphere with the Galactic midplane therefore very nearly forms a great circle, the **Galactic equator**. The **Galactic coordinate system** (l, b, d) is based on the Sun and reflects the symmetry of the Galactic plane as it is viewed from Earth (Figure 4.2). The two angles **Galactic longitude** l and **latitude** b give the direction of an object in the sky and

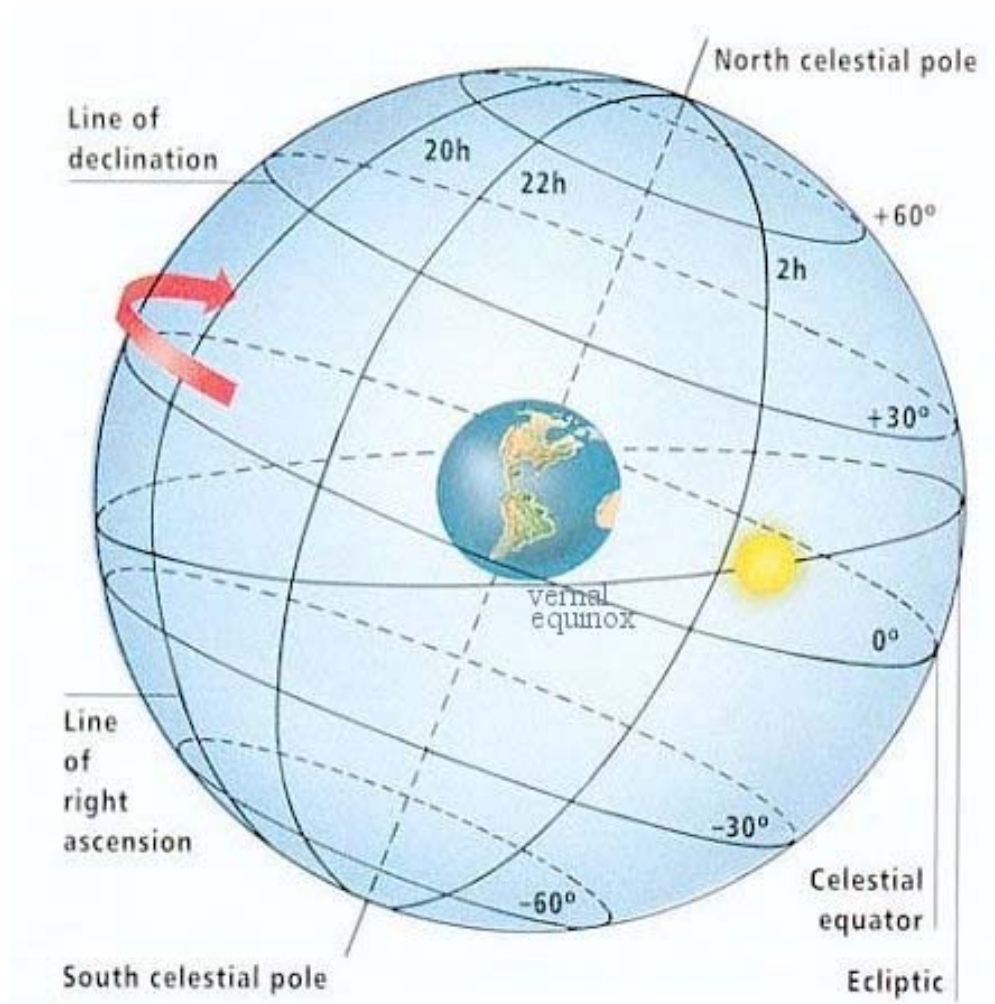


Figure 4.1: The Equatorial coordinate system. Right ascension α is measured in hours eastward along the celestial equator starting at the vernal equinox. Declination δ is measured in degrees north or south of the celestial equator.

d its distance. The latitude is measured in degrees north (b positive) or south (b negative) of the Galactic equator, so it ranges between $b = +90^\circ$ and $b = -90^\circ$. The longitude ranges from $l = 0^\circ$ (roughly in the direction of the Galactic center), eastwards through $l = 90^\circ$ (roughly in the direction of Galactic rotation), and on to $l = 360^\circ$. The International Astronomical Union (IAU) defined the Galactic coordinate system in reference to the Equatorial coordinate system in 1959 (Blaauw et al., 1960).

Besides the Galactic coordinate system, a heliocentric Cartesian coordinate system is very useful to describe the motion of stars in the Solar vicinity. We will use a right-handed coordinate system with the x -axis pointing towards the Galactic center ($l \simeq 0^\circ$), the y -axis in the direction of Galactic rotation ($l \simeq 90^\circ$) and the z -axis towards the North Galactic Pole ($b \simeq 90^\circ$)³

³The goal of setting up the Galactic coordinate system was to "choose a system which is so oriented that the direction of the pole is perpendicular to the mean plane of the Galaxy, and the zero of longitude passes through the Galactic center" (Blaauw et al., 1960); the small deviations of

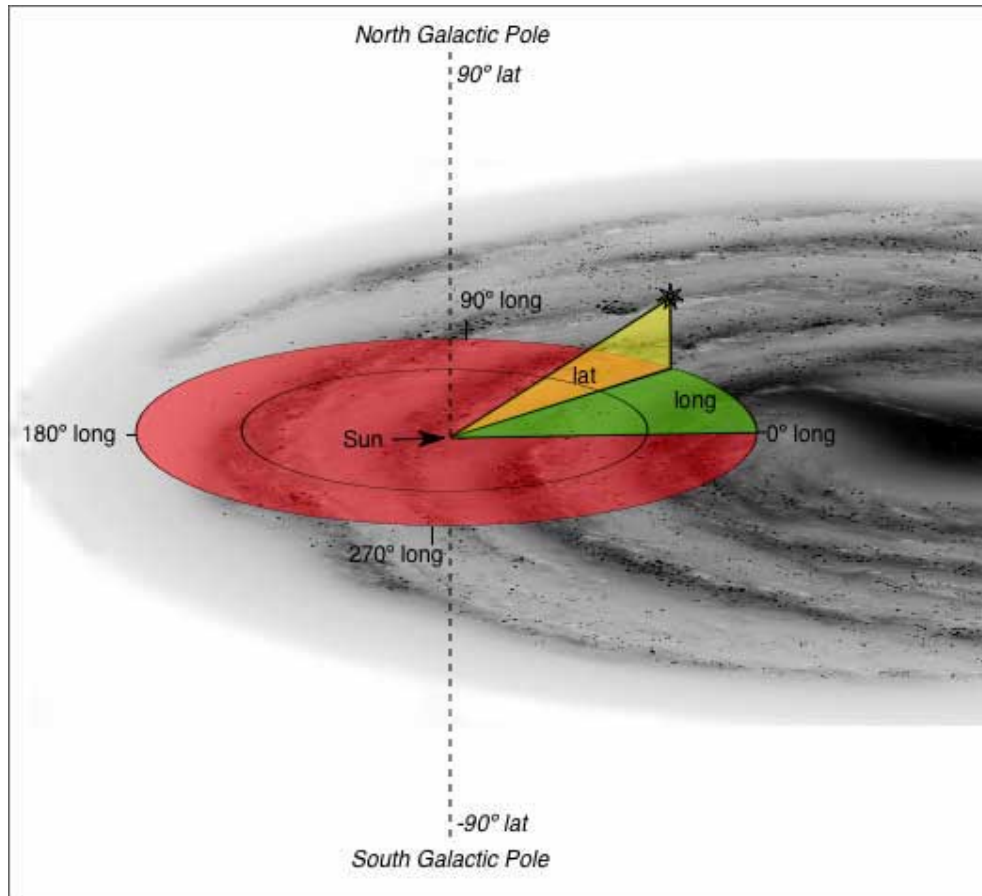


Figure 4.2: The Galactic coordinate system based on the Sun. Longitude l is measured along the Galactic equator and increases eastwards from the Galactic center. Latitude b is measured north or south of the Galactic equator.

Finally, for studies of large scale structure and kinematics of stars a cylindrical coordinate system (R, ϕ, z) is introduced with the origin at the center of the Milky Way. The radial coordinate R increases outwards, the angular coordinate ϕ is pointed in the direction of Galactic rotation and z increases to the north (and is equivalent to z in the Cartesian coordinate system defined above). Figure 4.3 recapitulates the different coordinates that can be assigned to a star and the unit vectors are given in equations (4.20a)-(4.20c).

$l = 0^\circ$ and $b = 0^\circ$ from the direction of the Galactic center and pole can be neglected compared to measurement accuracies.

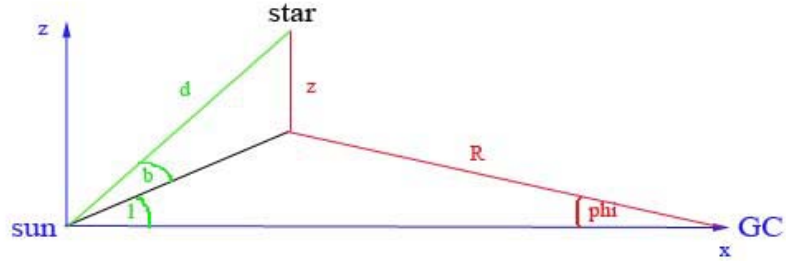


Figure 4.3: Coordinates normally assigned to stars when studying Galactic dynamics. The Cartesian and Galactic coordinate systems are heliocentric while the cylindrical coordinate systems is based on the Galactic center as the center of the gravitational potential.

$$\vec{e}_x = \begin{pmatrix} 1 \\ 0 \\ 0 \end{pmatrix}, \quad \vec{e}_y = \begin{pmatrix} 0 \\ 1 \\ 0 \end{pmatrix}, \quad \vec{e}_z = \begin{pmatrix} 0 \\ 0 \\ 1 \end{pmatrix} \quad (4.20a)$$

(Cartesian coordinates)

$$\vec{e}_d = \begin{pmatrix} \cos b \cos l \\ \cos b \sin l \\ \sin b \end{pmatrix}, \quad \vec{e}_b = \begin{pmatrix} -\sin b \cos l \\ -\sin b \sin l \\ \cos b \end{pmatrix}, \quad \vec{e}_l = \begin{pmatrix} -\sin l \\ \cos l \\ 0 \end{pmatrix} \quad (4.20b)$$

(Galactic coordinates)

$$\vec{e}_R = \begin{pmatrix} \cos \varphi \\ \sin \varphi \\ 0 \end{pmatrix}, \quad \vec{e}_\varphi = \begin{pmatrix} \sin \varphi \\ \cos \varphi \\ 0 \end{pmatrix}, \quad \vec{e}_z = \begin{pmatrix} 0 \\ 0 \\ 1 \end{pmatrix} \quad (4.20c)$$

(Cylindrical coordinates)

Velocities

Each of the coordinate systems described above implies different velocity components which are given by the derivatives of the coordinates. When observing the motion of stars from the Earth (or equivalently from the Sun) one can measure their line-of-sight and tangential velocity components. The tangential velocity appears as a slow, angular change in Equatorial or Galactic coordinates and is known as the **proper motion** $\vec{\mu}$. The

line-of-sight or **radial velocity** component is equal to the change in line-of-sight distance, $v_{rad} = \dot{d}$. Because the Sun itself is orbiting the Galactic center on a non-circular orbit, it is better for our studies to refer the spatial velocity of stars to the **Local Standard of Rest** (LSR) (\vec{v}_{LSR}) or to the Galactic center (\vec{v}_{gc}). The LSR is defined as the space velocity at a perfectly circular orbit around the Galactic Center through the position of the Sun. That means, the position of the LSR is exactly at the Sun at every time, while the Sun is moving away from it.

The velocity components referred to the LSR are given as:

$$\vec{v}_{LSR} = U \vec{e}_x + V \vec{e}_y + W \vec{e}_z \quad (4.21)$$

$$= v_{rad} \vec{e}_d + 4.74 d \mu_b \vec{e}_b + 4.74 d \mu_l \vec{e}_l, \quad (4.22)$$

with $U = \dot{x}$, $V = \dot{y}$, $W = \dot{z}$, $v_{rad} = \dot{d}$, $\mu_b = \dot{b}$ and $\mu_l = \dot{l} \cos b$. If μ_l and μ_b are taken in units of $[\text{mas yr}^{-1}]$ and d in $[\text{kpc}]$, the factor 4.74 gives the result in $[\text{km s}^{-1}]$.

The space velocity referred to the GC is given by:

$$\vec{v}_{gc} = \Pi \vec{e}_R + \Theta \vec{e}_\varphi + Z \vec{e}_z \quad (4.23)$$

$$= (U + U_\odot) \vec{e}_x + (V + V_\odot + V_{LSR}) \vec{e}_y + (W + W_\odot) \vec{e}_z, \quad (4.24)$$

with $\Pi \equiv \dot{R}$, $\Theta \equiv R \dot{\varphi}$ and $Z \equiv \dot{z}$. The Sun's space velocity relative to the LSR is (Dehnen and Binney, 1998)

$$U_\odot = 10.0 \pm 0.4 \text{ km/s} \quad (4.25a)$$

$$V_\odot = 5.2 \pm 0.6 \text{ km/s} \quad (4.25b)$$

$$W_\odot = 7.2 \pm 0.4 \text{ km/s}, \quad (4.25c)$$

while the current IAU standard for the LSRs circular velocity is

$$V_{LSR} = \Theta_\odot = 220 \text{ km/s} \quad (4.26)$$

. From now on I will drop the index gc and simply write \vec{v} . This velocity and its components actually goes into the calculation of a star's orbital energy and angular momentum (see Section 4.4.1). To derive \vec{v} from the measured velocity components ($v_{rad}, \vec{\mu}$), one has to know the transformations from one set of velocities to another. These will be given in the following subsection.

4.2.2 Transforming Coordinates and Velocities

We summarize the transformations between the different coordinate systems and velocity components. All coordinates can be calculated from Equatorial coordinates and among each other through straightforward matrix operations:

$$\begin{pmatrix} \cos b \cos l \\ \cos b \sin l \\ \sin b \end{pmatrix} = \mathbf{T} \begin{pmatrix} \cos \delta \cos \alpha \\ \cos \delta \sin \alpha \\ \sin \delta \end{pmatrix} \quad (4.27)$$

$$\begin{pmatrix} x \\ y \\ z \end{pmatrix} = d \cdot \begin{pmatrix} \cos b \cos l \\ \cos b \sin l \\ \sin b \end{pmatrix} \quad (4.28)$$

$$\begin{pmatrix} x \\ y \\ z \end{pmatrix} = \begin{pmatrix} R_{\odot} \\ 0 \\ 0 \end{pmatrix} + \begin{pmatrix} R \cos \phi \\ R \sin \phi \\ z \end{pmatrix}. \quad (4.29)$$

R_{\odot} is the distance of the Sun from the Galactic center; the transformation matrix \mathbf{T} is given in Johnson and Soderblom (1987, Section III) as

$$\mathbf{T} = \begin{pmatrix} -0.06699 & -0.87276 & -0.48354 \\ +0.49273 & -0.45035 & +0.74458 \\ -0.86760 & -0.18837 & +0.46020 \end{pmatrix}. \quad (4.30)$$

The calculations of a star's space velocity in the case that the proper motions are measured along right ascension α and declination δ is also given in Johnson and Soderblom (1987, Section III):

$$\begin{pmatrix} U \\ V \\ W \end{pmatrix} = \begin{pmatrix} U_{\odot} \\ V_{\odot} \\ W_{\odot} \end{pmatrix} + \mathbf{B} \begin{pmatrix} v_{rad} \\ 4.74 \mu_{\alpha} d \\ 4.74 \mu_{\delta} d \end{pmatrix} \quad (4.31)$$

The coordinate transformation matrix \mathbf{B} is defined in Johnson and Soderblom (1987) and we evaluated it for the epoch 2000 as

$$\mathbf{B} = \begin{pmatrix} -0.063491 \cos \alpha \cos \delta & 0.063491 \sin \alpha & 0.063491 \cos \alpha \sin \delta \\ -0.86554 \sin \alpha \cos \delta & -0.86554 \cos \alpha & +0.86554 \sin \alpha \sin \delta \\ -0.496799 \sin \delta & & -0.496799 \cos \delta \\ 0.493076 \cos \alpha \cos \delta & -0.493076 \sin \alpha & -0.493076 \cos \alpha \sin \delta \\ -0.460007 \sin \alpha \cos \delta & -0.460007 \cos \alpha & +0.460007 \sin \alpha \sin \delta \\ +0.738424 \sin \delta & & +0.738424 \cos \delta \\ -0.867666 \cos \alpha \cos \delta & 0.867666 \sin \alpha & 0.867666 \cos \alpha \sin \delta \\ -0.198076 \sin \alpha \cos \delta & -0.198076 \cos \alpha & +0.198076 \sin \alpha \sin \delta \\ +0.455984 \sin \delta & & +0.455984 \cos \delta \end{pmatrix} \quad (4.32)$$

If the proper motions are given as (μ_l, μ_b) , the transformations are:

$$\begin{pmatrix} U \\ V \\ W \end{pmatrix} = \begin{pmatrix} U_{\odot} \\ V_{\odot} \\ W_{\odot} \end{pmatrix} + \mathbf{D} \begin{pmatrix} v_{rad} \\ 4.74 \mu_b d \\ 4.74 \mu_l d \end{pmatrix} \quad (4.33)$$

$$\begin{pmatrix} v_{rad} \\ 4.74 \mu_b d \\ 4.74 \mu_l d \end{pmatrix} = \mathbf{D}^{-1} \begin{pmatrix} U - U_{\odot} \\ V - V_{\odot} \\ W - W_{\odot} \end{pmatrix} \quad (4.34)$$

where the transformation matrix \mathbf{D} is given as

$$\mathbf{D} = \begin{pmatrix} \cos b \cos l & -\sin b \cos l & -\sin l \\ \cos b \sin l & -\sin b \sin l & \cos l \\ \sin b & \cos b & 0 \end{pmatrix} \quad (4.35)$$

$$\mathbf{D}^{-1} = \begin{pmatrix} \cos b \cos l & \cos b \sin l & \sin b \\ -\sin b \cos l & -\sin b \sin l & \cos b \\ -\sin l & \cos l & 0 \end{pmatrix} \quad (4.36)$$

Note the addition of the sun's peculiar motion with respect to the LSR to the velocity components, because (U, V, W) refer to the LSR restframe.

When transforming velocity components from the Cartesian LSR-restframe (x, y, z) to the cylindrically symmetric restframe (R, ϕ, z) one can use the following formulas:

$$\begin{pmatrix} U \\ V \\ W \end{pmatrix} = \mathbf{E} \begin{pmatrix} \Pi \\ \Theta \\ Z \end{pmatrix} \quad (4.37)$$

$$\begin{pmatrix} \Pi \\ \Theta \\ Z \end{pmatrix} = \mathbf{E}^{-1} \begin{pmatrix} U \\ V \\ W \end{pmatrix}, \quad (4.38)$$

where the matrix \mathbf{E} is given as

$$\mathbf{E} = \mathbf{E}^{-1} = \begin{pmatrix} -\cos \varphi & \sin \varphi & 0 \\ \sin \varphi & \cos \varphi & 0 \\ 0 & 0 & 1 \end{pmatrix}. \quad (4.39)$$

The angle φ between star-GC-sun can be expressed through

$$\tan \varphi = \frac{d \cos b \sin l}{R_{\odot} - d \cos b \cos l} \quad (4.40)$$

Usually, φ is very small if we deal with stars in the solar neighbourhood, $\varphi \approx 7.12^\circ$ for a star at 1 kpc distance at $(l, b) = (90^\circ, 0)$, and the velocity components can be approximated by

$$\begin{aligned} U + U_{\odot} &\simeq -\Pi \\ V + V_{LSR} + V_{\odot} &\simeq \Theta. \end{aligned} \quad (4.41)$$

It's important to mention that all of the above velocity components are absolute, that means they refer to a fixed coordinate system with the Sun at rest. If we want to transform some galactocentric velocities (e.g. that are output from some simulations) to velocities as observed from the earth (e.g. v_{rad}, μ_b, μ_l), the solar motion around the Galactic center has to be concerned. Vice versa, if radial velocities and proper motions from some star catalogue should be transformed to absolute space velocities, the solar motion around the Galactic center must be added to the result.

4.3 Orbits in Spherical Potentials

In a spherically-symmetric potential $\Phi = \Phi(|\mathbf{r}|)$, the total angular momentum of a star, $\mathbf{L} = \mathbf{r} \times \frac{d\mathbf{r}}{dt}$, is conserved. It follows that the star moves in a plane perpendicular to its angular momentum vector, so it is intuitive to introduce a polar coordinate system $(R = |\mathbf{r}|, \phi)$. The phase-space associated with this system thus has 4 dimensions, of which 2 are spatial.

The Hamiltonian H of this system is given through

$$H(R, \phi, v_R, L) = \frac{1}{2}(v_R^2 + v_\phi^2) + \Phi(R), \quad (4.42)$$

where $v_R = \dot{R}$ is the radial and $v_\phi = R\dot{\phi} = L/R$ the azimuthal velocity component. $L = |\mathbf{L}|$ is the absolute value of the total angular momentum. v_R and L are the conjugate momenta to the coordinates R and ϕ , respectively.

The equations of motion follow from the Hamiltonian (4.42):

$$\begin{aligned} \frac{dR}{dt} &= \frac{\partial H}{\partial v_R} = v_R, & \frac{dv_R}{dt} &= -\frac{\partial H}{\partial R} = -\frac{d\Phi}{dR} + \frac{L^2}{R^3}, \\ \frac{d\phi}{dt} &= \frac{\partial H}{\partial L} = \frac{L}{R^2}, & \frac{dL}{dt} &= -\frac{\partial H}{\partial \phi} = 0. \end{aligned} \quad (4.43)$$

Here $\frac{dL}{dt} = 0$ because the conjugate coordinate ϕ does not appear in H ; ϕ is called a **cyclic coordinate**. Thus, there are two isolating integrals, namely the energy E , which is numerically equal to H , and the total angular momentum L . Each of these two integrals defines a hypersurface in phase-space, and the orbit is confined to the intersection of these two hypersurfaces.

For an orbit of given L , the system may be reduced to one degree of freedom by defining the **effective potential**

$$\Phi_{eff}(R) = \Phi(R) + \frac{L^2}{2R^2}. \quad (4.44)$$

Then the equations of radial motion (Eqs.4.43) reduce to

$$\begin{aligned} \frac{dR}{dt} &= v_R \\ \frac{dv_R}{dt} &= -\frac{d\Phi_{eff}}{dR}. \end{aligned} \quad (4.45)$$

The centrifugal barrier term $L^2/2R^2$ in the effective potential prohibits the star from coming too close to the center. The star will periodically move back and forth between the two turning points R_{min} , called **pericenter**, and R_{max} , called **apocenter**. These turning points depend on the energy and angular momentum of the star and are defined through the condition $E = \Phi_{eff}(R_{min/max})$.

Additionally, the star executes periodic azimuthal motions. When the radial and azimuthal periods are commensurable, as is the case only for the Keplerian and the harmonic potential, the orbit is called a **resonant orbit**; it will close upon itself in phase-space. For the Keplerian potential - the potential of a point mass - the radial and azimuthal periods for all bound orbits are equal and bound orbits form ellipses with the center of the potential in one focus. In the harmonic potential generated by a homogenous spherical mass distribution the radial period is half the azimuthal one. An orbit in the harmonic potential resembles an ellipse centered on the bottom of the potential well. In the Keplerian case all

stars advance in azimuth by $\Delta\phi = 2\pi$ between successive pericenters, while in the harmonic case they advance by $\Delta\phi = \pi$. Galaxies are more extended than point masses and less extended than homogenous spheres, so a star in a typical spherical galaxy will advance by an angle between π and 2π between successive pericenters. In configuration space, such an orbit with incommensurable frequencies describes a rosette in which a star will eventually pass through every point on an annulus whose inner and outer radii are the peri- and apocenter distances. Larger orbital energies result in larger apocenters, while smaller angular momentum gives a smaller pericenter. Orbits like these are an example of so called **loop orbits**, which generally fill elliptical annuli. The closed circular or elliptical orbits can be thought of as the **parents** of a **family** of loop orbits that have the same energy and angular momentum.

4.4 Orbits in Axisymmetric Potentials

4.4.1 The Meridional Plane

Orbits in potentials which are axisymmetric with respect to the z -axis are best studied using cylindrical coordinates (R, ϕ, z) . The potential can then be written as $\Phi = \Phi(R, z)$. Again, it is straightforward formulating the equations of motion starting with the Hamiltonian

$$H(R, \phi, v_R, L) = \frac{1}{2}(\Pi^2 + \Theta^2 + Z^2) + \Phi(R, z), \quad (4.46)$$

where $\Pi = \dot{R}$, $\Theta = R\dot{\phi}$ and $Z = \dot{z}$ (Section 4.2.1). The equations of motion of a star accord to the spherically symmetric case (equations 4.43) with additional expressions for z and Z :

$$\begin{aligned} \frac{dR}{dt} &= \Pi, & \frac{d\Pi}{dt} &= -\frac{d\Phi}{dR} + \frac{L_z^2}{R^3}, \\ \frac{d\phi}{dt} &= \frac{L_z}{R^2}, & \frac{dL_z}{dt} &= 0, \\ \frac{dz}{dt} &= Z, & \frac{dZ}{dt} &= -\frac{d\Phi}{dz}. \end{aligned} \quad (4.47)$$

The z -component of the angular momentum $L_z = R^2\dot{\phi}$ is conserved and hence an integral of motion, the second integral besides the energy E . This integral of motion reduces a star's orbit to a two-dimensional non-uniformly rotating plane, the **meridional plane**, under the influence of an effective potential

$$\Phi_{eff} \equiv \Phi(R, z) + \frac{L_z^2}{2R^2}. \quad (4.48)$$

Instead of governing motion along a line as in the spherical case, the effective potential now governs the star's motion in the meridional plane, which rotates about

the z -axis. The orbit in the meridional plane can also be regarded as the cylindrical projection of the three-dimensional orbit in a fixed plane (Ollongren, 1962). Again note that, as R decreases, the repulsive force of the effective potential grows.

Using the effective potential, the equations of motion (4.47) in the meridional plane reduce to

$$\begin{aligned}\ddot{R} &= -\frac{\partial \Phi_{eff}}{\partial R} \\ \ddot{z} &= -\frac{\partial \Phi_{eff}}{\partial z}.\end{aligned}\tag{4.49}$$

The meridional plane has cartesian coordinates (R, z) and rotates around the z -axis with the angular velocity defined through

$$\Omega(R) = \dot{\phi} = \frac{L_z}{R^2}.\tag{4.50}$$

The angular velocity gives the third velocity component of the three-dimensional space orbit:

$$\Theta(R) = R\Omega(R) = \frac{L_z}{R}.\tag{4.51}$$

The energy E is the sum of kinetic energy of motion in the (R, z) -plane and the effective potential energy:

$$E = \frac{1}{2}(\Pi^2 + \Theta^2 + Z^2) + \Phi(R, z) = \frac{1}{2}(\Pi^2 + Z^2) + \Phi_{eff}.\tag{4.52}$$

On the meridional plane the effective potential Φ_{eff} has a minimum where

$$\begin{aligned}0 &= \frac{\partial \Phi_{eff}}{\partial R} = \frac{\partial \Phi}{\partial R} - \frac{L_z^2}{R^3} \\ 0 &= \frac{\partial \Phi_{eff}}{\partial z}.\end{aligned}\tag{4.53}$$

The second condition is fulfilled everywhere on the plane where $z = 0$. The first is true for a certain radius, called the **guiding center** (or **epicenter**) radius R_0 , which is given through

$$\left. \frac{\partial \Phi}{\partial R} \right|_{(R_0, 0)} = \frac{L_z^2}{R_0^3} = R_0 \Omega^2(R_0).\tag{4.54}$$

This is the radius of a circular orbit of a particle which moves with angular speed $\Omega(R_0) \equiv \Omega_0$ and has angular momentum L_z . This circular path is the orbit with minimum energy E_0 for a given L_z . The energy of a star on the circular orbit at R_0 obviously is

$$E_0 = \Phi(R_0) + \frac{1}{2}R_0^2\Omega_0^2.\tag{4.55}$$

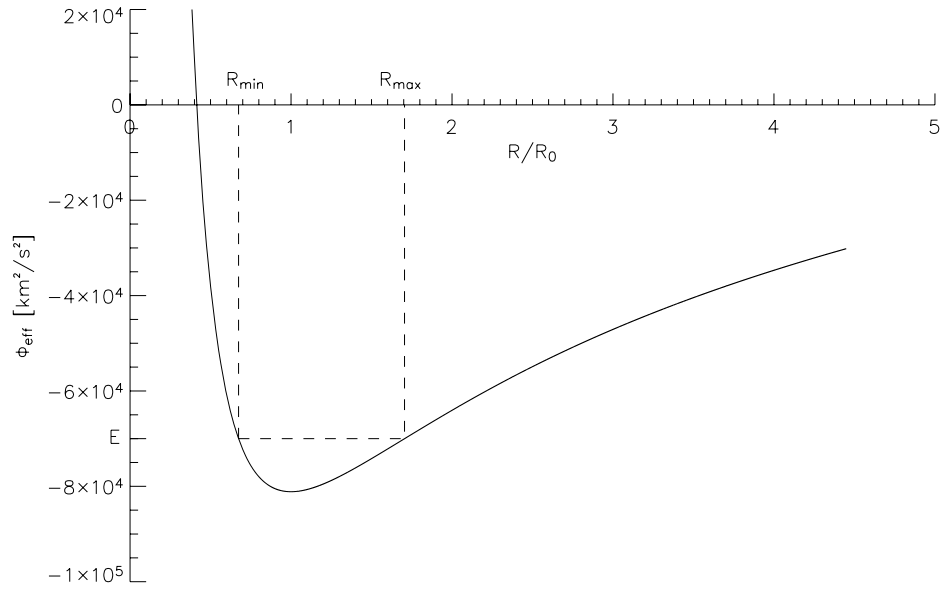


Figure 4.4: Effective potential for a particular choice of $\Phi(R, z)$ (see equation 5.1 in Section 5.1) and $L_z = 100 \text{ kpc km s}^{-1}$.

The circular orbit is stable, and any other orbit with the same L_z , but higher energy, must oscillate around it in vertical and radial direction. Figure 4.4 shows the effective potential which we have computed for a standard Milky Way potential (see Section 5.1 in Part II) and a star of angular momentum $L_z = 100 \text{ kpc km s}^{-1}$. The star will move between the two turning points R_{min} and R_{max} , that are defined by the condition $E = \Phi_{\text{eff}}(R_{\text{min}/\text{max}})$.

4.4.2 The Epicycle Approximation

If the oscillations of a star around its stable circular orbit are small, i.e. the orbit of a star is nearly circular, one can derive approximate solutions for the equations of motion (4.49). The most popular approximation, the **epicycle** approximation (Binney and Tremaine, 1987, Sect. 3.2.3), uses a Taylor expansion of the effective potential Φ_{eff} around its minimum $(R_0, 0)$ up to second order:

$$\Phi_{\text{eff}} = \Phi_{\text{eff}}(R_0, 0) + \frac{1}{2} \frac{\partial^2 \Phi_{\text{eff}}}{\partial R^2} \Big|_{(R_0, 0)} (R - R_0)^2 + \frac{1}{2} \frac{\partial^2 \Phi_{\text{eff}}}{\partial z^2} \Big|_{(R_0, 0)} z^2 + \dots \quad (4.56)$$

With the definition of the two frequencies

$$\kappa_0^2 \equiv \frac{\partial^2 \Phi_{\text{eff}}}{\partial R^2} \Big|_{(R_0, 0)} \quad \text{and} \quad \nu_0^2 \equiv \frac{\partial^2 \Phi_{\text{eff}}}{\partial z^2} \Big|_{(R_0, 0)}, \quad (4.57)$$

the equations of motion in the meridional plane (4.49) become

$$\begin{aligned} \ddot{R} &= -\kappa_0^2 (R - R_0) \\ \ddot{z} &= -\nu_0^2 z^2. \end{aligned} \quad (4.58)$$

Thus the motion of a star in the meridional plane on a nearly circular orbit can be described as two independent harmonic oscillations around $(R_0, 0)$ with the **epicycle frequency** κ_0 in radial and the **vertical frequency** ν_0 in vertical direction.

Inserting the definition of the effective potential from equation (4.48) into (4.57), one gets

$$\kappa_0^2 = \left. \frac{\partial^2 \Phi}{\partial R^2} \right|_{(R_0, 0)} + \frac{3L_z^2}{R_0^4} \quad (4.59)$$

$$\nu_0^2 = \left. \frac{\partial^2 \Phi}{\partial z^2} \right|_{(R_0, 0)}. \quad (4.60)$$

The epicycle frequency is connected to the angular frequency and velocity at R_0 through equations (4.50) and (4.51):

$$\kappa_0^2 = R \left. \frac{\partial \Omega^2}{\partial R} \right|_{R_0} + 4\Omega_0^2 = 2 \frac{\Theta^2(R_0)}{R_0^2}. \quad (4.61)$$

In the solar neighbourhood the ratio $\frac{\kappa_0}{\Omega_0} = 1.3 \pm 0.2$ (BT 1987) and $\frac{\nu_0}{\kappa_0} \approx 1.9$. That means, the sun makes 1.3 radial oscillations while one full rotation around the Galactic center and 1.9 vertical oscillations while one radial period. This is also the reason why phase-mixing is more efficient in the vertical direction. In general, the orbit of a star in an axisymmetric potential is not closed in an inertial frame, but forms a rosette figure.

4.4.3 The Keplerian Approximation

Dekker (1976) has shown that the epicyclic approximation is only valid if the orbit of a star is very close to circular, i.e. its eccentricity $e \ll 1$. For stronger deviations, up to $e = 0.5$, Dekker provides another approximation, which she calls the Keplerian approximation, because now the potential is expanded with respect to $\frac{1}{R}$ around $\frac{1}{R_0}$ (also up to second order). Here, R_0 denotes again the epicenter radius, where the effective potential has its minimum. We will concentrate on the planar motion in the plane $z = 0$ and simply write $\Phi(R, 0) = \Phi(R)$. Then we get

$$\Phi(R) = \Phi(R_0) + \left. \frac{\partial \Phi}{\partial \left(\frac{1}{R}\right)} \right|_{R_0} \left(\frac{1}{R} - \frac{1}{R_0}\right) + \frac{1}{2} \left. \frac{\partial^2 \Phi}{\partial \left(\frac{1}{R}\right)^2} \right|_{R_0} \left(\frac{1}{R} - \frac{1}{R_0}\right)^2 + \dots \quad (4.62)$$

Note that now we do not expand the effective potential, but the true potential. With the definition of the angular frequency $\Omega(R)$, equation (4.50), the Taylor coefficients are

$$\left. \frac{\partial \Phi}{\partial \left(\frac{1}{R}\right)} \right|_{R_0} = -R_0 \Omega_0^2 \quad (4.63)$$

$$\left. \frac{\partial^2 \Phi}{\partial \left(\frac{1}{R}\right)^2} \right|_{R_0} = R_0^4 (\kappa_0^2 - \Omega_0^2), \quad (4.64)$$

and expression (4.62) becomes

$$\Phi(R) = A_0 - \frac{B_0}{R} + \frac{C_0}{R^2}, \quad (4.65)$$

where

$$A_0 = E_0 + \frac{1}{2}R_0^2\kappa^2 \quad (4.66)$$

$$B_0 = R_0^3\kappa_0^2 \quad (4.67)$$

$$C_0 = \frac{1}{2}R_0^4(\kappa_0^2 - \Omega_0^2). \quad (4.68)$$

The effective potential, Φ_{eff} , then can be written as (up to second order):

$$\Phi_{eff}(R) = A_0 - \frac{B_0}{R} + \frac{2C_0 + R_0^4\Omega_0^2}{2R^2}, \quad (4.69)$$

similar to the one in the Kepler problem. Above we have shown that the turning points of the radial motion in the plane $z = 0$ in an axisymmetric potential are given by $E = \Phi_{eff}(R_{min/max})$. Inserting the effective potential (4.69), we get for the turning points in the Keplerian approximation

$$\frac{R_{min}}{R_0} = \frac{1}{1+e} \quad \text{and} \quad \frac{R_{max}}{R_0} = \frac{1}{1-e}, \quad (4.70)$$

with

$$e = \sqrt{\frac{2(E - E_0)}{R_0^2\kappa_0^2}} \quad (4.71)$$

being the eccentricity. The Keplerian approximation shows that the orbits are characterized through the isolating integrals E and L_z .

We will now derive expressions for e and L_z using a star's velocity components with respect to the LSR (U, V) for planar motion in the Solar neighbourhood (Fuchs, private communication). For stars near the Sun we have

$$L_z = R_0^2\Omega(R_0) = R_0V_{LSR} = R_\odot(V + V_{LSR}). \quad (4.72)$$

The last step assumes that the rotation curve is flat. It follows that

$$R_0 = R_\odot\left(1 + \frac{V}{V_{LSR}}\right) \quad (4.73)$$

Now we can express the effective potential (4.69) at the Solar position as

$$\begin{aligned} \Phi_{eff}(R_\odot) &= E_0 + \frac{1}{2}R_0^2\kappa_0^2\left(1 - 2\frac{R_0}{R_\odot} + \frac{R_0^2}{R_\odot^2}\right) \\ &\stackrel{(4.61),(4.26)}{=} E_0 + V_{LSR}^2\left(1 - \frac{R_0}{R_\odot}\right)^2 \\ &\stackrel{(4.73)}{=} E_0 + V_{LSR}^2\left(1 - 1 - \frac{V}{V_{LSR}}\right)^2 = E_0 + V^2. \end{aligned} \quad (4.74)$$

The energy in the effective potential at the Solar position follows from equation 4.52 as

$$E(R_\odot) = \frac{U^2}{2} + \Phi_{\text{eff}}(R_\odot) = E_0 + V^2 + \frac{U^2}{2} \quad (4.75)$$

So we have $2(E(R_\odot) - E_0) = U^2 + 2V^2$ and the eccentricity e of a nearby star's orbit follows from (4.71) as

$$e = \sqrt{\frac{U^2 + 2V^2}{R_0^2 \kappa_0^2}} \quad (4.76)$$

$$\stackrel{(4.61)}{=} \frac{1}{\sqrt{2}V_{\text{LSR}}} \sqrt{U^2 + 2V^2}$$

Dekker's Keplerian approximation is a very powerful tool when searching for stars on essentially the same orbits (stellar streams or moving groups). We will give a more detailed description in Section 5.3.

4.4.4 The Third Integral And Surfaces Of Section

In this section we describe in principle established material, but also present some new calculations geared towards a new method to estimate the K_z -force law.

The Third Isolating Integral Of Motion

It is interesting to ask what part of the phase-space associated with an axisymmetric potential will be filled if one follows a star over many revolutions within a galaxy. Because the phase-space $(R, \phi, z, \dot{R}, \dot{\phi}, \dot{z})$ is six-dimensional, any trajectory must be defined by 5 integrals of motion, corresponding to 5 hypersurfaces in phase-space (see Section 4.1.4). The trajectory is the intersection of these hypersurfaces. In the case of an axisymmetric potential, two isolating integrals are already known: The energy E , also called I_1 , and angular momentum L_z , also called I_2 . Besides these two integrals, there cannot be more than one additional independent isolating integral (Ollongren, 1962). If it exists, it is called the **third integral** I_3 .

Obtaining an analytical expression for I_3 is only possible in very special cases; one of them is if the stellar orbit oscillates with small amplitudes around the guiding center, i.e. if the epicycle approximation is valid. Then it follows from the equations of motion (4.58) that the energies of the two oscillators

$$E_R = \frac{1}{2}\dot{R}^2 + \kappa^2(R - R_0)^2 \quad (4.77)$$

$$E_z = \frac{1}{2}\dot{z}^2 + \nu^2 z^2$$

are conserved and hence integrals of motion. Additionally the angular momentum L_z is constant along the stellar orbit. All these integrals are isolating.

More generally, we have shown to our knowledge for the first time that for a realistic axisymmetric Milky Way potential (Johnston et al., 1999, see equation 5.1 in Section 5.1) the adiabatic integral of the vertical motions of the stars

$$J_z = \frac{1}{2}W^2(R, z) + \Phi(R, z) - \Phi(R, 0) / \sqrt{\rho(R, z)} \quad (4.78)$$

is an effective third integral of the stellar orbits for thin disk stars, $J_z = I_3$. This is true, even if the distribution of stars and the Galactic potential have non-negligible radial gradients. Here, $\rho(R, z)$ is the density associated with the potential as given by Poisson's equation (4.5). In Figure 4.5 we show a comparison between J_z and the vertical orbital energy E_z along stellar orbits. The stars have been launched at the Solar position $(R, z) = (8, 0)$ kpc, and their orbits have been integrated in the Johnston et al. (1999) potential (with a spherical dark halo). The initial Cartesian velocities of the stars are indicated in the panels as follows: The $J_z(R)$ - and $E_z(R)$ -curves run at higher values for higher W -velocities. The three colors purple, green and red correspond to the initial V -velocities as indicated in the box in the upper right of each plot. Finally, different panels corresponds to different initial U -velocities. Note how the radial excursions depend on the initial U - and V -velocities ($R^2 = U^2 + V^2$ at any time). While J_z does practically not vary during the radial excursions of a star and is thus quite close to "isolating", E_z shows a strong dependence on the radial variation of the orbit already at very low values of W .

The constancy of J_z along a star's orbit is not quite perfect; visible from Figure 4.5 is the trend that small radial variations emerge when the initial W -velocity component increases, leading to higher vertical oscillations. In Figures 4.6 and 4.7 we investigate the behaviour of J_z for more sets of initial velocities and show that the usability of J_z as an integral of motion breaks down at about $W \approx 30 \text{ km s}^{-1}$.

This study shows that the adiabatic integral of the vertical motions of the stars is approximately conserved along the orbit of a typical disk star and can be treated as an effective third integral of motion. It lays the theoretical groundwork for future investigations of the vertical gravitational potential of the Milky Way's disk. This has been determined in the past mainly under the assumption that its radial gradient is negligible (see Section 8 for more details); now such studies can be repeated, but in a column perpendicular to the Galactic plane with a broader base than in previous studies.

If it is not possible to derive an analytic expression for the third integral I_3 , one can still decide whether such an isolating integral exists by numerical orbit integrations. Therefore it is useful to introduce the concept of **surfaces of section**.

Surfaces of Section

The phase-space associated with the movement in the meridional plane under the influence of the effective potential (4.48) has four dimensions. So there must exist three integrals of motion, of which one, the energy $E(R, z, \dot{R}, \dot{z}) \equiv I_1$ is known to

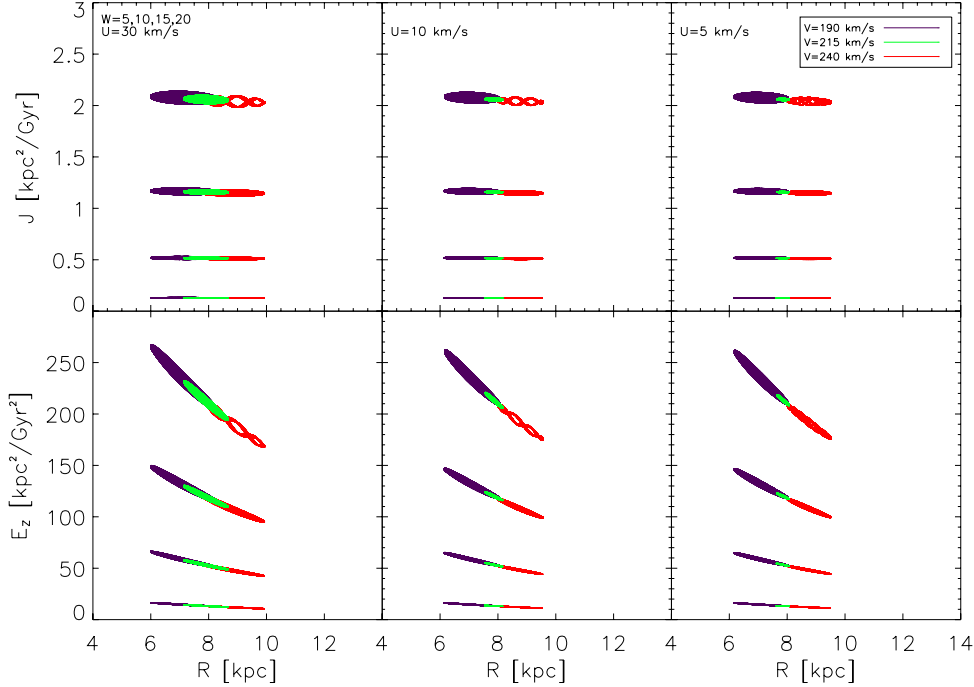


Figure 4.5: Behaviour of the adiabatic integral of the vertical motion J_z and the vertical energy E_z along stellar orbits in the Johnston et al. (1999) potential. The orbits have been integrated in a Johnston et al. (1999) potential starting at the Solar position $(R, z) = (8, 0)$ kpc. The values of J_z and E_z increase with increasing initial W -velocities. The radial R -excursions depend on the initial U - and V -velocities, which we indicate through different panels and colors, respectively.

be isolating. Note that the effective potential could be an arbitrary planar potential with no general symmetry, so there is no integral of angular momentum. The three-dimensional orbit, however, does respect an angular momentum isolating integral. Since the energy is conserved, one can restrict the movement to a three-dimensional sub-manifold, e.g. (R, z, \dot{R}) . \dot{z} would then be determined (to within the sign) through R, z, \dot{R} and the known value of E from

$$E = \frac{1}{2}(\dot{R}^2 + \dot{z}^2) + \Phi_{eff}(R, z). \quad (4.79)$$

Since the value of \dot{z}^2 found from (4.79) is always non-negative, we get the condition

$$E \geq \frac{1}{2}\dot{R}^2 + \Phi_{eff}(R, z). \quad (4.80)$$

This condition defines a bound volume in phase-space, which will be filled by the trajectory of a star, if E is the only isolating integral. It can be shown that one of the integrals, say I_3 , is generally non-isolating. However, the nature of the remaining integral I_2 can be determined from the condition whether the trajectory will fill the volume defined by equation (4.80), or will lie on a surface whose equation can be found by elimination of \dot{z} between (4.80) and $I_2 = \text{const.}$.

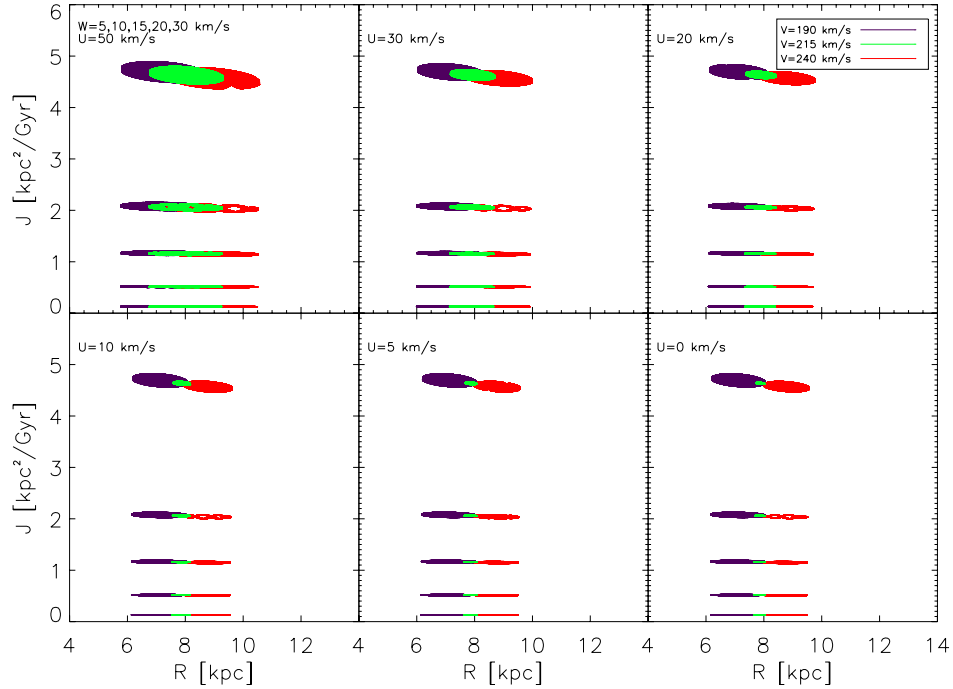


Figure 4.6: Evolution of J_z along stellar orbits with initial conditions as displayed in the panels. For values of $W \geq 20 \text{ km s}^{-1}$ the radial variations of I_3 become greater and its usability as an integral of motion is no longer warranted.

Because the three-dimensional trajectory is still hard to imagine, one can make things easier by plotting only the intersection of the trajectory with the plane $z = 0$ every time the star goes up, i.e. $\dot{z} > 0$. This is equivalent to plotting a point in the (R, \dot{R}) -plane every time the orbit satisfies

$$z = 0, \quad \dot{z} > 0. \quad (4.81)$$

If I_2 were non-isolating, the points would fill the area

$$E \geq \frac{1}{2} \dot{R}^2 + \Phi_{eff}(R, 0), \quad (4.82)$$

which is the intersection of the volume (4.80) with the plane $z = 0$. However, in practise it is observed that the points rather lie on a curve, implying the existence of a second isolating integral (Binney and Tremaine, 1987, Fig.3.4).

4.5 Summary

In this chapter we laid the theoretical groundwork for the following two parts of this thesis. Besides definitions of various coordinate systems and velocities, which we use to describe the position of stars in phase-space, we summarized the most important concepts of stellar orbits in spherical and axisymmetric potentials.

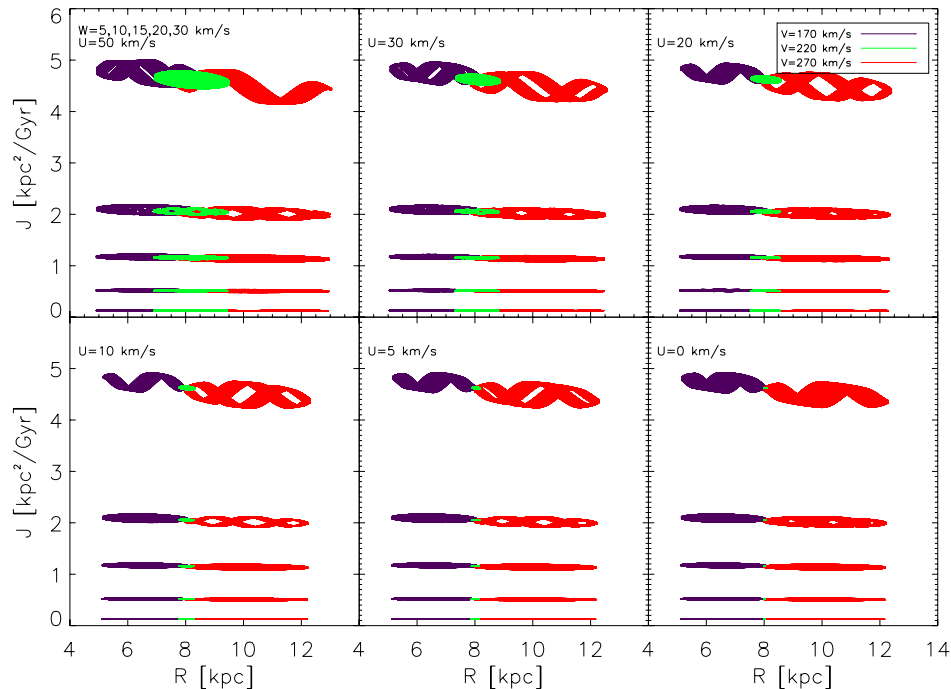


Figure 4.7: Same as Figure 4.6, but for different initial V -velocities.

In Chapter 6, where we mainly look for substructure among disk stars, we will assume an axisymmetric potential; in contrast our goal in Chapter 7 is to identify stellar halo streams, which are more subject to a (nearly) spherical potential. For these chapters Dekker's (1974) Keplerian approximation and its application to nearby stars with (U, V, W) -velocities is an essential tool.


The existence of an effective third integral of motion for thin disk stars in the form of the adiabatic vertical integral J_z for the first time justifies the separate estimation of the disk's potential in the vertical and radial direction. Also, in future studies a sample of stars with a broader base than in previous cone-samples can be used.

Part II

Searching for Stellar Streams in the Solar Neighbourhood

Chapter 5

Search Strategies and Stream Properties

ithin the last few years it has become more and more obvious that the phase space distribution of stars in the Solar neighbourhood is highly substructured (e.g. Eggen, 1996; Dehnen, 1998; Helmi et al., 1999; Chiba and Beers, 2000; Nordstrom et al., 2004; Arifyanto and Fuchs, 2006). The substructure is caused by stellar streams or moving groups, i.e. groups of stars on essentially the same Galactic orbits. The distribution of stellar streams in phase space is not uniform, reflecting the diversity of their origin, age and type. There are three possible reasons for phase-space overdensities. i) Stars that were born in the same molecular cloud keep moving at the same rate and in the same direction of space as the original cloud, but disperse on timescales of ~ 0.2 Gyr (Wielen, 1971). ii) Field stars of various origins that herded into small regions of phase space through dynamical resonances. iii) Stars that have been tidally stripped from their precursor system. Stellar streams show up also as clumps in the space of integrals of motion (e.g. Helmi et al., 1999), reflecting the strong connection between the stream stars even after spatial dispersion. Any attempt to detect such "overdensities" of stars either in phase- or integrals of motion-space depends on what one expects for the "smooth background". In this chapter we show what discriminates stellar streams from the "smooth expectations" and how the observables of stars (positions, proper motions, radial velocities, magnitudes, metallicities etc.) can be used to find groups of stars belonging to stellar streams.

5.1 Stellar Streams in Configuration Space

Neglecting young moving groups for now¹, one should distinguish between two types of streams: dynamical streams, that is, groups of stars that are trapped in a small region of phase space by dynamical resonances, and tidal streams, in which the stars originated from the same bound object, such as a globular cluster or

¹Of course, the very young open stars clusters appear as substructure in configuration space; however, in this section we concentrate on tidal streams.

a satellite galaxy. Dynamical streams consist of field stars with various origins herded into a small region of phase space, but they have no spatial connection. Therefore in this section we will only cover the spatial properties of tidal streams. Distinctive features of disrupting Milky Way satellites include the leading and trailing tidal tails which can be observed as a spectacular example stretching from the Sagittarius dwarf spheroidal (Ibata et al., 2001; Majewski et al., 2003; Belokurov et al., 2006) or globular cluster Palomar 5 (Odenkirchen et al., 2001; Grillmair and Dionatos, 2006). The physical processes that lead to the formation of these streamers are complex in nature because they involve a large number of stars (10^5 – 10^7) and depend on the shape of the Milky Way’s gravitational potential, the masses of the Milky Way and satellite including their halos and the eccentricity of the orbit. On the other hand, modelling the observed properties of tidal streams can give insights into the Milky Way’s potential and the stream progenitor as was shown e.g. by Johnston et al. (1999); Peñarrubia et al. (2005); Fellhauer et al. (2007).

Johnston et al. (1996) studied the disruption of satellites which were represented by a Plummer (1911) model in a three-component Milky Way potential (equation 5.1, see below). They found that, for a Milky Way with a spherical halo, debris trails can remain aligned in streamers near the parent satellite’s original orbit over the lifetime of the Galaxy if the initial satellites velocity dispersion is small compared to its orbital velocity. Helmi and White (1999) used similar simulations under the restriction that the satellite’s orbit passes the Solar neighbourhood. They pointed out that for non-spherical potentials the alignment in thin streams breaks down, because the orbital plane of the satellite no longer has a fixed orientation. The stream stars rather get spread over several tens of kpc within 10-14 Gyr. This would explain why no stream-like density structures have yet been found in the Solar vicinity (Seabroke et al., 2008).

We simulate the evolution of a tidal stream and study its spatial distribution at different times.² Therefore, we integrate N particles which have normally distributed velocities from the same starting position in a fixed Milky Way potential. We define the **progenitor** of the stream as the hypothetical particle which has the exact initial velocities (zero dispersion). For the Milky Way potential we choose a three-component potential consisting of a Miyamoto-Nagai disk, a Hernquist bulge and a logarithmic halo. This sort of potential is widely used in the literature (e.g. Johnston et al., 1996; Helmi and White, 1999):

$$\begin{aligned}\Phi_{disk} &= -\frac{GM_{disk}}{\sqrt{R^2 + (a + \sqrt{z^2 + b^2})^2}} \\ \Phi_{bulge} &= -\frac{GM_{bulge}}{r + c} \\ \Phi_{halo} &= \frac{1}{2} v_c^2 \ln(x^2 + \frac{y^2}{p^2} + \frac{z^2}{q^2} + d^2).\end{aligned}\tag{5.1}$$

²These simulations are very general and can describe the dissolution of a newly formed star cluster as well as that of a Milky Way satellite galaxy, but not a resonance trapping.

$R = \sqrt{x^2 + y^2}$ and $r = \sqrt{x^2 + y^2 + z^2}$ denote the cylindrical and spherical radii, respectively, in a galactocentric coordinate system. The values of the parameters are $M_{disk} = 1.0 \times 10^{11} M_{\odot}$, $M_{bulge} = 3.4 \times 10^{10} M_{\odot}$, $v_c = 180 \text{ km s}^{-1}$ and $a = 6.5, b = 0.26, c = 0.7, d = 12.0$, each in kpc. The parameters were chosen to match the Galactic rotation curve. The flattening parameters p and q can be adjusted to represent an oblate, spherical or prolate halo. Figure 5.1 shows the isodensity (a) and isopotential (b) contours of the total potential $\Phi = \Phi_{disk} + \Phi_{bulge} + \Phi_{halo}$. Because we later want to simulate observations of

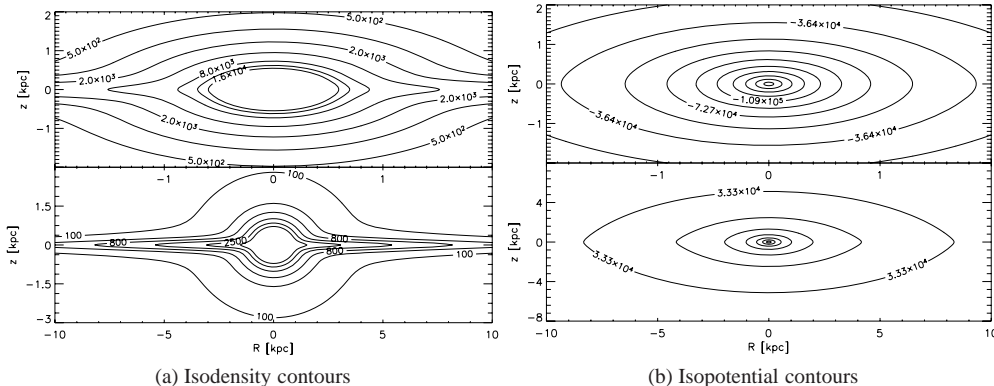


Figure 5.1: Form of the Milky Way potential given through equation 5.1 with $p=q=1$. This potential is used for our simulations of satellite disruption.

the stream particles in the Solar neighbourhood, we start with placing the stream’s progenitor at the Solar position $(x_{\odot}, y_{\odot}, z_{\odot}) = (-8.0, 0, 0.014) \text{ kpc}^3$ and choosing its infall direction (l_{gc}, b_{gc}) and velocity v_{gc} . Then we integrate it backwards in time using a leap frog integrator (Press, 2002) which is time reversible. At the new position we insert N particles with a Gaussian velocity distribution centered around the progenitor’s velocity components. Simulating the loss of particles at that position,⁴ we integrate each particle separately forward in time. We thereby neglect the gravitational attraction between the stars.

5.1.1 The Global Morphology of Stellar Streams

We use, as examples, four models with different initial conditions which are displayed in Table 5.1. In Figure 5.2 we show for models 1 and 2 the spatial distribution of $N = 200$ stream particles at different times of their orbital paths. The black filled circles mark the position of the progenitor orbit at times $t = 0, 0.1, 0.2, 0.5, 1.0$ and 2.0 Gyr, respectively, and the different colors correspond to the star’s positions at these times according to the legend.

³The distance of the Sun from the Galactic center was adopted from Reid (1993), and the vertical Solar offset $z_{\odot} = 14 \text{ pc}$ was taken from Jurić et al. (2008).

⁴We are interested only in the phase space distribution of the stream particles after a given time since disruption. Therefore we determine the position where stream particles are lost not through N-body-simulated tidal shocks as a result of the interaction between the precursor object and the Milky Way, but through the evolution time we are interested in.

Model	l_{gc} [°]	b_{gc} [°]	v_{gc} [km s ⁻¹]	t_{end} [Gyr]	σ [km s ⁻¹]	p	q	P [Gyr]
1	0	90	300	2	5	1	1	0.23
2	200	-45	300	2	5	1	1	0.22
3	a	60	30	216	2	5	1	0.15
	b	60	30	216	2	10	1	
	c	60	30	216	2	5	1	
	d	60	30	216	2	5	1	
	e	60	30	216	10	5	1	
4	30	-70	400	10	5	1	1	0.26

Table 5.1: Parameters of the models we use for our stream simulations. (l_{gc}, b_{gc}, v_{gc}) denote the direction and total velocity of the progenitor when it crosses the Sun at time t_{end} ; σ is the initial velocity dispersion of the stream particles at time $t = 0$. p and q are the halo potential’s flattening parameters from equation (5.1) and P the orbital period.

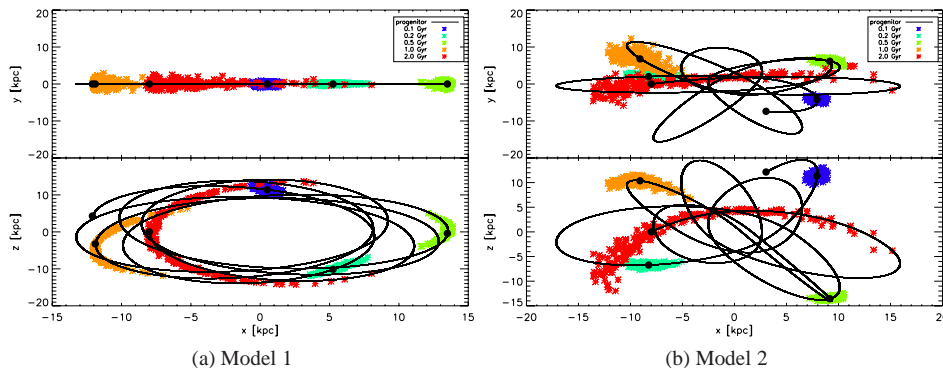


Figure 5.2: Orbital evolution of 200 stars from models 1 and 2. The black filled circles mark the position of the progenitor at times $t = 0, 0.1, 0.2, 0.5, 1.0$ and 2.0 Gyr in a Cartesian coordinate system (x, y, z) where the Sun is at $(-8.0, 0, 0.014)$ kpc. The initial velocity dispersion gives rise to a stream-like evolution of the particles which initially started at the same position at $t = 0$. Different colors represent the position of the stream particles at different times on their orbit.

The initial velocity dispersions alone lead to the formation of a leading and trailing tail, which increase their length and width with time. The stream particles stay principally aligned along the progenitor’s orbit at least until 2 Gyr after disruption. We further investigate how a change of the initial velocity dispersion and flattening of the halo potential effects the distribution of stream stars. Therefore we have changed these parameters in model 3 and show the resulting distributions in Figure 5.3.

As expected, an increase in the initial velocity dispersion σ leads to a broadening of the tails and a breakdown of the alignment at later times⁵. However, for this model the alignment in general is not as good as in models 1 and 2. This is due to the shorter period of model 3 compared to the other models; Helmi and White (1999) also found that the satellites with the shortest periods develop the greatest state of mixing, but that this process is still not completed after a Hubble time. We finally evolve model 3a over 10 Gyr and show the resulting distribution of stream

⁵In general, a cluster at the Solar radius with an initial velocity dispersion σ will be dispersed over all azimuths in a time $2\pi R/\sigma \approx 10$ Gyr for $\sigma = 5$ km s⁻¹ (Dehnen, 1998).

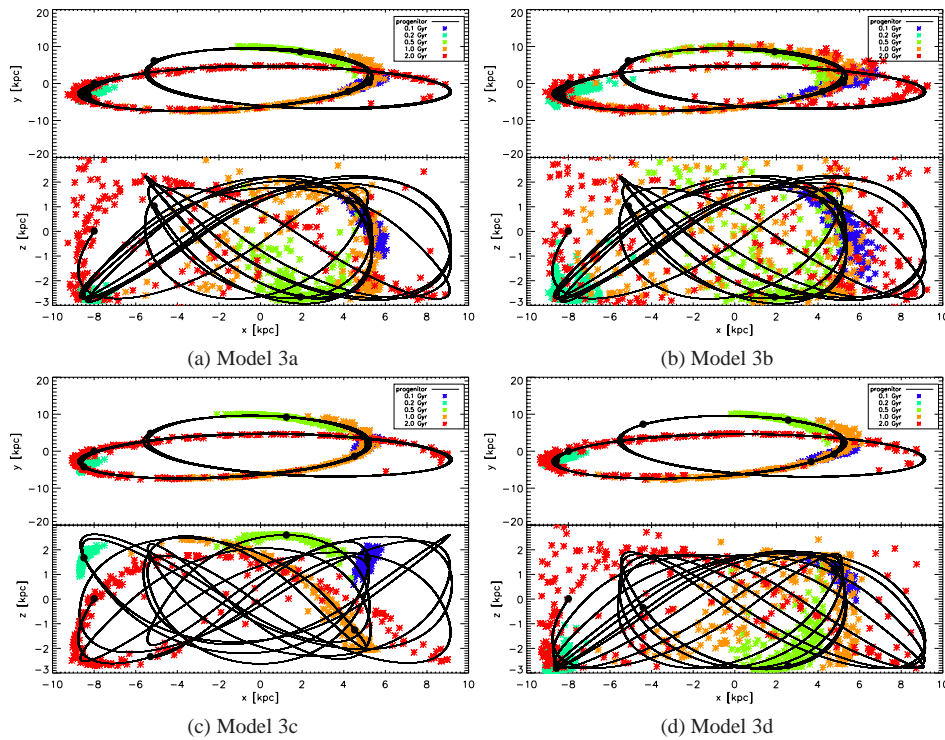


Figure 5.3: Same as Figure 5.2, but for different variations of model 3.

particles at 2.5, 5 and 10 Gyr in Figure 5.4 in the left panel. The right panel shows the analogue distribution for model 4 at 0.5, 1, 2.5, 5 and 10 Gyr. While for model 3a the alignment into stream-like structures breaks down between 2 and 2.5 Gyr (compare to panel mod3a in Figure 5.3), model 4 stays aligned at least until 5 Gyr. However, model 4 also reaches a much larger apocentric distance and its debris tails have a width of several kpc.

Although our simulations are very basic, because they neglect the time-varying potential of the satellite, they nevertheless give insights into how an initial velocity – or energy – dispersion leads to a spatial dispersion of particles with time. Recently, however, Choi et al. (2007) performed more detailed simulations of satellite disruption in a Λ CDM cosmology. They found that only for circular orbits the tails of small satellites (up to the size of Sagittarius) approximately followed the progenitor’s orbit. But for more massive satellites, and eccentric orbits in general, they found little correlation between the tail location and the satellite orbit. The ejected particles in the leading (trailing) tails continue to be decelerated (accelerated) by the satellite’s gravity, so that the leading tail fills the inner halo with ejecta. However, in a small enough volume these tails would behave like our simulated streams and we can ask what is the best way to characterize members of a given stream passing the Solar vicinity.

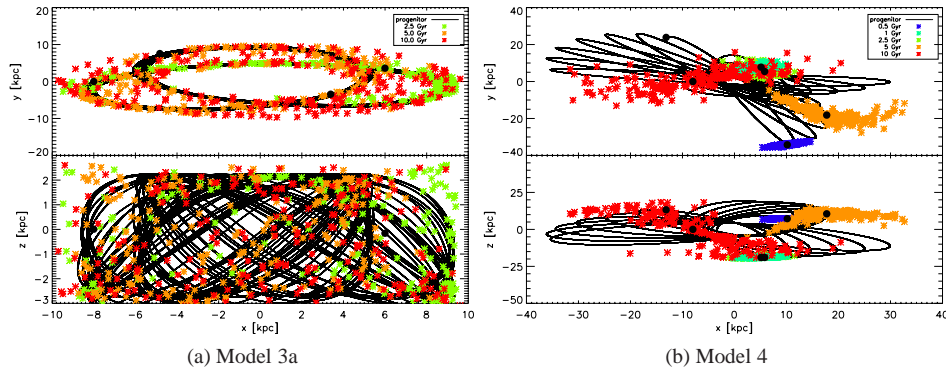


Figure 5.4: Orbital evolution of 200 stars from models 3a and 4. The black filled circles mark the position of the progenitor at times $t = 0, 0.5, 1.0, 2.0$ Gyr (left panel) and $t = 0, 0.1, 0.2, 0.5, 1.0, 2.0$ Gyr, respectively. Different colors represent the position of the stream particles at different times on their orbit, according to the legends in each plot.

Conclusions

We have seen that, even if the tail morphology is conserved, the stream particles can extend over several kpc. Therefore, to detect stellar streams as substructure in configuration space, two priors have to be fulfilled: i) the disruption process must have occurred not too long ago for the stars to be fully phase mixed and ii) due to the spatial extent of the debris, which increases with satellite mass and time, a large observational sky coverage is needed. If an old stellar stream passes the Solar neighborhood, a sphere of at most 2 kpc around the Sun, it will therefore not be recognized as a thin coherent stream. Instead any observer who wants to find tidal debris of disrupted satellites has to find out if other non-spatial correlations between the stream particles exist. Therefore the question is, how close the debris particles stay to the "same orbit", that is, the progenitor's orbit in our simulations. Apparently, the answer to this question depends on the parameters that are used to define an orbit. For example we have seen that in the Keplerian approximation, which is valid for eccentricities up to $e = 0.5$ (Section 4.4.3) an orbit in the (x, y) -plane is fully constrained by its energy E and z-component of the angular momentum L_z , that is, by its integrals of motion. In Section 5.3 we will investigate – again with the help of the simulations described above – what are the best proxies for characterizing the orbits of stars in order to find "overdensities" of stars on similar orbits. We will show that the stream particles are clustered in a space spanned by orbital eccentricity, azimuthal velocity and inclination angle of the orbital plane. But first, we stay in phase space and investigate the velocity distribution of stellar streams in more detail.

5.2 Stellar Streams in Velocity Space

Stellar streams are also called moving groups, because they show typical features in velocity space and appear as groups of stars moving in the same direction. In

this section we describe the velocity distribution of stellar streams in the Solar neighborhood, first for streams that share a common origin (tidal streams and dispersed young clusters) and then for dynamical streams that move close to resonant orbits.

5.2.1 The Velocity Distribution of Tidal Streams

The collisionless Boltzmann equations (equations 4.14 in Section 4.1.3) state that the phase space density around the phase point of any particular star is constant. It follows that, as a sub-population of stars disperses in configuration space, at any particular point in phase space they will grow together kinematically in an infinitesimally small volume around that point. It has been shown for example by Helmi and White (1999) that the velocity dispersions at each point along a *single* stellar stream consisting of stars lost at the same passage decrease overall with t^{-1} with some periodic oscillations due to the spatial density enhancements at the turning points. This is only of theoretical use, however, because in reality an observer measures the spatial and kinematical distribution of stars not at a point on a single stream, but in a finite volume. Phase mixing will lead to a steady decrease of the coarse-grained phase space density. The result is a broadening in the velocity distribution which is most prominent in the W -component, because the vertical frequency is shorter than the horizontal frequencies (see Figures 5.2-5.4). Nearby stream stars must have a narrow distribution in azimuthal velocity, because these stars have basically the same azimuthal frequency or, equivalently, angular momentum. It gets broader as the observational volume increases.

Old tidal streams near their apocenters will show a typical "banana"-shaped distribution in U and V and a symmetric distribution in U and W (Helmi and White, 1999; Helmi et al., 2006). The banana shape results because the stream stars have slightly different orbital phases. Stars located at the apocenter have $\Pi = 0$ and their lowest azimuthal velocity while those on their way towards or away from the apocenter have positive or negative Π -velocity, respectively.⁶ For similar reasons stars near their pericenter will show a switched and kinematically hotter banana-shaped (U, V) distribution. If the stars move on orbits that are highly inclined with respect to the Galactic plane, the azimuthal velocity can no longer be approximated by V ; instead, we can substitute the V -velocity by the azimuthal velocity in a spherical potential

$$V_{\text{az}} = \begin{cases} +\sqrt{(V + V_{\text{LSR}})^2 + W^2} & \text{if } V \geq 0, \\ -\sqrt{(V + V_{\text{LSR}})^2 + W^2} & \text{if } V < 0. \end{cases} \quad (5.2)$$

The banana shape will then show up in the (U, V_{az}) -distribution and only approximately in the (U, V) -distribution, if the dispersion in W is narrow. We will show in Section 5.3.2, equation (5.10), that the banana shape is predicted when stars move on orbits with similar eccentricities. In Dekker's Keplerian approximation the expression for the eccentricity describes an ellipse in U and V_{az} (see equation (4.76)

⁶For stars in the Solar vicinity $U \simeq -\Pi$ (Section 4.2.2).

for the case of motion in the (x, y) -plane, and equation (5.9) in Section 7.2). Even if the stars are somewhere between apo- and pericenter their (U, V_{az}) -distribution will form part of an ellipse; in this case a more clumplike (U, V) and a tilted (U, W) distribution will result (Helmi and White, 1999, their Figure 5). In reality, measurement errors tend to sphericalize the typical shapes of the velocity distribution. Also stellar encounters and scattering processes will randomly change stellar orbits and lead to a loss of the stream signature for these stars.

We try to confirm the theoretically expected distributions with our own simulations. Therefore we plot the velocity distribution of all stars from a given model with $N = 100,000$ stars that ended up within a given radius d_{max} around the Sun after 10 Gyrs of evolution. Figure 5.5 shows the velocity distribution of 173 stars from model 3e that ended up in a sphere of $d_{\text{max}} = 1$ kpc radius around the Sun. The stars belong to a stream of $N = 100,000$ stars that had been lost 10 Gyr ago. The progenitor's orbit at $t = 0$ passes exactly through the Sun in the direction given in Table 5.1. The spatial distribution of the stars can be derived from Figure 5.4, where 200 of the 100,000 stars are plotted. After 10 Gyr they are thoroughly phase-mixed and occupy a very large volume; only 173 out of 100,000 stars have ended up near the Sun. The exact velocities of these stars are displayed in the upper left panel in Figure 5.5, while in the other panels the velocities have been convolved with simulated observational errors. The upper right, lower left and lower right panels show how the velocity distribution gets affected when taking into account i) errors of 4 mas yr^{-1} in the proper motions (μ_l, μ_b) only, ii) 15% relative distance errors only, and iii) the effect of 4 mas yr^{-1} proper motion, 5 km s^{-1} radial velocity and 15% relative distance errors together. The symbols are color-coded according to the star's distance from the progenitor (and the Sun), the velocity of which is displayed as the black cross. From Figure 5.4 we see that the progenitor orbit at 10 Gyr is between apo- and pericenter, so we would expect a symmetric bimodal (U, V) - and (U, W) -distribution with a "gap" around $U = 0$, similar to that in Figure 5 in Helmi and White (1999). Indeed we find such a distribution in the upper left panel, although ours is much more concentrated in W . The difference is that we observe a single stream, while Helmi and White (1999) show a phase-mixed population of stars lost at different times (mainly at each pericentric passage). The velocity dispersion along the V - and V_{az} -velocity is narrow as expected. The dispersions in all directions increase with the distance from the progenitor. This behaviour is conserved even with observational errors, which sphericalize and broaden the velocity distribution. A proper motion error of $\sigma_\mu = 4 \text{ mas yr}^{-1}$ corresponds to an error of 19 km s^{-1} in the transverse velocity, v_\perp , at 1 kpc distance. The effect of the 15% relative distance error, $\frac{\sigma_d}{d}$, depends on the value of the proper motion. Both errors change the transverse velocity by the same amount, if at a given distance the total proper motion $|\vec{\mu}| = \sqrt{\mu_b^2 + \mu_l^2}$ is equal to $\sigma_\mu / \text{frac} \sigma_d \approx 27 \text{ mas yr}^{-1}$. We find that the mean product of the total proper motion and the distances of the 173 stars is $\langle d \cdot \sqrt{\mu_b^2 + \mu_l^2} \rangle = 25.6 \text{ kpc mas yr}^{-1}$, so we expect that the distance errors increase the velocity dispersion by a similar amount as the proper motion errors. This is what is observed in Figure 5.5.

However, when we include the effects of all observational errors, the transverse velocity will change by approximately $4.74d\sqrt{\sigma_\mu^2 + (\langle\mu/d\rangle\sigma_d)^2} = 26.3 \text{ km s}^{-1}$, which – together with the radial velocity error of $\sigma_{v_{\text{rad}}} = 5 \text{ km s}^{-1}$ – results in a $\sim 26.8 \text{ km s}^{-1}$ change in the total velocity.

The particles in Figure 5.5 sojourn in the Solar neighborhood at the same time at which the progenitor’s orbit passes the Sun, so these presumably are the particles that initially had the most similar velocity components with respect to the progenitor’s orbit. We investigate a second case, where the debris particles pass the Sun not coincidentally with the progenitor’s orbit. We insert 100,000 stars in model 2 (see Table 5.1) and pick out those that ended up inside a radius of $d_{\text{max}} = 2 \text{ kpc}$ of the Sun after 10 Gyr integration. In this model, the progenitor’s orbit passes the Solar position already after 2 Gyr and after 10 Gyr is in the halo at position $(x, y, z) = (12.4, -2.83, 11.9) \text{ kpc}$. We show in Figure 5.6 that the debris particles (marked as colored dots) pass the Solar neighborhood with approximately the same velocities as the progenitor’s orbit (marked by the black cross) 8 Gyr earlier, except for the W -component, which has the opposite sign for most stars. The colors show the displacement of each particle with respect to the Sun, and we can observe again a correlation between velocity dispersion and distance from the Sun. Also, simulating observational errors now leads to a larger effect than in model 3e, because the stars are on average farther away ($d_{\text{max}} = 2 \text{ kpc}$ instead of 1 kpc). Some errors change the value of the V -velocity such that its sign becomes positive, leading to a positive value of the azimuthal velocity V_{az} , which explains the few "outliers" in the (U, V_{az}) -distribution.

5.2.2 The Velocity Distribution of Young Moving Groups

A similar behaviour as described above for old tidal streams is true for young moving groups which consist of stars that were born in the same cluster or association in Giant Molecular Clouds. Through encounters of star-forming clusters with massive objects like the Giant Molecular Clouds themselves, they dissolve on a short timescale of about 0.2 Gyr; only 2% of them live longer than 1 Gyr (Wielen, 1971). The stars from these clusters, however, keep moving at approximately the same velocity in the same direction of the original cluster. Young moving groups can even be compact in the W -velocity, if the dynamical time in the vertical direction is shorter than the time since dissolution of the cluster. Again, they span a very narrow range in V velocity, because in the Solar neighbourhood they have the same azimuth. The (U, V) distribution is symmetrically elongated along the U -axis; one can think of it as only the middle part of the "banana", because stars have not yet spread over a high range of U velocities. Further, it is found that their orbits are more circular than that of old moving groups: the distribution of moving groups in the Solar vicinity follows an asymmetric drift relation similar to the smooth background (Dehnen, 1998). Almost all old moving groups have low angular momenta. One explanation is that some of these groups stem from a disrupted satellite galaxy and have been accreted on a highly eccentric orbit. Another

explanation is that some of these streams have been born inside the Solar circle on more eccentric orbits and immigrated radially outwards through their interaction with spiral arms (Sellwood and Binney, 2002).

It should be mentioned that the spatial density contrast of young moving groups in any surveyed volume of the Solar vicinity is higher than for old moving groups, so younger groups will always dominate the sample over older ones.

5.2.3 The Velocity Distribution of Dynamical Streams

The main moving groups observed in the Solar neighbourhood display structures different from those expected for dissolved or disrupted star clusters or galaxies. The distribution function in the (U, V) plane is dominated by a few branches that are parallel to each other and inclined to the U -axis by an angle of $\sim 15^\circ - 25^\circ$, but have no clearly defined shape nor boundary (Skuljan et al., 1999; Dehnen, 1998; Famaey et al., 2005, Antoja et al. 2008, in press). These structures are now thought to be of dynamical origin, consisting of stars that are trapped in a small region of phase space through perturbations of the axisymmetric potential (e.g. Sridhar and Touma, 1996; Dehnen, 2000; Fux, 2001; De Simone et al., 2004; Quillen and Minchev, 2005, Antoja et al., in press) Their location is primarily set by the rotational velocity component V , because V is a measure for the guiding radius of a star in the Solar neighbourhood, which itself is a measure for the location of Lindblad resonances with a periodic perturbation (Binney and Tremaine, 1987; Quillen and Minchev, 2005).

In practise it is not easy to clearly distinguish dynamical streams from young moving groups (or tidal streams) by their (U, V) distribution alone, because it is influenced by measurement errors and its theoretically predicted shape varies with the parameters of the perturbation (e.g. the bar pattern speed). In this context, age and abundance measurements can be used to constrain the true origin of phase space clumps.

5.2.4 Conclusions

Stellar streams near the Sun have distinct velocity distributions that depend on their origins. A common feature of all moving groups is that they have a narrow azimuthal velocity-distribution, because for stars on similar orbits to be in the Solar neighborhood at the same time means they must have the same azimuths. The azimuthal velocity for stars with disk-like kinematics (small orbital inclinations with respect to the plane) is described by Θ ($\approx V$ in the Solar neighborhood), while for halo streams on more inclined orbits a better quantity is the azimuthal velocity in a spherical potential $V_{\text{az}} = \sqrt{(V + V_{\text{LSR}})^2 + W^2}$. Only very young moving groups (~ 0.2 Gyr) are focused in the W -velocity distribution, because phase mixing in the vertical direction is most effective.

The local velocity distribution is dominated by a few braches that are inclined to the U -axis and belong to the dynamical streams Sirius, Coma Berenices,

Hyades-Pleiades and Hercules (e.g. Skuljan et al., 1999). There is even substructure among this substructure, because resonances can trap field stars together with stellar clusters (Famaey et al., 2005). Tidal streams, which would belong to the stellar halo and thick disk population, are hard to detect among the vast majority of thin disk stars, with the local thick-to-thin disk and halo-to-thin disk ratios being 12% and 0.5%, respectively (Jurić et al., 2008). Gould (2003) showed that if the local stellar halo is composed of stellar streams, their average density contrast should be around 0.25% with no stream contributing to more than 5% alone. However, samples that concentrate on very low-metallicity or high-velocity stars would allow the detection of some tidal streams in sparsely populated regions of velocity space.

5.3 Stellar Streams in Integrals of Motion Space

5.3.1 The Classical Integrals of Motion (E, L_z, L)

Initially, Helmi et al. (1999) and Helmi and de Zeeuw (2000) proposed to search for streams from the same progenitor in the space spanned by the integrals of motion – that is, the energy E and angular momenta $L_z, L_\perp = \sqrt{L_x^2 + L_y^2}$ or L_{total} . Because these quantities characterize the orbits of stars one would expect stellar streams to form clumps in integrals of motion space. Indeed it was shown by Helmi and de Zeeuw (2000) that this is true for small satellites that were accreted in a fixed Milky Way potential. Later, however, Helmi et al. (2006) argued that (E, L_z, L) is only suboptimal, for several reasons: First, the total angular momentum L is only strictly conserved in a spherical potential which is not the case for the Milky Way. Second, continuing accretion and merging events would have changed the potential steadily and altered the energy of an orbiting satellite. Third, massive satellites suffer from dynamical friction so that stars lost at different passages end up having different energy levels. Still, Helmi et al. (1999) detected two fossil streams originating from the same progenitor as a clump of solar neighbourhood halo stars in (L_z, L_\perp) space. Using cosmological N-body simulations, Peñarrubia et al. (2006) showed that stream particles respond adiabatically to a change in the Milky Way’s potential, that is, while L_z is adiabatically invariant, the energy E can only constrain the present-day Milky Way potential. Also, the $(E; L_z)$ -distribution shows a bimodality reflecting the different energy levels of leading and trailing tail. Later, Choi et al. (2007) confirmed these findings by showing that over 8 Gyr the overall position of a disrupting satellite and its tidal tails basically remains the same in (E, L_z) space, but the shape of the distribution shifts and one satellite can produce several apparently disassociated clumps. This, together with the fact that the total angular momentum is not really an integral of motion, can obscure the signature of a moving group that is otherwise well defined in phase space. Because of this arguments, it seems that L_z remains the most reliable parameter that characterizes a moving group. This especially holds for the Solar vicinity, since there $L_z \approx R_\odot(V + V_{\text{LSR}})$.

5.3.2 Alternate Ways to Define a Nearby Stellar Orbit

Other effective integrals of motion that characterize the orbits of stream stars have been proposed by various authors. The philosophy behind such proposals is to stay as close as possible to the observables and account for the errors. That is, the goal is to find "effective" integrals of motion that are most suitable for a comparison with observations. For example, Helmi et al. (2006) proposed to look for stellar streams in a space spanned by the apocenter, pericenter and angular momentum L_z . Moving groups then cluster around lines of constant eccentricity. However, to calculate the eccentricity, a guess of the true potential is required. Arifyanto and Fuchs (2006) followed a similar approach in the sense that they tried to find stars with the same orbital eccentricity. Their strategy in finding nearby stellar streams in velocity space is based on the Keplerian approximation for orbits developed by Dekker (1976) (see Section 4.4.3). They assumed an axisymmetric potential and that stars in the same stellar stream move on orbits that stay close together, which is justified by numerical simulations of satellite disruption (Helmi et al., 2006). These stars should form a clump in the projection of velocity space spanned by $\sqrt{U^2 + 2V^2}$ and V . The latter is related to the angular momentum L_z , which defines the guiding center orbits of the stars. The first quantity is a measure of a star's eccentricity e . For a flat rotation curve e is given by equation (4.76) in Section 4.4.3:

$$e = \frac{1}{\sqrt{2}V_{\text{LSR}}} \sqrt{U^2 + 2V^2}.$$

Also, it can be shown that the radial action integral J_R in the Keplerian approximation is approximately equal to $\frac{\pi R_\odot}{2V_{\text{LSR}}}(U^2 + 2V^2)$ (Burkhard Fuchs 2007, private communication). Therefore, the quantity $\sqrt{U^2 + 2V^2}$ should be robust even if the Milky Way's potential underwent slow changes in the past.

By deriving the expressing e through U and V , we have assumed that the stars move on planar orbits in the plane $z = 0$. While this assumption seems reasonable for thick and thin disk stars, for halo stars we have to project this formalism onto their orbital plane (Dettbarn et al., 2007). We assume a spherical potential and neglect any asphericity of the dark halo potential and the flattening of the disk potential. This is justified by the work of Chiba and Beers (2000), who showed that the distribution of halo stars in the space spanned by isolating integrals of motion in an aspherical Stäckel-type potential can be closely mapped into the integrals of motion-space of a spherical potential. Also, even for stars that move in axisymmetric flattened potentials, L_\perp is approximately conserved (Binney and Tremaine, 1987) and the orbits can be thought of as approximately planar. As an example we refer to Section 6.8.2, where we show that stellar thick- and thin-disk streams detected in $(V, \sqrt{U^2 + 2V^2})$ -space are also clumped in (L_z, L_\perp) -space.

In a spherical potential, a star with Cartesian velocity components (U, V, W) moves in a fixed orbital plane that is inclined by an angle ν relative to the direction towards the North Galactic Pole. ν is given through

$$\nu = \arctan\left(\frac{V + V_{\text{LSR}}}{W}\right) \quad (5.3)$$

and ranges from 0° to 180° . Stars with inclination angles $\nu > 180^\circ$ are treated as stars moving on retrograde orbits in a plane with inclination angle $\nu - 180^\circ$. The azimuthal velocity of a star is

$$V_{\text{az}} = \sqrt{(V + V_{\text{LSR}})^2 + W^2}, \quad (5.4)$$

so if the star is near the Sun we can approximate its total angular momentum by

$$L = R_\odot \cdot V_{\text{az}} = R_0 \cdot V_{\text{LSR}}. \quad (5.5)$$

For the last step we have assumed a constant rotation curve. It follows that the guiding center radius, R_0 , is related to the Solar radius through

$$R_0 = R_\odot \frac{V_{\text{az}}}{V_{\text{LSR}}}. \quad (5.6)$$

We can proceed like in Section 4.4.3 to calculate the effective potential and the energy of the star at the Solar radius in the Keplerian approximation:

$$\Phi_{\text{eff}}(R_\odot) = E_0 + (V_{\text{LSR}} - V_{\text{az}})^2 \quad (5.7)$$

$$E(R_\odot) = E_0 + (V_{\text{LSR}} - V_{\text{az}})^2 + \frac{U^2}{2} \quad (5.8)$$

Its eccentricity $e = \sqrt{\frac{2(E-E_0)}{R_0^2 \kappa_0^2}}$ then yields

$$e = \frac{1}{\sqrt{2}V_{\text{LSR}}} V_{\Delta E}, \quad (5.9)$$

where we have introduced the quantity

$$V_{\Delta E} = \sqrt{U^2 + 2(V_{\text{LSR}} - V_{\text{az}})^2}. \quad (5.10)$$

$V_{\Delta E}$ is the difference between the energy of a star at the guiding center and the Solar radius and a measure of its orbital eccentricity. Also, $V_{\Delta E}$ is related to the radial action integral and robust against slow changes in the gravitational potential (Burkhard Fuchs 2007, priv. comm.). Although the Keplerian approximation breaks formally down for highly eccentric orbits ($e > 0.5$, Dekker, 1976), stars on similar orbits will still get projected into the same region of phase space. Looking for "overdensities" in $(V_{\text{az}}, V_{\Delta E}, \nu)$ -space is a practical way to find stellar streams, because we don't need to assume any form of the gravitational potential and any pre-history of the stream. The first successful application of the generalized Keplerian approximation has been done by Dettbarn et al. (2007), who were able to re-discover amongst others the 'H99' stream, which has been found by Helmi et al. (1999) in (L_z, L_\perp) -space.

We use two of our simulations as described in Section 5.2.1 to confirm that stellar streams indeed cluster in $(V_{\text{az}}, V_{\Delta E}, \nu)$ -space. We show in Figure 5.7 the distribution in $(V_{\text{az}}, V_{\Delta E})$ of all stars from model 3e and 2 that ended up within

1 and 2 kpc, respectively, of the Sun after 10 Gyr of integration. On the left (a) we show the exact values, while on the right (b) we have simulated observational errors of 5 km s^{-1} for the radial velocity, 4 mas yr^{-1} for the proper motions and 15% for the distance. The black crosses give the values of the progenitor’s orbit as it exactly passes through the Sun after 10 and 2 Gyr, respectively. The stream belonging to model 3e occupies only a small region in $(V_{\text{az}}, V_{\Delta\text{E}})$ -space, and the Keplerian approximation is strictly valid because of the low eccentricity. On the other hand, it formally breaks down for the model 2 stream (a value of $V_{\Delta\text{E}} \approx 660 \text{ km s}^{-1}$ would predict an eccentricity of ≈ 2.1), but still this stream occupies a well-defined region in $(V_{\text{az}}, V_{\Delta\text{E}})$ -space. The feature is more elongated along the V_{az} -axis, and it is not clear whether this is only caused by the larger distances of its stars (there is no clear correlation between distance from the Sun and $(V_{\text{az}}, V_{\Delta\text{E}})$ -difference to the progenitor). The effect of observational errors is mainly to broaden the features (*right panel*), but still the streams can be identified as distinct clumps. Note the few stars that get projected towards positive V_{az} -values, because the errors change the sign of some V -velocities.

We show a histogram of the orbital inclination angles of the two stellar streams in Figure 5.8. The left panels, (a) and (c), show the exact ν -angles obtained through equation (5.3), while the right panels, (b) and (d), show the effect of velocity errors that get introduced by assuming proper motion, distance and radial velocity errors of 4 mas yr^{-1} , 15% and 5 km s^{-1} , respectively. The arrow in each panel denotes the ν angle of the progenitor’s orbit as it passes the Sun at $t = 2 \text{ Gyr}$ for model 2 and $t = 10 \text{ Gyr}$ for model 3e. For model 2, *panels* (a) and (b), the solid and dotted histograms show all stars inside a sphere around the Sun with 2 kpc and 1 kpc radius, respectively. The fact that stars that are closer together spatially show a narrower ν -distribution is presumably explained by the more similar initial velocities of these stars. Both distributions peak at the ν -angle of the progenitor’s orbit *mirrored at* $\nu = 90^\circ$. Also, there are two stars that are distributed around the progenitor’s ν -value. The overall ν -distribution reflects the bimodal W -distribution displayed in Figure 5.6. The effect of observational velocity errors is to broaden the ν -distribution; however, most stars are included in the range $\pm 15^\circ$ around the exact peak. For model 3e, where we only show stars within 1 kpc of the Sun, we can observe similar effects of velocity errors, whereas the bimodality in the ν -distribution is more prominent than for model 2.

5.3.3 Conclusions

The space where stellar streams show up most clearly is the space of the (nearly) conserved quantities (E, L_z, L) . This is confirmed by both simulations (e.g. Helmi and de Zeeuw, 2000; Peñarrubia et al., 2006; Choi et al., 2007) and observations (e.g. Helmi et al., 1999; Chiba and Beers, 2000; Navarro et al., 2004). However, in reality we don’t know the gravitational potential and the integrals of motion perfectly; we also don’t know the pre-history of the stream and if all stars from the same precursor object actually have the same integrals of motion (because

the gravitational potential of the Milky Way and the satellite underwent changes). Therefore we explored a practical way to identify stellar streams within a given sample kinematically. We find that the Keplerian approximation, generalized to orbits with arbitrary inclination angles (Dettbarn et al., 2007), is suited well to project stellar stream members into a small region of a space spanned by total angular momentum, eccentricity and orbital inclination with respect to the direction towards the North Galactic Pole. The first two quantities are approximated by $V_{\text{az}} = \sqrt{(V + V_{\text{LSR}})^2 + W^2}$ and $V_{\Delta\text{E}} = \sqrt{U^2 + 2(V_{\text{az}} - V_{\text{LSR}})^2}$ respectively, while the third is given through $\nu = \arctan\left(\frac{V + V_{\text{LSR}}}{W}\right)$. Through our simulations we have confirmed that tidal streams are concentrated in distinct regions of $(V_{\text{az}}, V_{\Delta\text{E}})$ -space around the respective values of their progenitor's orbit. Also, their orbital inclination angles are very similar, which allows to search for stellar streams in discrete ν -bins.

Stellar streams will even get projected into the same region of $(V_{\text{az}}, V_{\Delta\text{E}})$ -space, if the Keplerian approximation formally is not valid (for $e > 0.5$). In addition, we have proved that this approximation can be applied to stars as far as 2 kpc from the Sun. Observational errors will broaden the $(V_{\text{az}}, V_{\Delta\text{E}}, \nu)$ -distribution of a stream, but not destroy its lumpiness completely. Therefore we conclude that the Keplerian approximation of orbits near the Sun is a useful tool to detect stellar streams in samples with 6D phase-space information.

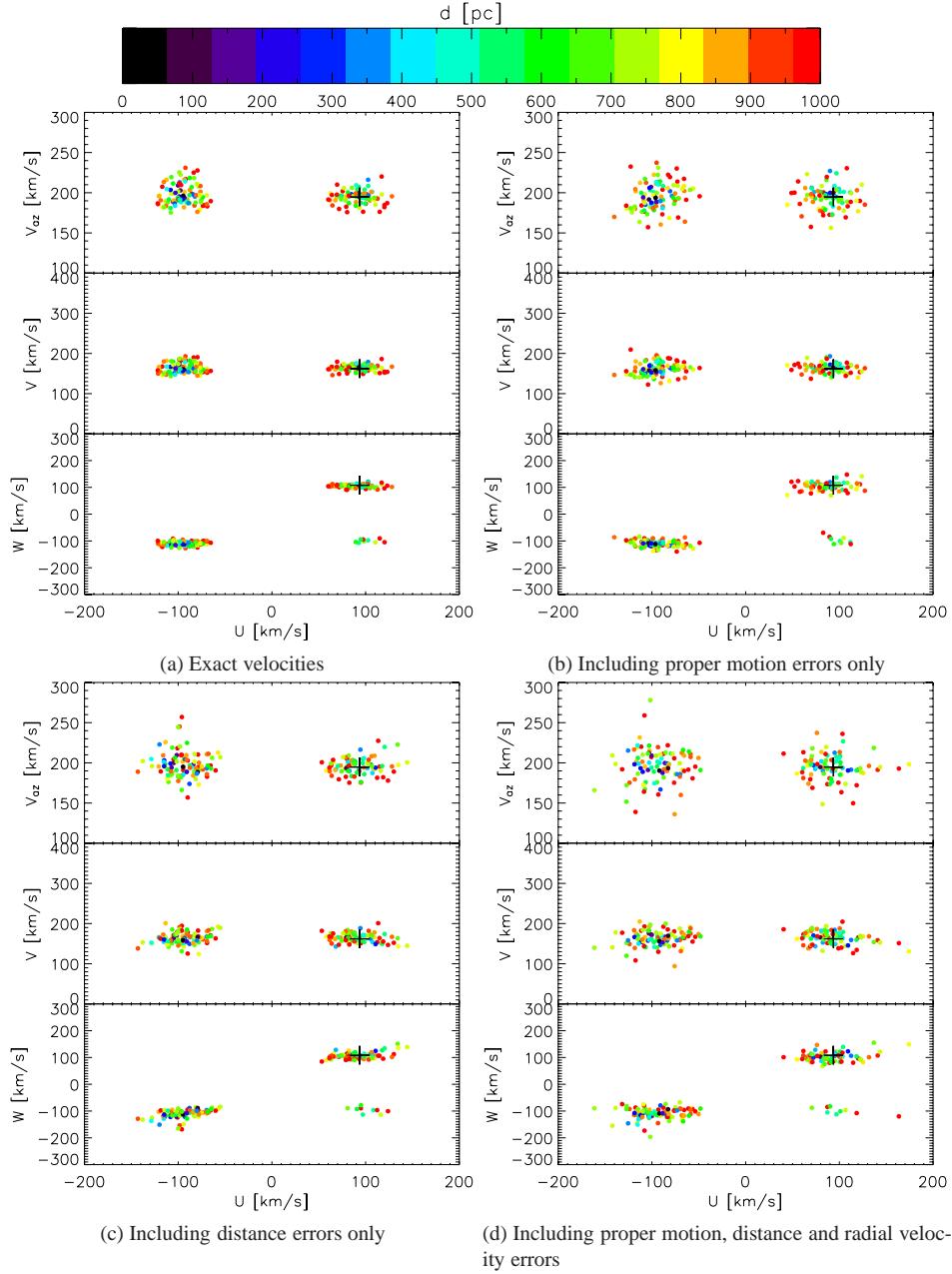


Figure 5.5: Velocity distribution of the 173 stars that ended up in a sphere of 1 kpc around the Sun from a stellar stream that resulted from disruption 10 Gyr ago (model 3e). $V_{\text{az}} = \sqrt{V^2 + W^2}$ is the azimuthal velocity of a star in a spherical potential. The black cross denotes the velocity of the progenitor's orbit which exactly passes through the Sun and the symbols are color-coded according to their distance from the progenitor's orbit. (a) Exact velocities. Note the symmetry with respect to the U - and W -velocities, indicating the high degree of mixing. (b) The effect of estimating proper motions of the stars with a 4 mas yr^{-1} error has been included. (c) The effect of estimating distances of the stars with a 15% relative distance error has been included. These errors contribute comparably to proper motion errors for this particular stream. (d) The effect of estimating proper motions, distances and radial velocities of the stars with errors of $\sigma_{\mu} = 4 \text{ mas yr}^{-1}$, $\sigma_d = 0.15d$ and $\sigma_{v_{\text{rad}}} = 5 \text{ km s}^{-1}$ has been included.

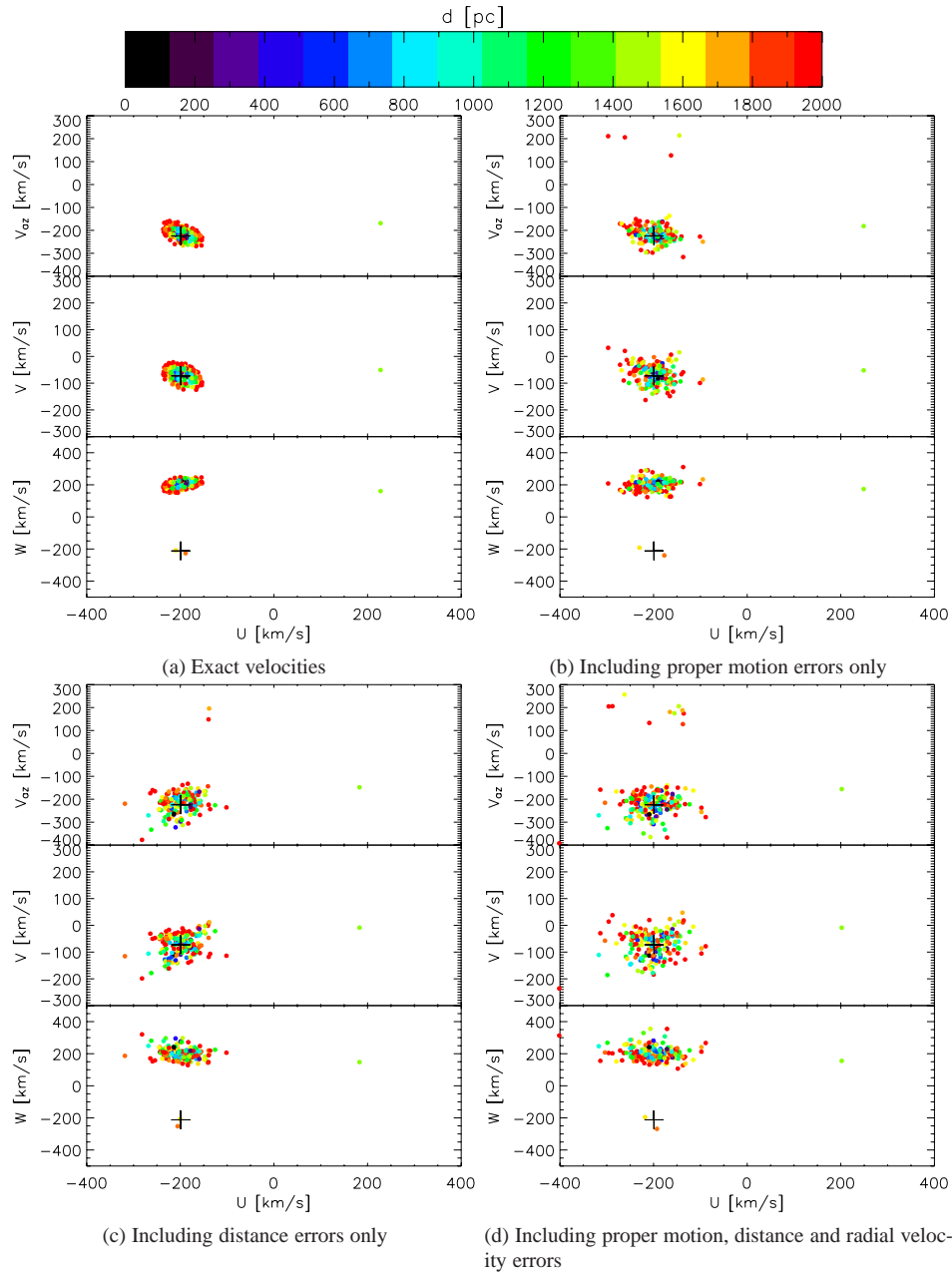


Figure 5.6: Same as Figure 5.5, except for 172 stars of model 2 that ended up within a 2 kpc radius around the Sun after 10 Gyr since disruption. The colors correspond to the distance from the Sun, and the black cross marks the velocities of the progenitor at $t = 2$ Gyr, when its orbit exactly crossed the Solar position. Note the outliers in V_{az} that emerge when observational errors change the sign of V .

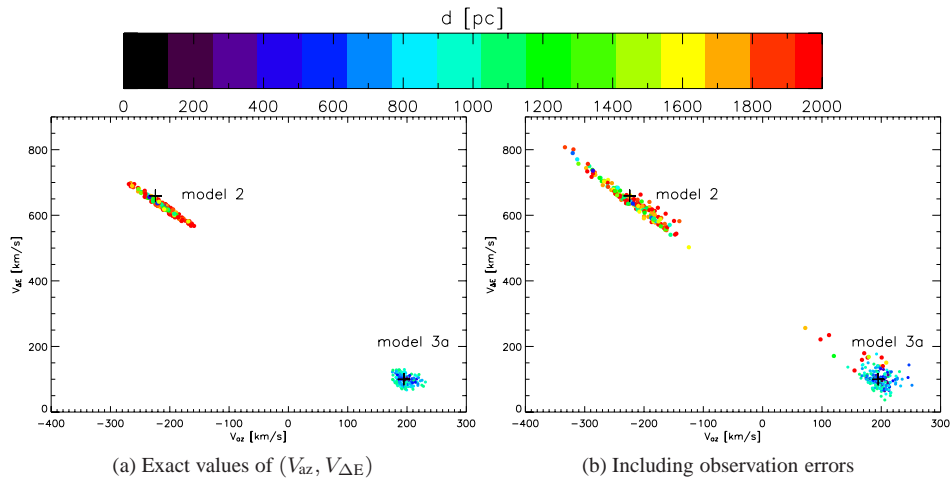


Figure 5.7: Distribution in $(V_{az}, V_{\Delta E})$ of ~ 173 and 172 stars respectively that have been lost 10 Gyr ago (models 3e and 2) and the position of which at time $t = 10$ Gyr is in a sphere of radius 1 kpc and 2 kpc respectively around the Sun. The black crosses denote the $(V_{az}, V_{\Delta E})$ -values of the progenitor's orbit which exactly passes through the Sun after $t = 10$ and $t = 2$ Gyr respectively and the symbols are color-coded according to their distance from the Sun. Note the few stars that have been "transformed" to positive values of V_{az} , because the assumed error changed the sign of their V -velocity.

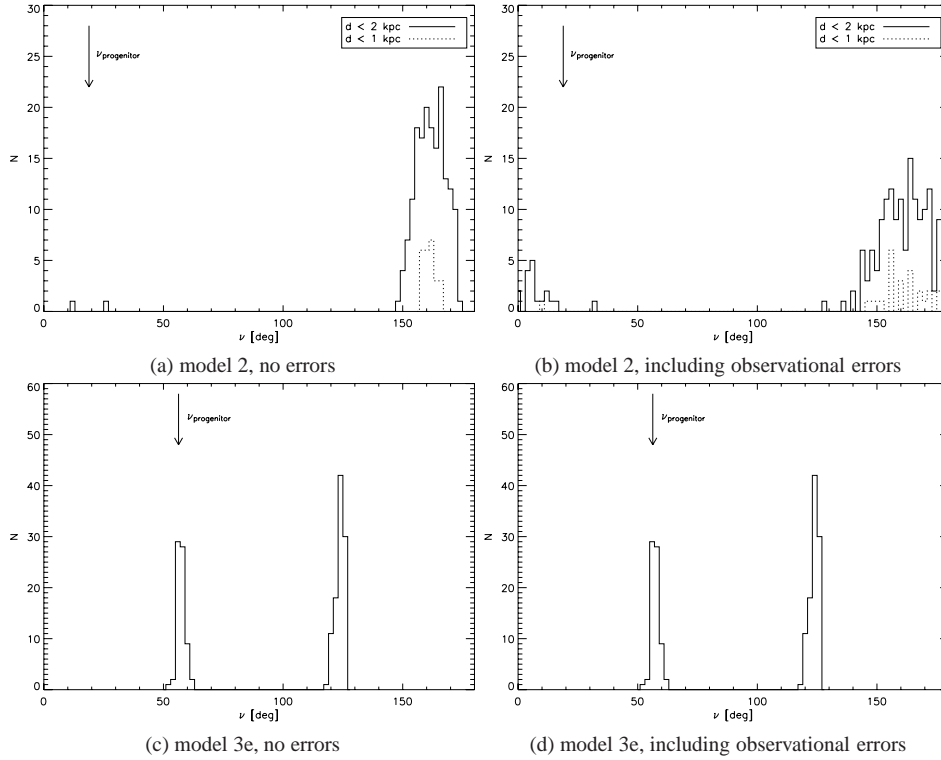


Figure 5.8: ν -histograms of simulated tidal debris in the Solar neighborhood. (a) The solid histogram shows the exact ν -angles for stars from model 2 that ended up in a 2 kpc sphere around the Sun after 10 Gyr. The dotted histogram is for the sub-sample of stars within 1 kpc of the Sun. (b) The same as (a), but the velocities have been re-calculated after simulating observational errors of μ_l , μ_b , d and v_{rad} . (c) Histogram of the exact ν -angles for stars from model 3e inside a 1 kpc sphere around the Sun. (d) Same as (c), but the velocities have been re-calculated after simulating observational errors of μ_l , μ_b , d and v_{rad} . The arrow marks the ν -angle of the progenitor's orbit when it passes the Sun after 2 Gyr in case of model 2, or 10 Gyr in case of model 3.

Chapter 6

Identifying Stellar Streams in the 1st RAVE Public Data Release

With the first data release (DR1) from the Radial Velocity Experiment (RAVE Steinmetz et al., 2006) a large new data sample of stars in the Milky Way became available, which is ideally suited for kinematical studies. To explore RAVE's potential, we analyze the velocity distribution of more than 7000 stars within a distance of 500 pc and search for overdensities in phase space using the projection technique of Arifyanto and Fuchs (2006, hereafter AF06). Even the first data release sample is so substantive that we can determine signal-to-noise ratios for orbital "overdensities" and show the statistical significance of the detected overdensities.

6.1 The Data

The RAVE DR1 (Steinmetz et al., 2006) contains 25,274 radial velocities for 24,748 individual stars together with proper motions and photometry from other major catalogs (Starnet 2.0, Tycho-2, SuperCOSMOS, USNO-B, DENIS and 2MASS). Its total sky coverage is $\sim 4760 \text{ deg}^2$ and is shown in Figure 6.1.

6.1.1 Estimation of Distances using a Photometric Parallax Relation

The only missing parameter to obtain all the velocity and position components is a distance estimate. The photometric data, however, allows the application of a photometric parallax relation.¹ To calibrate such a relation for RAVE stars, we used main-sequence (MS) stars (luminosity class V) from the Hipparcos Catalog (Perryman and ESA, 1997). In detail, the following steps were completed:

¹We assume that the vast majority of RAVE stars are main sequence stars, because giants in the RAVE magnitude range would lie so far away, that the star density is substantially decreased. See also the discussion in Siegel et al. (2002)

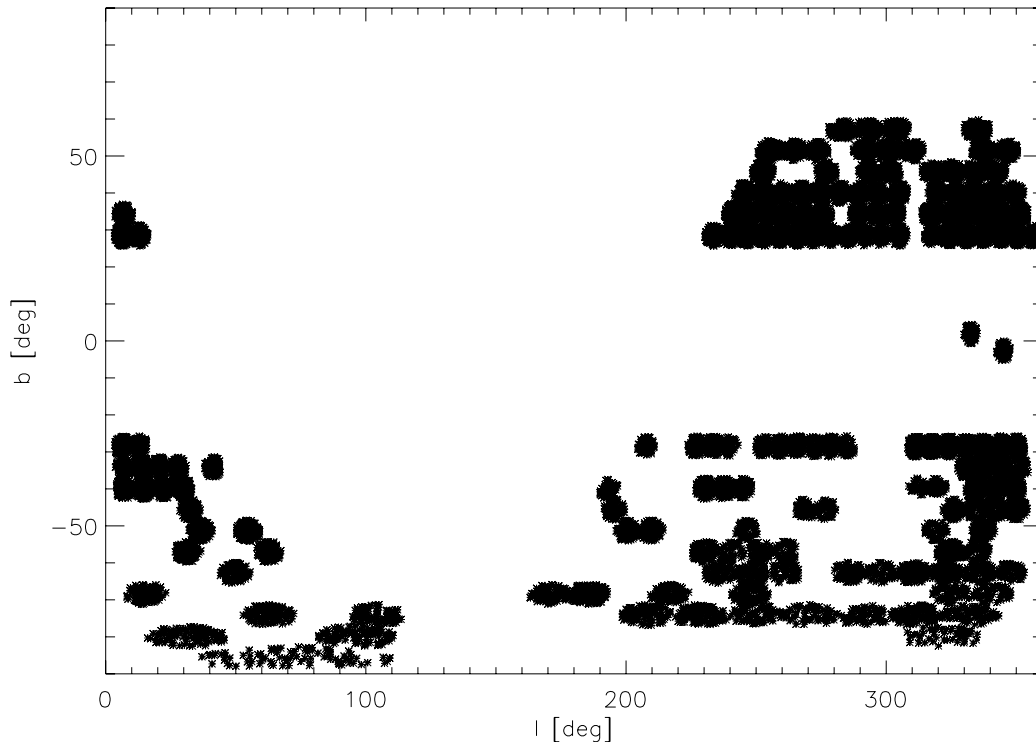


Figure 6.1: Sky coverage of the RAVE DR1. Each star is plotted individually.

1. We downloaded the *Hipparcos* catalog (Perryman et al., 1997) and kept only those stars satisfying the following selection criteria: accurate parallaxes ($\frac{\sigma_\pi}{\pi} < 0.1$), non-periodic, no 'CCDM' and 'multi flag' entries and a cross-identification in the Tycho-2, USNO-B and 2MASS data. These other catalogs contain B_1 , V_T and H -band magnitudes².

The choice of using the H magnitude in the color – either $B_1 - H$ or $V_T - H$ – is motivated by its very good accuracy and availability for nearly all stars in RAVE. We then calculated the absolute magnitudes M_{V_T} and M_{B_1} according to

$$M = m - 10 + 5 \log \frac{\pi}{\text{mas}}. \quad (6.1)$$

2. We considered two color-magnitude relations: $V_T - H$ vs. M_{V_T} and $B_1 - H$ vs. M_{B_1} . These are shown in Figure 6.2 and Figure 6.3, respectively. In both plots the solid black line was chosen to remove all stars that seemed to be mis-classified as MS stars in the *Hipparcos* Catalog. This cut was done

²We do not consider very metal-poor (sub-) dwarfs, which can lie up to $\gtrsim 1$ mag below the Solar-metallicity MS; for metal-poor stars we would overestimate the distance and hence velocity. The effect for disk stars, however, will be negligible, because they exhibit approximately Solar metallicity. We will come back to the subdwarf problem in Section 6.6 in the context of the detection of a new halo stream in the RAVE data.

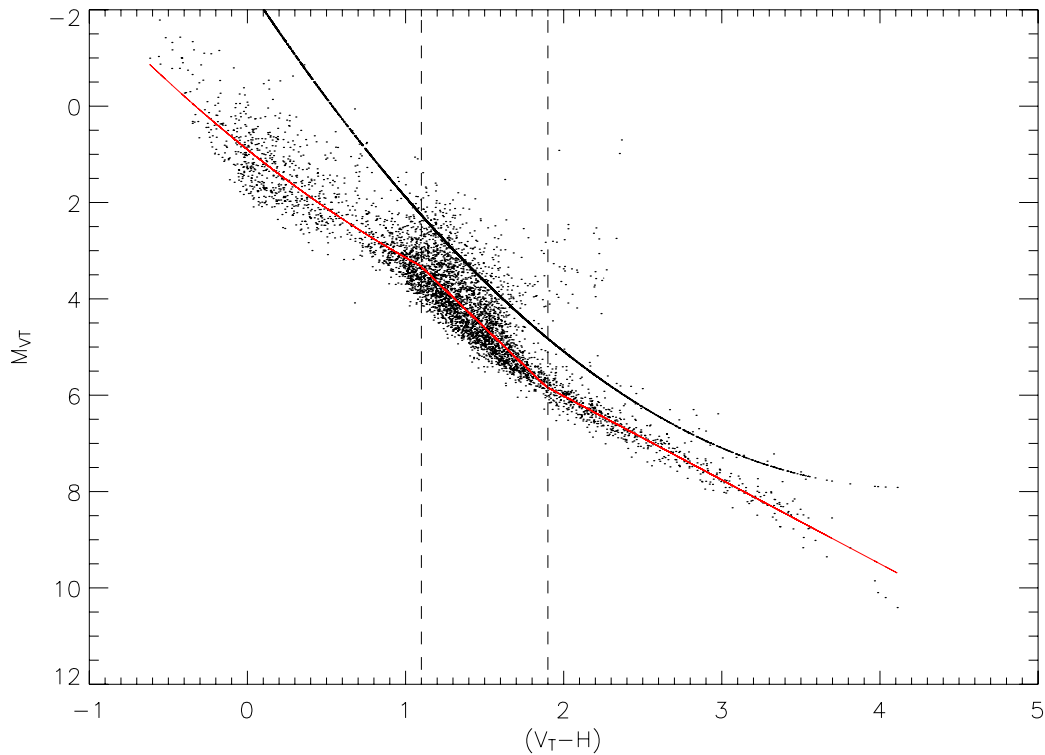


Figure 6.2: Absolute magnitude calibration for *Hipparcos* main sequence stars with a parallax accuracy better than 10% with $V_T - H$ as the color. All stars above the solid black line are assumed to be (sub-)giants incorrectly classified as MS stars and are not considered for the color-magnitude fit. The red line shows the adopted $M_{V_T} - (V_T - H)$ -relation, and the dispersions σ about this mean relation are indicated in three color regimes.

by eye, since one could only reliably distinguish a (sub-)giant from a MS star in the vicinity of the MS by measuring its surface gravity which is not available. The selection of giant stars in the $B1 - H$ diagram also includes all giants from the $V_T - H$ -selection, plus an additional 114 stars.

Next, the color-magnitude diagrams were divided into three color bins (dashed lines) in which we separately fitted a color-magnitude relation (red solid lines). For each bin, the intrinsic scatter of the color-magnitude relation was calculated as follows: We took the differences ΔM between the true absolute magnitudes (obtained through the parallax) and those obtained through the fit. These deviations were plotted in a cumulative distribution diagram. Figure 6.4 shows the result. The upper panel displays the cumulative distribution of the deviations ΔM for the three color bins in $V_T - H$, the lower panel for $B1 - H$. The red lines mark the 1σ error, given through the width of the cumulative distribution between 16% and 84%.

For our analysis we adopted the M_{V_T} vs. $V_T - H$ -relation, because its intrinsic scatter is slightly smaller than that of M_{B1} vs. $B1 - H$. Also, the errors of $B1$ for each star in the RAVE catalog are unknown, while the errors in V_T are given. The formal error in H (from 2MASS) is typically

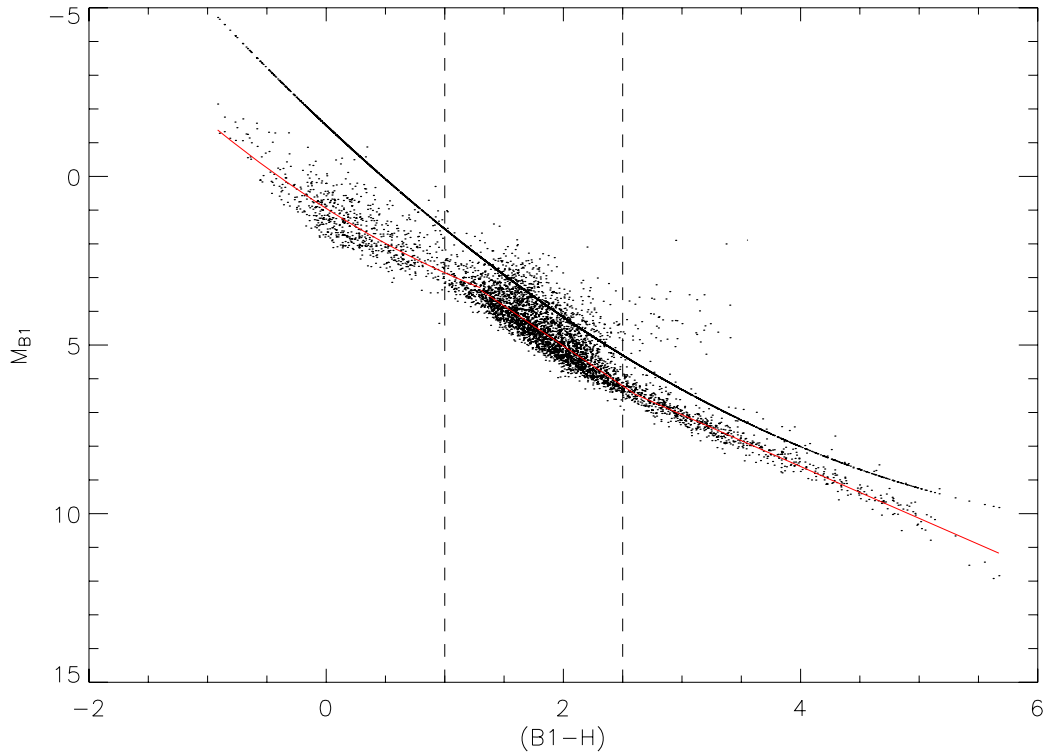


Figure 6.3: Same as Figure 6.2, but for $B1 - H$ vs. M_{B1} . The red line shows the adopted $M_{B1} - (B1 - H)$ relation, and the dispersions σ about this mean relation are indicated in three color regimes.

very small, ~ 0.01 mag. For these reasons we chose the $M_{V_T}(V_T - H)$ -relation to calculate absolute magnitudes M_{V_T} for the RAVE stars:

$$M_{V_T} = 0.903301 + 2.62445(V_T - H) - 0.384382(V_T - H)^2 \quad (6.2a)$$

$$(-0.6 < (V_T - H) \leq 1.1)$$

$$M_{V_T} = -0.121440 + 3.14517(V_T - H) \quad (6.2b)$$

$$(1.1 < (V_T - H) \leq 1.9)$$

$$M_{V_T} = 2.53352 + 1.74142(V_T - H) \quad (6.2c)$$

$$(1.9 < (V_T - H) < 4.1)$$

3. The calibrations (6.2) were used to calculate M_{V_T} for the RAVE stars, assuming all of them to be MS stars. Because the catalog is not complete in magnitude, the goal was to derive the color $V_T - H$ for as many stars as possible. Therefore, the RAVE catalog has been sorted by V_T to get all stars with that magnitude (12836 stars). For the stars without V_T , we tried to derive that magnitude from the USNO-B color $B1 - R1$. All stars without V_T have been sorted by $B1$ and $R1$ and eliminated, if they lacked those magnitudes. Thus, 21094 stars remained with either V_T or $B1 - R1$.
4. The stars with both V_T and $B1 - R1$ were used to get color and magnitude

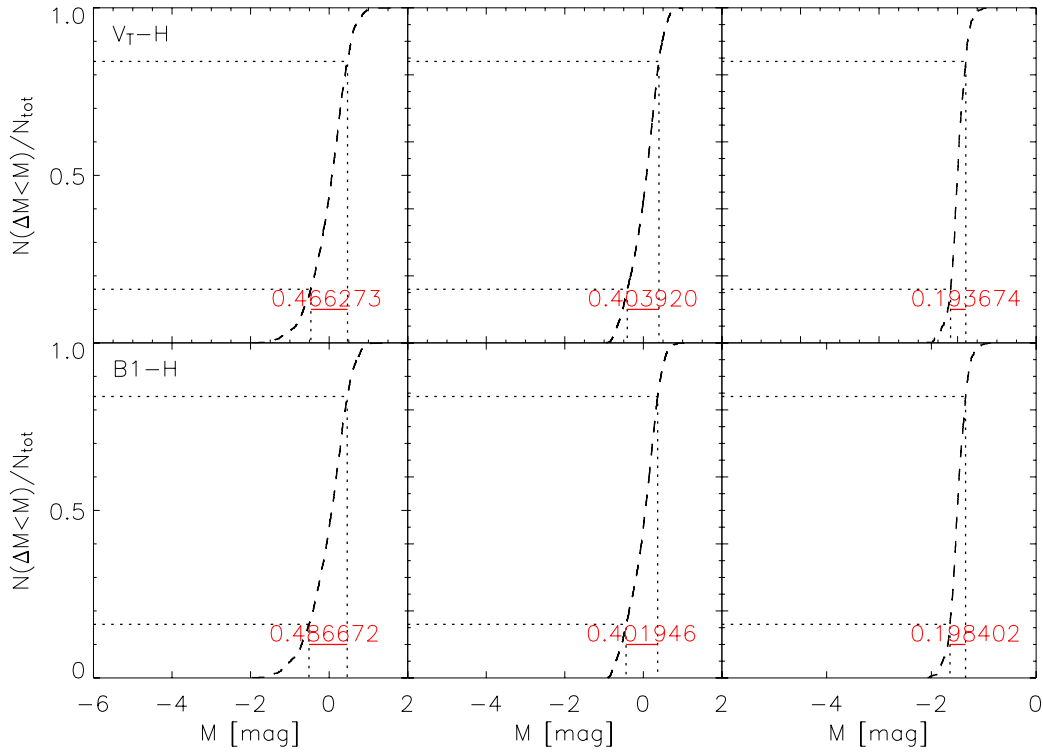


Figure 6.4: A comparison of the intrinsic scatter of the color-magnitude relations discussed above. The three upper panels correspond to the three color bins in $V_T - H$ and the three lower panels to the bins in $B1 - H$. The scatter is marked through the red line in the corresponding diagram and its value is written above that line.

conversion formulas:

$$V_T = B1 + 0.0088 - 0.7167(B1 - R1) + 0.2073(B1 - R1)^2; \\ (-0.25 \leq B1 - R1 < 0.6) \quad (6.3a)$$

$$V_T = B1 + 0.0641 - 0.645(B1 - R1); \\ (0.6 \leq B1 - R1 < 2.5) \quad (6.3b)$$

$$V_T = B1 + 0.7289 - 0.907(B1 - R1); \\ (2.5 < B1 - I \leq 3.06) \quad (6.3c)$$

5. Because the chosen color-magnitude relation requires $V_T - H$, 6 stars without 2MASS H magnitudes were removed, leaving 21088 stars.
6. If unknown, V_T was calculated by equations (6.3). However, 75 stars lay beyond the scope of the conversion formulas ($-0.25 \leq B1 - R1 \leq 3.06$) and were eliminated.
7. All stars with $V_T - H \leq -0.6$ or with $V_T - H \geq 4.1$ were removed because they are beyond the scope of the color-magnitude relations (6.2). 20605 stars remained.

8. Finally, 14 stars with no proper motions were removed, leaving 20591 stars in the catalog.
9. For all of the remaining stars it was possible to calculate, if necessary, V_T and estimate the absolute magnitude M_{V_T} through equations (6.2).

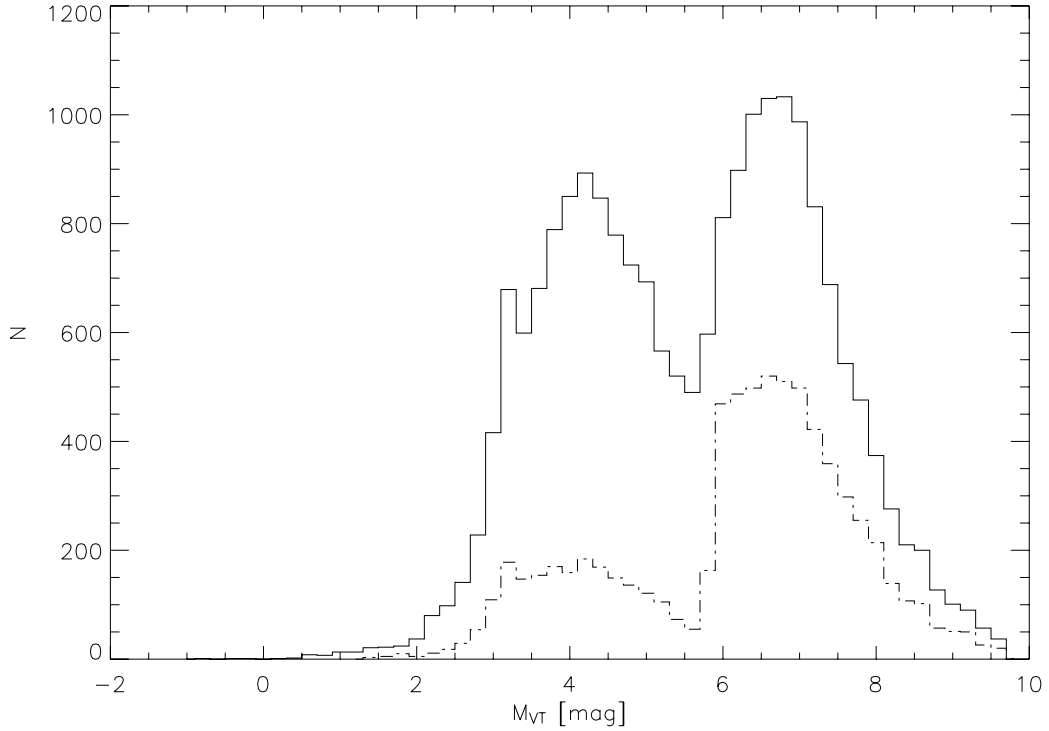


Figure 6.5: Distribution of absolute magnitudes of all DR1 RAVE stars (solid line) and our selected sample (dash-dotted line). A large fraction have $M_{V_T} > 6$.

Figure 6.5 shows that a large fraction of all DR1 stars has absolute magnitudes fainter than $M_{V_T} = 6$, i.e. lie in the section of the color-magnitude relation where its intrinsic scatter is smallest. Therefore one would expect to get a large sample of stars with distance estimates good to 10%–20% in most cases (see below and Figure 6.5, where the M_{V_T} -distribution of the final sample is shown).

The distances follow from (V_T, M_{V_T}) via equation (6.1):

$$d [\text{kpc}] = \frac{1}{100} \times 10^{(V_T - M_{V_T})/5}. \quad (6.4)$$

The distance error σ_d is determined through

$$\sigma_d = \frac{1}{5} d \ln 10 \sqrt{(\sigma_{V_T})^2 + (\sigma_{M_{V_T}})^2}, \quad (6.5)$$

where σ_{V_T} and $\sigma_{M_{V_T}}$ denote the errors of V_T and M_{V_T} respectively. σ_{V_T} either is given in the catalog or follows from the conversion formulas (6.3) as

$$\sigma_{V_T}^2 = [(0.2833 + 0.4146(B1 - R1))\sigma_{B1}]^2 + [0.4146(B1 - R1)\sigma_{R1}]^2$$

$$(-0.25 \leq B1 - R1 < 0.6)$$
(6.6a)

$$\sigma_{V_T}^2 = (0.355\sigma_{B1})^2 + (0.645\sigma_{R1})^2 \approx 0.22^2;$$

$$(0.6 \leq B1 - R1 < 2.5)$$
(6.6b)

$$\sigma_{V_T}^2 = (0.093\sigma_{B1})^2 + (0.907\sigma_{R1})^2 \approx 0.27^2;$$

$$(2.5 < B1 - I \leq 3.06)$$
(6.6c)

The error of $B1$ and $R1$ is not given in RAVE, but assumed to be 0.3 mag (USNO-B information).

The absolute magnitude error $\sigma_{M_{V_T}}$ follows from the color-magnitude relations (6.2) and

$$\sigma_{M_{V_T}}^2 = \left[\frac{\partial M_{V_T}}{\partial (V_T - H)} \sigma_{(V_T - H)} \right]^2 + \sigma_{M_{V_T}, intrinsic}^2$$

$$\sigma_{M_{V_T}}^2 = [(2.62445 - 0.768764(V_T - H))\sigma_{(V_T - H)}]^2 + 0.47^2$$

$$(-0.6 < (V_T - H) \leq 1.1)$$
(6.7a)

$$\sigma_{M_{V_T}}^2 = (3.14517\sigma_{(V_T - H)})^2 + 0.40^2$$

$$(1.1 < (V_T - H) \leq 1.9)$$
(6.7b)

$$\sigma_{M_{V_T}}^2 = (1.74142\sigma_{(V_T - H)})^2 + 0.19^2$$

$$(1.9 < (V_T - H) < 4.1)$$
(6.7c)

The intrinsic scatter $\sigma_{M_{V_T}, intrinsic}$ is taken from the fittings in Figure 6.2. It introduces the main error in M_{V_T} .

6.1.2 Deriving the velocities

We established a right-handed Cartesian coordinate system (x, y, z centered at the Local Standard of Rest (LSR) with the x -axis pointing in the direction of the Galactic center, the y -axis pointing in the direction of Galactic rotation, and the z -axis in the direction of the North Galactic Pole. The velocity components of a star can then be calculated from its position, radial velocity v_{rad} and proper motions (μ_α, μ_δ) through Equation (4.31) given in Section 4.2.2. The uncertainties in the velocity components depend on the uncertainties in radial velocity, proper motions

and distance (Johnson and Soderblom, 1987):

$$\begin{pmatrix} \sigma_U^2 \\ \sigma_V^2 \\ \sigma_W^2 \end{pmatrix} = \mathbf{C} \begin{pmatrix} \sigma_{v_{rad}}^2 \\ (4.74d)^2 [\sigma_{\mu_\alpha}^2 + (\mu_\alpha \sigma_d/d)^2] \\ (4.74d)^2 [\sigma_{\mu_\delta}^2 + (\mu_\delta \sigma_d/d)^2] \end{pmatrix} \quad (6.8)$$

$$+ 2\mu_\alpha \mu_\delta (4.74\sigma_d)^2 \begin{pmatrix} b_{12} \cdot b_{13} \\ b_{22} \cdot b_{23} \\ b_{32} \cdot b_{33} \end{pmatrix}$$

The elements of the matrix \mathbf{C} are the squares of the corresponding elements of matrix \mathbf{B} which has been defined by Equation (4.32) in Section 4.2.2, that is, $c_{ij} = b_{ij}^2$ for all (i, j) . About 80% of the stars in the DR1 have radial velocity accuracies better than 3.4 km s^{-1} , and 69.1% have a mean proper motion error of at most 2.6 mas yr^{-1} (Steinmetz et al., 2006). If we restrict our sample to stars within $d_{max} = 500 \text{ pc}$ from the Sun, that is, within a volume $V_{max} = \frac{4\pi}{3} d_{max}^3$, we can assume a typical distance for a star as the distance where the volume is half as large: $\langle d \rangle = 0.5^{1/3} d_{max} \approx 400 \text{ pc}$. If we further restrict the sample to stars with relative distance errors $\frac{\sigma_d}{d} \leq 0.25$ and assume a typical proper motion of 15 mas yr^{-1} , we get as an estimate for the uncertainty of the transverse velocity $\lesssim 8.6 \text{ km s}^{-1}$. The velocity error distribution in U and V is shown in Figure 6.6. It peaks at errors smaller than 5 km s^{-1} .

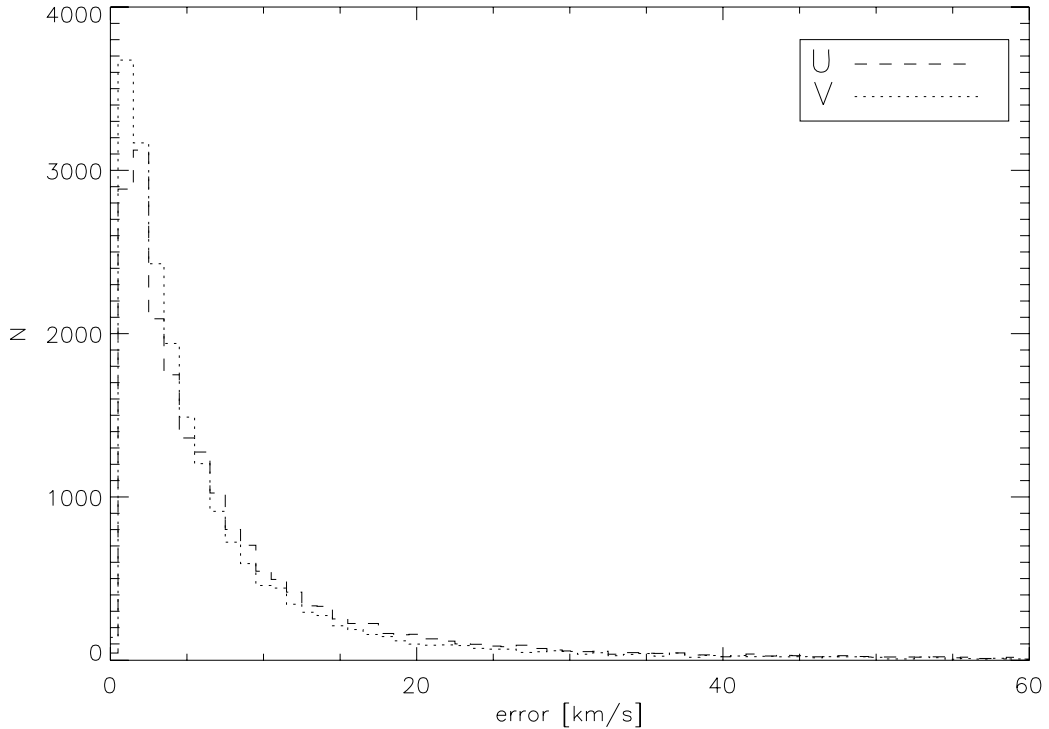


Figure 6.6: Distribution of errors for the velocity components U (*dashed line*) and V (*dotted line*) for all stars in RAVE DR1 as derived from equation 6.8. These errors include radial velocity errors, proper motion errors and distance uncertainties. Both distributions have a peak around $2\text{--}3 \text{ km s}^{-1}$ and a long tail reaching to much higher values.

For the kinematic stream search we selected only those stars that satisfy the following criteria: $\frac{\sigma_d}{d} \leq 0.25$, $d \leq 500$ pc, a total space velocity $|\vec{v}_{\text{tot}}| \leq 350$ km s⁻¹, and $\sigma_U, \sigma_V \leq 35$ km s⁻¹. We also restricted ourselves to stars at $l > 200^\circ$ and $b > 20^\circ$, because in this field the observation density was highest. This leaves 7015 stars, among which we searched for signatures of local stellar streams.

6.2 Search strategy for streams

According to Helmi et al. (1999) and Helmi and de Zeeuw (2000) a good approach to searching for streams is in the space spanned by the integrals of motion – that is, the energy E and angular momentum L_z , $L_\perp = (L_x^2 + L_y^2)^{1/2}$ or L_{total} . For example, Helmi et al. (1999) detected two fossil streams originating from the same progenitor as a clump of solar neighbourhood halo stars in (L_z, L_\perp) space. Using cosmological N-body simulations, Choi et al. (2007) showed that over 8 Gyr the overall position of a disrupting satellite and its tidal tails basically remains the same in (E, L_z) -space, but the shape of the distribution shifts and one satellite can produce several apparently disassociated clumps. This, together with the fact that the total angular momentum is not really an integral of motion, can obscure the signature of a well defined moving group in phase space. Therefore, Helmi et al. (2006) proposed looking for stellar streams in a space spanned by the apocenter, pericenter and angular momentum L_z . Moving groups then cluster around lines of constant eccentricity.

We use the approach of Arifyanto and Fuchs (2006), that is, we search for clumps in the space spanned by $\sqrt{U^2 + 2V^2}$ and V . The first quantity is a measure of a star's eccentricity e and also for the radial action integral. The latter is a measure for the angular momentum L_z . More details can be found in Section 4.4.3 and 5.3.

For the current investigation we do not include W -velocity components in our search for local streams because – as mentioned in Section 5.2 – strong phase-mixing will smear out any coherent features over short timescales. However, in Section 6.8 we will make use of the W velocities when we compare our method with the more traditional searches in (U, V, W) - and (L_z, L_\perp) -space.

6.3 Results and Discussion

We now use the distribution of the 7015 selected RAVE stars in $\sqrt{U^2 + 2V^2}$ versus V , shown in Figure 6.7, to search for substructure in the kinematic distribution. Figure 6.7 also shows the error ellipses for some points; most of the relative errors are rather small, and even though some of the larger errors produce an uncertainty in the exact position of the data points and tend to smear out substructure, several suggestive "overdensities" of stars are visible by eye. In this section we focus on identifying overdensities and on quantifying their significance.

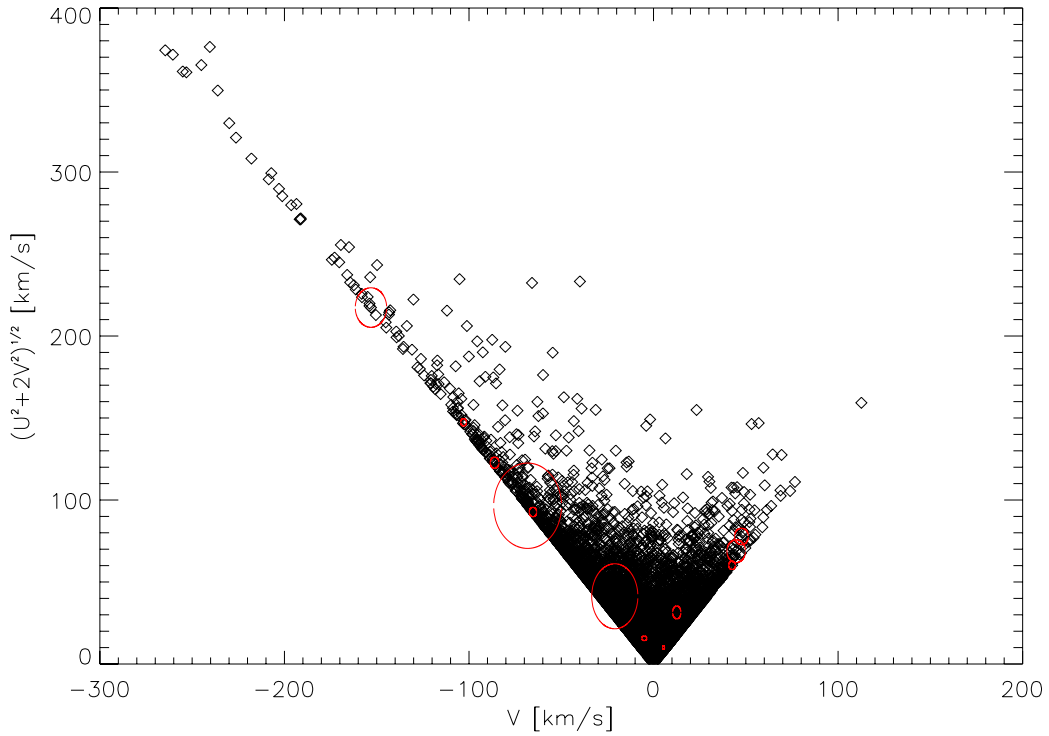


Figure 6.7: Distribution of our sample of RAVE stars in $\sqrt{U^2 + 2V^2}$ vs. V . We also show error ellipses for a small subset of stars; note that while the large error ellipses are most prominent, most ellipses are very small.

6.4 The Wavelet Transform

To this end, we follow the same procedure outlined by AF06 and use the wavelet-transform technique using a two-dimensional analyzing wavelet $\Psi(x, y)$. We bin the data in pixels of 2 km s^{-1} width on each side and calculate the value of the wavelet-transform in each bin through

$$\begin{aligned}
 w(x, y) &= \int \int dx' dy' \Psi(x - x', y - y') \times \\
 &\quad \sum_{i=0}^{N-1} \delta(x' - x_i) \delta(y' - y_i) \\
 &= \sum_{i=0}^{N-1} \Psi(x - x_i, y - y_i),
 \end{aligned} \tag{6.9}$$

where $N = 7015$ is the number of stars in our sample.

Motivated by the work of Skuljan et al. (1999), AF06 used a Mexican-hat-shaped kernel function to detect overdensities in $\sqrt{U^2 + 2V^2}$ versus V . However, since the former quantity is not uncorrelated with the latter, we expect clumps that would be roughly spherical in, for example, U versus V , to be elongated along $U = 0$. This means that the performance of a Mexican-hat kernel is sub-optimal and might influence the significance of the overdensities. Therefore, we build a

kernel function that is elongated about a factor q along the V-shaped $U = 0$ lines, in the following way.

We rotate the coordinate axes such that the new V -axis, V' , lies along the line $U = 0$ and the new $\sqrt{U^2 + 2V^2}$ axis is perpendicular to V' . For simplicity we rename V as x and $\sqrt{U^2 + 2V^2}$ as y . This implies two different rotations, depending whether the features are elongated in the region $V \leq 0$ (clockwise rotation by an angle $\varphi = \arccos \sqrt{1/3}$) or in the region $V > 0$ (counter-clockwise rotation by φ). Based on the Mexican-hat-shaped function, we then express the analyzing wavelet as a function of the new coordinates (x', y') and elongate it along the x' -axis by a factor q :

$$\Psi(x', y') = \left(2 - \frac{x'^2}{(qa)^2} - \frac{y'^2}{a^2}\right) \exp\left(-\frac{x'^2}{2(qa)^2} - \frac{y'^2}{2a^2}\right). \quad (6.10)$$

This function is normalized in the sense that its volume integral is zero. The scale parameter a is a measure for the extent of the "bumps". With the transformation equations

$$x' = \sqrt{\frac{1}{3}}x \mp \sqrt{\frac{2}{3}}y \quad (6.11a)$$

$$y' = \pm\sqrt{\frac{2}{3}}x + \sqrt{\frac{1}{3}}y, \quad (6.11b)$$

where the upper signs stand for the case $V \leq 0$, it is straightforward to calculate the kernel in the unrotated coordinate system:

$$\begin{aligned} \Psi(x, y) = & \left(2 - \frac{1}{3(qa)^2} \left((1 + 2q^2)x^2 + (2 + q^2)y^2 \mp (1 - q^2)2\sqrt{2}xy \right)\right) \times \\ & \exp\left(-\frac{1}{6(qa)^2} \left((1 + 2q^2)x^2 + (2 + q^2)y^2 \mp (1 - q^2)2\sqrt{2}xy \right)\right) \end{aligned}$$

Then equation (6.9) can be used to calculate the value of the wavelet transform in each bin.

For the elongation parameter q , we used $\sqrt{3}$ because the projection of a given range in V along the line $U = 0$ is $\sqrt{3}$ times as long. For the scale parameter a we chose 7 km s^{-1} , comparable to the mean errors, which extracts the overdensities most clearly (Figure 6.8).³

Figure 6.8 shows that the bulk of our sample stars have thin-disk-like kinematics, with $|U|$ and $|V|$ -values $\lesssim 20 \text{ km s}^{-1}$. The contour levels do not reflect some finer structures at $-80 \text{ km s}^{-1} \lesssim V \lesssim 20 \text{ km s}^{-1}$. In this range we would expect the Hercules stream ($V \approx -50 \text{ km s}^{-1}$), as well as the Hyades-Pleiades ($V \approx -20 \text{ km s}^{-1}$) and Sirius/UMa ($V \approx +4 \text{ km s}^{-1}$) streams (Famaey et al., 2005). Indeed, the distribution in $(\sqrt{U^2 + 2V^2}, V)$ is somewhat bulged at these velocities.

Among the stars with high orbital eccentricities, presumably thick-disk or halo stars, Figure 6.8 appears to show five different overdensities. The first, at $V \approx -95$

³We also tested different choices for the set (q, a) , such as $(\sqrt{2}, 8 \text{ km s}^{-1})$ and obtained essentially unchanged results.

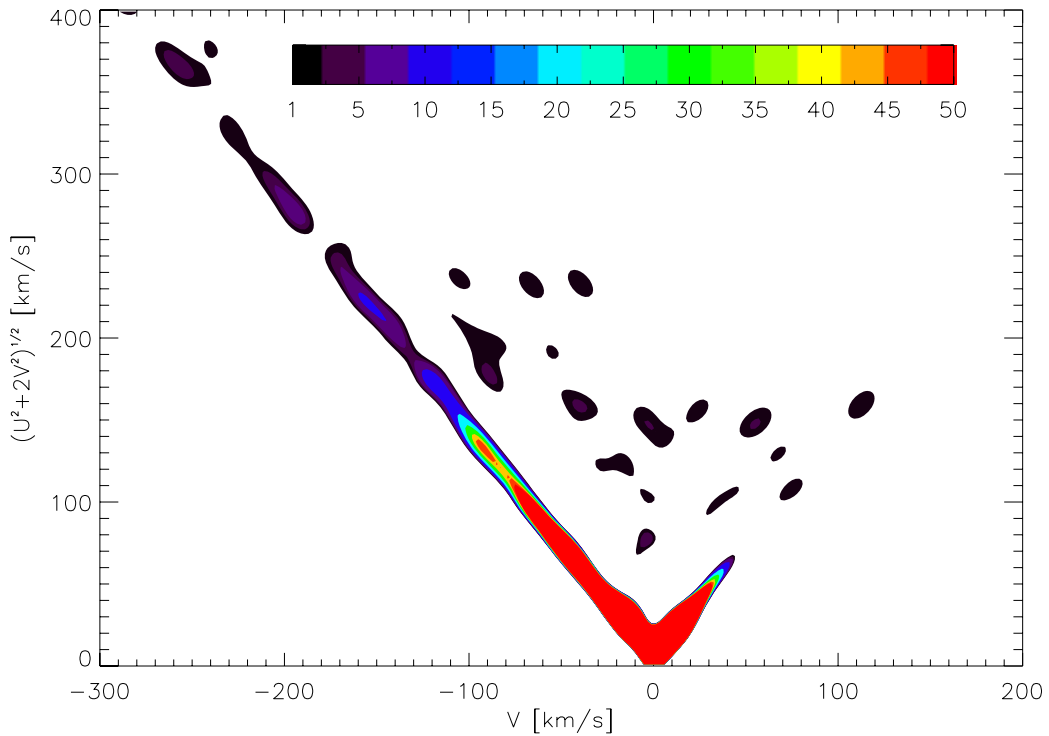


Figure 6.8: Contours of the wavelet transform of the distribution of our sample of RAVE stars (equation (6.9)) in $\sqrt{U^2 + 2V^2}$ vs. V . The contour levels are displayed in the color bar; the scale parameter of the analyzing wavelet is 10 km s^{-1} .

km s^{-1} , is most probably the stream that was discovered independently by Arifyanto and Fuchs (2006) and Helmi et al. (2006). The second overdensity, at $V \approx -120 \text{ km s}^{-1}$, has the same kinematics as the Arcturus group, discovered by Navarro et al. (2004). Both streams are now believed to be related to resonances with the Galactic bar. For example, chemical tagging of Arcturus member stars suggests that Arcturus consists of field stars (Williams, 2008); its kinematics would place it at the 4:1 resonance with the bar (Burkhard Fuchs 2008, private communication). The third feature, at $V \approx -160 \text{ km s}^{-1}$, has to our knowledge not yet been described in the literature. The same is true for the two clumps at $V \approx -200 \text{ km s}^{-1}$ and $V \approx +50 \text{ km s}^{-1}$. However, at these velocities our sample is very sparsely populated, so that just a few stars are enough to create a high value of the wavelet transform. Every isolated star in the middle of a bin increases the value of the wavelet in that bin by 2. This also explains the other clumps lying off the V-shaped main feature in Figure 6.8.

6.5 Subtracting a Smooth Velocity Distribution

To test whether any of these kinematic overdensities, or streams, reflected as peaks or clumps in the wavelet transform, are significant, we performed 250 Monte Carlo (MC) simulations of the same number of stars as in our sample, which

we randomly draw from a Galactic model consisting of three Schwarzschild distributions (Binney and Tremaine, 1987) to represent the thin and thick disk and the halo. The goal was to create a "smooth" reference model velocity distribution that matches the overall velocities of the RAVE sample. To this distribution, we then added normally distributed velocity errors, based on the observed error distributions shown in Figure 6.6. We chose local thick-to-thin disk and halo-to-thin disk normalizations of 0.1 and 0.001, respectively, in agreement with the value from Chen et al. (2001) and Jurić et al. (2008) and the upper limit given by Siegel et al. (2002). The thin and thick disk and halo are assumed to have velocity dispersions ($\sigma_U, \sigma_V, \sigma_W$) and rotational offsets from the LSR equal to (25,21,17,-5), (74,50,50,-44), and (189,97,100,-219) km s⁻¹, respectively. The values for the thin disk were chosen to best match the smooth part of the observed velocity distribution (Figure 6.9), although the ratio σ_U/σ_V in the thin disk should be approximately 1.6 (Dehnen and Binney, 1998). Also, we chose offsets in the W -distribution of +3 and +10 km s⁻¹ for the thin and thick disks to obtain a good match.⁴ The matches shown in Figure 6.9 are not perfect, but the slope of the velocity distribution at negative V -velocities is reproduced well in the simulation. The distributions differ most clearly around $V = 0$, because – possibly as a consequence of the Sirius moving group – the RAVE stars are peaked around $V \approx +5$ km s⁻¹. Moreover, the assumption of a Schwarzschild distribution does not reflect the skewness of the velocity distribution due to the asymmetric-drift effect.

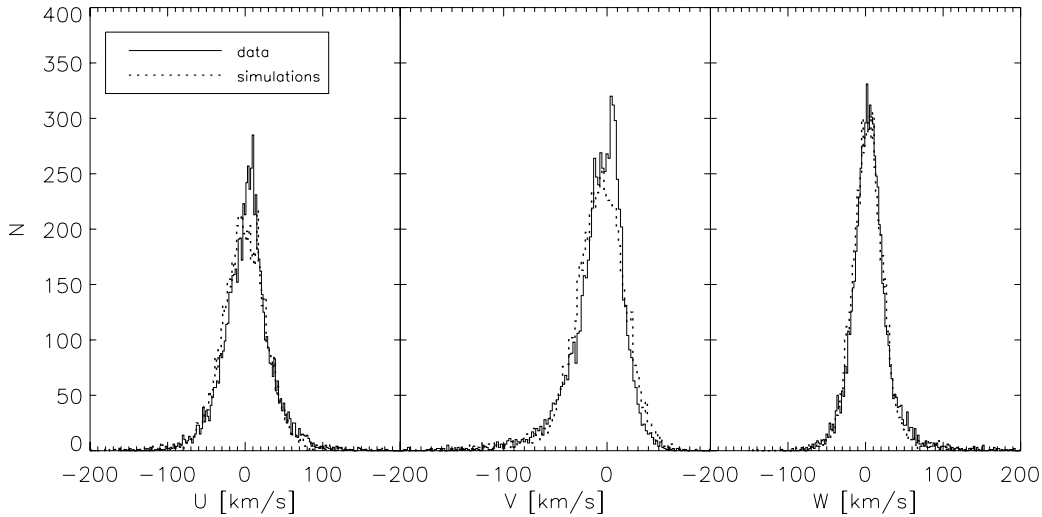


Figure 6.9: Velocity distributions of our selected RAVE-stars compared with one MC realization. The MC sample consists of three Schwarzschild distributions for the thin and thick disk and the halo, respectively. Note the peak in the data at around $V = +4$ km s⁻¹, which we interpret as the Sirius moving group below.

For each MC sample of 7015 stars, we binned the velocities and calculated the wavelet transform in each bin the same way as for the real sample. Figure 6.10

⁴This deviation from the expected mean value of $\overline{W} = 0$ could be due to the limited sky coverage of our sample.

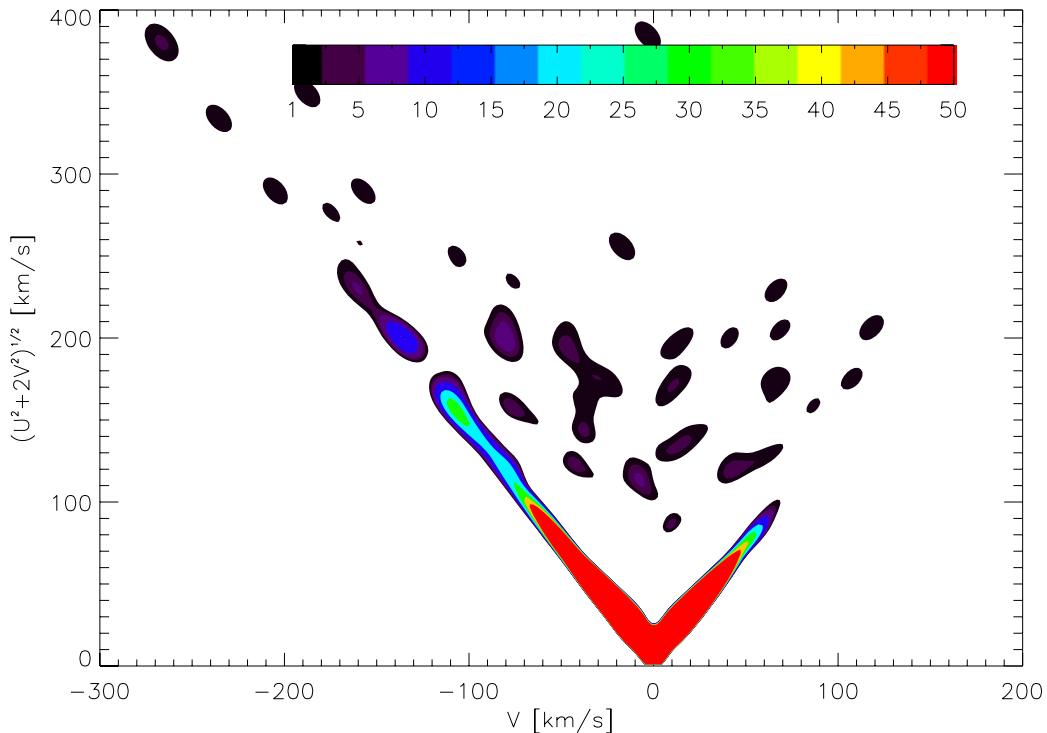


Figure 6.10: Same as Figure 6.8, but now for one of our 250 Monte Carlo samples of 7015 stars drawn from a smooth velocity model (Section 6.3). Because of Poisson noise, some overdensities emerge.

displays one randomly chosen MC realization. One can clearly detect several peaks in the wavelet transform, seeming "overdensities" which must be, however, by construction due to Poisson noise. This shows that in our real sample the possibility for such "fake" streams also exists.

We proceeded to calculate the mean value $\bar{w}_{i,j}$ and the standard deviation $\sigma_{i,j}$ of the 250 MC wavelet transforms in each (i, j) -bin. Because many bins are not populated with stars, the standard deviation in those formally has values $\sigma_{i,j} < 1$; when this was the case, we set $\sigma_{i,j} = 1$. The contours of the mean and the standard deviation are shown in Figures 6.11 and 6.12, respectively.

While a single Monte Carlo sample shows various kinds of clumps and overdensities due to statistical fluctuations (Figure 6.10; see also AF06), the mean value of all wavelet transforms represents a very smooth distribution, because the clumps disappear when averaging over all samples.

The standard deviations $\sigma_{i,j}$ define the significance of structure in our real sample in the following way: because we are only interested in overdense regions, that is, "pixels" where the wavelet transform takes positive values, we set the value of the wavelet transform of the data, $w_{i,j}^{obs}$, as well as the mean value of the wavelet transform of the 500 MC samples, $\bar{w}_{i,j}^{MC}$, to zero whenever it is ≤ 0 . By doing so, we make sure that the residual $w_{i,j}^{obs} - \bar{w}_{i,j}^{MC} \geq 0$ in each pixel, where our "smooth" model contains no stars. By dividing the residuum $w_{i,j}^{obs} - \bar{w}_{i,j}^{MC}$ in each pixel by $\sigma_{i,j}$ we define the significance of peaks of $w_{i,j}^{obs}$. For a positive stream

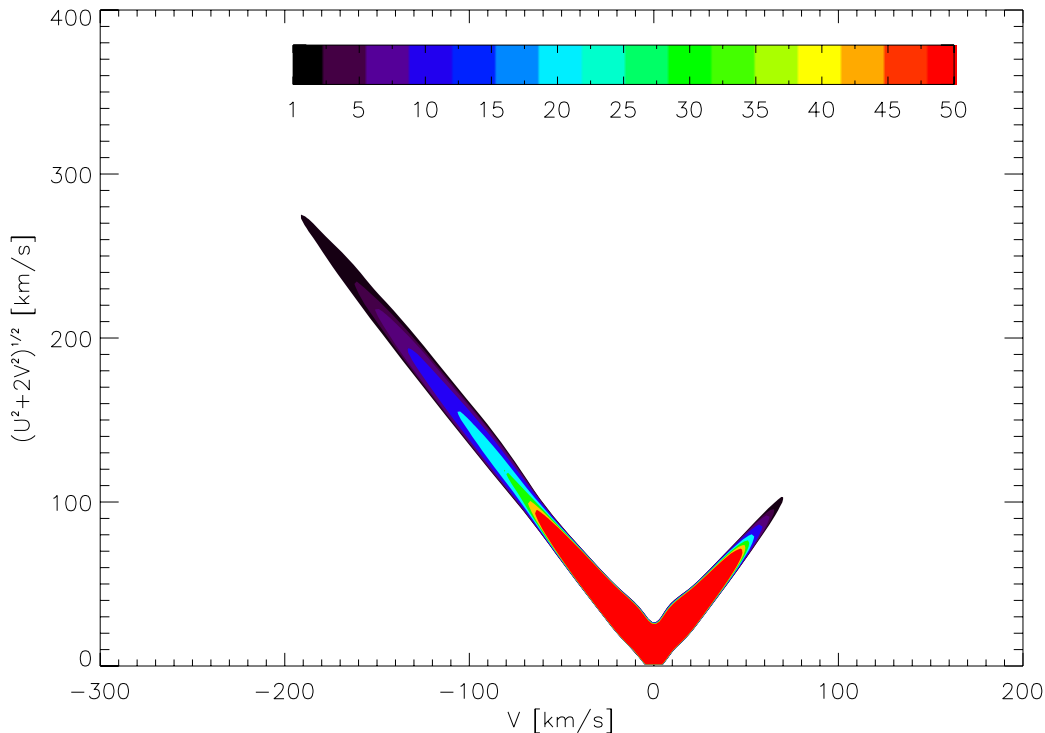


Figure 6.11: Same as Figure 6.10, but now the mean value of the wavelet transform for all 250 Monte Carlo samples is shown. Only values ≥ 1 are displayed.

detection, we require a significance of at least 2. Figure 6.13 shows the result.

6.6 Significance of the Streams

The first thing to mention is that in all bins where the standard deviation has a value of 1, the significance has the same value as the residuum $w_{i,j}^{obs} - \bar{w}_{i,j}^{MC}$. In these bins, one or a few stars will result in a significant overdensity with $\sigma_{i,j} \gtrsim 2$, since for every star in the middle of a bin, the value of w^{obs} increases by 2. This effect could then produce "fake" stellar streams, just because of Poisson noise in our RAVE sample and the smoothness of the combined Monte Carlo samples. Since a solution to this problem is difficult, we don't want to speculate about the overdensities in bins with $\sigma_{i,j} = 1$, which we have circled in red in Figure 6.13. We only give the number of stars that are contained in these features, as derived from the scatterplot, Figure 6.7. For example the extended clump at $V \approx -200$ km s⁻¹ corresponds to a group of 8 stars, while the one at $V \approx -230$ km s⁻¹ contains only 2 stars. Further investigations with more data could provide more hints for the nature of this features.

We try to match the remaining statistically significant peaks with streams that have been already described in the literature.

Centered at $V \approx +4$ km s⁻¹ and $|U| \approx 10$ km s⁻¹ there is a large clump, significant at a level of $\gtrsim 10$. This is probably the Sirius-UMa moving group (Dehnen,

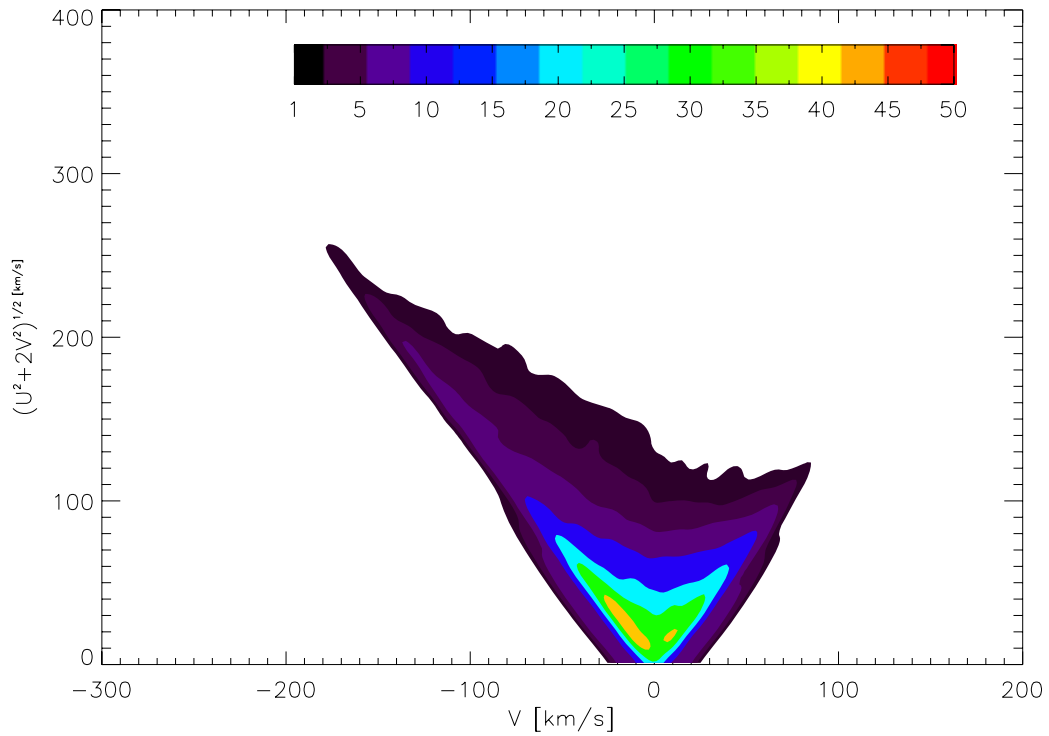


Figure 6.12: Same coordinates as Figure 6.10 and 6.11, but here the standard deviation of the wavelet transform among the 250 Monte Carlo samples is shown. Outside of the contoured region, the variance is set to unity. This variance map is used to assess the significance of wavelet transform peaks in Figure 6.8.

1998; Famaey et al., 2005), its signal possibly amplified through the inability of our simple three-component MC models to fully match the observed thin disk distribution (see also Figure 6.9). The core of this group is in the direction of Ursa Major. Its members are distributed all around the sky and can be very close (Sirius at 2.65 pc distance is a member of the group), putting the Sun inside the group (Bannister and Jameson, 2007, and references therein). The current understanding is that the Sirius stream consists not only of a cluster of coeval stars, but also of different kinds of field stars, which altogether could have been forced onto similar orbits by a spiral wave’s gravitational field (Sellwood and Binney, 2002; Famaey et al., 2005; Quillen and Minchev, 2005).

The elongated clump stretching from $V \approx -50 \text{ km s}^{-1}$ to $V \approx -75 \text{ km s}^{-1}$, with peak significance $\sigma = 4.5$, can probably best be described as the Hercules stream. This stream can be explained by the scattering of stars off the Galactic bar, induced by the Outer Lindblad Resonance (Dehnen, 2000). Famaey et al. (2005) also found a group of, most likely, thick-disk and halo stars located at $V = -53.3 \pm 41.36 \text{ km s}^{-1}$. Further, at $V = -60 \text{ km s}^{-1}$ there exists the moving group HR 1614, which is thought to be a dispersed open cluster because of its chemical homogeneity (Eggen, 1996; De Silva et al., 2007). It is possible that these groups are present in our data, too, amplifying and elongating the signal of the Hercules stream. Better velocity estimates would be needed in order to clearly

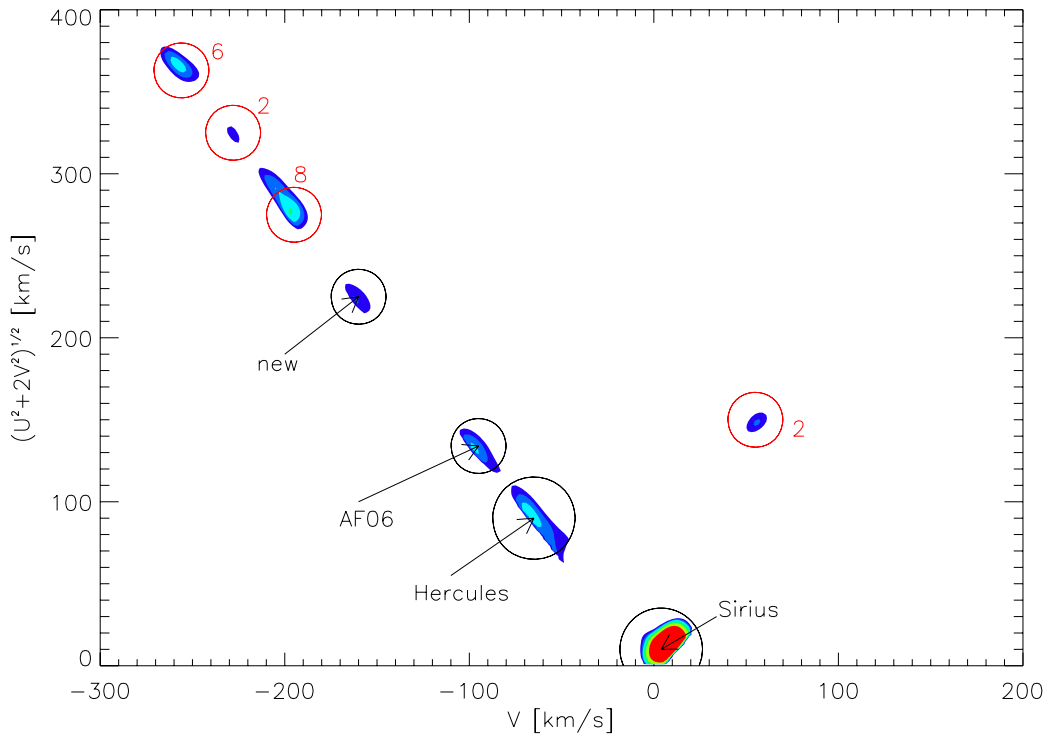


Figure 6.13: Significance of the overdensities seen in Figure 6.8, obtained as described in the text. Note that only areas with $\sigma \geq 2$ are displayed. We encircled in black and labeled all features that we consider to be stellar streams. We are not making further suggestions about the four features circled with red but instead give the number of stars that make up these features.

distinguish between these features.

The feature at $V \approx -100 \text{ km s}^{-1}$ stands out at the 4.3σ -level. It corresponds to the "AF06" stream discovered independently by AF06 and Helmi et al. (2006). This stream most likely has a dynamical origin resulting from a higher resonance with the bar, similar to Arcturus (Williams, 2008).

At a velocity of $V \approx -160 \text{ km s}^{-1}$, there is an overdensity that stands out at the 3.0σ level in the center. A comparison with Figure 6.8 reveals that this feature is probably more elongated, as one would also expect for a moving group of stars at such velocities. However, with the current sample size our method seems not to be fully able to recover the range from $V = -180 \text{ km s}^{-1}$ to $V = -140 \text{ km s}^{-1}$ as a statistically significant overdensity. Figure 6.14 shows the stars that make up the new feature in a color-magnitude diagram consisting of $V_T - H$ color and absolute magnitude M_{V_T} . Stars that lie in the area with a significance greater than 2 are plotted with heavy asterisks, while those that lie in the range $V = -180 \text{ km s}^{-1}$ to $V = -140 \text{ km s}^{-1}$ and presumably also belong to the stream have light asterisks. We also show isochrones for a 13 Gyr old population of stars with metallicities $[\text{Fe}/\text{H}]$ of -1.5 , -1.0 and 0.0 (from left to right). Most of the stars seem to be consistent with having Solar metallicity; however, this is a result that would be expected from the way we calculated their distances and velocities. Our assumption was that all are MS stars of luminosity class V, and therefore

we a priori excluded the possibility of having very metal-poor (sub-) dwarfs with fainter luminosities (see also footnote 2, in Section 6.1). Right now, we can only wait for future data releases that provide metallicity estimates to solve this issue.

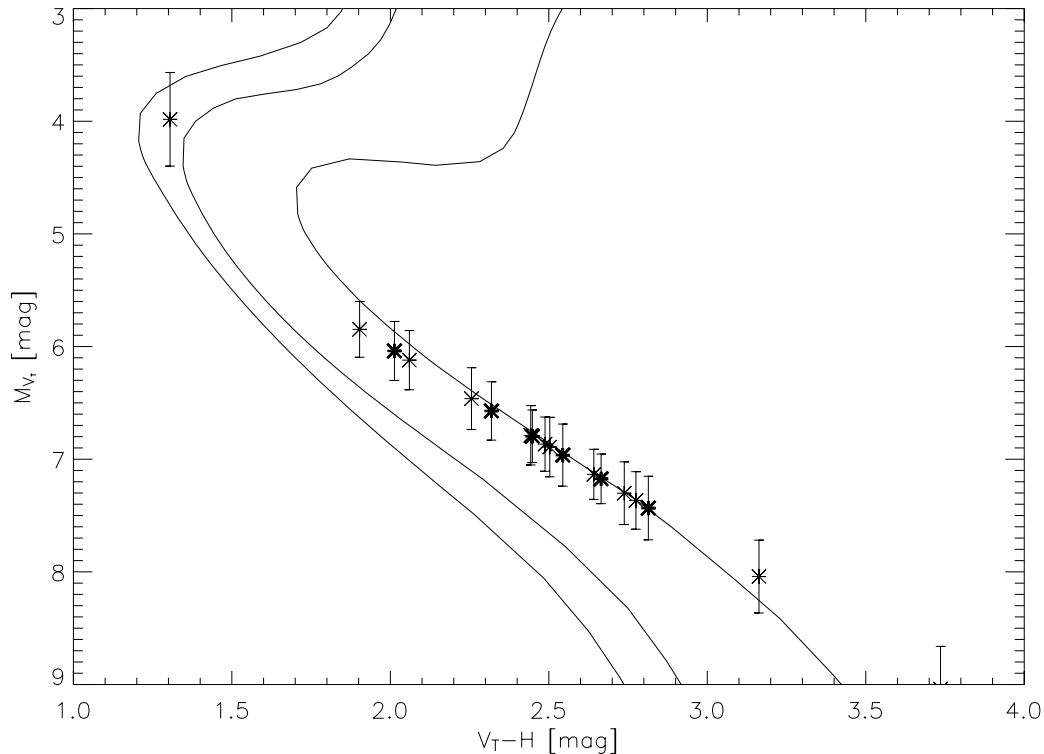


Figure 6.14: Color-magnitude diagram of the stars that make up the feature between $V \approx -140$ km s^{-1} and $V \approx -180$ km s^{-1} , highlighting those in the significantly overdense region -167 $\text{km s}^{-1} < V < -153$ km s^{-1} (heavy asterisks). Also, isochrones for a 13 Gyr old population with metallicities $[\text{Fe}/\text{H}]$ of -1.5 , -1.0 , and 0.0 are plotted. The linearity of our adopted photometric parallax relation in the range $V_T - H > 1.9$ is clearly visible.

In Section 6.7 we investigate the Geneva-Copenhagen Survey of the Solar Neighborhood (Nordstrom et al., 2004) with our method; although we do not determine the significance of overdensities with the help of MC sampling, we can see the same strong features detected by Helmi et al. (2006). It is striking that the same stellar streams can be detected in different datasets using different methods.

Therefore – through the detection of three already known stellar streams in our small RAVE dataset – we have enough confidence to claim that the new feature centered on $V = -160$ km s^{-1} is a strong candidate for a new stellar stream. The W -velocities of stars in this feature show a wide range of values, which makes it likely that this stream was accreted long ago as tidal debris during the formation of the Galaxy. To draw more conclusions, one would need metallicity measurements, which will be available from RAVE in the future.

It is possible to place constraints on the density contrast in the streams in the Milky Way stellar halo. Therefore, we estimate how many stars are needed to yield a significant stream detection and divide this number by the total number of halo stars. Because from kinematics alone it is very difficult to delimit halo from

thick-disk stars (and even with metallicities there is no clear boundary; see Chiba and Beers, 2000), we simply take all stars outside $(V \pm 2\sigma_V)_{\text{thin disk}} = -5 \pm 42$ as halo stars and accept a contamination from the thick disk. This gives 554 stars, of which 230 (42%) are part of the Hercules stream, 47 (9%) belong to the AF06 stream, and seven (1%) make up the newly detected stream. We conclude that a few-percent density contrast is enough to provide a significant stream detection.

6.7 Streams in the Geneva-Copenhagen survey

Here we demonstrate the performance of our method with the data taken from the Geneva-Copenhagen Survey of the Solar Neighborhood (Nordstrom et al., 2004). Helmi et al. (2006) searched for stellar streams in velocity and apocenter-pericenter-angular momentum (APL) space in these data. While the dynamical streams (Sirius, Hyades-Pleiades, and Hercules) can be seen as clumps in velocity space, a detailed statistical analysis of the APL space revealed around 10 further overdensities oriented along two to three segments of constant eccentricity. Helmi et al. (2006) divided the stars in the overdense regions into three groups based on their metallicities. There seems to be a relation of these three groups, the Arcturus stream and the stream detected by Arifyanto and Fuchs (2006).

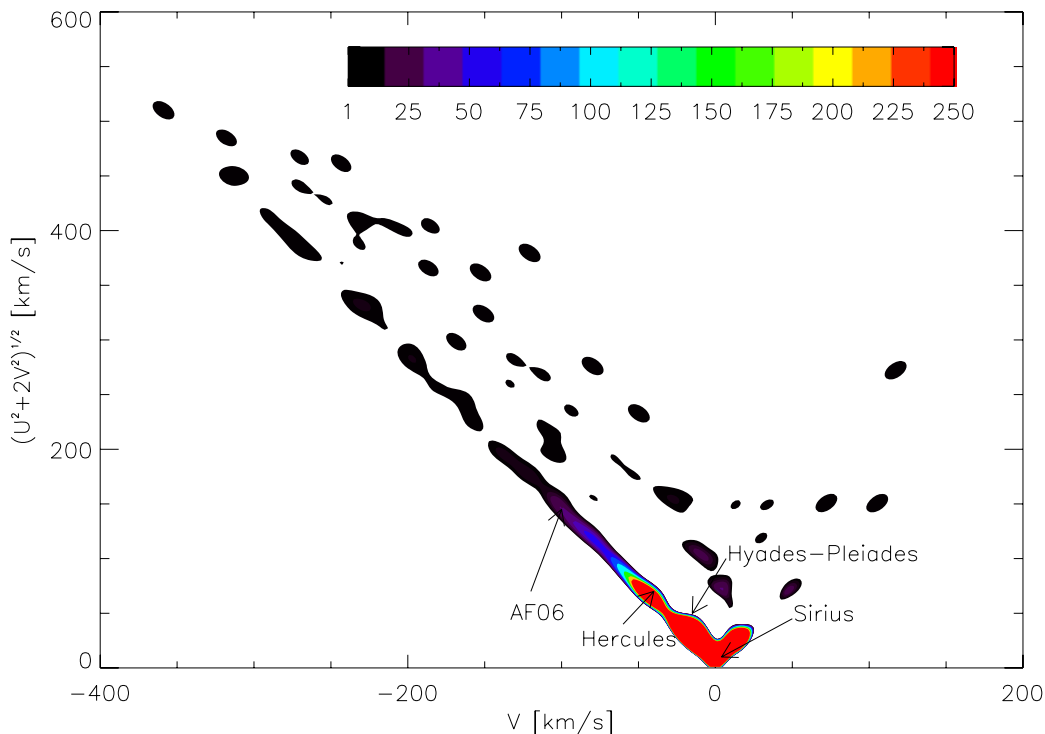


Figure 6.15: Contours of the wavelet transform of 13440 stars from the Geneva-Copenhagen Survey plotted in V vs. $\sqrt{U^2 + 2V^2}$. The features described by Helmi et al. (2006) have been labeled.

In Figure 6.15, we just show the distribution of the 13240 Geneva-Copenhagen stars in V versus $\sqrt{U^2 + 2V^2}$, after convolution with the analyzing wavelet given

by equation (6.10).⁵ The most striking features are those that were also found by Helmi et al. (2006). In addition, a comparison with our RAVE sample (Figure 6.8) seems to suggest that there is much more substructure present in the Geneva-Copenhagen Survey, although it contains only ~ 2 times more stars. We find that 10,582 of the 13,240 stars are included in these features with a value of the wavelet transform $w_{i,j} \geq 1$. That accounts for 79.9% of the sample. Our RAVE sample contains 7015 stars, of which 5601, or 79.8%, correspond to regions with $w_{i,j} \geq 1$. So, it seems that the size of the sample is the main reason that in the Geneva-Copenhagen Survey we find more distinct overdensities. Furthermore, if we connect the number of patches above the V-shaped $U = 0$ line (30 in Geneva-Copenhagen, 14 in the RAVE sample) to the number of stars in the sample, we find a similar relation; the larger number of stars increases the probability of finding outliers in less populated regions. Finally, stars in the Geneva-Copenhagen Survey have accurate trigonometric parallaxes from *Hipparcos* with relative errors (σ_π/π) better than 10%, in contrast to the less accurate photometric parallaxes of our RAVE stars. This implies less accurate velocities, which tend to smear out small nearby features in phase space.

Although it is unlikely that the majority of the small features in Fig.12 have any statistical significance, this example still shows that a large sample size together with good distance estimates is crucial for detecting stellar streams in phase space. Still, our photometric parallaxes seem to be good enough, and our sample large enough, for significant stream detections. We don't investigate the statistical significance of the features in Figure 6.15, but leave this example as further evidence that stellar streams will be detectable as clumps in $(V, \sqrt{U^2 + 2V^2})$ space.

6.8 Searching for Stellar Streams in (U, V, W) and (L_z, L_\perp) space

The traditional concept of moving groups refers to distinct clumps in (U, V, W) velocity space (Eggen, 1996, and references therein). However, as explained in Section 6.2, this space is not immune to the effects of phase-mixing: over time, distinct clumps will disperse as a result of small initial differences in the oscillation periods of the constituent stars and encounters with, for example, molecular clouds. For a part of a stellar stream to be in the Solar neighborhood at the same time means that its stars must have similar V -motions, but the U - and W -velocities can differ by hundreds of kilometers per second.

In contrast, stellar streams can remain coherent features in the space of integrals of motion. Therefore, in the style of Helmi's work (Helmi et al., 1999), we investigate to what extent the detected streams from Figure 6.13 can be recovered in (U, V, W) - and (L_z, L_\perp) -space.

⁵Arifyanto and Fuchs (2006) also performed this analysis, but using the presumably not optimal Mexican-hat analyzing wavelet.

6.8.1 Analyzing the RAVE Data in (U, V, W) -Space

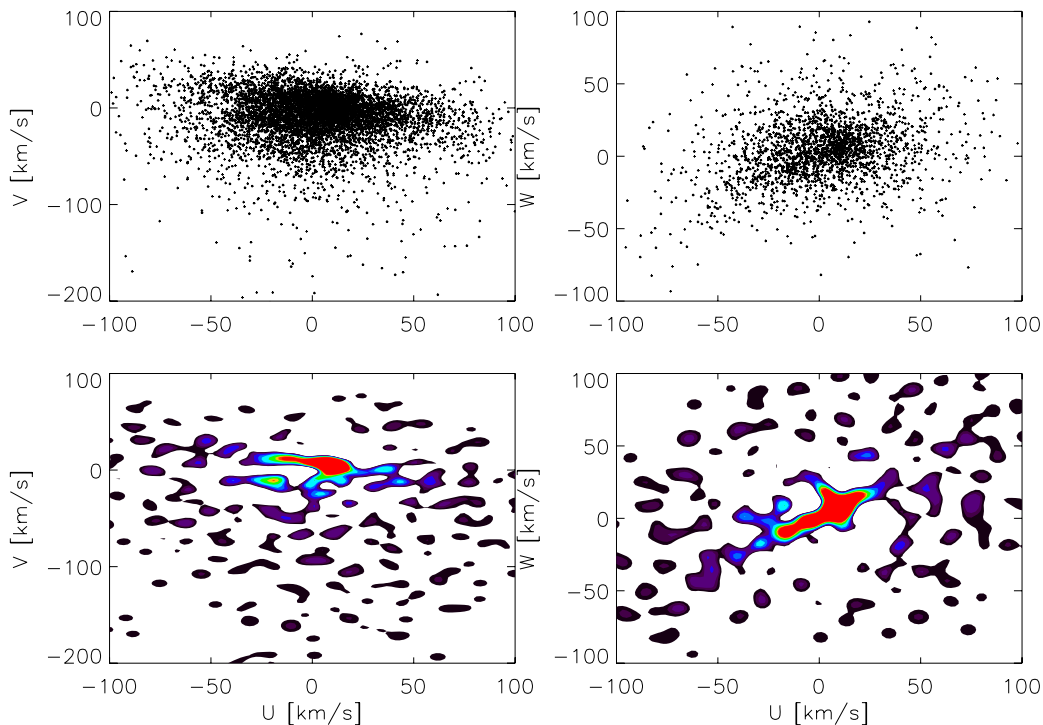


Figure 6.16: Distribution of RAVE stars in velocity space. The top panels show scatter plots of U vs. V and U vs. W , respectively. A great deal of substructure can be seen. In the bottom panels, we show contours of a wavelet transform of the data. The convolution has been made using a Mexican-hat kernel with scale parameter $a = 5 \text{ km s}^{-1}$.

In Figure 6.16, we show the distribution of our 7015 RAVE stars in velocity space. The upper panels show how the stars are distributed with respect to their (U, V, W) -velocities. The distribution is far from smooth, as can be seen more clearly in the bottom panels, where we display the wavelet transform of the velocity components. For the convolution we chose a Mexican-hat kernel with a scale parameter of $a = 5 \text{ km s}^{-1}$ (similar to Skuljan et al., 1999). The contour levels range from 1 (black) to 50 (red). The most striking features are located around $V = 0, U = 0$ and most probably can be attributed to dynamical thin-disk streams such as the Sirius moving group. The elongated shape along the U -axis is typical of stellar streams and is caused by the fact that we observe stars with slightly different orbital phases. The classical moving groups Sirius, at $(U, V) \approx (+6, +4) \text{ km s}^{-1}$, the Hyades-Pleiades, at $(U, V) \approx (-25, -15) \text{ km s}^{-1}$, and Hercules, at $(U, V) \approx (-20, -50) \text{ km s}^{-1}$, can be found with good agreement with the values given by Famaey et al. (2005). The incomplete sky coverage of our sample as well as the already described effects of phase-mixing makes it hard to speculate about the meaning of the many other clumps. We nevertheless performed a statistical Monte Carlo analysis analogous to that described in Section 6.5 using 200 Monte Carlo simulations. Figure 6.17 provides the significance map of the velocity space, showing all overdensities from Figure 6.16 that have a significance of

at least 2.

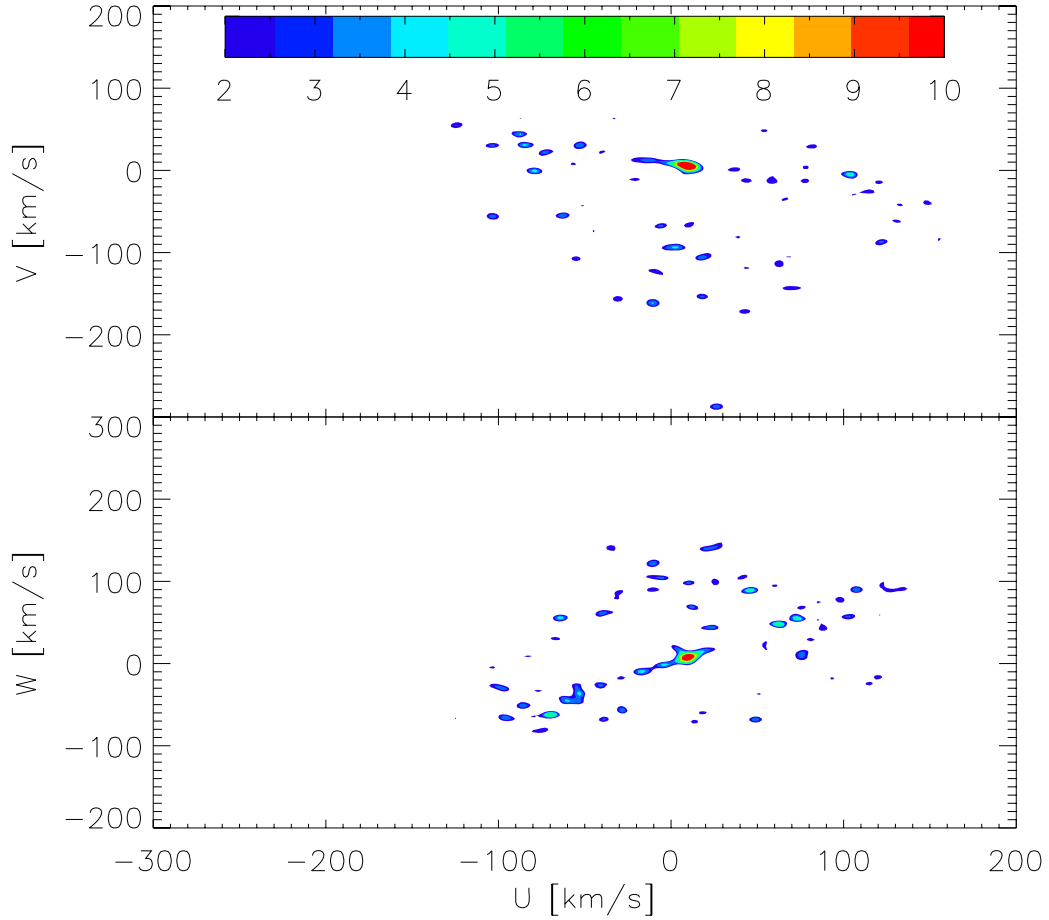


Figure 6.17: Significance of the overdensities seen in Figure 6.16. Only areas with $\sigma \geq 2$ are displayed. Note the richness of features compared with Figure 6.13, with many having a very small extension.

Compared with $(V, \sqrt{U^2 + 2V^2})$ -space (cf. Figure 6.13), there are more features present, but most are very small and at lower significance levels. Besides the prominent red feature around $(U, V) \approx (0, 0)$, which can be attributed to the Sirius stream, it is not easy to associate the identified streams from Figure 6.13 with clumps in the (U, V) - or (U, W) -diagrams. Because old moving groups are not expected to remain coherent small clumps in velocity space, we have likely over resolved substructure due to the small deviations of our Monte Carlo model from the data. These deviations can also lead to a washing out of the banana-shaped structures in (U, V) that are expected for old tidal streams (Helmi et al., 2006). Large errors in the velocities can wash out these structures, too, but in our case the errors should allow their detection. The facts that a clear classification of particularly old stellar streams from the (U, V) - and (U, W) -distributions is not possible and that many small features are even less significant than the overdensities in $(V, \sqrt{U^2 + 2V^2})$ -space let's us conclude that (U, V, W) -space is not well suited to the detection of moving groups.

6.8.2 Analyzing the RAVE Data in (L_z, L_\perp) -Space

Assuming a spherical static potential, the two components of the angular momentum, L_z and $L_\perp = (L_x^2 + L_y^2)^{\frac{1}{2}}$, are integrals of motion. In this case, tidal and dynamical streams will remain coherent clumps in (L_z, L_\perp) -space. The assumption of a spherical potential seems valid for large heights above or below the disk that are reached only by halo stars, but not necessarily in our case of nearby stars with planar orbits. These stars move under the influence of a flattened potential, and the radial action integral J_R would be better suited as a conserved quantity. The space of integrals of motion has been shown to be useful for the detection of stellar halo streams in recent studies (Helmi et al., 1999; Helmi and de Zeeuw, 2000; Chiba and Beers, 2000).

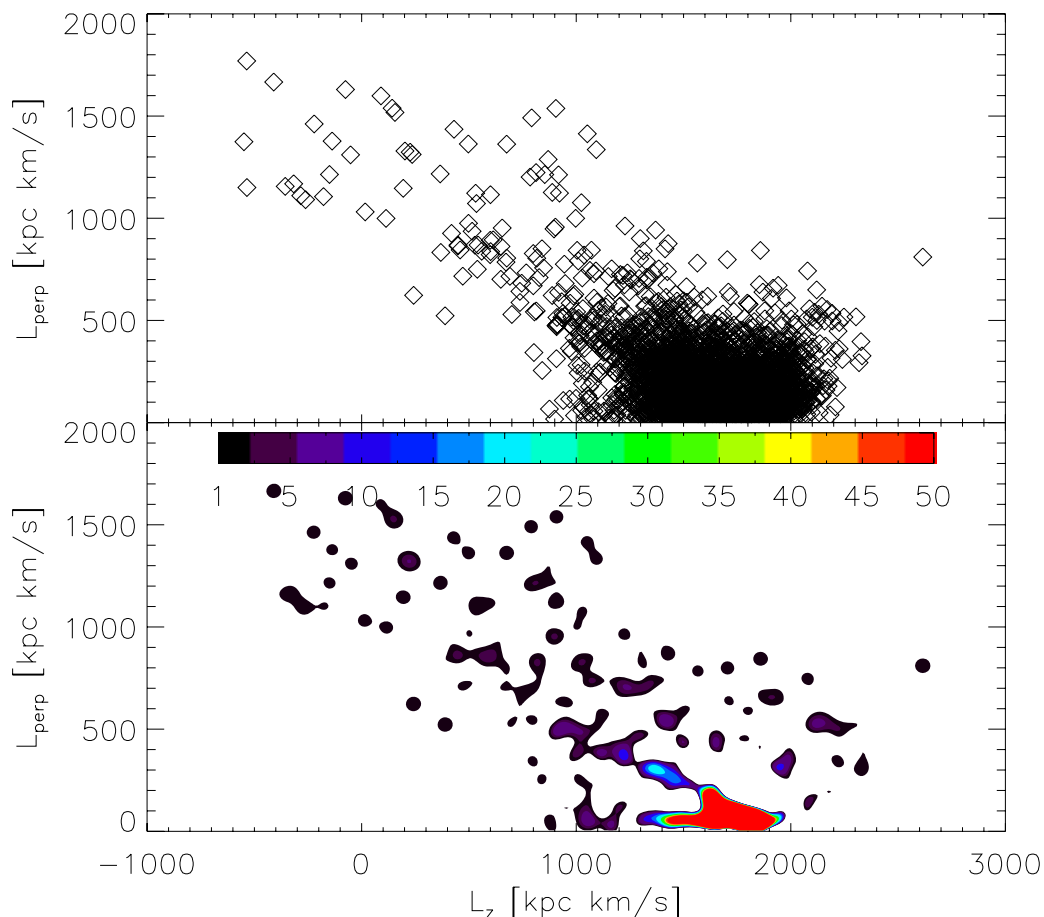


Figure 6.18: Distribution of RAVE stars in (L_z, L_\perp) space. The top panel is a scatter plot of the data. In the bottom panel, we show contours of a wavelet transform of the data. The convolution has been made using a Mexican hat kernel with scale parameter $a = 45 \text{ km s}^{-1}$.

In Figure 6.18, we show the distribution of our RAVE stars in (L_z, L_\perp) space, again as a scatter plot (*top*) and after wavelet transformation using a Mexican-hat kernel with scale parameter $a = 45 \text{ kpc km s}^{-1}$. For stars near the Sun, $L_z \simeq R_\odot(V + V_{LSR})$, so we expect to again identify the overdensities from Figure 6.8.

A comparison shows first of all that (L_z, L_\perp) -space seems to be much more structured than $(V, \sqrt{U^2 + 2V^2})$ -space, but this is partly due to the applied chosen scale parameter a in the kernel function. The other reason is that now all three velocity components go into the calculation of the angular momentum components. Also, there are no "forbidden regions" like in case of $(V, \sqrt{U^2 + 2V^2})$ -space.

Some overdense regions in the bottom panel can be related to overdensities in $(V, \sqrt{U^2 + 2V^2})$ space. For example, the "bump" in the distribution in Figure 6.8 at $V \approx -15 \text{ km s}^{-1}$ is also present in Figure 6.18 at $L_z \approx 1650 \text{ kpc km s}^{-1}$. Also, the Hercules stream is present at $L_z \approx 1350 \text{ kpc km s}^{-1}$.

We proceeded to investigate which overdensities prove significant in the same way as before, by using 200 MC samples that were drawn from the three-component Galaxy model described in Section 6.5. After building the mean value and standard deviation of their wavelet transforms we derived the significance map, which is shown in Figure 6.19 in the upper panel.

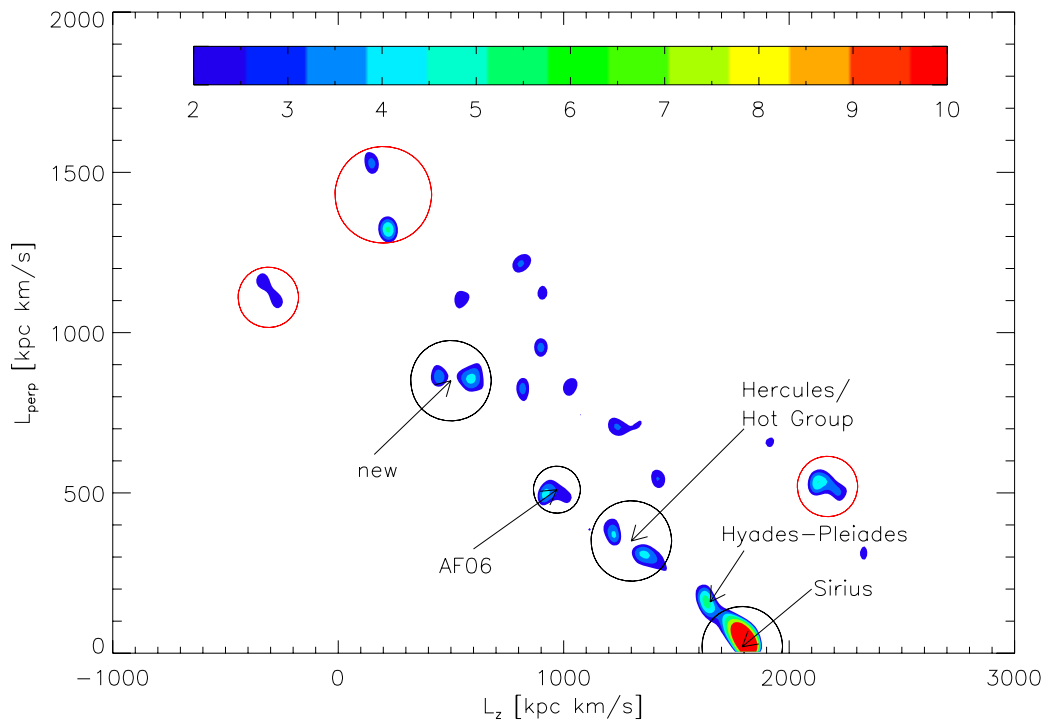


Figure 6.19: Significance of the overdensities seen in Figure 6.18. Only areas with $\sigma \geq 2$ are displayed. Black circles mark features that we connect to the detections of Figure 6.13; there is further evidence for the now significant Hyades-Pleiades group. Red circles mark features that can be connected to doubtful features in Figure 6.13. Note that for stars near the Sun $L_z \approx R_\odot V$, where we take $R_\odot = 8 \text{ kpc}$.

As in the case of (U, V, W) -space, the number of features with significance $\sigma \geq 2$ is larger than in Figure 6.13. We think that this is caused by the extra information of the W -velocity required for the MC samples. Some of these features are very small and again belong to regions of phase space that are sparsely sampled, but others seem to be comparable to the already known ones. We circled all features that correspond to the detections of Figure 6.13 with black for the

appointed streams and with red for the doubtful ones, respectively. In addition, there is a new feature present at $L_z \approx 1650 \text{ kpc km s}^{-1}$, which we identify as the Hyades-Pleiades group. A hint to the presence of this group has already been seen as a "bump" in the distribution of stars in $(V, \sqrt{U^2 + 2V^2})$ -space (Figure 6.8). It is interesting that some distinct features in (L_z, L_\perp) -space (e.g. the new stream) get projected onto the same feature in $(V, \sqrt{U^2 + 2V^2})$ -space. Furthermore, when we select stars from the fastest rotating clumps (Hyades-Pleiades, Sirius and the red encircled clump on the right in Figure 6.19), we find that they span a wide range of values in $\sqrt{U^2 + 2V^2}$. On the other hand, we also find that clumps in $(V, \sqrt{U^2 + 2V^2})$ -space are not necessarily projected onto clumps in (L_z, L_\perp) -space, indicating that L_\perp is not conserved for their motion (Figure 6.20). Therefore, we conclude that L_\perp , compared with $\sqrt{U^2 + 2V^2}$, is not a good choice as an approximate integral of motion if the disk's potential dominates the movement of the stars.

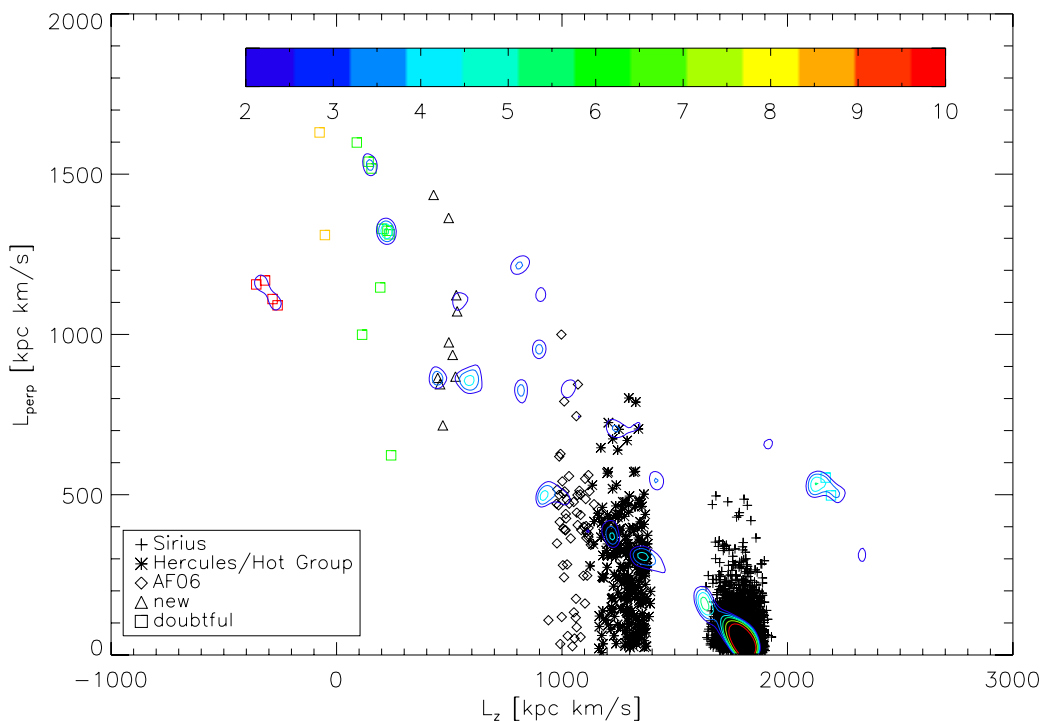


Figure 6.20: Same as Figure 6.19 with all stars that belong to the features from Figure 6.13 over-plotted. The doubtful detections are shown with different colors to better discriminate between them. The fact that clumps from $(V, \sqrt{U^2 + 2V^2})$ -space do not necessarily get projected onto clumps in (L_z, L_\perp) -space indicates that L_\perp is not conserved for their motion.

We note as a main result that the significances of the detected features are comparable, no matter which space we use for the stream search. As explained above, we expect the significance of the detections to go up with a larger sample size. For best results, it would probably be good to combine searches in (L_z, L_\perp) - and $(V, \sqrt{U^2 + 2V^2})$ -space to find stellar streams on both inclined and planar orbits. Also, the significance is influenced by the statistical method used to identify over-dense regions. Our MC method has the drawback that a good Galactic velocity

distribution model is needed in order to avoid "fake" detections in regions where data points are scarce. A combination of different analyses might also enhance the detection efficiency.

6.9 Conclusions

To explore RAVE's practical potential for finding kinematic substructures (streams, or moving groups) in the Solar neighborhood, we have studied a sample of 7015 nearby stars from the first RAVE public data release, which was selected to have acceptable distance and velocity estimates. Distances were derived from a photometric parallax relation, based on *Hipparcos* main-sequence stars using the V_T and H bands. For our sample, we required a distance error better than 25%, while the mean velocity errors in U and V are approximately -5 km s^{-1} , respectively.

To search for streams, we plotted V -velocities against the quantity $\sqrt{U^2 + 2V^2}$, which essentially corresponds to angular momentum L_z versus orbital eccentricity e . Streams should form clumps in this projection of phase space. To make such clumps more identifiable, we applied a wavelet transform with a modified two-dimensional Mexican-hat kernel as the analyzing wavelet. Several overdensities are visible in this sample, presumably corresponding to stellar streams. We tested whether these clumps are real or due to Poisson noise using 250 Monte Carlo simulations drawn from a three-component Schwarzschild distribution. While it is very difficult to draw conclusions about the amount and significance of substructure present in the very few halo stars, we did detect three already known stellar streams and one candidate for a newly discovered stream. The latter is present as a broad feature in the range $-180 \text{ km s}^{-1} \leq V \leq -140$, centered at $V \approx -160 \text{ km s}^{-1}$ and, from its kinematics, would belong to the stellar halo population. Its other velocity components (high W -velocities, with mean $\langle W \rangle = 121 \pm 2 \text{ km s}^{-1}$, $\langle U \rangle = 15 \pm 2 \text{ km s}^{-1}$) make it likely that this stream is part of the tidal debris from an accreted satellite rather than being due to a dynamical resonance. The kinematics, however, could be somewhat biased, because we did not correct for metallicity effects in the photometric parallax relation. The other moving groups are the Sirius stream, at $V \approx +4 \text{ km s}^{-1}$, the Hercules stream, centered at $V \approx -65 \text{ km s}^{-1}$ (Dehnen, 1998; Famaey et al., 2005), and the stream discovered by AF06 and Helmi et al. (2006) at $V \approx -100 \text{ km s}^{-1}$.

We are missing a detection of the Hyades-Pleiades and Arcturus streams which were still present as peaks in the wavelet transform of the data in Figure 6.8. Here the difference $w_{i,j}^{obs} - \bar{w}_{i,j}^{MC}$ is too small to make the peak in $w_{i,j}^{obs}$ statistically significant.


However, we were able to detect the Hyades-Pleiades moving group in velocity and angular momentum space, which we used to complement our stream search. By comparing the detections in (U, V, W) -, (L_z, L_\perp) - and $(V, \sqrt{U^2 + 2V^2})$ -space we showed (1) that the significances of the features are comparable, (2) that velocity space is sub-optimal for detecting stellar streams but may be useful for additional information on the age and origin of a stream (tidal streams look dif-

ferent from dynamical streams, old streams disperse), and (3) that L_{\perp} is a poor approximate integral of motion compared with $\sqrt{U^2 + 2V^2}$ if the stars are mainly moving under the influence of the disk's potential.

The fact that only a fraction of the RAVE DR1 stars were enough to find significant substructure in the Solar neighborhood shows the power of the method used. Subsequent data releases will not only enlarge the sample of stars and eventually allow the detection of further clumps in phase space but will also provide measurements of $\log g$, T_{eff} and $[M/H]$. The full data set will include these measurements for up to 1 million stars (Steinmetz et al., 2006). Simply speaking, and neglecting an increase in spatial coverage, an enlargement of the sample size by a factor of N leads to N times more stars in a stellar stream, while the standard deviation of the MC samples will be increased by a factor of \sqrt{N} (Poisson noise). The mean value of the wavelet transform of the MC samples stays the same, so that the significance of the features will be $N/\sqrt{N} = \sqrt{N}$ times as high. In this way we can hope to detect more features and place further constraints on the exact nature and origin of the detected streams.

Chapter 7

Halo Streams in the Seventh SDSS Data Release

he Sloan Digital Sky Survey (SDSS York et al., 2000) has provided data of both unprecedented quantity and quality to study the overall structure and kinematics of the Milky Way (e.g. Carollo et al., 2007; Jurić et al., 2008; Ivezić et al., 2008; Xue et al.). As part of SDSS-II, the Sloan Extension for Galactic Understanding and Exploration (SEGUE) will obtain some 250,000 spectra of stars in the Galaxy allowing to derive the six-dimensional phase-space distribution of various components of the Milky Way.

Our goal is to find stellar streams among the halo population of stars in the Solar neighborhood, which are presumably remnants of past accretion events. We have available $\sim 155,000$ stars targeted by SEGUE which have radial velocities, iron abundance ratios and proper motions from USNO-B accurate to $5\text{-}10\text{ km s}^{-1}$, 0.18 dex and a few mas yr^{-1} , respectively. A crucial quantity to estimate the 6D phase-space coordinates of stars is their distance, which enters in \vec{r} and $v_{\perp}^2 = d\vec{\mu}$. We use the photometric parallax relation from Ivezić et al. (2008), which includes a correction for metallicity, to estimate distances to all stars. We examine and quantify the accuracy of this relation by applying it to a set of globular and open clusters observed by the SDSS and comparing the resulting sequence to the fiducial cluster sequences obtained by An et al. (2008, in prep.). Our final sample consists of 22,321 nearby ($d \leq 2\text{ kpc}$), metal-poor ($[\text{Fe}/\text{H}] \leq -0.5$) main sequence stars, with 6D estimates of (\vec{r}, \vec{v}) , which allow us to conduct a search for stellar streams using the method outlined in Dettbarn et al. (2007).

7.1 The Data

We start the sample selection from all stars targeted by SEGUE with $S/N > 10$, photometry in all five bands and estimates for the radial velocity, $[\text{Fe}/\text{H}]$ and proper motions. These stars have been taken from the seventh data release (DR7.2) and their proper motions have been corrected for a systematic error that occurred in the data reduction procedure (Munn 2008, internal SDSS memorandum). There are

a number of repeated observations for quality insurance reasons, mainly among the photometric calibration stars. These repeats are independent observations and listed separately with different identification numbers. Therefore we only keep one single object, to which we assign a radial velocity averaged over all repeats. We show the sky coverage of the resultant sample of 154,888 stars in Figure 7.1. The data covers a large, almost contiguous area in the Northern Galactic Cap plus three stripes in the South Galactic Cap.

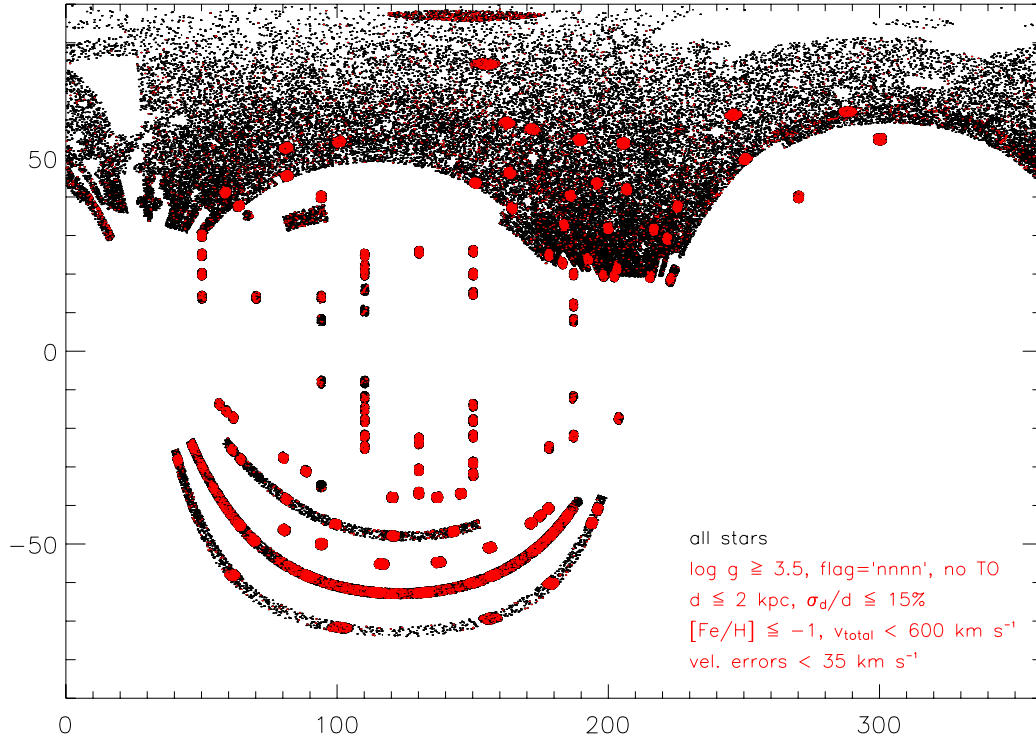


Figure 7.1: Sky coverage of our sample of SEGUE stars. Each star is plotted individually. The red data points give the positions of metal-poor stars that meet the selection criteria of our final sample (see Section 7.1.2). Note the sparse sampling obtained during SDSS-I vs. the focussed sampling of the SDSS-II SEGUE pointings.

7.1.1 Distance Estimates

The majority of stars observed by SDSS are main-sequence stars ($\sim 99\%$, Finlator et al., 2000). Although the targets selected by SEGUE explicitly include giants, their fraction based on spectroscopic surface gravity estimates remains low. This is shown in Figure 7.2, where we show the $\log g$ -distribution of the total sample. Only 8.8% of the stars have $\log g < 3.5$, where we make the separation between dwarfs and giants. This is a bit more stringent than the separation made e.g. by Ivezić et al. (2008) at $\log g = 3$, but we want to make sure to only select late-type dwarfs and sub-dwarfs.¹ Presuming a sample dominated by main-sequence stars,

¹A subdwarf is defined as a star with luminosity 1.5 to 2 magnitudes lower than that of a main-sequence star of the same spectral type.

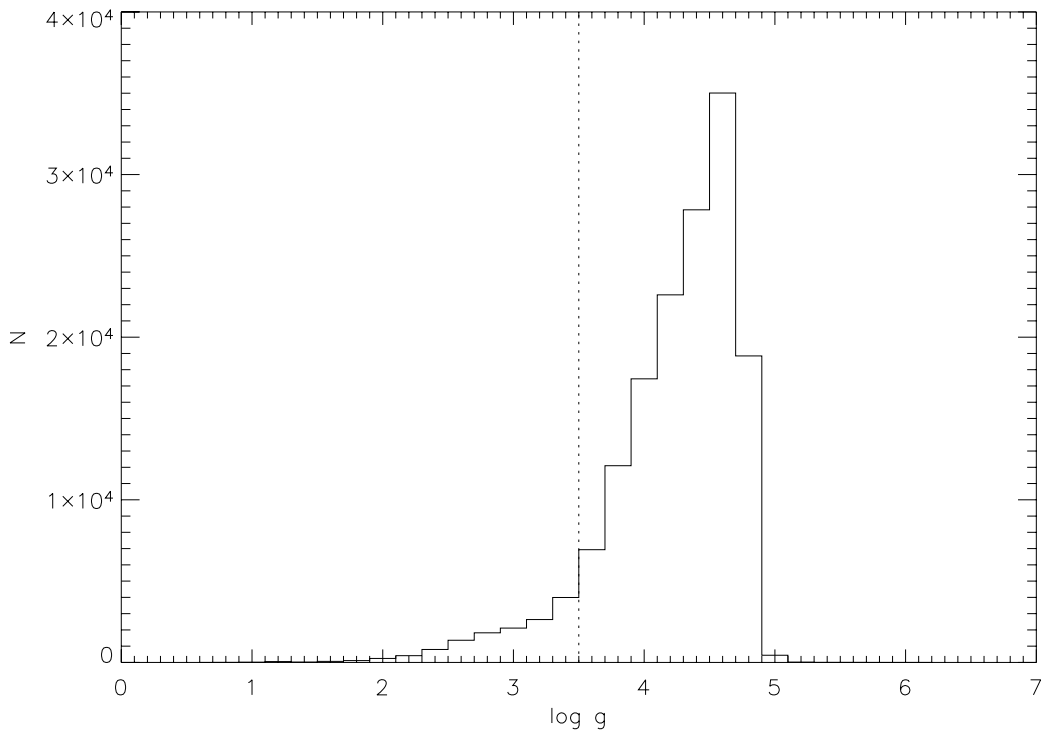


Figure 7.2: Distribution of surface gravities of the total sample of 154,888 SEGUE stars. We cut at $\log g = 3.5$ to select only the dwarfs and sub-dwarfs.

we can apply a photometric parallax relation to derive distances. Because we want to concentrate on a wide range of metal-poor stars, the effect of metallicity on the absolute magnitude at a given color becomes important. There have been several attempts to include a metallicity correction in the photometric parallax relation. For example, Siegel et al. (2002) give a correction based on the distance of a star from the Galactic plane, assuming that the mean metallicities of tracer stars like K giants also apply to the dwarf population. Another approach makes use of the ultraviolet excess, $\delta(U - B)$, which has been found to be correlated to the metal-deficiency for F and G stars (Wallerstein, 1962, and references therein). $\delta(U - B)$ is originally defined as the difference between a star's $U - B$ color and that of a Hyades member star at the same $B - V$ color. The ultraviolet excess, however, loses its sensitivity as a metallicity estimator outside a restricted color range (roughly $0.4 \leq (B - V) \leq 0.8$ Carney, 1979) and any relations based on $\delta(U - B)$ -derived metallicities are doubtful beyond this range (e.g. Laird et al., 1988; Karaali et al., 2003, 2005).

Another problem with the previous photometric parallax relations is that they are not expressed in the SDSS photometric system. Therefore Jurić et al. (2008) converted several relations from the literature into a $(r - i)$ vs. M_r relation using color conversion formulas from Ivezić et al. (2007) and fits to the stellar locus in SDSS color-color diagrams from Ivezić et al. (2004). They then constructed a relation which attempts to fit the different relations at the red end ($r - i \gtrsim 1.4$) and reproduces SDSS observations of globular cluster M13 at the blue end

($r - i = 0.10$). Because this relation is tied to nearby metal-rich stars via relations that have been calibrated using geometric parallaxes, and to M13 on the blue end, it implies metal-richness for red stars and lower metallicity for bluer stars. It is therefore not suited for our purpose to detect stellar streams among nearby metal-poor stars. Also we have spectroscopic metallicities available for each star, so we wish to adopt a photometric parallax relation which explicitly accounts for metallicity over a wide range of colors.

Such a relation has been derived by Ivezić et al. (2008). They use the $g - i$ color instead of $r - i$, because $g - i$ spans a wider color range for a given stellar type and they argued that it has better signal-to-noise properties. The shape of the color-magnitude relation, $M_r^0(g - i)$, is constrained by simultaneously fitting SDSS data of five globular clusters that have been normalized to the same arbitrary magnitude scale by requiring the same median magnitude of $r = 0$ for stars in the color range $0.5 < g - i < 0.7$. By assuming that this shape only depends on color, not metallicity and its normalization depends only on metallicity, not color, the absolute magnitude offset of each cluster from the mean relation can be expressed as a function of metallicity. The absolute magnitude of a star is then calculated as

$$M_r(g - i, [\text{Fe}/\text{H}]) = M_r^0(g - i) + \Delta M_r([\text{Fe}/\text{H}]) \quad (7.1)$$

With distances adopted from Harris (1996) and six additional open and globular cluster data from VandenBerg and Clem (2003), they derive the following absolute magnitude correction:

$$\Delta M_r([\text{Fe}/\text{H}]) = 4.50 - 1.11[\text{Fe}/\text{H}] - 0.18[\text{Fe}/\text{H}]^2 \quad (7.2)$$

The correction (7.2) suggests an offset of the mean relation of 4.5 for Solar metallicity. This is caused by the scaling of the individual cluster sequences to a median of $r = 0$ in the color range $0.5 < g - i < 0.7$. Ivezić et al. (2008) further expand the mean photometric parallax relation to the color range $0.2 < g - i < 4.0$ by using constraints from trigonometric parallaxes given in Bochanski et al. (2008, in prep.), additional cluster data observed in the SDSS from Clem et al. (2008) and an age correction for turn-off stars. The result is a fifth-order polynomial

$$M_r^0(g - i) = -5.06 + 14.32(g - i) - 12.97(g - i)^2 + 6.127(g - i)^3 - 1.267(g - i)^4 + 0.0967(g - i)^5, \quad (7.3)$$

which – together with Equations (7.1) and (7.2), is the final photometric parallax relation.

We test the validity of this relation for our sample using different approaches which are described in the following.

Comparison of the Photometric Parallax Relation with Cluster Fiducial Sequences

An et al. (2008, hereafter An08) have reduced the SDSS imaging data for 17 globular and 3 open clusters and estimated fiducial sequences from the color-magnitude diagrams (CMDs). The sequences give the r band magnitude as a

function of either $u - g$, $g - r$, $g - i$ or $g - z$ color. This is the first time that cluster fiducial sequences have been evaluated in the native SDSS $ugriz$ system. This allows us to test the photometric parallax relation from Ivezić et al. (2008) without relying on color transformations.

We use 15 of the cluster fiducials and compare them to the sequences derived from Equations (7.1)-(7.3). In addition, we show the fiducial sequences from Clem et al. (2008) for five clusters after transforming them into the $ugriz$ system using the transformations given by Tucker et al. (2006). These sequences have been shown to match the An08 fiducials within the errors of the photometric zero points. Because they were obtained from observations with various integration times, they extend over a broader magnitude range than the An08 sequences. We calculated the absolute magnitude M_r for each cluster by adopting the distance modulus and metallicity as given in An08. From the distance modulus and the absolute magnitude difference, ΔM_r , between the fiducials and the Ivezić et al. (2008) sequences we calculate the absolute relative distance error $|\Delta d/d|$. The results are shown in Figures 7.3-7.6, sorted by descending cluster metallicity.

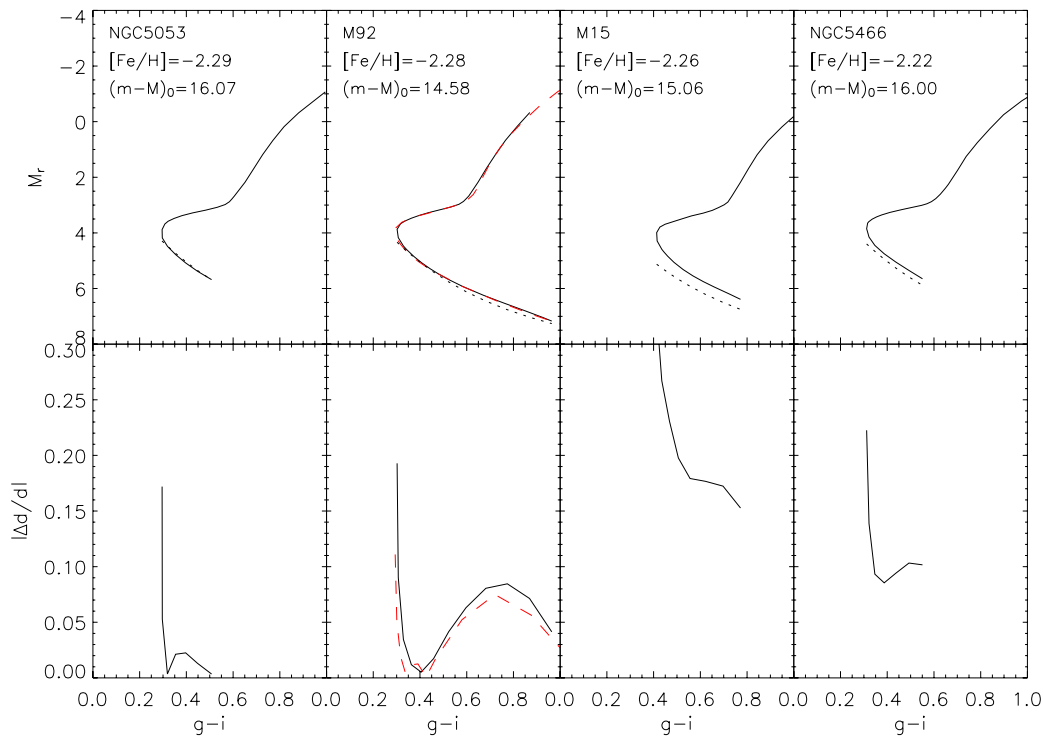


Figure 7.3: Comparison of cluster fiducial sequences taken from An08 (*solid black lines*) and Clem et al. (2008) (*dashed red line*), respectively, and the $[\text{Fe}/\text{H}]$ -dependent photometric parallax relation from Ivezić et al. (2008) (*dotted line*) for the metal-poor clusters NGC5053, M92, M15 and NGC5466. The upper panels show the absolute magnitude M_r as a function of the $g - i$ color. The lower panels show the corresponding absolute relative distance error. The adopted distance moduli and metallicities are taken from various sources in the literature (see An08, section 2 for all references).

The photometric parallax relation of Ivezić et al. (2008) fits the fiducial main sequences remarkably well for most of the clusters. For most of the metal-poor

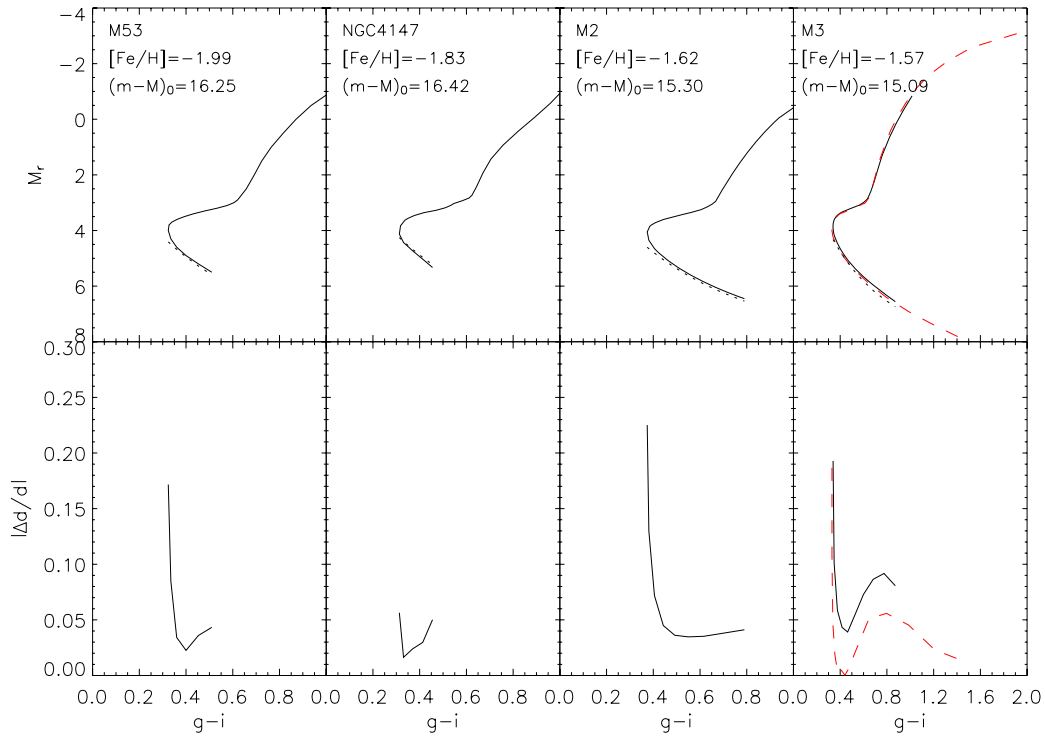


Figure 7.4: Same as Figure 7.3, but for clusters M53, NGC4147, M2 and M3.

clusters with $[\text{Fe}/\text{H}] < -1.0$ the relative distance error stays below $\sim 10\%$ for $g - i \gtrsim 0.4$. An exception is M15 where the turn-off is slightly redwards from $g - i \approx 0.4$ and the relative distance error roughly drops from 20% at $g - i \approx 0.5$ to 15% at $g - i \approx 0.8$. Note also the good agreement between the An08 and Clem et al. (2008) fiducial sequences.

From the clusters with intermediate metallicities, M13 and M5 show very good agreements, while for Palomar 5 and M17 the discrepancies are large. For Palomar 5 the discrepancy is more than 30%; however, this cluster is known to be in the process of tidal disruption (Odenkirchen et al., 2001; Grillmair and Dionatos, 2006) and is sparsely populated in the observations – a contamination by foreground and background stars is possible. Also, the color range spanned by the main sequence is very small compared with the giant branches and it may not extend far enough from the turn-off for the photometric parallax relation to be valid. The An08 fiducial sequence of M17 has to be taken with caution, because the zero points for the M17 photometry were very uncertain, and there was a strong contamination by background stars (An08). The uncertain fiducial sequence could account for the offsets. The cluster M5 is an example for the shift of the turn-off towards redder colors with increasing metallicity.

For the metal-rich open cluster NGC2420 (Figure 7.6) the absolute relative distance error stays below 5% for roughly half the main sequence ($g - i \approx 1.4$), but rises steeply to 25% at $g - i \approx 2.2$. For M67 we find an absolute relative distance error smaller than 15% along the main sequence from $g - i \approx 0.5$ to

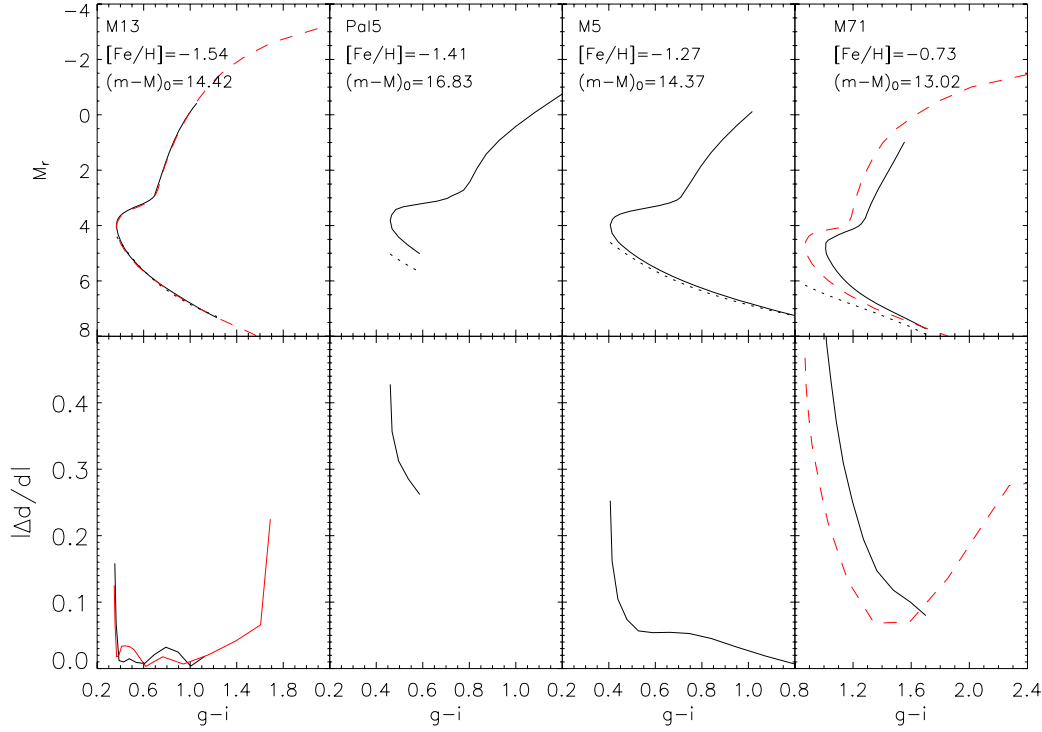


Figure 7.5: Same as Figure 7.3, but for the more metal-rich clusters M13, Pal5, M5 and M71. Note that the fiducial sequence from An08 for M71 can't be trusted because of a wrong photometric zero point and contamination by background stars.

$g - i \approx 2.4$. Finally, NGC6791 is fitted well to within a distance error smaller than 20% for the color range $1.1 < g - i < 2.0$.

To derive an estimate of the systematic distance error of the photometric parallax relation, we average over the differences between the distance that is predicted by the relation, d_{phot} , and the distance given by the distance modulus of each cluster, d_{cluster} , using $\Delta d/d$ instead of $|\Delta d|/d$ here. To this end, we concentrate on the color range $(g - i)_{\text{TO}} + 0.05 < g - i < 1.6$, where $(g - i)_{\text{TO}}$ denotes the turn-off color, that is, the color at which a cluster's main sequence runs vertically.² $g - i = 1.6$ corresponds approximately to the reddest color in our sample (see Figure 7.8 below). If available, we prefer the cluster sequences of Clem et al. (2008) for calculating $\Delta d/d$. Eliminating two outliers (M15 and Pal5), we find across $-2.0 < [\text{Fe}/\text{H}] < -0.3$ relative distance errors $\Delta d/d = (d_{\text{phot}} - d_{\text{cluster}})/d_{\text{cluster}}$ that are displayed in Figure 7.7. Nine of the eleven considered cluster sequences suggest very small systematic errors, while the distances to NGC5466 and M71 get under-estimated by 9.61% and 17.44%, respectively. Averaging over all considered clusters, the systematic distance error comes out as

$$\left\langle \frac{\Delta d}{d} \right\rangle = \begin{cases} -3.28\% \pm 1.78\% & \text{including M71,} \\ -1.86\% \pm 1.19\% & \text{excluding M71.} \end{cases} \quad (7.4)$$

²This is the bluest color for which a value of the fiducial sequence exists.

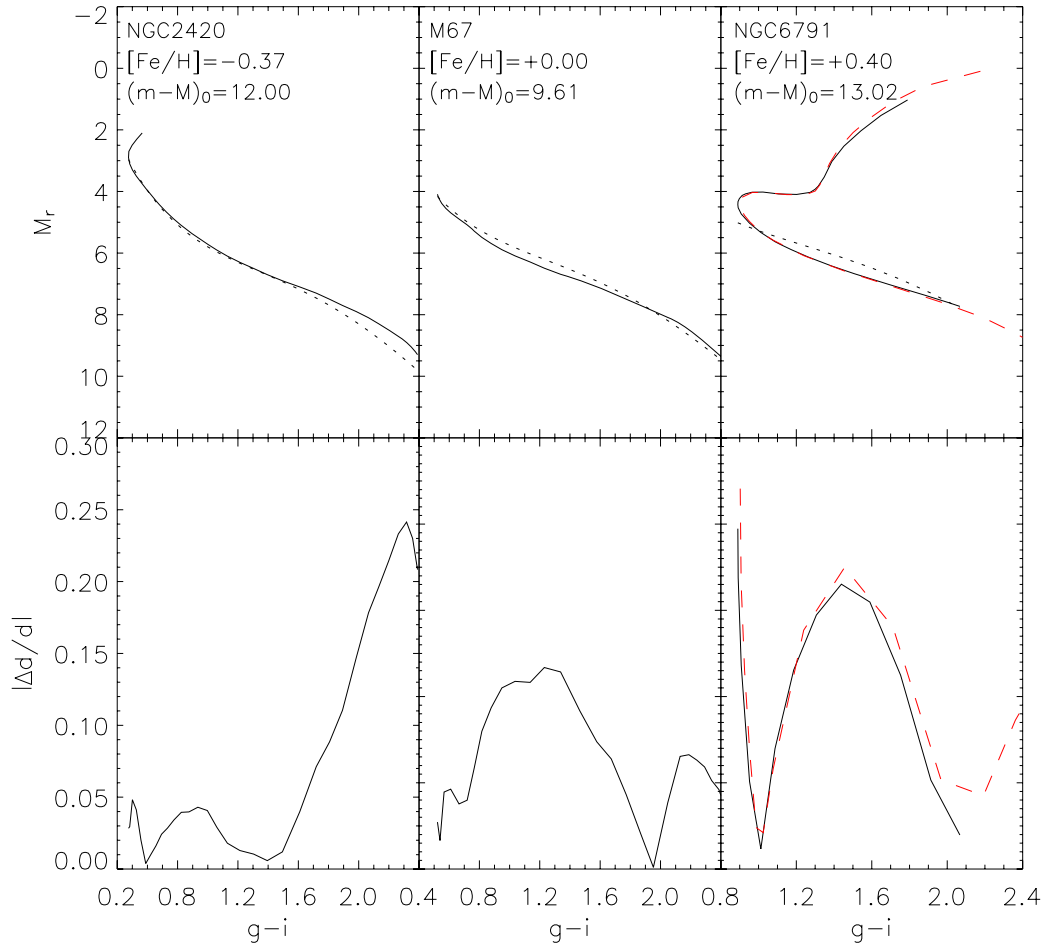


Figure 7.6: Same as Figure 7.3, but for the metal-rich clusters NGC2420, M67 and NGC6791. Note the different color ranges between the cluster sequences.

Because we have found no annotation in Clem et al. (2008) that their sequence for M71 might be unreliable, we will use the more stringent value of -3.28% when we deal with the effects of velocity errors on our results.

The photometric parallax relation of Ivezić et al. (2008) is constructed from redder than turn-off stars. Although the authors included an correction for age effects and give a validity of their formula over the color range $0.2 < g - i < 4.0$, we see from Figures 7.3-7.6 that the application of the formula breaks down near the turn-off, the color of which depends on metallicity and cluster age. Metal-poor F stars in the disk, for example, have a lifetime considerably shorter than the age of the stellar disk and are already in the turn-off phase. Having turn-off stars in our sample can result in additional systematic distance and hence velocity errors, which could lead to false stream detections. Theoretical isochrones could be used to determine the color at which stars of a given metallicity and age are in the turn-off phase. For example, the Girardi et al. (2004) *ugriz* isochrones would predict a turn-off color of $g - i \approx 0.36$ (0.22) for a 13.5 Gyr old stellar population with $[\text{Fe}/\text{H}] = -1.0$ (-2.0). However, An08 have shown that the theoretical isochrones

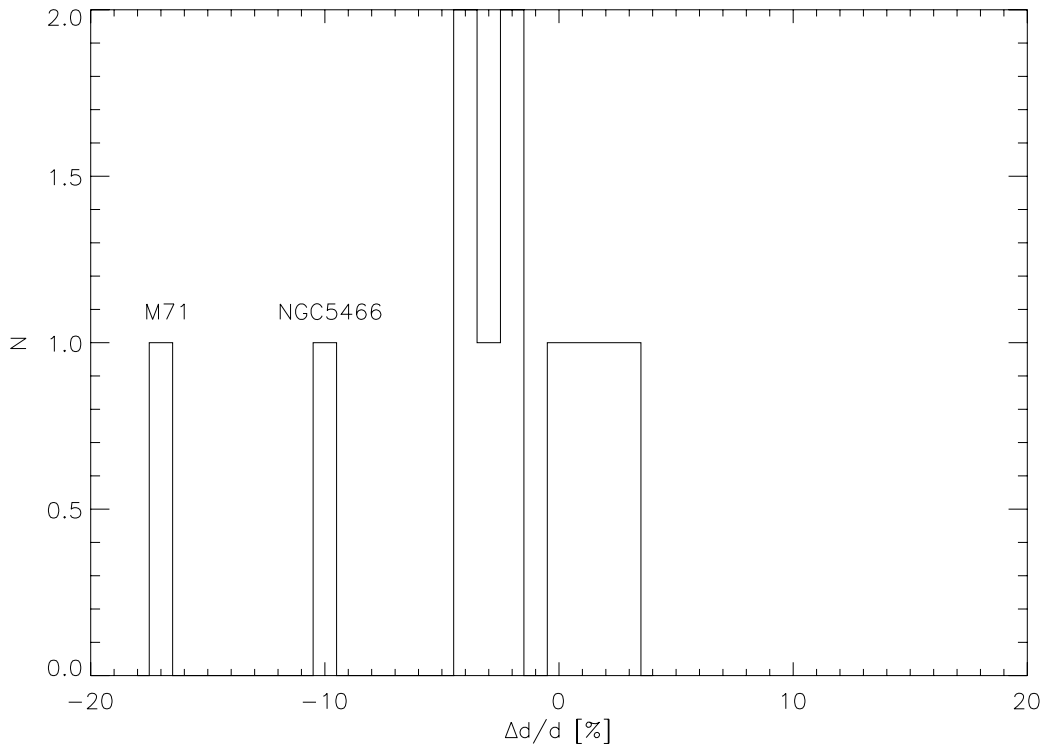


Figure 7.7: Distribution of relative distance errors $\Delta d/d = (d_{\text{phot}} - d_{\text{cluster}})/d_{\text{cluster}}$ derived from eleven of the 13 clusters that lie in the metallicity range $-2.0 < [\text{Fe}/\text{H}] < -0.3$. The errors of each cluster have been averaged over the color range $(g - i)_{\text{TO}} + 0.05 < g - i < 1.5$. The two clusters M15 and Pal5 have not been considered, while M71 has been kept, because it has a sequence measured by Clem et al. (2008) with deep photometry.

of Girardi et al. (2000) are not consistent with their fiducial sequences; the model colors for the main sequence are 2-5% too blue. Therefore we apply to our sample a color cut that is based on the location of the turn-off and the behaviour of the distance errors in Figures 7.3-7.5 rather than on theoretical models.

We show in Figure 7.8 the $g - i$ -distribution of all stars with $\log g > 3.5$, $\text{flag} = \text{'nnnn'}$ (indicating normal spectra), $d \leq 2.0$ kpc, $\sigma_d/d \leq 0.15$ and $[\text{Fe}/\text{H}] \leq -0.5$. This is basically our final sample before applying a color cut. The distribution of the most metal-poor stars peaks at $g - i = 0.4$, at the approximate position of the turn-off for thick-disk stars. Excluding all these stars from our sample would yield more accurate distances, but decrease our sample by some thousands of stars. One has to balance the more robust statistics of a larger sample size against the more reliable velocities and avoidance of "fake" stellar stream detections. We decide in favour of the latter and apply a stringent color cut in order to remove turn-off stars. We will, however, later investigate if we obtain the same results using a larger sample, where we only require $g - i > 0.2$ in order to stay in the valid range of the photometric parallax relation given by Ivezić et al. (2008). We choose the color cuts depending on the metallicity of the stars as

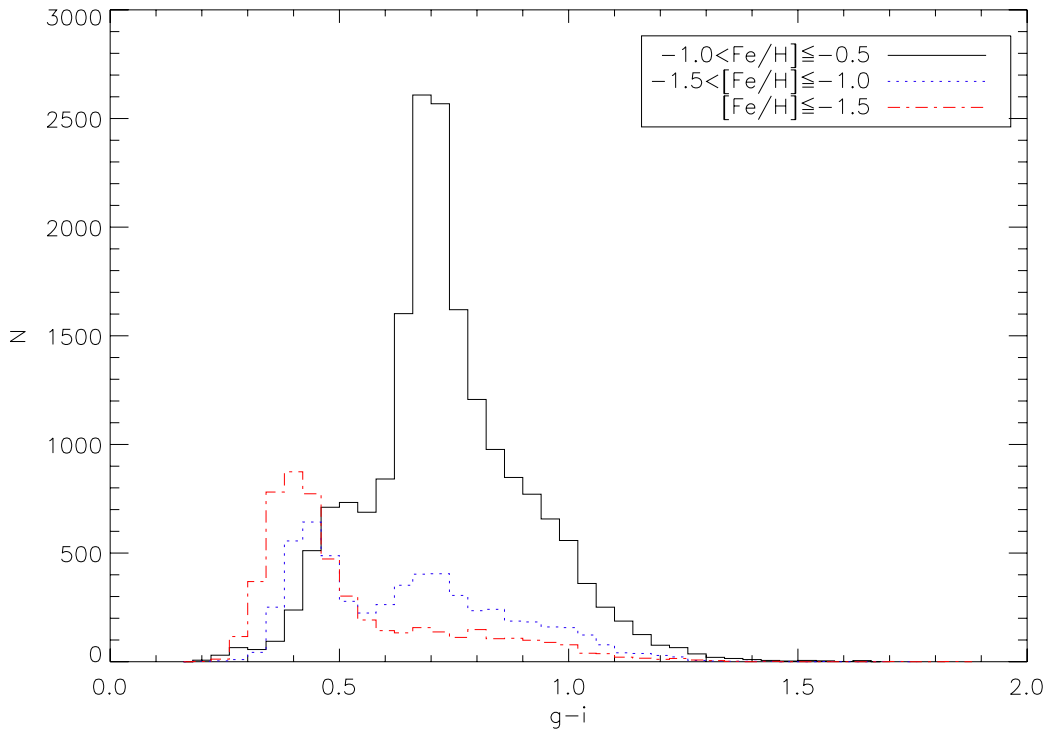


Figure 7.8: Distribution of the $g - i$ color for all stars with flag='nnnn', $\log g \geq 3.5$, $d \leq 2$ kpc, $\sigma_d/d \leq 15\%$, and $[\text{Fe}/\text{H}] \leq -0.5$. The peak at $g - i = 0.4$ approximately corresponds to the location of the turn-off for clusters with thick-disk-like metallicities (Figure 7.5). In good part, these histograms reflect the (complex) SDSS/SEGUE spectroscopic target selection.

follows:

$$g - i \geq \begin{cases} 0.55 & \text{if } [\text{Fe}/\text{H}] > -1.0 \\ 0.50 & \text{if } -1.5 < [\text{Fe}/\text{H}] \leq -1.0 \\ 0.45 & \text{if } -2.0 < [\text{Fe}/\text{H}] \leq -1.5 \\ 0.40 & \text{if } [\text{Fe}/\text{H}] \leq -2.0 \end{cases} \quad (7.5)$$

These color cuts ensure that we select stars that are at least 0.05 mag redwards of the cluster turn-offs in the corresponding metallicity bins. We will not use stars from the most metal-rich bin for our stream search, so we do not divide this bin further. The color cut, however, should be valid for stars up to Solar metallicity. For reference, the Sun (a G2 star) has a $g - i$ color of 0.546 - 0.595, depending on the color transformations used (Andreas Just 2008, priv. comm.).

To summarize our results, the photometric parallax relation from Ivezić et al. (2008) performs very well in fitting the main sequences for clusters with metallicities of $[\text{Fe}/\text{H}] \lesssim -0.3$. On average, it predicts distances that are wrong by $-3.28\% \pm 1.78\%$. For this reason we adopt it to determine distances to all the dwarfs and sub-dwarfs ($\log g > 3.5$) in our sample. For more metal-rich clusters ($[\text{Fe}/\text{H}] \gtrsim -0.3$) the uncertainties are generally higher, although they can vary a lot along the main sequence. Further investigations with a larger number of clusters will be needed in order to clearly determine the accuracy of the relation for

metal-rich stars. The location of the turn-off in the cluster sequences allows us to apply a color cut to get rid of turn-off stars without relying on theoretical models.

3D Velocities, from v_{rad} , d_{phot} and $\vec{\mu}$

From the photometric parallax relation, Equation (7.1)-(7.3), and the dereddened r -band magnitudes we calculate the distance to each star via

$$d[\text{kpc}] = \frac{1}{100} \times 10^{0.2(r-M_r)}. \quad (7.6)$$

We calculate the statistical distance error from the Gaussian error propagation:

$$\sigma_d = \frac{1}{5} d \ln 10 \sqrt{(\sigma_r)^2 + (\sigma_{M_r})^2}, \quad (7.7)$$

σ_r is given for each star in our sample. σ_{M_r} follows from Equations (7.1)-(7.3) and the given errors for $[\text{Fe}/\text{H}]$ and $g - i$. The mean statistical relative distance error of our sample account for $7.58\% \pm 0.01\%$. The intrinsic (systematic) scatter of 3.28% (equation 7.4) is less than half of this value, and can be neglected against the statistical errors (see Section 7.4 below). Later, we restrict our selection to stars with statistical distance errors $\frac{\sigma_d}{d} \leq 15\%$ and distances $d \leq 2\text{kpc}$, so in the worst case when we add statistical and systematic errors the actual distance could be 2.37 kpc instead of 2 kpc (with a total distance error of 28.28%).

Typical proper motion errors are 3.5 mas yr^{-1} (Munn et al., 2004), so a typical proper motion of 10 mas yr^{-1} together with 15% (25%) distance error leads to an error of the transverse velocity of a star of $18 \cdot d [\text{kpc}]$ ($20 \cdot d [\text{kpc}]$) km s^{-1} . We show in Figure 7.9 the statistical velocity error distribution of 37,136 stars satisfying $\text{flag}='nnnn'$, $\log g \geq 3.5$, $d \leq 2 \text{ kpc}$, $\sigma_d/d \leq 15\%$, and our color cuts, equation (7.5). Additionally, we show in the small window all 23,512 stars that also fulfill $[\text{Fe}/\text{H}] \leq -0.5$, because we cut at this metallicity for our final sample of metal-poor stars. The velocities and their errors have been calculated using equations (4.30) and (4.32) in Section 4.2.2 and equation (6.8) in Section 6.1.2. The velocity error distribution rises to its peak around 10 km s^{-1} for W and around $12\text{--}15 \text{ km s}^{-1}$ for U and V and then falls off quickly. If we only select metal-poor stars from the above sample, the error distribution for U and V shifts to a peak around $13\text{--}15 \text{ km s}^{-1}$. For W the errors increase only slightly. The reason is that the more metal-poor stars are on average σ farther away. We choose to accept errors up to 35 km s^{-1} for all three velocity components.

We look at the metallicity-velocity-distribution for all stars that have $\text{flag}='nnnn'$, $\log g \geq 3.5$, $d \leq 2 \text{ kpc}$, $\sigma_d/d \leq 15\%$ and satisfy the color cuts, equation (7.5), to get further support for the correctness of our adopted distances. In Figure 7.10 we have plotted $[\text{Fe}/\text{H}]$ versus the radial, rotational and vertical velocity components, respectively³.

³ v_ϕ and v_R are the azimuthal and radial velocity components in cylindrical coordinates and equal to Θ or Π , respectively, which have been introduced in Equation (4.23), Section 4.2.1.

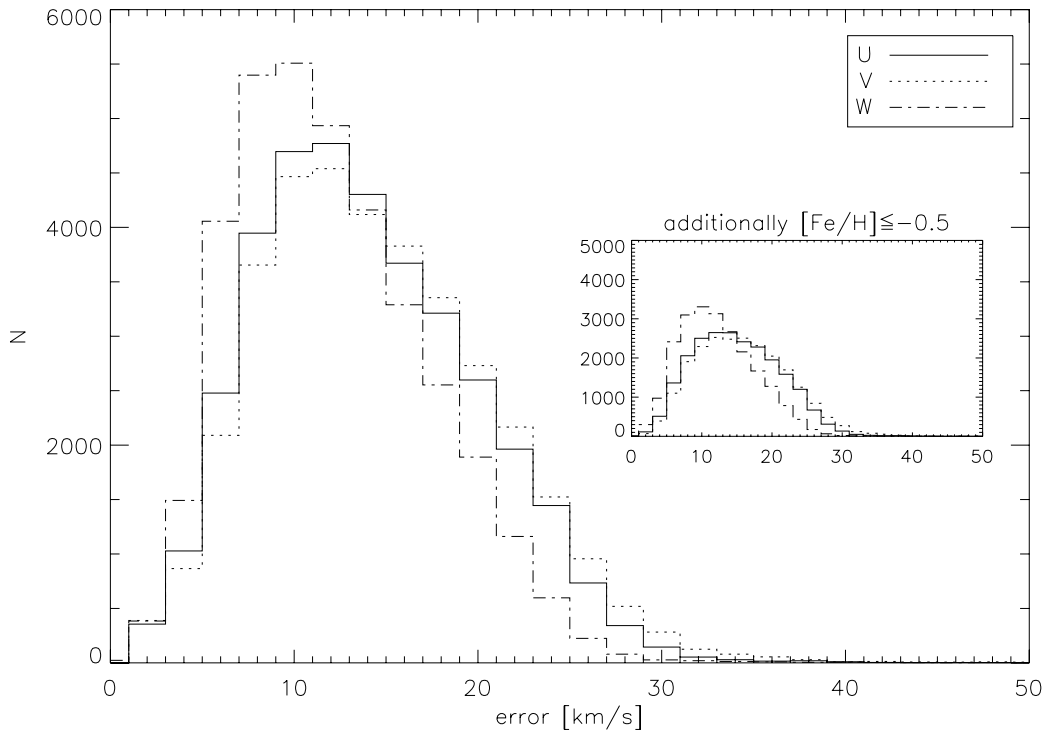


Figure 7.9: Distribution of errors for the velocity components U (solid), V (dotted) and W (dash-dotted) for all stars with flag='nnnn', $\log g \geq 3.5$, $d \leq 2$ kpc and $\frac{\sigma_d}{d} \leq 15\%$. The small window shows the same distribution, but now for stars with the additional restriction $[\text{Fe}/\text{H}] \leq -0.5$.

Figure 7.10 not only shows the trend of decreasing rotational velocity with decreasing metallicity, but also exhibits the stellar components of the Milky Way near the Sun. The thin disk is visible as a horizontal balk of metal-rich stars ($[\text{Fe}/\text{H}] \gtrsim -0.3$) on nearly circular orbits, lagging the LSR with about 20 km s^{-1} on average. At $[\text{Fe}/\text{H}] \approx -0.5$ there is a smooth transition to a balk of stars that is tilted towards lower v_ϕ values and has increasing velocity dispersions. This is the thick disk which is usually considered to be dominated by stars within $-1 < \text{Fe}/\text{H} < -0.5$ (Freeman, 1987; Carney et al., 1989). We confirm the findings of e.g. Chiba and Beers (2000) and Arifyanto et al. (2005) of a large number of stars with disk-like kinematics at intermediate metallicities in the range $-1.7 \lesssim \text{Fe}/\text{H} \lesssim -1$. Some authors found this metal-weak tail of the thick disk even reaching beyond $[\text{Fe}/\text{H}] \approx -2$ (e.g. Beers and Sommer-Larsen, 1995). For even lower metallicities the stars "purely" belong to the halo component, which is clearly visible as the spheroidal distribution centered at $[\text{Fe}/\text{H}] \approx -1.7$ at slightly prograde rotation. The stars with $[\text{Fe}/\text{H}] < -2.0$ move on average with velocities $(v_R, v_\phi, W) = (-2 \pm 4, 37 \pm 4, 0 \pm 3) \text{ km s}^{-1}$ with velocity dispersions of $(\sigma_R, \sigma_\phi, \sigma_W) = (121 \pm 3, 106 \pm 3, 100 \pm 2)$, in good agreement with the results obtained by Chiba and Beers (2000). This gives us further reason to believe that our adopted distances are correct.

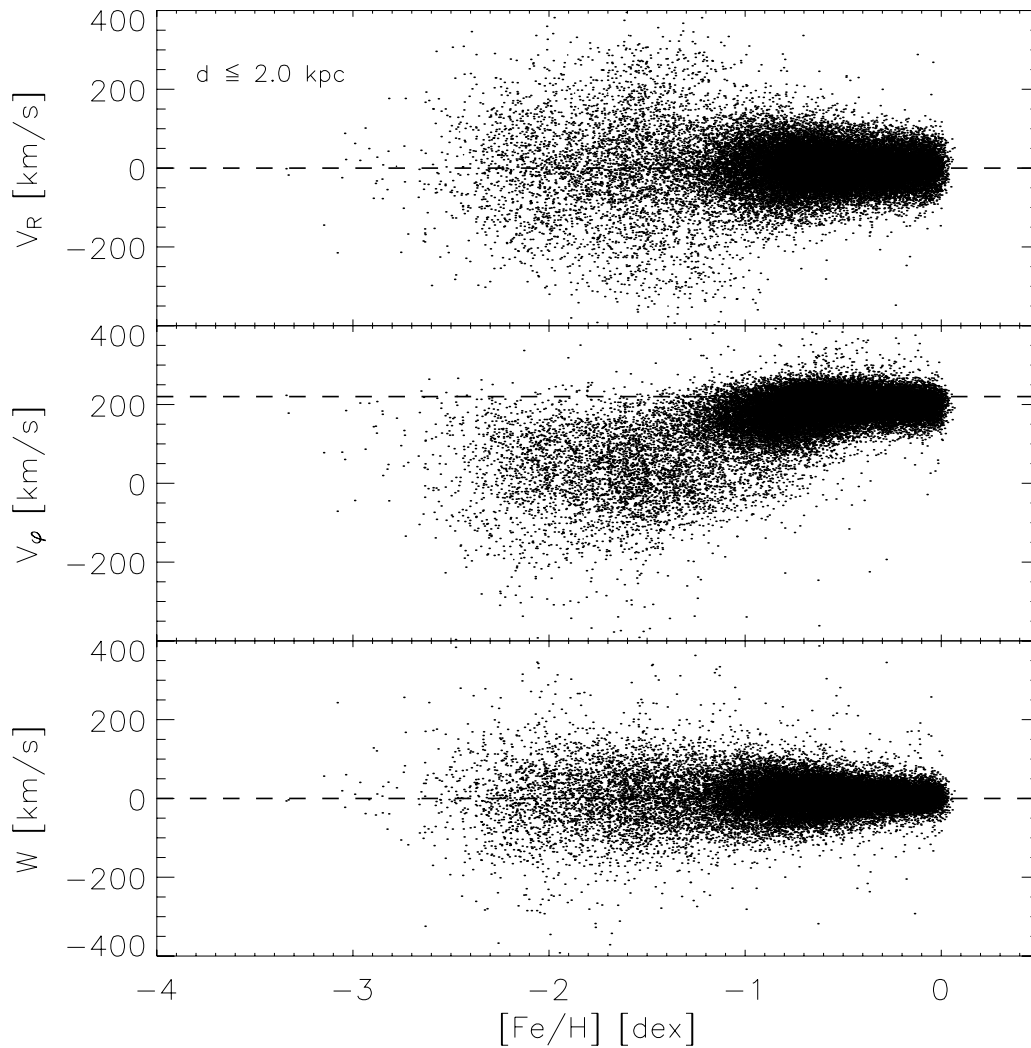


Figure 7.10: Distribution of stars that have flag='nnnn', $\log g \geq 3.5$, $d \leq 2$ kpc and $\frac{\sigma_d}{d} \leq 15\%$, and satisfy the color cuts, equation (7.5), in $[\text{Fe}/\text{H}]$ versus v_φ , v_R and W . The components of the Milky Way near the Sun are clearly visible from the middle panel: the thin disk ($[\text{Fe}/\text{H}] \gtrsim -0.3$), thick disk (the tilted thick bulk dropping towards lower v_φ from $[\text{Fe}/\text{H}] \approx -0.3$) and the stellar halo (the spheroidal distribution centered at $[\text{Fe}/\text{H}] \approx -1.6$, v_φ slightly above 0). The dotted lines are for reference and mark the velocity of the LSR ($v_\varphi = 220 \text{ km s}^{-1}$).

7.1.2 A Sample of Metal-Poor Stars within 2 kpc with 6D Phase-Space Coordinates

In order to get the best available sample regarding accuracy of distances and suitability for our stellar stream search, we only keep stars satisfying the following criteria (the number in parentheses indicates the number of stars that are left after each step):

- $\log g \geq 3.5$ in order to only select (sub-)dwarfs to which we can apply the photometric parallax relation (141,286)
- flag='nnnn', indicating that there is no problem with the spectrum (118,584)

- distance $d \leq 2$ kpc, because our search strategy requires nearby stars; also, the proper motions are more accurate for nearby stars (44,484)
- relative distance errors $\sigma_d/d \leq 0.15$ (44,087)
- total space velocity $v_{total} < 600$ km s⁻¹ to exclude stars with apparently false proper motion measurements (44,034)
- velocity errors smaller than 35 km s⁻¹ for U , V and W (43,512)
- $g - i \geq (g - i)_{TO}$, where $(g - i)_{TO}$ depends on the metallicity of a star according to equation (7.5), to exclude turn-off stars (35,864)
- we restrict ourselves to $[Fe/H] \leq -0.5$, because we concentrate on thick-disk and halo substructure⁴(22,321)

The distance-cut of 2 kpc is necessary, because our search strategy for streams assumes a constant rotation curve and that we can approximate the radial and rotational velocities by U and V , respectively. In addition, we gain higher accuracy in the velocities, because the proper motions are more accurate for more nearby stars. The spatial distribution of our sample is shown in Figure 7.1 as the red dots. It is distributed over the same volume as the full DR7 sample.

Although our final sample is only 14% of the original 154,888 stars, we have a sample of nearby metal-poor stars of both unprecedented quantity and quality (compare to e.g. Helmi et al., 1999; Chiba and Beers, 2000; Arifyanto and Fuchs, 2006; Dettbarn et al., 2007). We show the color, distance and metallicity distribution of our final sample in Figure 7.11. The distribution peaks at $g - i = 0.7$ (the color of a G star) with a tail extending to $g - i \approx 1.3$ (K6-K7 stars). It is interesting that there remain some presumable turn-off stars in the $g - r$ -distribution at $g - r \approx 0.3$ for the most metal-rich bin ($-1.0 < [Fe/H] \leq -0.5$)⁵, although this is not the case in the $g - i$ -distribution. It is known that the $g - r$ color has worse signal-to-noise properties than the $g - i$ color (Ivezic et al., 2008), which could cause some larger scatter in the $g - r$ -distribution. Also, the fraction of presumable turn-off stars is so small that the influence of their systematically wrong distances on our analysis can be neglected.

7.2 Search Strategy for Streams

To search for stellar halo streams in our sample we adopt the method outlined by Dettbarn et al. (2007) and described more detailed in Section 5.3.2. This method is a generalization of the formalism outlined in Section 4.4.3 and used in Chapter 6 to identify stellar streams in RAVE data. For the RAVE stars, which are dominated by stars with disk-like kinematics, we assumed that their azimuthal velocity could

⁴Also, higher metallicities are unreliable because of a calibration error that has only been fixed recently and is not yet corrected in the CAS (Timothy Beers 2008, private communication)

⁵For the more metal-poor bins the turn-off lies bluewards of $g - r = 0.3$.

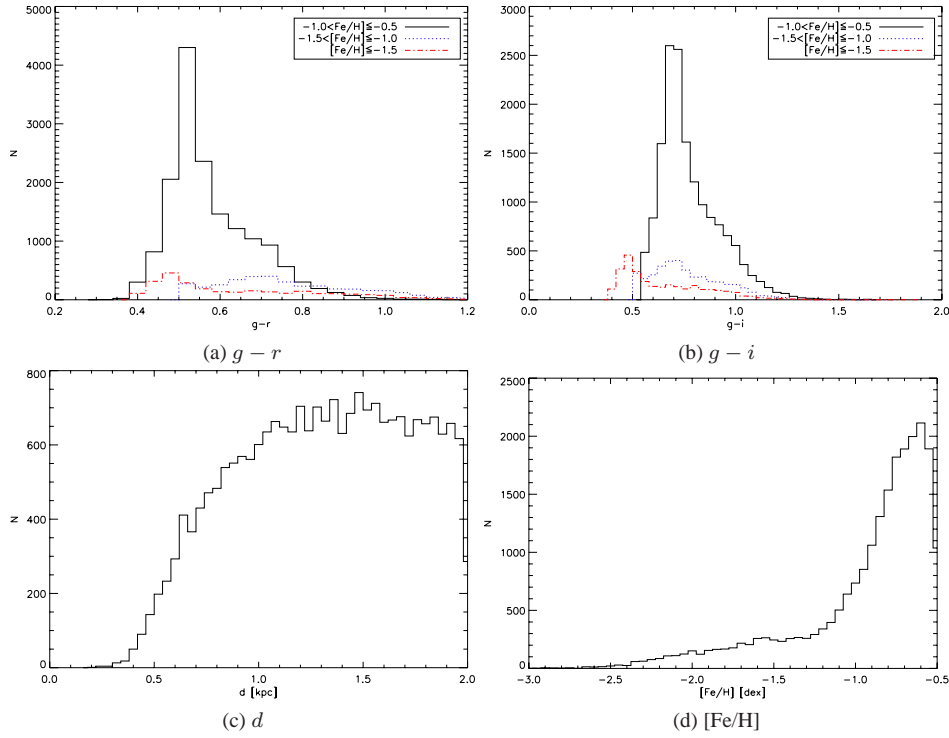


Figure 7.11: Distribution of stars from our final sample in colors $g - r$ (a), $g - i$ (b), distance d (c), and metallicity $[\text{Fe}/\text{H}]$ (d). Because of the applied color-cuts, the sample consists of G and K stars. In panels a and b we display the color distribution for three bins in $[\text{Fe}/\text{H}]$. The different panels show that our sample is dominated by stars of the thick disk.

be approximated by $V + V_{\text{LSR}}$, thereby projecting their orbits into the meridional plane. Halo stars move on random, more eccentric orbits, and we can apply the same formalism if we group them together according to the inclination of their orbital planes. According to our simulations in Section 5.3.2, stellar streams will then show up as overdensities in $(V_{\text{az}}, V_{\Delta\text{E}})$ -space, even for highly eccentric orbits.

We use metallicities $[\text{Fe}/\text{H}]$ to discriminate between stellar populations with different origins. We divide our sample into 4 sub-samples (hereafter s1,s2,s3,s4) with decreasing metallicity:

- s1: $-1.0 < [\text{Fe}/\text{H}] \leq -0.5$ (15856)
- s2: $-1.5 < [\text{Fe}/\text{H}] \leq -1.0$ (3676)
- s3: $-2.0 < [\text{Fe}/\text{H}] \leq -1.5$ (1931)
- s4: $[\text{Fe}/\text{H}] \leq -2.0$ (858)

The number in parenthesis is the number of stars in the corresponding sub-sample. For each sub-sample, we collect the stars with similar orbital inclinations in small ν -slices. We bin the inclination angles into 30° wide bins that overlap by 15° . Thereby we make sure to reduce bin boundary effects on the results. In each ν -slice we conduct the search for stellar streams in the space spanned by angular momentum and eccentricity, or $(V_{\text{az}}, V_{\Delta\text{E}})$. To amplify the overdensities we

use the wavelet transform technique with a skewed Mexican-hat-shaped analyzing wavelet (see Section 6.4 for more details). We set the scale parameter to $a = 12 \text{ km s}^{-1}$, comparable to the velocity errors, and the elongation parameter to $q = \sqrt{3}$. We use cells in $(V_{\text{az}}, V_{\Delta\text{E}})$ -space of 3 km s^{-1} width on each side. The resulting contours of the wavelet transform are shown in Figures 7.12-fig:w1-s4.

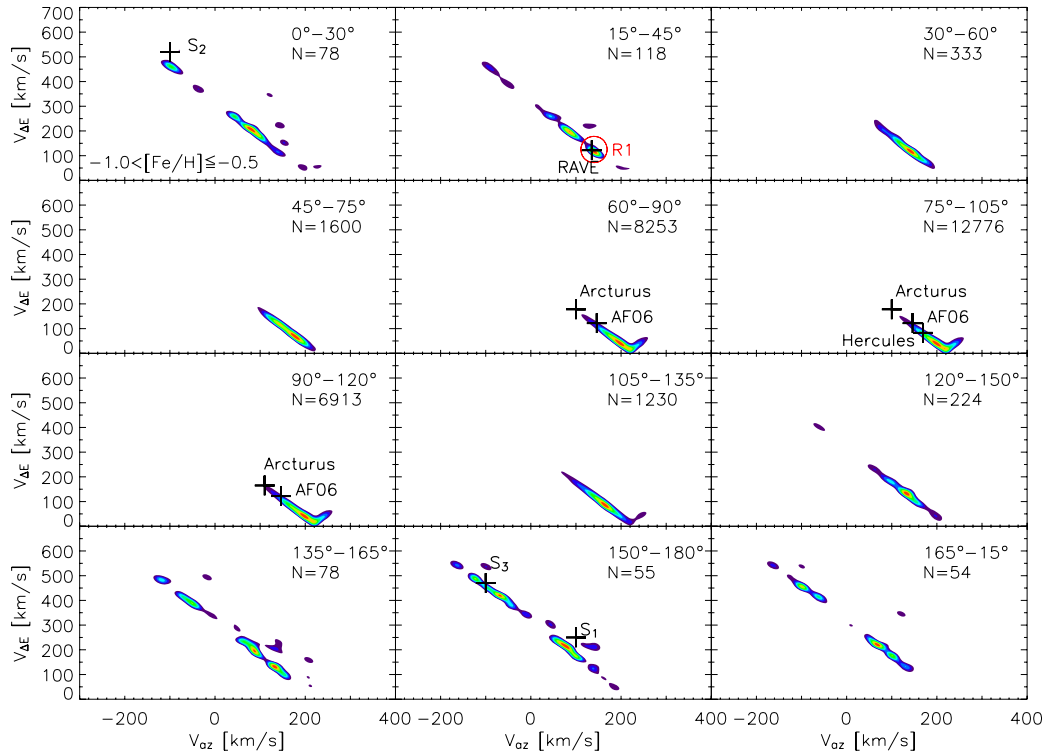


Figure 7.12: Wavelet transform of the distribution of stars from the metallicity sub-sample s1 (defined on page 111) in $(V_{\text{az}}, V_{\Delta\text{E}})$ -space, shown in bins of different orbital inclination. The contours in each ν -bin range from 10% to 100% of the maximum value of the wavelet transform and are color coded accordingly from purple to red. We have marked the positions of all already known stellar streams given in Table 7.3 with thick crosses and circled in red overdensities that we discuss in Section 7.6.

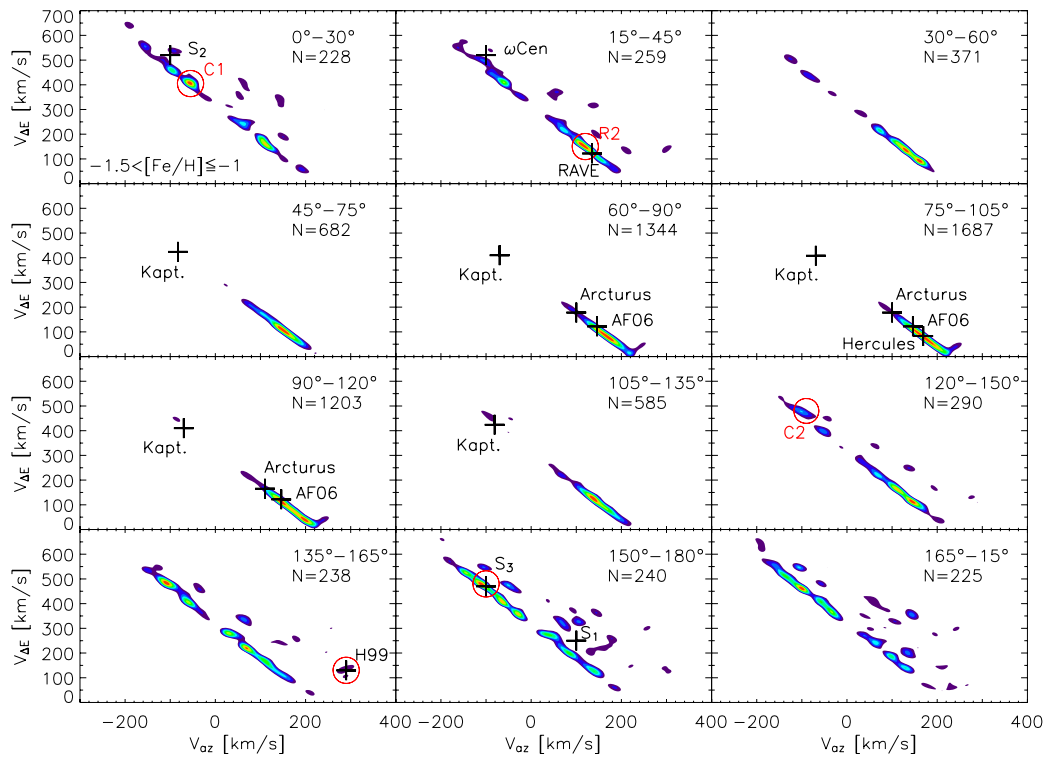


Figure 7.13: Same as Figure 7.12, but now for stars in the metallicity sub-sample s2.

7.3 Placing Solar Neighborhood Streams in the $(V_{\text{az}}, V_{\Delta\text{E}})$ -Plane

An important difference between tidal streams in the halo and dynamical streams in the disk is the expected shape of the velocity distribution function $f(U, V, W)$. Dynamical streams, that is, stars trapped around resonant circular orbits, perform small radial oscillations around their closed parent orbit; the vertical motion, however, is unaffected by the resonance and can be treated as independent from the planar motion. In the flattened disk potential phase-mixing is most efficient in the vertical direction, hence increasing the W -velocity dispersion of the stars faster than in the other two directions. These streams can be identified by their distinct location in (U, V) -space, but not in W . Therefore, their inclination angles ν , which depend on W , can not be clearly assigned. However, the W -velocities usually are so small that they can be neglected, and the stars are concentrated around $\nu = 90^\circ$ in both ν -directions. For tidal streams that generally are expected to reach higher distances above and below the plane, the vertical and planar motions are not independent, but express the tidal origin of the stream. The stars show a characteristic shape of $f(U, V, W)$ and move on orbits with both similar eccentricities and inclinations (see Sections 5.2.1 and 5.3.2).

As a first step in the analysis of the SDSS data, we explore whether we see evidence in these data for the already known streams. We have taken the velocities

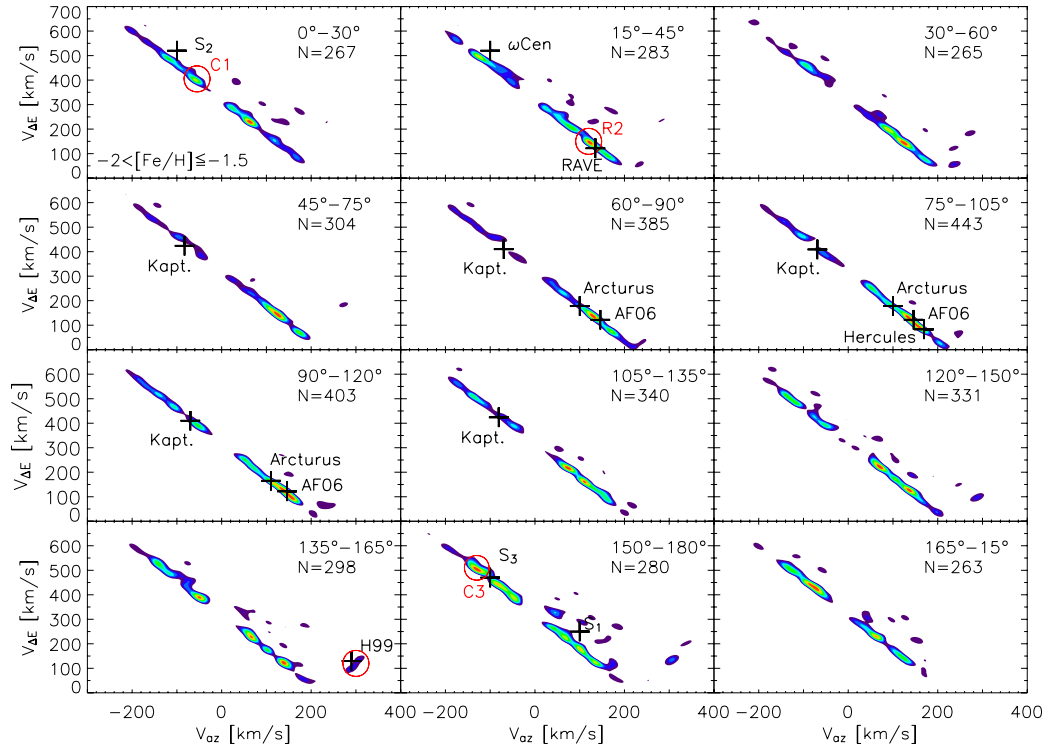


Figure 7.14: Same as Figure 7.12, but now for stars in the metallicity sub-sample s_3 .

of already known stellar streams from the literature and evaluated their velocities V_{az} , $V_{\Delta E}$, and orbital inclinations ν . The results are given in Table 7.3 and marked with thick crosses in Figures 7.12- 7.15. For the streams AF06, Arcturus and Kapteyn's stream we give mean values of their W -velocities for both the stars moving upwards and downwards. This locates these streams in a broad band of ν -angles around $\nu = 90^\circ$ (the plane), which we delimit by marking the stream location over multiple panels in Figures 7.12-7.15.

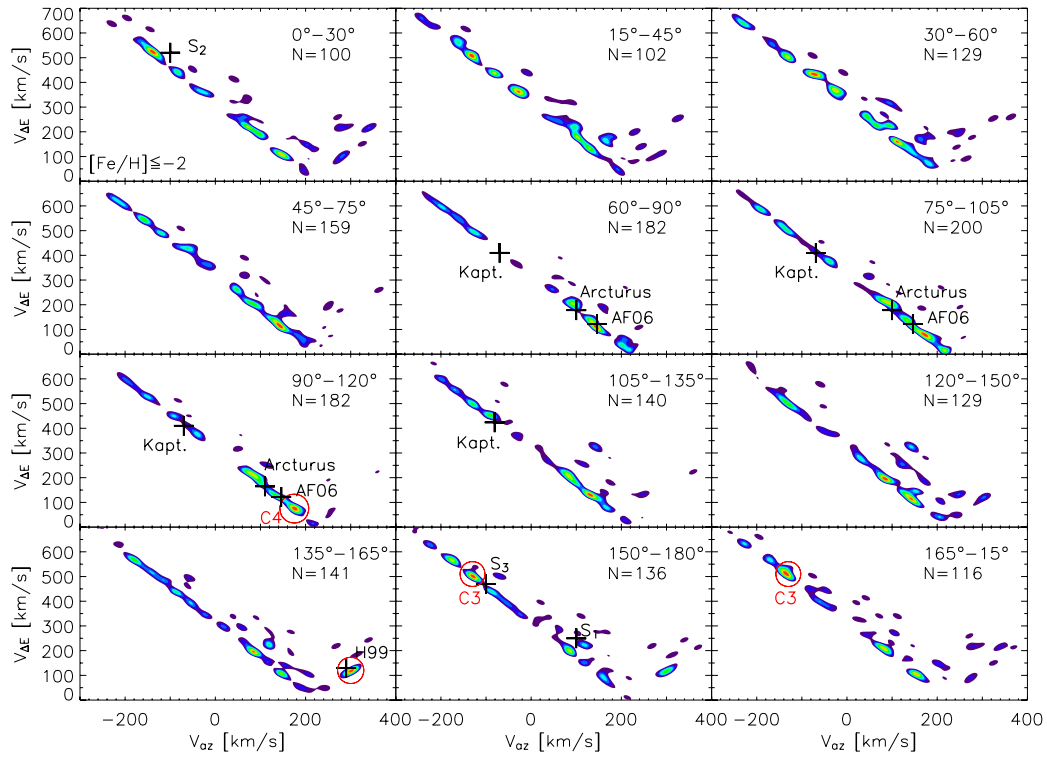


Figure 7.15: Same as Figure 7.12, but now for stars in the metallicity sub-sample s_4 .

stream	$\langle U \rangle$	$\sigma_{ U }$	$\langle V \rangle$	σ_V	$\langle W \rangle$	σ_W	$\langle V_{az} \rangle$	$\langle V_{\Delta E} \rangle$	$\langle \nu \rangle$	expected in sub-sample
Hercules ^a	42	28	169	9	-8	17	52	240	81	s1,s2,s3
AF06 ^b	64		140		-46 41	27 30	147 146	121 121	108 74	all
Arcturus ^b	55		95		-57 31	31 26	110 100	163 180	120 72	all
Kapteyn ^c	13	82	-69	6	-47 -43	42 38	-83 -81	425	56 122	s1,s2,s3
RAVE ^d	24	15	61	5	121	30	135	122	27	un-known
H99 ^e	80		150		-250		290	130	150	s2,s3,s4
S ₁ ^f							100	250	165	un-known
S ₂ ^f							-100	520	6	un-known
S ₃ ^f							-100	470	170	un-known
ω Cen ^g							\sim -100	\sim 520	\sim 25	s2,s3

^a Famaey et al. (2005)

^b Arifyanto and Fuchs (2006)

^c Eggen (1996)

^d Section 6.6

^e Helmi et al. (1999)

^f Dettbarn et al. (2007)

^g Dinescu (2002); Brook et al. (2004a)

Table 7.1: Velocities and derived effective integrals of motion for already known solar neighborhood streams.

7.4 The Effects of Systematic Distance Errors

To test the effects of possible systematic errors on our results, we have added the -3.28% systematic distance error that we found through comparison of the photometric parallax relation to cluster fiducial sequences in Section 7.1.1 to each star and then re-calculated their velocities and the wavelet transform for a subset of stars. As an example we show in Figure 7.16 contours of the wavelet transform of the distribution of stars from sub-sample s4 in the ν -slice 150° - 180° without (a) and with additional distance errors (b). The effect of additional errors is to slightly change the shape and relative "height" of some features, but the location of the overdensities does not change much. Therefore our results should be robust against any systematic distance errors.

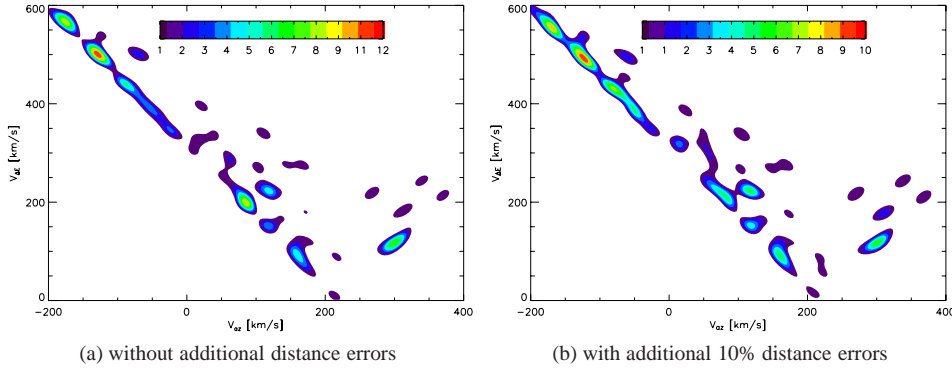


Figure 7.16: Contours of the wavelet transform of the distribution of stars from sub-sample s4 that lie in the ν -range 150° - 180° (a). Panel (b) is the same distribution, but after adding a systematic distance error of -3.28% to the data. Note that the overdensities slightly change shape and relative "height", but keep their position.

7.5 Estimating the Significance of Overdensities

It is clear that overdensities in $(V_{az}, V_{\Delta E})$ can and will emerge through Poisson noise, especially in regions that are sparsely sampled by the data. As described in Section 6.5, we can address this problem by performing Monte Carlo simulations with stars randomly drawn from a smooth distribution. From these we can build the residuals of the wavelet transforms of each individual simulation against the mean value of all wavelet transforms, which represents a smooth distribution. For each cell in $(V_{az}, V_{\Delta E})$ we can calculate the variance and use it to obtain a significance map of the overdensities (more details are given in Section 6.5).

For the smooth halo and thick disk components, we adopt the results of Chiba and Beers (2000), who characterize the halo through a mean rotational velocity at $\langle \Theta \rangle \approx 30 \text{ km s}^{-1}$ with a radially elongated velocity ellipsoid $(\sigma_U, \sigma_V, \sigma_W) = (141 \pm 11, 106 \pm 9, 94 \pm 8) \text{ km s}^{-1}$. We further use $\langle \Theta \rangle = 190 \text{ km s}^{-1}$ and $(\sigma_U, \sigma_V, \sigma_W) = (46 \pm 4, 50 \pm 4, 35 \pm 3)$ for the thick disk and adopt their estimated fraction of thick disk stars in our sub-sample s0 as 80%, in s1 as 30% and in s2

as 10%. We are aware that the azimuthal drift for the thick disk stars is at the lower end of values given in the literature; for example, Soubiran et al. (2003) find $\langle\Theta\rangle = 159 \pm 5 \text{ km s}^{-1}$ from spectroscopic and kinematical analysis of nearly 400, mostly clump giant stars. However, their sample was limited to stars with abundances $[\text{Fe}/\text{H}] > -0.65$ and distances $d \lesssim 800 \text{ pc}$, so the Chiba and Beers (2000) data more closely resemble our own data.

To each velocity drawn from the smooth kinematic models with Gaussian velocity ellipsoids we assigned as an additional velocity error the mean velocity error of our data, that is, $(\langle\Delta U\rangle, \langle\Delta V\rangle, \langle\Delta W\rangle) = (14.9, 15.7, 12.2) \text{ km s}^{-1}$. For each metallicity sub-sample we built 30 Monte Carlo realizations with (by construction) smooth velocity distributions, consisting of the same number of stars as the sub-sample. The Monte Carlo samples were then analyzed in the same way as the real data, that is, through collecting the stars in different ν -bins and performing the wavelet analyses in these bins. Because the number of stars in each ν -bin is small, we expect a considerable amount of shot-noise. Also, because the velocity dispersions are very large, small deviations from our choice of the velocity ellipsoid would probably result in large changes of the significances. We therefore treat the significances not as the definitive proof that an overdensity is real, but more as an additional support. The significance maps for sub-samples s1-s4 are shown in Figures 7.17 - 7.20, where we have only displayed areas with $\sigma \geq 2$. Apparently the Monte Carlo samples predict to few stars on disk-like orbits, especially for the metallicity sub-samples s1 and s2.

7.6 The Results: Stellar Halo Streams

Here we explore the best "slicing" in orbit parameter and metallicity space by using $(V_{\text{az}}, V_{\Delta\text{E}}, \nu, [\text{Fe}/\text{H}])$. Metallicity is an additional constraint to distinguish tidal and dynamical streams, or different streams that occupy the same region in $(V_{\text{az}}, V_{\Delta\text{E}}, \nu)$ -space. Tidal debris still carries the chemical information of its progenitor, while dynamical streams are composed of stars that lack a common origin. We will start our discussion with a short investigation of substructure in the thick disk, but then concentrate on presumable halo stars on non-disk-like orbits.

7.6.1 Substructure in the Thick Disk

We will discuss the phase-space distribution of the stars starting with the highest metallicity bin s1 (Figure 7.17). Stars in this metallicity range between $[\text{Fe}/\text{H}] = -0.5$ and -1.0 should be dominated by members of the thick disk; this is clearly discernible as the smooth distribution of stars with inclination angles around 90° that rotate with $\langle V_{\text{az}} \rangle \approx 200 \text{ km s}^{-1}$ around the Galactic center. A hint of the Hercules stream is present, marked by a cross symbol. The streams Hercules, AF06 and Arcturus are thought to be different resonances with the bar of the Milky Way and as such to affect also thick-disk stars.

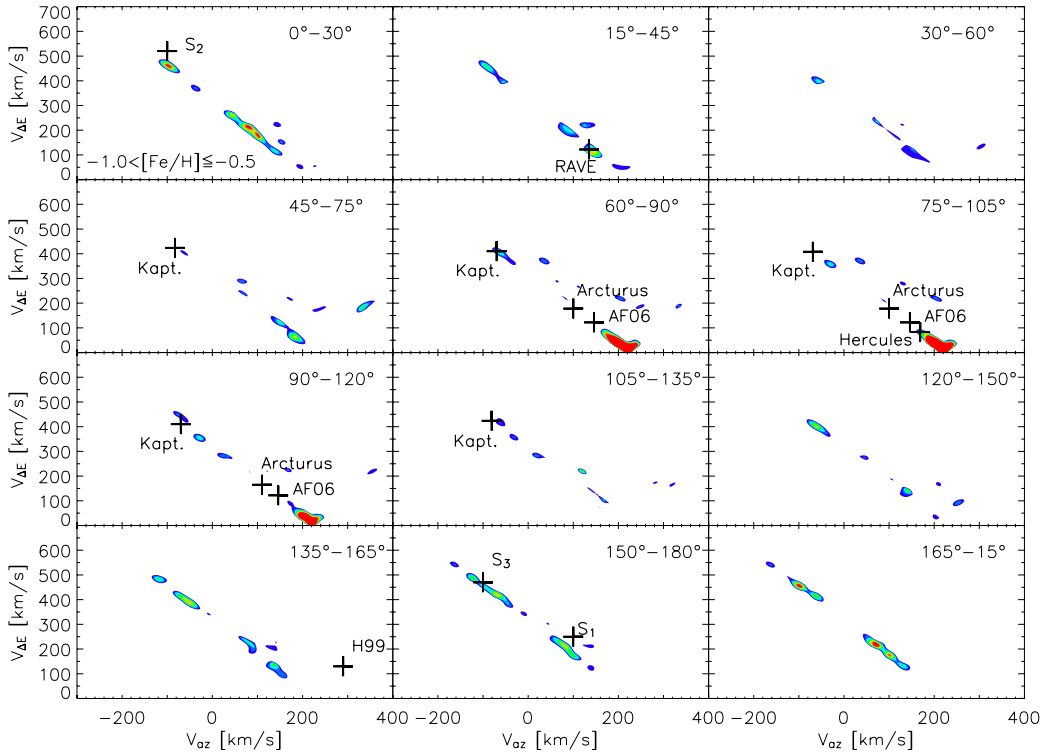


Figure 7.17: Significance map of the overdensities from Figure 7.12. Only areas with a $\sigma \geq 2$ are shown. The contours range from 2 (blue) to 10 (red). Note the abundance of stars on disk-like orbits. The crosses mark the expected position of already known stellar streams. Some appear more than once, because the streams associated with them are well-defined in (U, V) , but not W , so they span a broader range of orbital inclinations (because $\nu = \arctan \frac{V}{W}$).

For higher inclined orbits the distribution of stars peaks at lower azimuthal velocities (see also Figure 7.12), indicating that the fraction of halo stars increases. In addition, at angles of $|\nu - 90^\circ| \gtrsim 45^\circ$ overdensities of stars on retrograde orbits start to show up. There is no more smooth stellar component on such orbits. At such orbital inclinations, a few stars are enough to create an artificially high signal, because the variances of the residuals between the single Monte Carlo realizations and their smooth superposition are nominally very small. Therefore we question such overdensities in s1 to be real, unless they also show up in other metallicity sub-samples.

The amount of substructure increases for the sub-sample s2, which consists of stars in the range $-1.5 < [\text{Fe}/\text{H}] \leq -1.0$ (Figure 7.18). There is still a large amount of stars on disk-like orbits, with 46% of the stars having orbital inclinations between 75° and 105° . The mean rotational lag with respect to the LSR increases further. According to Chiba and Beers (2000), $\langle V \rangle$ decreases linearly with $[\text{Fe}/\text{H}]$ for $[\text{Fe}/\text{H}] \gtrsim -1.7$ and stays approximately constant below $[\text{Fe}/\text{H}] = -1.7$. It is hard to make out substructure among the stars on disk-like orbits, but we think we see a hint of the stream detected by Arifyanto and Fuchs (2006) and Helmi et al. (2006), labeled 'AF06'. Its stars have orbital inclinations ranging from slightly below to slightly above the Galactic plane, depending on whether

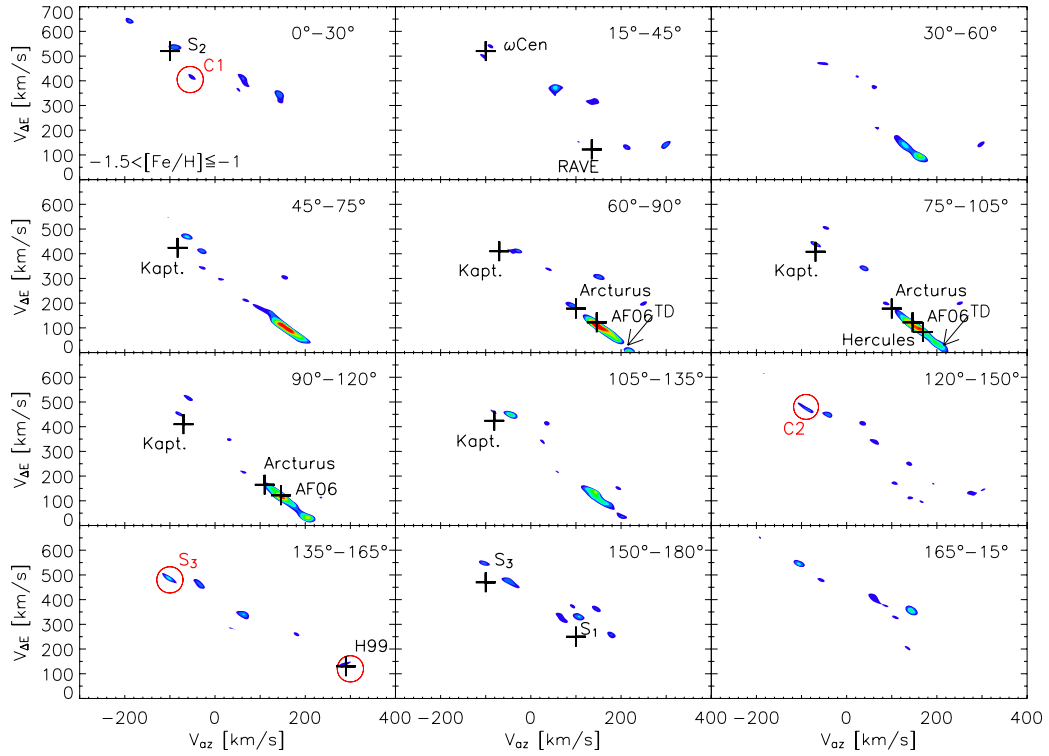


Figure 7.18: Same as Figure 7.17, but now for the significances of the sub-sample s_3 . Also in this sub-sample, there are too few stars on disk-like orbits predicted by the smooth model.

we take stars with positive or negative W -velocities from the list of member stars given in Arifyanto and Fuchs (2006). These stars move on no well-defined "orbital planes", because they are sensitive to the flattened disk-potential. We detect a signal of this stream at $(V_{az}, V_{\Delta E}) \approx (140, 110)$ km s $^{-1}$ in the ν -slice 90° - 120° , maybe even extending towards 105° - 135° .

In the sub-sample s_3 , at metallicities in the range $-2.0 < [\text{Fe}/\text{H}] \leq -1.5$ (Figure 7.14), the fraction of halo stars dominates above the thick disk stars. In the regions of the dynamical streams Hercules and AF06 we detect signals that are significant above $\sigma \geq 2$ (Figure 7.19). These signals remain even for the sub-sample s_4 , where the fraction of thick disk stars should be negligible, showing that still some thick disk stars are present (Figure 7.20).

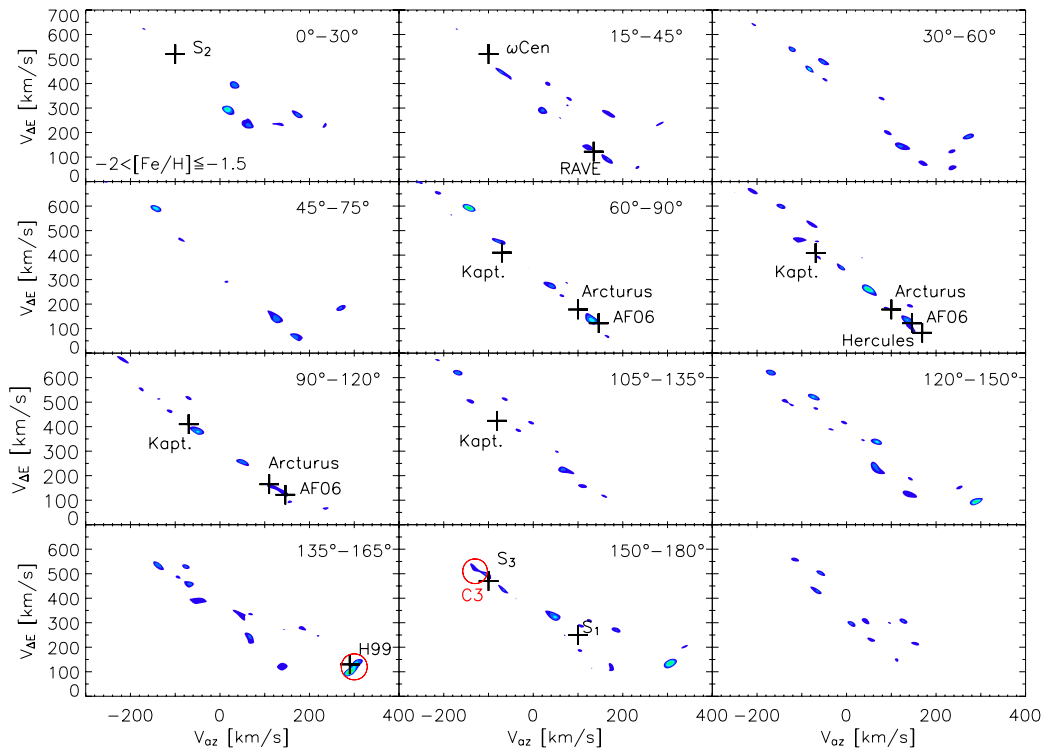


Figure 7.19: Same as Figure 7.17, but now for the significances of the sub-sample s3.

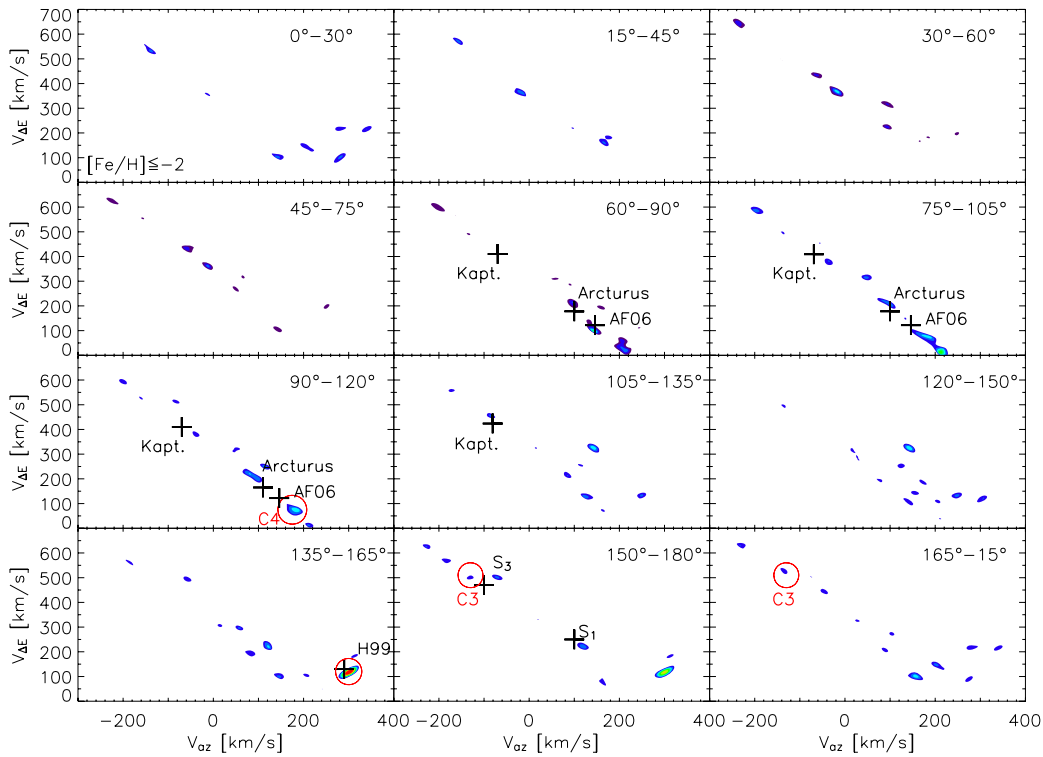


Figure 7.20: Same as Figure 7.17, but now for significances of the sub-sample s4.

7.6.2 Confirming the Discovery of the RAVE DR1 Stream

We now concentrate on the location of the stream that we discovered in the RAVE DR1 (Chapter 6). This stream is centered at a mean of $(V_{\text{az}}, V_{\Delta\text{E}}) \approx (135, 122)$ km s^{-1} and $\nu \approx 30^\circ$.⁶ The stars of this stream possess high vertical and low radial velocity components, $\langle W \rangle = 121 \pm 2 \text{ km s}^{-1}$ and $\langle U \rangle = 24 \pm 2 \text{ km s}^{-1}$ (Section 6.9). Their V -velocities range from $-180 \text{ km s}^{-1} \lesssim V \lesssim -140 \text{ km s}^{-1}$, so their orbital plane is inclined at an angle of $\nu \approx 30^\circ$. Indeed, in the ν -range 15° - 45° there exist overdensities very close to the predicted position of the 'RAVE' stream: one in sub-sample s1, at $V_{\text{az}} \approx 140 \text{ km s}^{-1}$, which we labeled as 'R1' (Figure 7.12), and one in sub-samples s2 and s3, at lower azimuthal velocities of $V_{\text{az}} \approx 120 \text{ km s}^{-1}$, which we labeled 'R2' (Figures 7.13 and 7.14). The fact that 'R2' is located at the same position in s2 and s3 makes it unlikely that it is created from Poisson noise. The possibility exists that 'R1' and 'R2', which possess slightly different angular momenta, are connected, maybe resembling two distinct streams from a disrupted satellite.

To test this hypothesis, we proceed as follows: we first look at the distribution of ν -angles of all stars that lie at the positions of 'R1' and 'R2' in $(V_{\text{az}}, V_{\Delta\text{E}})$ -space in order to check which orbital inclinations can be assigned to the overdensities, and if they differ for 'R1' and 'R2'. Then we can pick stream member stars according to their positions in $V_{\text{az}}, V_{\Delta\text{E}}$, and ν , and look at their metallicity-distributions.

We select the $(V_{\text{az}}, V_{\Delta\text{E}})$ -position of the two streams in the following way: for the stream at $V_{\text{az}} \approx 140 \text{ km s}^{-1}$, 'R1', we require $|(V_{\text{az}}, V_{\Delta\text{E}}) - (140, 120)| \leq (30, 30) \text{ km s}^{-1}$, $|\nu - 30^\circ| \leq 30^\circ$ and a value of the wavelet transform in s1 of at least 90% of its maximum value in that ν -range (which corresponds to the red-colored contours in Figures 7.12-7.15). We also add stars from sub-samples s2 and s3 that lie in this region of $(V_{\text{az}}, V_{\Delta\text{E}})$ -space as possible stream-members at lower metallicities, although their signature is not visible in the significance maps 7.18 and 7.19. For the stream 'R2' at $V_{\text{az}} \approx 120 \text{ km s}^{-1}$, we require $|(V_{\text{az}}, V_{\Delta\text{E}}) - (120, 150)| \leq (30, 30) \text{ km s}^{-1}$, $|\nu - 30^\circ| \leq 30^\circ$ and a value of the wavelet transform in s2 of at least 90% of its maximum value in that ν -range. We also add stars from s1 that lie at this position as possible stream members of higher metallicity. The distribution of ν -angles is shown in Figure 7.21

From Figure 7.21 we can not clearly assign an orbital inclination to the stream 'R1'; stars distributed around $\nu \approx 25^\circ$ and $\nu \approx 40^\circ$ contribute both to the signal in the wavelet-transform in Figure 7.12. In contrast, at the position of 'R2' there is a group of stars that peak around $\nu = 30^\circ$, which is the orbital inclination of the 'RAVE' stream. Assuming that 'R1' and 'R2' stem from the same progenitor, it is possible that the difference in the ν -distributions is caused by accelerations and

⁶In the analysis of the RAVE stars we projected their azimuthal motions onto the Galactic plane by adopting a cylindrical coordinate system and setting $V_{\text{az}} = V$, $V_{\Delta\text{E}} = \sqrt{U^2 + 2(V_{\text{az}} - 220 \text{ km s}^{-1})^2}$. This worked because the RAVE sample did not contain many halo stars. The elongation of the stream in the RAVE sample, however, could be a hint that we actually projected more than one stream on different orbital planes onto the Galactic midplane.

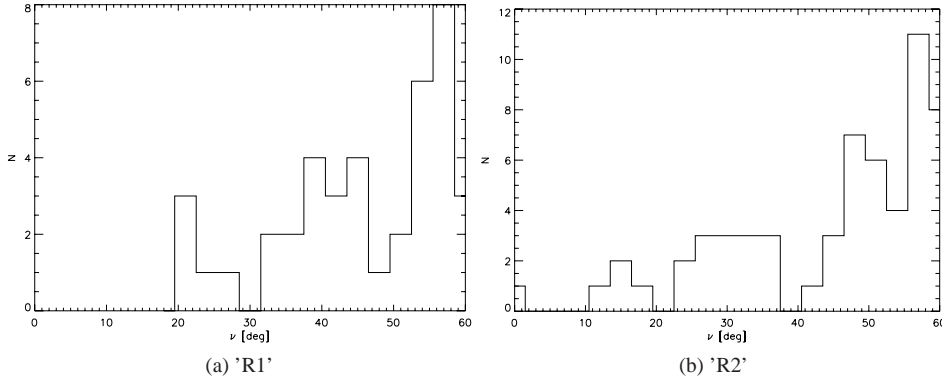


Figure 7.21: Distribution of orbital inclinations ν of stars that lie at the same $(V_{az}, V_{\Delta E})$ -position as the red contoured peaks of the overdensities 'R1' in Figure 7.12 (a) and 'R2' in Figure 7.13 (b). 'R1' is not clearly peaked around a distinct orbital inclination, while 'R2' is centered at $\nu \approx 30^\circ$. The ν -range of $0\text{-}60^\circ$ is part of the preliminary condition for presumable member stars of 'R1' and 'R2'.

decelerations of the streams particles by their precursor object's potential (Choi et al., 2007). However, in this case they still should exhibit the same metallicity distributions. The fact that 'R1' is mostly present in the sub-sample s1, while 'R2' shows up in s2 and s3, suggests that the $[\text{Fe}/\text{H}]$ -distributions are different. We compare the $[\text{Fe}/\text{H}]$ -distributions in Figure 7.22, where we now confine the presumable stream members into the ν -range $|\nu - 30^\circ| \leq 15^\circ$. In the large panels the stars are further selected to lie at the position where the wavelet transform takes on at least 90% of its maximum value in this ν -range, while we lessen this requirement to 75% in the small panels to obtain more stars.

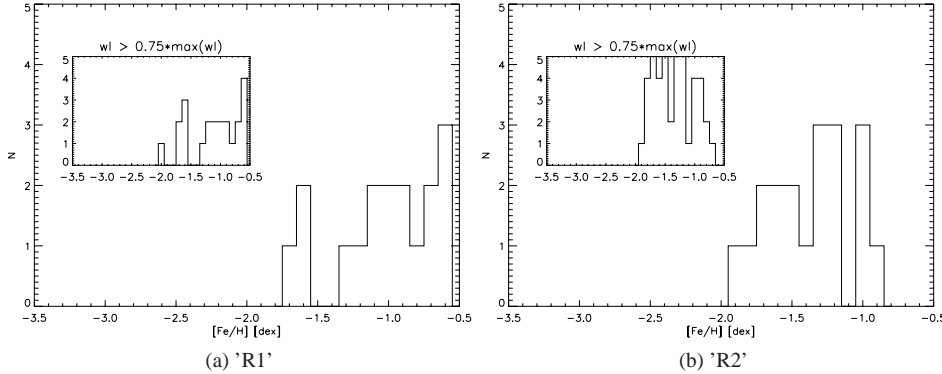


Figure 7.22: *Large panels:* $[\text{Fe}/\text{H}]$ -distribution of stars that lie at the same $(V_{az}, V_{\Delta E})$ -position as the red contoured peaks ($wl = 0.9 \cdot wl_{\max}$) of the overdensities 'R1' in Figure 7.12 (a) and 'R2' in Figure 7.13 (b). 'R1' seems to peak at lower metallicity than 'R2'. *Small Panels:* Same as the large panels, but now stars have been selected from a larger region confined through $wl = 0.75 \cdot wl_{\max}$. The difference between both $[\text{Fe}/\text{H}]$ -distributions is more pronounced.

The two $[\text{Fe}/\text{H}]$ -distributions are not compatible with the theory that both streams originate from the same precursor object. The $[\text{Fe}/\text{H}]$ -distributions of 'R2' peaks at metallicities between -1.2 and -1.8 , and the stream does not seem to contain stars more metal-poor than $[\text{Fe}/\text{H}] = -0.5$. On the other hand, 'R1'

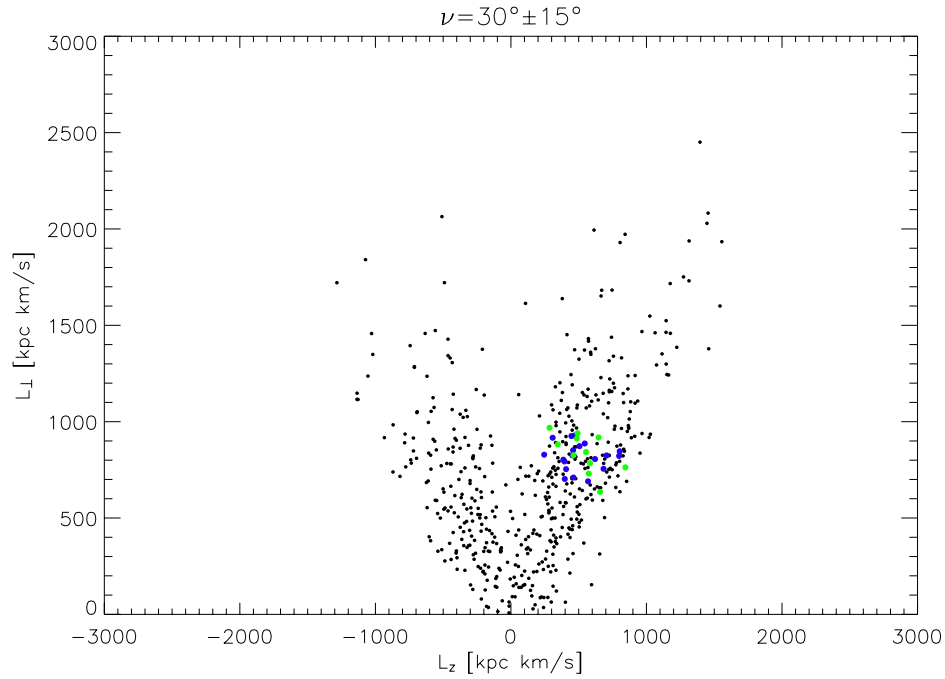


Figure 7.23: Distribution of presumable members of the stream discovered in RAVE data in (L_z, L_\perp) -space. Light blue dots show stars in the range $-1.0 < \text{Fe}/\text{H} \leq -0.5$, blue dots show stars in the range $-1.5 < \text{Fe}/\text{H} \leq -1.0$ and green dots stars with $-2.0 < \text{Fe}/\text{H} \leq -1.5$. The small black dots are all stars in our sample with $-2.0 < \text{Fe}/\text{H} \leq -0.5$ and $|\nu - 30^\circ| \leq 15^\circ$.

has one peak at $[\text{Fe}/\text{H}] \approx -1.6$, and a broad plateau possibly continuing beyond $[\text{Fe}/\text{H}] = -0.5$. We have checked whether there is a correlation between the double-peaked ν -distribution and the $[\text{Fe}/\text{H}]$ -distribution of 'R1', but such a correlation does not exist. Therefore we conclude from the ν - and $[\text{Fe}/\text{H}]$ -distributions that a tidal origin of 'R1' is ruled out. 'R1' and 'R2' are not correlated in the sense that they originate from a single progenitor, and the high significance of 'R1' (figure 7.17) could be a result of the small variance of our smooth reference model in this region of $(V_{\text{az}}, V_{\Delta E}, \nu)$ -space.

We keep 'R2' as a tidal stream candidate and show its (L_z, L_\perp) - and (U, V, W) -distribution in Figures 7.23 and 7.24, respectively. We use light blue dots for stars in the metallicity range $-1.0 < \text{Fe}/\text{H} \leq -0.5$, blue dots for stars with $-1.5 < \text{Fe}/\text{H} \leq -1.0$ and green dots for stars in the range $-2.0 < \text{Fe}/\text{H} \leq -1.5$. The small black dots are stars in the range $-2.0 < \text{Fe}/\text{H} \leq -0.5$ and $|\nu - 30^\circ| \leq 15^\circ$ and are displayed as the background population. The stars approximately show a "banana" shaped distribution in (U, V) , which is typical for tidal streams near their apocenters (Helmi et al., 2006). The banana shape results from the condition $V_{\Delta E} = \text{const.}$, which describes an ellipse in (U, V_{az}) , that is, in the radial and azimuthal velocity in the orbital plane of the stream (compare also to our simulations in Section 5.2.1). If the distribution in W is sufficiently narrow, this shape also appears in the (U, V) -distribution.

The U -, V - and W -velocities are consistent with those found in the RAVE sample: $(\langle U \rangle, \langle V \rangle, \langle W \rangle) = (-5 \pm 13, 59 \pm 5, 98 \pm 3) \text{ km s}^{-1}$. Also the re-

gion occupied in (L_z, L_\perp) -space resembles that which we have assigned to the new stream in the significance map, Figure 6.19. We have good reason to believe that we have rediscovered our proposed new stream. The metallicity-distribution, Figure 7.22(b), suggests that the stream consists of stars mainly in the range $-1.8 \lesssim [\text{Fe}/\text{H}] \lesssim -1.2$.

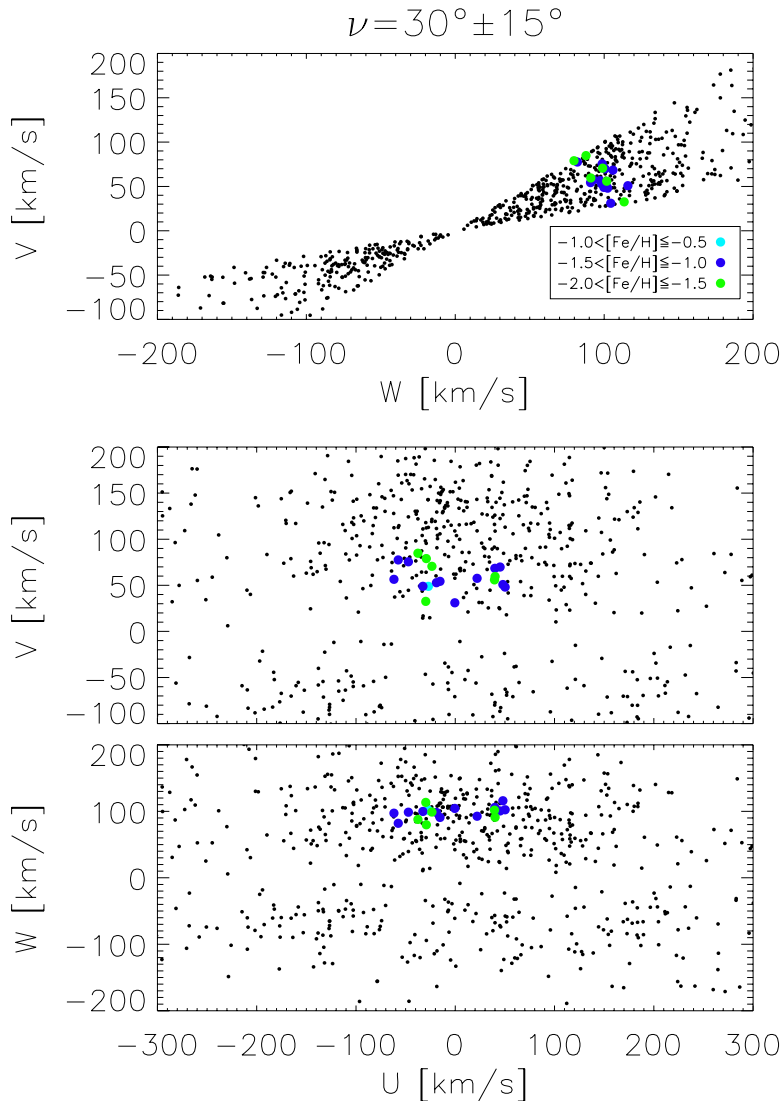


Figure 7.24: Distribution of presumed members of the stream discovered in RAVE data in (U, V, W) . Note the banana shaped (U, V) distribution centered at $U = 0$, indicating that the stream stars are near their apocenters.

7.6.3 A New Stream Candidate

Centered at even lower orbital inclination than the 'RAVE' stream in sub-sample s2 (Figure 7.13), we find an overdensity of stars around $(V_{\text{az}}, V_{\Delta\text{E}}) \approx (-60, 400)$. This overdensity extends towards the sub-sample s3, so it is unlikely to be caused

by Poisson noise. Because we do not know of any stream in the literature with such kinematics, we have labeled this overdensity 'C1' for our first new stream candidate. The significance of this feature is ≥ 2 in Figure 7.18, but not in Figure 7.19. We analyze its velocity-, angular momentum- and [Fe/H]-distribution in Figure 7.25.

Because the velocity-distribution is symmetric around $U = 0$, these stars must be moving towards and away from their apocenters. The typical banana shape is indicated in the (U, V) -distribution, but not perfect: because of the high orbital inclination, the banana shape in (U, V_{az}) (which is predicted by the condition $V_{\Delta E} = \text{const.}$) does not perfectly translate into (U, V) . The metallicity distribution is roughly symmetric around $[\text{Fe}/\text{H}] = -1.5$ and hints towards the distribution of tidal debris from a single metal-poor progenitor. We propose C1 to be a newly discovered halo stream passing the Solar vicinity.

7.6.4 Two Related Streams?

The retrograde stream labeled 'S₃' was discovered by Dettbarn et al. (2007) as an overdensity centered at $(V_{\text{az}}, V_{\Delta E}, \nu) = (-100, 470, 170^\circ)$. We also find an overdensity of stars at this position in sub-sample s2, but peaked at $\nu \approx 155^\circ$. Nevertheless, we identify this overdensity with 'S₃', because from Figure 3 in Dettbarn et al. (2007) we can see that the wavelet contours of their feature seem to extend towards $\nu \approx 155^\circ$.

In the ν -slice 120° - 150° we detect another overdensity at nearly the same $(V_{\text{az}}, V_{\Delta E})$ -values like 'S₃', to which we assign the name 'C2'. This corresponds to a second peak in the ν -distribution of stars in the $(V_{\text{az}}, V_{\Delta E})$ -range centered at $\approx (-105, 480)$, to which we assign the name 'C2'. We suspect that both 'C2' and 'S₃' contribute to the high signal of the wavelet transform in the ν -slice 135° - 165° in Figure 7.13. This is shown in Figure 7.26, where we have plotted the ν -distribution of all stars that are located at the same $(V_{\text{az}}, V_{\Delta E})$ -position as the overdense region in this ν -slice. The two peaks at $\nu \approx 155^\circ$ and $\nu \approx 135^\circ$ correspond to the streams 'S₃' and 'C2', respectively.

'S₃' and 'C2' appear to be two distinct streams that move with nearly the same orbital inclinations and eccentricities, but on different orbital planes that differ by only $\sim 20^\circ$. The double-peaked ν -distribution could hint towards two tidal streams lost at different times from a progenitor which orbital plane has precessed slightly during many orbits in the Milky Way. We test this hypotheses by analyzing the kinematical and chemical properties of both streams.

In Figure 7.27 we show the (U, V, W) -, (L_z, L_\perp) - and [Fe/H]-distributions for 'C2' (*left column*) and 'S₃' (*right column*). Although it seems that 'C2' does not contain stars in the range $-2.0 < [\text{Fe}/\text{H}] \leq -1.5$ from the "gap" in the wavelet transform contours in Figure 7.14, we include stars from sub-sample s3 and also s4 that lie in the same region as the presumable stream members from s2. This is justified from the [Fe/H]-distribution in the left column in Figure 7.27, which peaks at $[\text{Fe}/\text{H}] \approx -1.5$ and falls off along a tail towards lower metallicities. It

resembles the distribution of a tidally disrupted stellar population at the same age. We do the same for 'S3' and include all stars in the range $[\text{Fe}/\text{H}] \leq -0.5$ and $|\nu - 155^\circ| < 15^\circ$. Also this stream peaks around $[\text{Fe}/\text{H}] \approx -1.5$.

The banana-shaped (U, V) -distribution for the stream 'C2' indicates that its stars are near their apocenters. The velocity-distribution of 'S₃' is only slightly different. The stars seem to be not as close to their apocenters as the 'C2' stars. Both the (U, V, W) and $[\text{Fe}/\text{H}]$ -distributions seem to support the hypothesis that 'C2' and 'S₃' are two streams with a common origin. In this case we would classically expect that the L_z -components are similar for both streams, if the potential is static and axisymmetric. However, Choi et al. (2007) have shown that a disrupted satellite can produce several dissociated clumps in (E, L_z) -space owing to decelerations and accelerations of the tail particles by the satellite potential. This effect would depend on the satellite mass, host halo mass, and time since disruption, but could account for the small differences between the two streams. Also, dynamical friction could have altered the precursor object's orbit during the times when 'C2' and 'S₃' became unbound (Quinn and Goodman, 1986; Quinn et al., 1993).

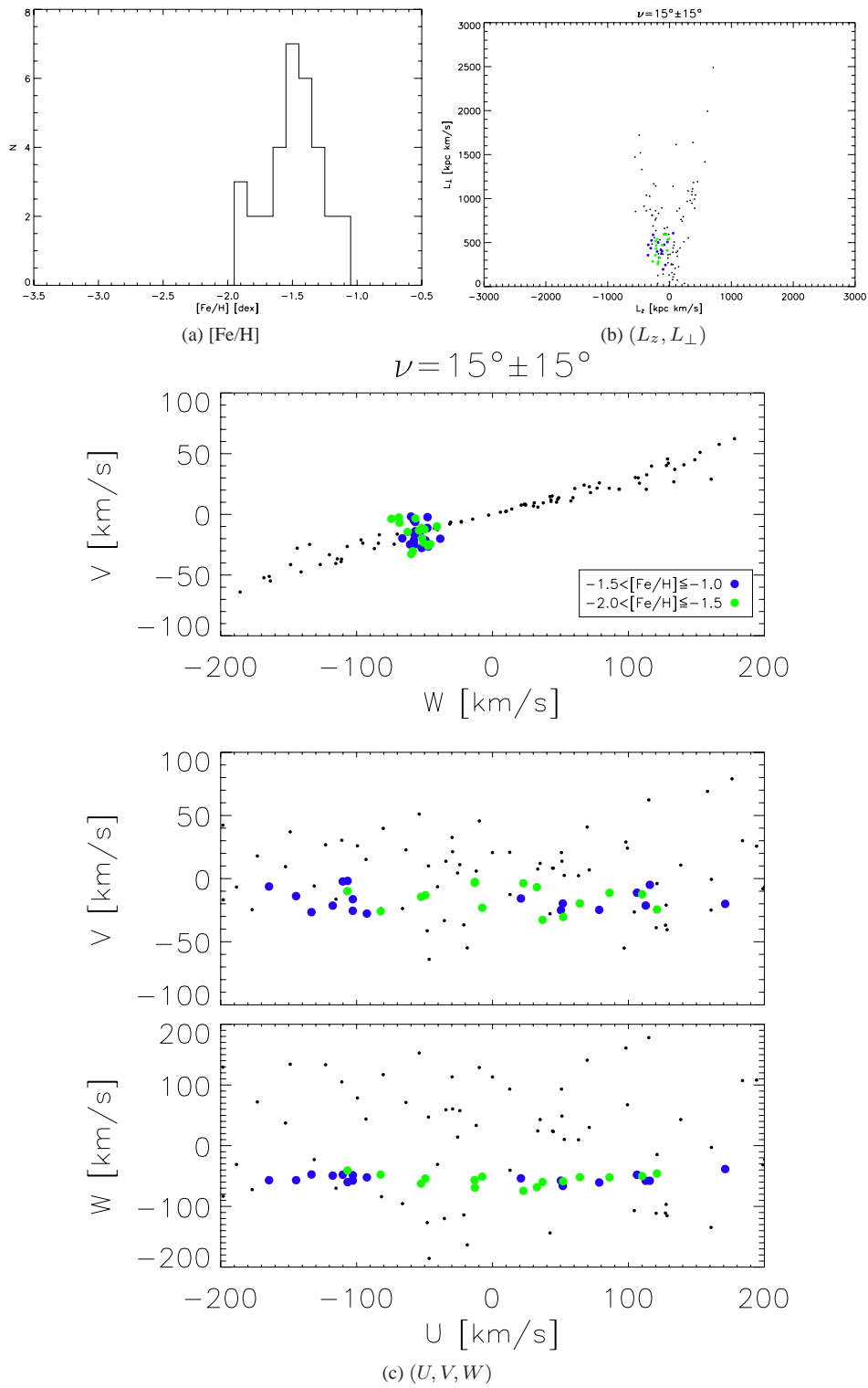


Figure 7.25: Distribution of members of the stream candidate 'C1' in (a) (L_z, L_\perp) , (b) metallicity $[\text{Fe}/\text{H}]$, and (c) (U, V, W) . Blue dots show stars in the range $-1.5 < \text{Fe}/\text{H} \leq -1.0$ and green dots stars with $-2.0 < \text{Fe}/\text{H} \leq -1.5$. The small black dots are all stars in our sample with $-2.0 < \text{Fe}/\text{H} \leq -1.0$ and $|\nu - 15^\circ| \leq 15^\circ$. The (U, V) distribution is symmetric around $U = 0$, indicating that the stream stars are well-mixed and near their apocenters.

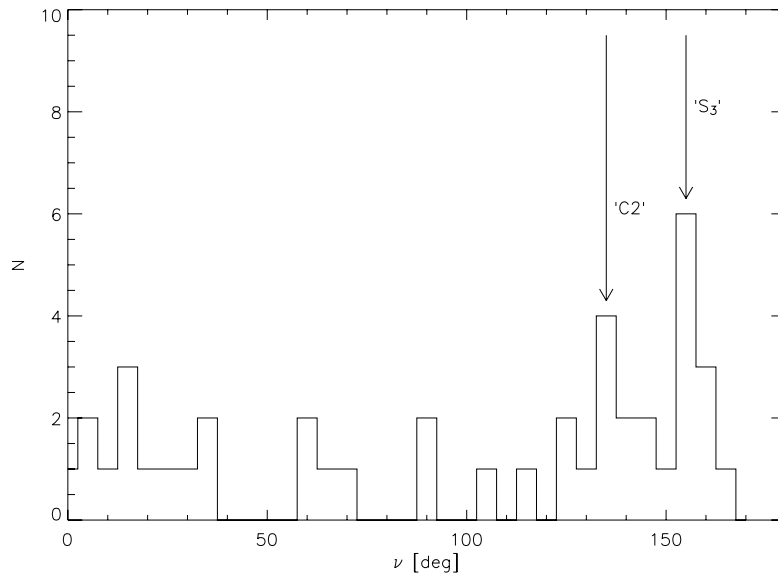


Figure 7.26: Distribution of orbital inclinations ν for all stars in sub-sample s2 that occupy the same region in $(V_{az}, V_{\Delta E})$ -space like the overdensity labeled 'S₃' in Figure 7.13, ν -slice 135° - 165° . The location of the overdensity is selected from the appropriate ranges in V_{az} and $V_{\Delta E}$ and the condition that the wavelet transform has at least 50% of its maximum value (to select the green-framed "bump").

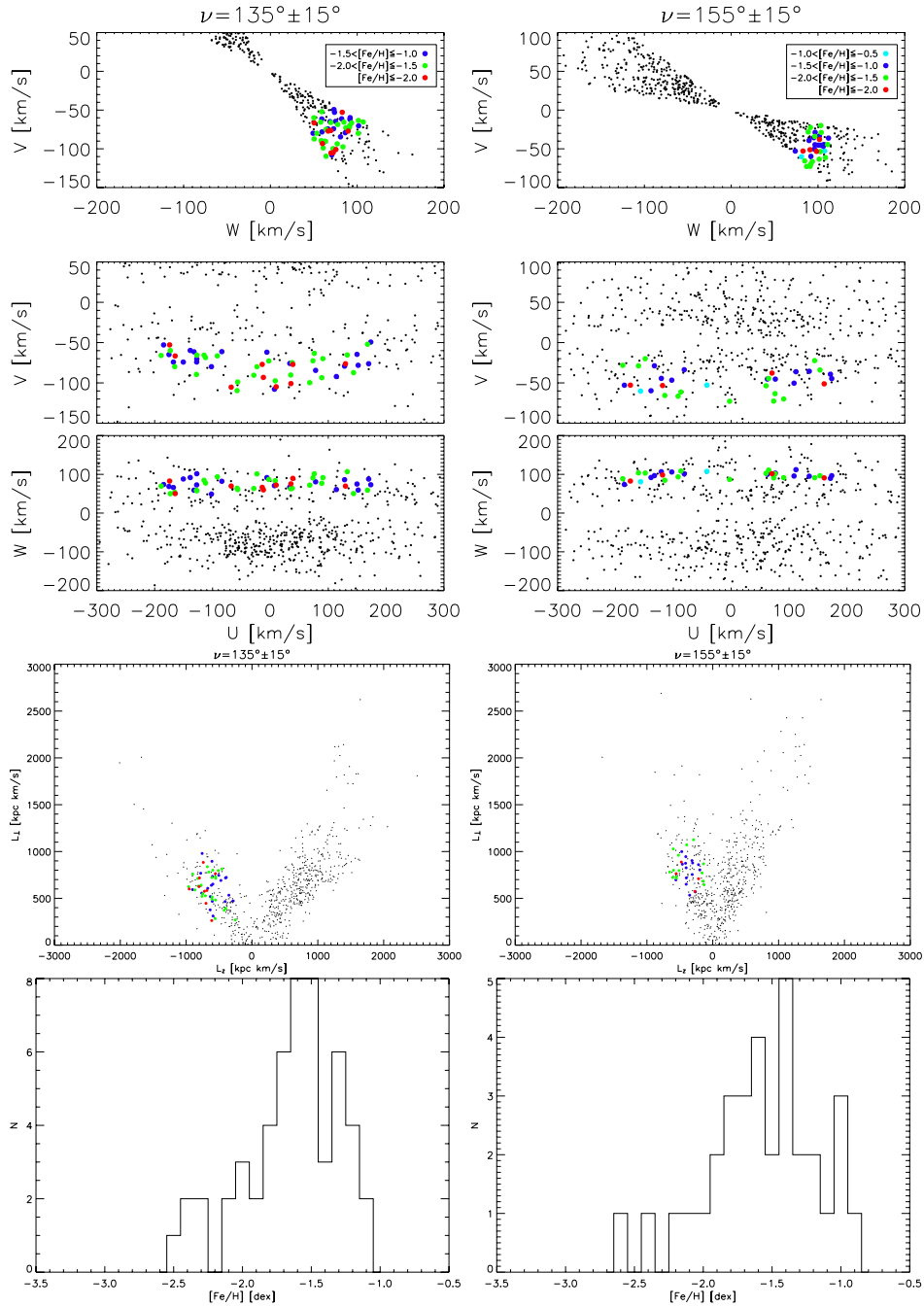


Figure 7.27: (U, V, W) -, (L_z, L_\perp) -, and $[\text{Fe}/\text{H}]$ -distribution of stars belonging to the stream candidate 'C2' (left column) and 'S₃' (right column), respectively. Light blue dots show stars in the range $-1.0 < \text{Fe}/\text{H} \leq -0.5$, dark blue dots in the range $-1.5 < \text{Fe}/\text{H} \leq -1.0$, and green dots stars with $-2.0 < \text{Fe}/\text{H} \leq -1.5$. The small black dots are all stars in our sample that occupy the same $[\text{Fe}/\text{H}]$ - and ν -ranges as the member stars of 'C2' and 'S₃', respectively.

7.6.5 The Helmi Stream

We again look at the metallicity range of sub-sample s2, $-1.5 < \text{Fe}/\text{H} \leq -1.0$, and find an overdensity of stars on a highly prograde orbit inclined at $\nu \approx 150^\circ$. This is the stream discovered by Helmi et al. (1999), located at $(V_{\text{az}}, V_{\Delta\text{E}}, \nu) = (300, 120, 150^\circ)$, in very good agreement with the signal of this stream in the dataset of Dettbarn et al. (2007) (see Table 7.3). The stream, labeled 'H99' was originally discovered as an overdensity of stars in angular momentum space. Later, Chiba and Beers (2000) confirmed the existence of this stream in their own dataset and identified a possible extension towards higher azimuthal rotation. Although their dataset was approximately three times the size of the sample used by Helmi et al. (1999), the number of stream stars ($N = 10$) stayed constant. They hypothesized that the 'H99' stream could be related to the "trail" extension, if this "trail" gained angular momentum from the interaction of the progenitor with the Milky Way's gravitational potential.

In Figure 7.28 we show that the Helmi-stream not only stands out as an overdensity in $(V_{\text{az}}, V_{\Delta\text{E}})$ -space if we select the appropriate $(\nu, [\text{Fe}/\text{H}])$ -slice, but also in $(\nu, [\text{Fe}/\text{H}])$ -space, if we select the right $(V_{\text{az}}, V_{\Delta\text{E}})$ -range. The gray-scaled contours display the $[\text{Fe}/\text{H}]-\nu$ -distribution of the whole sample on a logarithmic scale, while the colored contours show the $[\text{Fe}/\text{H}]-\nu$ -density distribution of all stars with $[\text{Fe}/\text{H}] \leq -1.0$ in a square of 30 km s^{-1} width centered on $(V_{\text{az}}, V_{\Delta\text{E}}) = (300, 120) \text{ km s}^{-1}$. The 'H99' stream shows up as an overdensity of stars at $(\nu, \text{Fe}/\text{H}) \approx (150^\circ, -2.0)$. This shows that tidal streams form distinct clumps in $(V_{\text{az}}, V_{\Delta\text{E}}, \nu, [\text{Fe}/\text{H}])$ -space.

We show the (L_z, L_\perp) -, $[\text{Fe}/\text{H}]$ -, and (U, V, W) -distribution of all stars that we connect to the 'H99' stream in Figure 7.29. The stream extends towards lower metallicities and is highly significant in the sub-sample s4. The (U, V, W) - and (L_z, L_\perp) -distributions agree very well with those in the original work of Helmi et al. (1999, their Figure 2). The $[\text{Fe}/\text{H}]$ -distribution peaks at $[\text{Fe}/\text{H}] \approx -2.0$ and does not extend beyond $[\text{Fe}/\text{H}] \approx -2.3$. The number of stars in our sample that we identify as 'H99' members is $N = 21$, approximately doubled compared with previous studies. But the number is too small to account for as much as one-tenth of the halo stars that are currently present in the Solar neighbourhood, as suggested by Helmi et al. (1999).

7.6.6 More Substructure at Very Low Metallicities

In the sub-samples s3 and s4 the amount of substructure further increases. We expect a contribution of only $\sim 10\%$ thick disk stars in s3 and 100% halo stars in s4 (Chiba and Beers, 2000). While about 46% of the stars in sub-sample s2 move on disk-like orbits ($75^\circ \leq \nu < 105^\circ$), this number drops to 23% for both s3 and s4. It seems that also for stars more metal-poor than $[\text{Fe}/\text{H}] = -2$ a small fraction of stars with thick-disk-like kinematics remains constant.

Besides the already discussed streams that are also visible in s3, 'AF06', 'RAVE', 'H99' and 'C1', we find an overdensity centered at $(V_{\text{az}}, V_{\Delta\text{E}}, \nu) =$

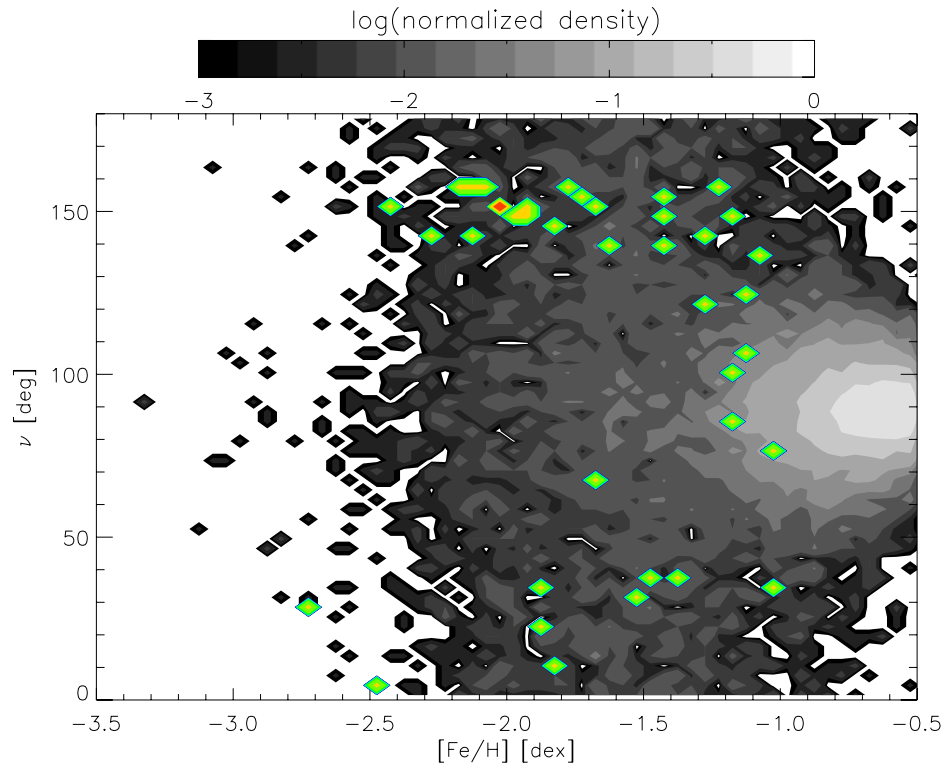


Figure 7.28: Density distribution of all stars in our sample in $[\text{Fe}/\text{H}]$ vs. ν on a logarithmic scale (*gray-scaled*), overplotted with the density distribution of all stars in sub-samples s_2, s_3, s_4 that lie in a square of 30 km s^{-1} width centered on $(V_{\text{az}}, V_{\Delta\text{E}}) = (300, 120) \text{ km s}^{-1}$. The ‘H99’ stream is manifested as the overdensity of stars at $(\nu, \text{Fe}/\text{H}) \approx (150^\circ, -2.0)$. Note the smooth underlying distribution of stars which is dominated by the thick disk.

$(-130, 510, 170^\circ)$, which we label as ‘C3’. It is located near the stream ‘S₃’ and maybe related to it. The peak in the ν -distribution of stars in this region of $(V_{\text{az}}, V_{\Delta\text{E}})$ -space at $\nu = 170$ would fit exactly to the ν -value originally assigned to ‘S₃’ by Dettbarn et al. (2007). However, the $[\text{Fe}/\text{H}]$ -distribution peaks at $[\text{Fe}/\text{H}] \approx -1.8$ and is therefore different from that of ‘S₃’ or ‘C2’ (Figure 7.30). This, together with the difference in the velocity- and angular momentum-distributions, suggests that this stream has a different origin. The mean rotational and vertical velocities of ‘C3’ in a cylindrical coordinate system are $(\langle\Theta\rangle, \langle W\rangle) = (-22 \pm 3, 125 \pm 2) \text{ km s}^{-1}$.

We gain confidence that ‘C3’ is not a feature created from Poisson noise from the fact that the wavelet transform at ‘C3’s position in $(V_{\text{az}}, V_{\Delta\text{E}})$ -space has values greater than 90% of its maximum in both sub-samples s_3 and s_4 . Further, ‘C3’ appears in the significance map of sub-sample s_3 (Figure 7.19) at a significance level greater than 2.

In the most metal-poor sub-sample s_4 , where the fraction of halo stars is close to 100%, there exists a lot of substructure and it is hard to identify any smooth component. Many of the overdensities in Figure 7.15 consist of only a few stars, and their realness can be doubted. We will now concentrate at a highly signifi-

cant feature located at $(V_{\text{az}}, V_{\Delta\text{E}}, \nu) = (175, 75, 100^\circ)$ and labeled with 'C4'. At this region of $(V_{\text{az}}, V_{\Delta\text{E}}, \nu, [\text{Fe}/\text{H}])$ -space a density enhancement of stars is not expected. We place a square with 30 km s^{-1} side length on $(V_{\text{az}}, V_{\Delta\text{E}}) = (175, 75) \text{ km s}^{-1}$ and plot the normalized density of stars in this square projected onto $(\nu, [\text{Fe}/\text{H}])$ -space where $[\text{Fe}/\text{H}] \leq -2.0$. The density contours are shown in Figure 7.31, overlaid upon the normalized $(\nu, [\text{Fe}/\text{H}])$ -density distribution of all stars in our sample. 'C4' is visible as a distinct clump around $(\nu, [\text{Fe}/\text{H}]) \approx (100^\circ, -2.2)$, while the density of the whole sample shows no more concentration of stars around $\nu = 100^\circ$ for $[\text{Fe}/\text{H}] \lesssim -1.7$. This clearly distinguishes the clump 'C4' from a smooth feature.

We show the (L_z, L_\perp) -, metallicity-, and (U, V, W) -distribution of 'C4' in Figure 7.32. The very low excentricity, $e = V_{\Delta\text{E}}/\sqrt{2}V_{\text{LSR}} \simeq 0.2$, of 'C4' suggests that it belongs to the metal-weak thick disk. However, according to Chiba and Beers (2000) even the metal-weak tail of the thick disk should not contain stars as metal poor as $[\text{Fe}/\text{H}] \lesssim -2.2$, where the $[\text{Fe}/\text{H}]$ -distribution of 'C4' peaks. These authors argued that the fraction of low-excentricity stars with $[\text{Fe}/\text{H}] \leq -2.2$ remains the same regardless of their height $|z|$, implying that they purely belong to the halo. In addition, stars in the clump 'C4' are not distributed symmetrically around $\nu = 90^\circ$, but are centered at an orbital inclination of roughly 100° with a longer tail towards higher inclinations.

On the other hand, the formation of the stellar halo and thick disk might underlie a common principle: the accretion of satellite galaxies. It has been shown that the metal-weak tail of the thick disk could consist of tidal debris stemming from a progenitor on a planar orbit that has been circularized prior to disruption through dynamical friction (Quinn and Goodman, 1986; Quinn et al., 1993; Abadi et al., 2003b). The very low abundances of the 'C4' stars favour this scenario. Even if these stars do not belong to a single progenitor exclusively, we have found evidence that tidal debris exists on disk-like orbits, giving further support for the hierarchical build-up of the Milky Way.

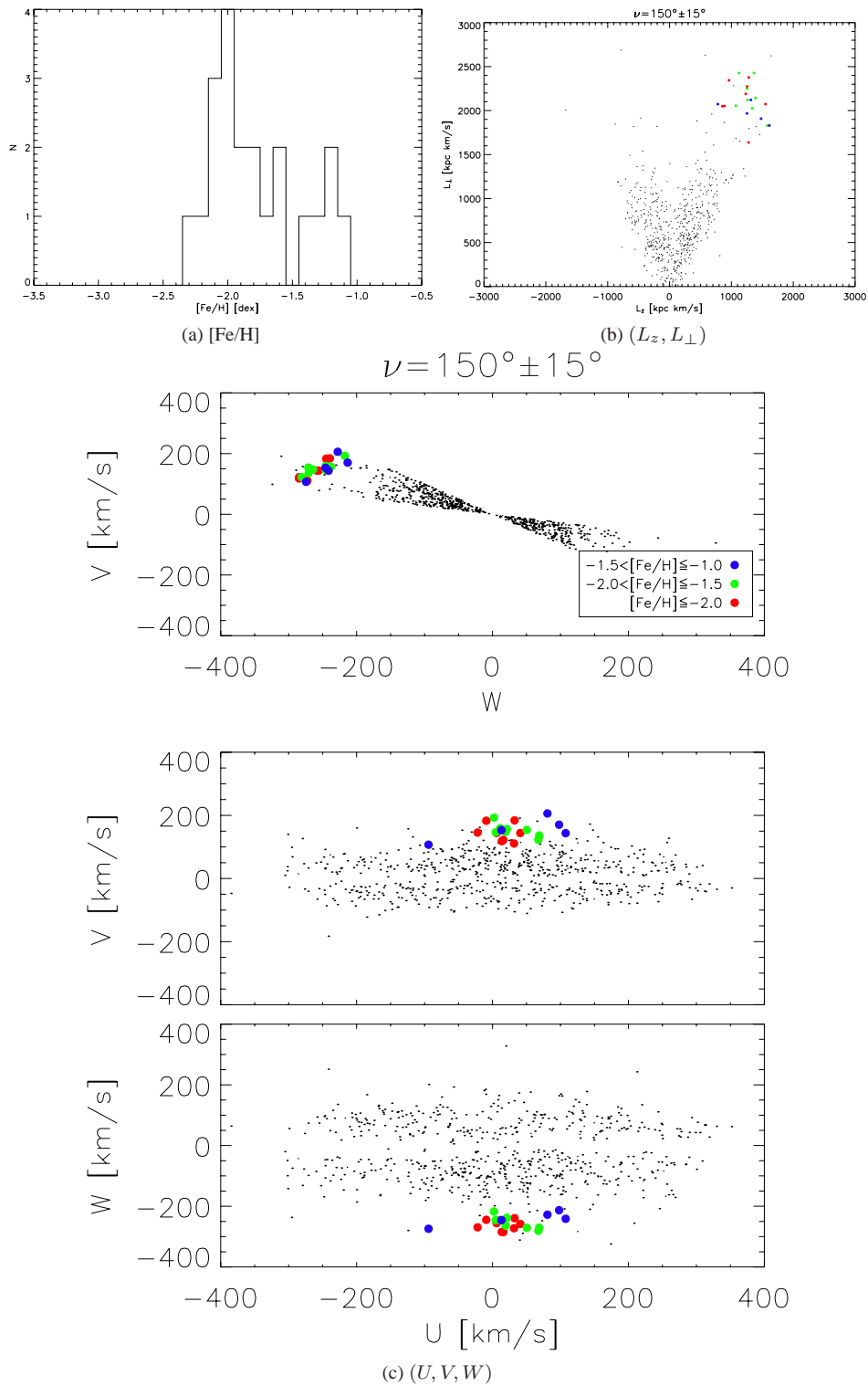


Figure 7.29: Distribution of members of the 'H99' stream in (a) (L_z, L_\perp), (b) metallicity [Fe/H], and (c) (U, V, W). Blue dots show stars in the range $-1.5 < \text{Fe}/\text{H} \leq -1.0$, green dots stars with $-2.0 < \text{Fe}/\text{H} \leq -1.5$, and red dots stars with $\text{Fe}/\text{H} \leq -2.0$. The small black dots are all stars in our sample with $\text{Fe}/\text{H} \leq -1.0$ and $|\nu - 150^\circ| \leq 15^\circ$. The (U, V, W)-distribution is in very good agreement to that shown by Helmi et al. (1999, their Figure 2).

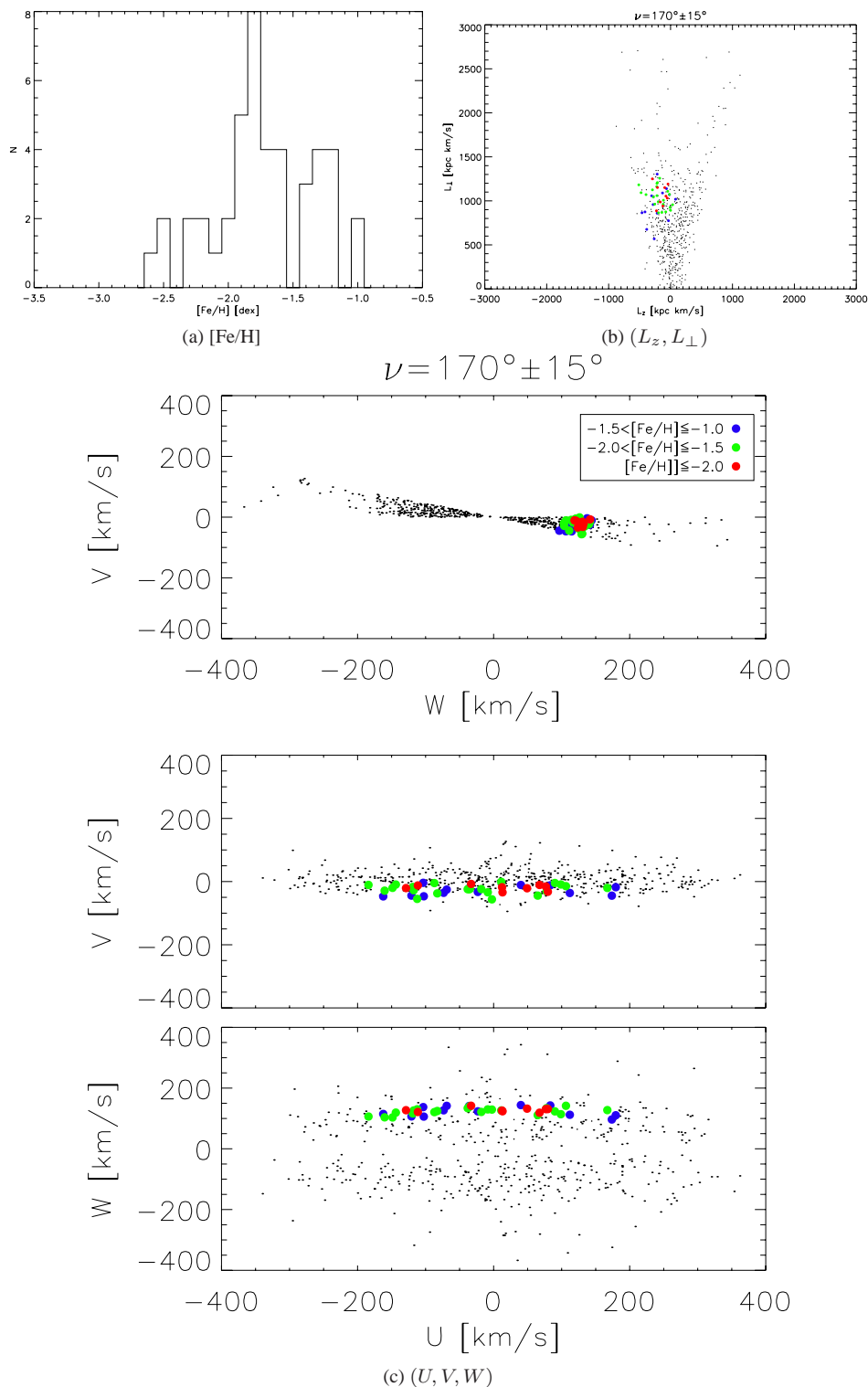


Figure 7.30: Distribution of members of the 'C3' stream candidate in (a) (L_z, L_\perp), (b) metallicity [Fe/H], and (c) (U, V, W). Blue dots show stars in the range $-1.5 < \text{Fe}/\text{H} \leq -1.0$, green dots stars with $-2.0 < \text{Fe}/\text{H} \leq -1.5$, and red dots stars with $\text{Fe}/\text{H} \leq -2.0$. The small black dots are all stars in our sample with $\text{Fe}/\text{H} \leq -1.0$ and $|\nu - 170^\circ| \leq 15^\circ$.

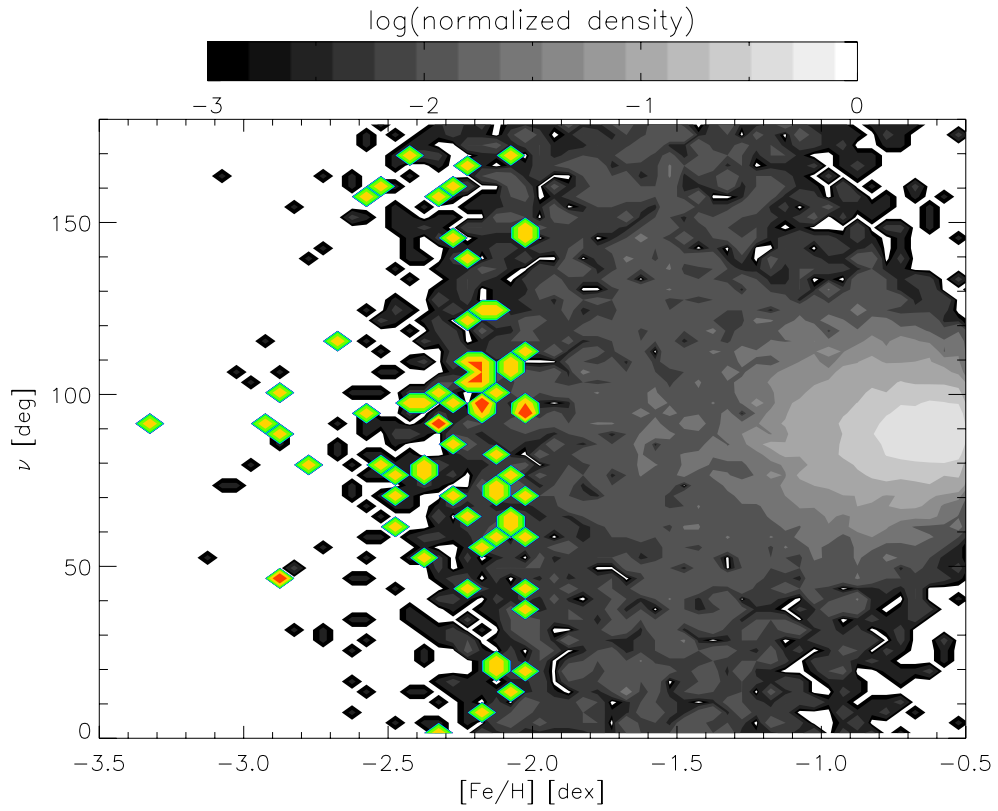


Figure 7.31: Normalized $(\nu, [Fe/H])$ -density distribution of stars with $(V_{az}, V_{\Delta E})$ -velocities in a square centered on $(175, 75) \text{ km s}^{-1}$ with contours ranging from 10^{-3} (black) to 1 (red). The grey-scaled background contours show the normalized density distribution of all stars in our sample.

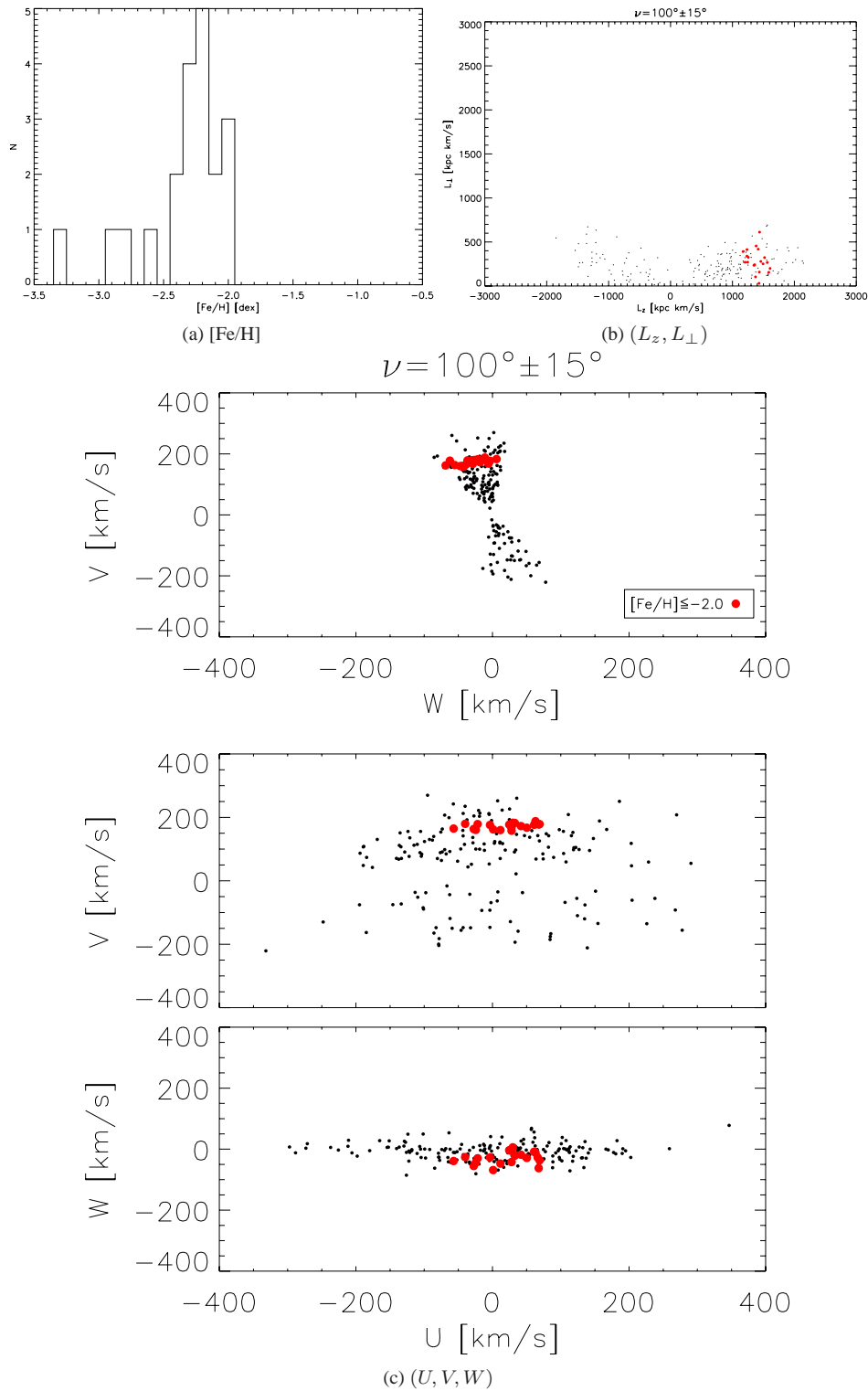


Figure 7.32: Distribution of members of the 'C4' stream candidate in (a) (L_z, L_\perp) , metallicity (b) $[\text{Fe}/\text{H}]$, and (c) (U, V, W) . The small black dots are all stars in our sample with $\text{Fe}/\text{H} \leq -2.0$ and $|\nu - 100^\circ| \leq 10^\circ$.

7.7 Conclusions

We used SEGUE data from the seventh SDSS data release to search for halo streams in a 2 kpc sphere centered on the Sun. Using the catalog values for $\log g$, $g - i$ color and $[\text{Fe}/\text{H}]$ together with distance estimates based on the photometric parallax relation from Ivezić et al. (2008), we assembled a sample of 22,321 sub-dwarfs with $[\text{Fe}/\text{H}] \leq -0.5$ and excluding turn-off stars. A comparison with fiducial sequences for 12 globular clusters from An et al. (2008) suggests that our distances are accurate to within systematic errors of $\lesssim 10\%$.

We divided our sample into four sub-samples equally spaced by 0.5 dex in metallicity. Assuming a spherical potential, we searched for stellar streams in each sub-sample in a space spanned by the quantities $V_{\text{az}} = \sqrt{V^2 + W^2}$, $V_{\Delta\text{E}} = \sqrt{U^2 + 2(V_{\text{az}} - V_{\text{LSR}})^2}$ and $\arctan \frac{U}{V}$. These quantities are approximations for a star's azimuthal velocity, eccentricity and orbital inclination with respect to the positive z -axis.

Our basic results can be summarized as follows:

1. Our sample is dominated by stars on disk-like orbits; the fraction of these stars with orbital inclinations between 75° and 105° is 81% (80%) for stars with $-1.0 \leq [\text{Fe}/\text{H}] < -0.5$, 46% (44%) for stars with $-1.0 \leq [\text{Fe}/\text{H}] < -0.5$, and remains constant at 23% (16%-17%) for all stars more metal-poor than $[\text{Fe}/\text{H}] = -1.5$ (the number in parenthesis gives the fraction of stars on prograde orbits). This implies that beyond $[\text{Fe}/\text{H}] \simeq -1.5$ the fraction of the thick disk remains constant.
2. In the metallicity range $-1.0 \leq [\text{Fe}/\text{H}] < -0.5$ it is hard to make out sub-structure among the thick disk, because the smooth component dominates. As the fraction of thick-disk stars decreases, we detect signals of the stream 'AF06', which has first been described by Arifyanto and Fuchs (2006) and Helmi et al. (2006).
3. We find an overdensity of stars moving with disk-like kinematics, but too metal-poor to belong to the classical metal-weak thick disk, which should not extend beyond $[\text{Fe}/\text{H}] \simeq -2.2$ (Chiba and Beers, 2000). We interpret this clump, named 'C4', as a tidal stream accreted on an orbit in the plane of the protodisk. Halo streams on such orbits are predicted both from numerical simulations of spiral galaxy formation (Quinn and Goodman, 1986; Quinn et al., 1993; Abadi et al., 2003b) and from a considerable 20%-fraction of halo stars on low-eccentricity orbits (Chiba and Beers, 2000).
4. We confirm the existence of previously detected halo streams: The 'RAVE'-stream, which we discovered in data from the first RAVE data release, the stream 'S₃' found by Dettbarn et al. (2007), which crosses the Solar neighborhood from the direction of the South Galactic Pole on a diagonally retrograde orbit, and the 'H99'-stream discovered by Helmi et al. (1999) at high angular momentum. The latter is the most significant stream in our sample

($\sigma > 10$), which explains why Helmi et al. (1999) has found it in a sample of only 275 stars. However, even with our much larger sample size the number of stars that belong to this stream is only approximately doubled. This speaks against the conclusion of Helmi et al. (1999), that as much as 10% of the nearby halo stars originate from a single progenitor.

The fact that both the 'RAVE'- and the 'S₃' stream have been found in two independent samples makes it very unlikely that they are "fake" detections. The 'S₃'-stream is significant at a level of $\sigma \gtrsim 2.8$ in our data (Figure 7.19), and in the data from Dettbarn et al. (2007), corresponding to a confidence level of 99.5%. That means, the probability that this stream is created by chance in both samples is $(0.005)^2 = 0.0025\%$. The significance levels of the 'RAVE' stream in the RAVE data and in the SEGUE data are $\sigma \gtrsim 3$ (Figure 6.13) and $\sigma \gtrsim 2.5$ (Figure 7.19), respectively, which also makes it very unlikely that both streams are "fake" detections created through Poisson noise.

5. Besides the already known features we find evidence for a large amount of substructure, particularly in the most metal-poor bins. In particular, we identify three candidates for genuine halo streams, which have not yet been described in the literature. Two of them, 'C1' and 'C3', move on highly inclined orbits nearly in the direction towards the North and South Galactic Pole, respectively. Although 'C3' possesses similar kinematics as 'S₃', their [Fe/H]-distribution suggests that these streams have different precursor objects. Instead, we find a stream, 'C2', with nearly identical angular momentum and eccentricity as 'S₃', which is probably related to it judged by the [Fe/H]-distribution. The orbital inclinations differ by $\sim 20^\circ$, which could be explained by precession of the common progenitor's orbit during the times when 'C2' and S₃ became unbound.
6. Metallicities are very helpful when it comes to deciding about the origin of a moving group. Our stream candidates show a [Fe/H]-distribution with a single peak, indicating that their progenitor had a well-defined star-forming epoch.

This study shows the power of current and future large-scale surveys to probe substructure in the Solar neighborhood, and the Milky Way in general.

Part III

Exploring the Local Gravitational Potential

Chapter 8

Introduction to the K_z -force problem

Since the pioneering works of Oort, Lindblad and Schwarzschild, the " K_z -force problem" is one of the most instructive problems in astronomy. Probably the most important question in this context is the value of the density of all gravitating mass in the Galactic disk. A comparison of this value with the observed density of visible matter gives conclusions about the amount of dark matter in the disk. The determination of the amount of dark matter is crucial for understanding the formation of the Galaxy. For example, if the majority of the oldest stars in the disk, and the thick disk itself, originates in accreted satellites, like predicted from recent Λ CDM simulations (Abadi et al., 2003b), a considerable fraction of the disk mass should be dark.

The shape of the gravitational potential of the Milky Way has been explored on kpc scale in the past mainly in the direction perpendicular to the Galactic plane. Using the Poisson equation, the aim was then to derive the vertical density distribution of all gravitating mass from the force $K_z \equiv \frac{\partial \Phi}{\partial z}$ to which it gives rise. The classical method makes two assumptions: First, it assumes that the stellar populations are in a well-mixed state according to the coordinates z and W . Then, according to the Jeans theorem (Section 4.1.4), stars observed at various altitudes above or below the midplane, and the vertical velocity components W can be mapped into a phase space distribution function $f(z, W) = f(E_z)$, which depends on the energy associated with the vertical motions of the stars, $E_z = \frac{1}{2}W^2 + \Phi(z)$. The second assumption is that the z -motions of the stars are decoupled from their radial motions, which is the case if the potential is separable into a radial and vertical term (see, however the discussion of this assumption by Statler (1989)). The Galactic disk is then assumed to be plane stratified and a one-dimensional model of the vertical gravitational potential $\Phi(z)$ is constructed. Thereby, the gravitational potential ϕ is usually modelled by an analytical "Ansatz". Then the stellar volume density can be computed from the distribution function through an integration over velocities (equation (4.7), Section 4.1.2), and compared with the observed local mass density. This allows to constrain the parameters of the model (Kuijken and Gilmore, 1989a,b; Fuchs and Wielen, 1993; Flynn and Fuchs, 1994;

Holmberg and Flynn, 2000; Korchagin et al., 2003; Bienaymé et al., 2006).

Early investigations by Oort (1932, 1960) found that a significant amount of the local disk mass is dark, which was later corroborated by Bahcall (1984), who derived mass (the "Oort limit") and column mass densities of the disk of $0.185M_{\odot}\text{pc}^{-3}$ and $67M_{\odot}\text{pc}^{-2}$, respectively. The latter authors assumed that the disk potential is composed of a superposition of a finite number of isothermal components and that the disk dark matter is distributed proportional to the visible matter. However, Kuijken and Gilmore (1989c) pointed out that some of the data on which these results have been based, are internally inconsistent. In their series of papers 1989a; 1989b; 1991, Kuijken and Gilmore used a sample of K dwarfs to derive a surface mass density of all matter (disk + halo) within 1.1 kpc of the Sun of $71 \pm 6M_{\odot}\text{pc}^{-2}$. They estimated the disk to contribute to this surface density with $48 \pm 9M_{\odot}\text{pc}^{-2}$, fully consistent with the surface density of visible matter of about $48 \pm 8M_{\odot}\text{pc}^{-2}$. Using a complete magnitude-limited sample of K giants in a cone at the South Galactic Pole, Bahcall et al. (1992) again inferred the presence of disk dark matter at the 86% confidence level with the same method used by Bahcall (1984).

In 1994, Flynn and Fuchs used the space motions of nearby K giants which they regarded as the local counterpart of the Bahcall et al. (1992) cone sample, to infer a disk surface density of $52 \pm 13M_{\odot}\text{pc}^{-2}$. Their analysis was based on the procedure of Fuchs and Wielen (1993) and the observation of von Hoerner (1960), which states that the vertical velocity distribution function $f(W_0)$ at the Galactic midplane in fact represents the phase space density in the two-dimensional (z, W) -space, provided that the gravitational potential separates into vertical and radial components:


$$f(W_0) = f(\sqrt{W^2 + 2\Phi(z)})$$

Recent studies of Korchagin et al. (2003) and Bienaymé et al. (2006), who estimated the Oort limit and disk surface densities of $(\rho(z=0), \Sigma(|z| < 350)) = (0.1M_{\odot}\text{pc}^{-3}, 42 \pm 6M_{\odot}\text{pc}^{-2})$ and $(\rho(z=0), \Sigma(|z| < 390)) = (0.07 - 0.09M_{\odot}\text{pc}^{-3}, 67M_{\odot}\text{pc}^{-2})$, seem to confirm the lack of dark matter in the disk. However, uncertainties of $\sim 10\%$ remain and more precise measurements are required.

In addition, the radial variation of the gravitational potential of the Milky Way has not been studied in this detail. It is usually modelled by combining a highly flattened Miyamoto disk and nearly spherical models for the bulge and dark halo, respectively (see Section 5.1). The parameters of these models were constrained by observations of the Galactic rotation curve (Johnston et al., 1999). The models were aimed at the large scale structure of the Milky Way, but in investigations of the local variation of the Galactic potential its radial gradient is at present neglected.

Chapter 9

A New Method to Determine the K_z Force Law

he orbits of stars in the Solar neighbourhood are fully constrained by their current positions, velocities and the shape of the gravitational potential, while the potential is connected to the density distribution through Poisson's equation (4.5). So there exists a correlation between the spatial density distribution of stars and the orbits they move on. The orbits produce an orbital density distribution through the amount of time that stars spend in a given space volume. It was shown by Schwarzschild (1979) that it is possible to reproduce the density distribution of a stellar system in equilibrium by occupying a certain number of orbits with non-negative numbers of stars. So if one assumes a population of disk stars to have settled in a state of equilibrium, a superposition of orbital densities that equals the observed spatial density must exist.

We therefore try to reproduce an observed density distribution through integration of stellar orbits in a test potential. If the test potential represents the true potential that influences the movement of the stars, then the density distribution that is generated through their orbits has to match the observed distribution. While Schwarzschild (1979) asks whether a dynamical equilibrium configuration exists that has the chosen density distribution, we a priori assume that such a configuration exists supported by the orbits of the observed stars. We then try to find an analytic expression for the potential that leads to the observed density distribution. We will outline our procedure in the following section.

9.1 Description of the Method

We intend to study the local gravitational potential on the kpc scale. As a first step we concentrate again on the vertical K_z force law, with the goal of later applying the method to the 3-D case. Our basic assumption is that the stars move in an axisymmetric potential respecting three isolating integrals of motion, of which two – the energy E and z -component of angular momentum L_z – are exact integrals. The "third integral" has been introduced in Section 4.4.4 as the adiabatic integral

of the vertical motion of the stars $\frac{1}{2}W^2 + (\Phi(R, z) - \Phi(R, 0))/\sqrt{\rho(R, z)}$ (equation 4.78). The existence of a third effective integral of motion allows one to use a sample population of stars in a column perpendicular to the Galactic plane with a broader base than in previous studies. This follows from the Jeans theorem (Section 4.1.4), which states that the phase-space density is a function of the integrals of motion for a population of stars in dynamical equilibrium. Further, it allows us to reduce the orbit integrations to the one-dimensional case. The following steps will give a description of how our procedure is applied to a stellar sample.

i) **Observing the Vertical Density Distribution**

The goal of our method is to find an analytical expression for the potential which reproduces the observed density distribution of an "adequate" sample of stars. Adequate in this context means that the stars should be old enough to justify the assumption of having settled in a dynamical equilibrium. Also, one needs to know the vertical position z and velocity component W of each star to be used as initial conditions for the later orbit integrations.

The column being observed is divided into N cells of constant thickness d above and below the midplane $z = 0$.¹ The thickness of each cell depends on the accuracy to which the positions of the stars are known and on the maximal height of the observed column. The cells are numbered from $j = 1, \dots, N$ for $z > 0$ or from $j = -1, \dots, -N$ for $z < 0$, with the cells $j = 1$ and $j = -1$ touching the midplane. The number of stars in each cell is counted and divided by the total number of stars in the sample M in order to get the normalized observed density distribution. The density distribution is stored in an array $\rho_{obs}[j]$. Because of the symmetry with respect to $z = 0$ it is sufficient to store densities only for $z > 0$ without loss of generality. The density distribution $\rho_{obs}[j]$ will later be compared to the density produced by integrating the orbits in the test potential.

ii) **Choosing a Test Potential**

Since no analytic expression of the density distribution $\rho(z)$ is known, it is not possible to get an expression for the potential $\Phi(z)$ or the vertical force K_z directly. Therefore, the potential is approximated by a higher order spline function. In the simplest case with only two parameters, the test potential could be modeled as:

$$\Phi = k_{fit} z_{fit}^2 \left(\frac{|z|}{z_{fit}} - \ln\left(1 + \frac{|z|}{z_{fit}}\right) \right) \quad (9.1a)$$

$$\frac{d\Phi}{dz} = k_{fit} \frac{z}{1 + \frac{|z|}{z_{fit}}} \quad (9.1b)$$

$$\rho = \frac{k_{fit}}{4\pi G} \frac{1}{\left(1 + \frac{|z|}{z_{fit}}\right)^2}. \quad (9.1c)$$

¹Although the word "layer" would be better suited in this context, we use the word "cell" like Schwarzschild (1979), keeping in mind that we plan to apply the same procedure to the distribution of stars in the meridional plane (R, z) .

Here, k_{fit} and z_{fit} are constants with units $1/\text{Gyr}^2$ and kpc , respectively. This form of the potential makes sure that at small heights z the force rises proportionally to k_{fit} . Without loss of generality, the potential (9.1) will be used for the remainder of this description.

iii) Orbit Integrations

Starting with the observed heights and velocities (z_{obs}, W_{obs}) each star can now be integrated in the test potential of which an example is given through equations (9.1). The restriction to integration only in the z -direction is justified through the assumption of the existence of the third integral. In contrast to N-body modelling, each star is integrated one at a time. The integration time t is chosen long enough for the stars to fulfill enough oscillations to represent a characteristic equilibrium state of the Galaxy. As the i th star ($i = 1, \dots, M$) moves on its orbit up and down, the fraction of time it stays in each cell j above the midplane ($j = 1, \dots, N$) is recorded in a two-dimensional array $A[i, j]$. These time fractions represent the time-averaged density distribution a star places in each cell. Integration of the stars provides snapshots of the equilibrium distribution of the stars settling in the test potential.

iv) χ^2 -fitting and Iteration

After all stars have been integrated, for each cell one can sum up and normalize the density contribution of all stars to get the total orbital density $\rho_A[j]$ in that cell.

$$\rho_A[j] = \frac{1}{M \cdot t} \sum_{i=1}^M A[i, j]. \quad (9.2)$$

$M \cdot t$ is the total amount of time that has been used integrating all M stars. Through the division one makes sure to have the density as a normalized, unitless quantity that can then be compared to the observed density $\rho_{obs}[j]$.

Now the χ^2 can be computed according to

$$\chi^2 = \sum_{j=1}^N N \frac{(\rho_{obs}[j] - \rho_A[j])^2}{\rho_{obs}[j]}, \quad (9.3)$$

where we have assumed Poissonian errors for the observed densities.

The goal is to obtain the best-fitting parameters (z_{fit}, k_{fit}) that minimize χ^2 in subsequent iterations of steps ii to iv. This is a classical nonlinear least squares problem and can be solved using one of the standard methods such as a Levenberg-Marquart algorithm (e.g. Press, 2002). During the iterations the initial values for the integrations (z_{obs}, W_{obs}) remain fixed, because they represent the state of equilibrium that underlies the method.

A first guess of the fit-parameters is not always straightforward, especially if the potential should be expressed as a spline function of order ≥ 3 . It can be useful to consult recent estimates of K_z (e.g. Holmberg and Flynn, 2000, Figure 4) and draw some test- K_z curves for different combinations of the fit-parameters.

To investigate the performance of our method in dependence of variables like the number of stars in the sample, we chose to create artificial data of which the phase space distribution is analytically known. These tests will be described in the next section.

9.2 Validity of the New Method

9.2.1 The Disk Models

To test the validity of our method, we use two disk models for which the phase space distribution function $f(z, W)$ and the gravitational potential $\Phi(z)$ are analytically known. If we use $\Phi(z)$, which depends on two parameters, as the test potential, the best fit should yield the parameters that have been used for the set-up of the artificial data.

The disk models we use are Spitzer's isothermal (Spitzer, 1942) and Camm's (Camm, 1950) disk models. For the isothermal disk the potential-density pairs and the distribution function are given as

$$\Phi(z) = k_z z_0 \ln \left(\cosh \left(\frac{z}{z_0} \right) \right) \quad (9.4a)$$

$$\frac{d\Phi}{dz} = k_z \tanh \left(\frac{z}{z_0} \right) \quad (9.4b)$$

$$\rho(z) = \rho_0 \cosh^{-2} \left(\frac{z}{z_0} \right); \quad \rho_0 = \frac{k_z}{4\pi G z_0} \quad (9.4c)$$

$$f(W, z) = f(W|z)\rho(z) = \frac{\rho_0}{\sqrt{\pi k_z z_0}} e^{-\frac{W^2}{k_z z_0}} \cosh^{-2} \left(\frac{z}{z_0} \right). \quad (9.4d)$$

For Camm's disk we have

$$\Phi(z) = k_z \sqrt{z_0^2 + z^2} \quad (9.5a)$$

$$\frac{d\Phi}{dz} = k_z \frac{z}{\sqrt{z_0^2 + z^2}} \quad (9.5b)$$

$$\rho(z) = \rho_0 \frac{z_0^3}{(z_0^2 + z^2)^{3/2}}; \quad \rho_0 = \frac{k_z}{4\pi G z_0} \quad (9.5c)$$

$$f(W, z) = f(W|z)\rho(z) = \frac{15}{16\sqrt{2}} k_z^3 \rho_0 \left(\frac{W^2}{2} + \Phi(z) \right)^{-\frac{7}{2}}. \quad (9.5d)$$

Choosing the parameters z_0 and k_z in units of kpc and kpc/Gyr² together with $4\pi G = 56.73 \cdot 10^3 \text{ pc}^3 \text{ M}_\odot^{-1} \text{ Gyr}^{-2}$ yields the density in [$\text{M}_\odot \text{ pc}^{-3}$].

Given the phase space density $f(W, z)$ it is possible to create a Monte Carlo sample of stars having initial positions and velocities (z_{ini}, W_{ini}) .

Figure 9.1 shows the initial density distribution of a sample of 10^5 stars in the isothermal and Camm's disk, respectively. The blue curves are the analytical

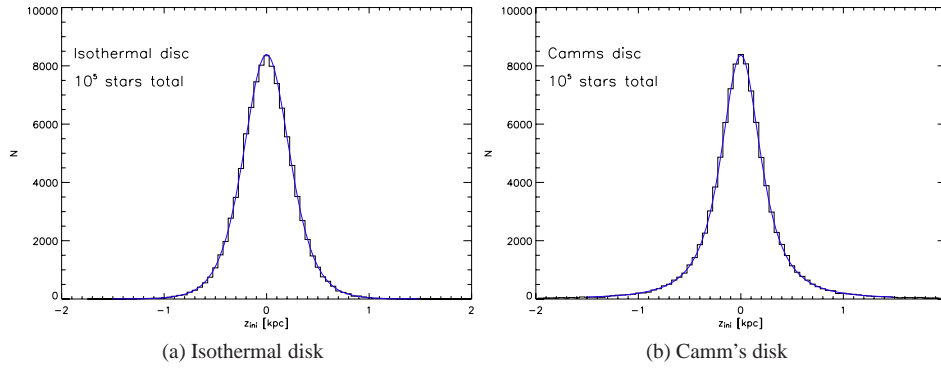


Figure 9.1: Density distribution ρ_{obs} of 10^5 stars in the isothermal and Camm's disk. The solid blue curve displays the exact density, given through Equations (9.4c) and (9.5c), respectively.

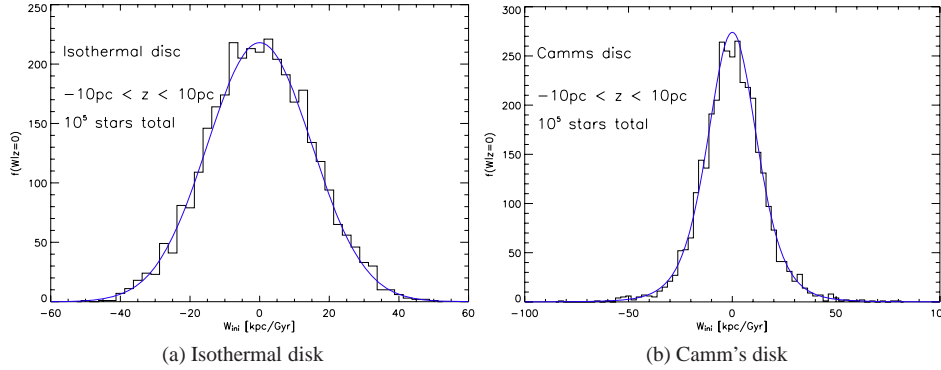


Figure 9.2: Initial velocity distribution at the midplane of all stars satisfying $-10pc < z_{ini} < 10pc$. The stars belong to a sample of 10^5 stars that have been drawn randomly in the isothermal and Camm's disk potential. The solid blue curve displays the exact distribution function given through equations (9.4d) and (9.5d), respectively.

density distributions given through Equations (9.4c) and (9.5c). They fit very well the distribution of stars that have been randomly drawn from our disk models.

The distributions of initial velocities at the midplane are shown in Figure 9.2. Again, the theoretical distributions $f(W|z=0)$, which are given through Equations (9.4d) and (9.5d), fit the data very well. This proves that the set-up of initial conditions in our two disk models is correct.

With the knowledge of the parameters (z_0, k_z) of the potential and distribution function of a sample of stars we can try to use the same potential with modified parameters to integrate the stars and see if minimization of the χ^2 (equation 9.3) yields the original parameters.

9.2.2 Direct Comparison of the Analytical and Orbital densities

We set the potential parameters (z_0, k_z) to $(0.3 \text{ kpc}, 1500 \text{ kpc/Gyr}^2)$ and use them for both the set-up of the initial conditions and integration of the stars. This choice of (z_0, k_z) gives a local mass density of $0.088 \text{ M}_\odot \text{ pc}^{-3}$, which agrees with recent

estimates of the volume density of visible disk matter (Flynn and Fuchs, 1994; Creze et al., 1998; Holmberg and Flynn, 2000). In all following tests we use a leap frog integrator with time steps of $dt = 0.01$ Myrs and a total integration time of $t = 2.0$ Gyr. During this time the typical number of oscillations a star performs is ≈ 15 in both disk models. We further set the thicknes of the cells along the z -axis to 50 pc.

In Figure 9.3 we show the conservation of energy of a typical star for different time steps (in Gyr). For both potentials a time step of 0.01 Myr is a good compromise between accuracy and faster computing time. After each integration step of the i th star the density array $A[i, j]$ gets increased by the fraction of time the star has spent in cell j (for $j > 0$, see step iii in Section 9.1). This is a little bit more complicated than just increasing $A[i, j]$ by dt if the i th star is in cell j after one integration step, but ensures that no entries into $A[i, j]$ get missed even if a star "leaps" over a cell (especially near the midplane where stars have their highest velocities).

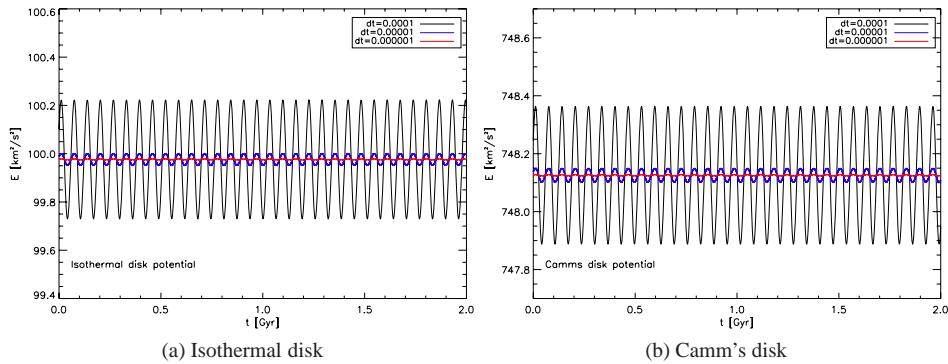


Figure 9.3: Evolution of the energy E of one randomly chosen star while orbiting in the isothermal and Camm's disk potentials, respectively, for different integration time steps. The time steps are given in Gyr. Note the difference of energy of the star in the two different potentials.

After all M stars have been integrated for the time t , the total orbital density in each cell $\rho_A[j]$ can be calculated through equation 9.2; we compare this density with the normalized column density in each cell which is given through

$$\rho_{obs}[j] = \left[2 \int_0^\infty \rho(z) dz \right]^{-1} \int_{(j-1)d}^{jd} \rho(z) dz. \quad (9.6)$$

The integration is made from the lower cell boundary at $(j - 1)d$ to the upper boundary at jd , where d is the thicknes of the cells. We divide through the total density to normalize $\rho_{obs}[j]$ and make it unitless. Inserting the expressions for the densities in the isothermal and Camm's disk, respectively, (equations 9.4c

and 9.5c) leads to:

$$\rho_{obs}[j] = \frac{1}{2} \left[\tanh\left(\frac{z}{z_0}\right) \right]_{(j-1) \cdot d}^{j \cdot d} \quad (\text{Isothermal disk}) \quad (9.7)$$

$$\rho_{obs}[j] = \frac{1}{2} \left[\frac{z}{\sqrt{z^2 + z_0^2}} \right]_{(j-1) \cdot d}^{j \cdot d} \quad (\text{Camm's disk}) \quad (9.8)$$

In Figure 9.4 we show the result of performing our method on a set of 1000, 5000 and 20000 stars, respectively. The red and black lines trace the orbital and analytical densities $\rho_A[j]$ and $\rho_{obs}[j]$, respectively, along increasing cell numbers. For the smallest sample of 1000 stars some discrepancies are visible in both disk models, particularly in the very first cells; in case of the isothermal disk they vanish as the sample size increases. For Camm's disk, however, discrepancies remain and we will come back to this issue later.

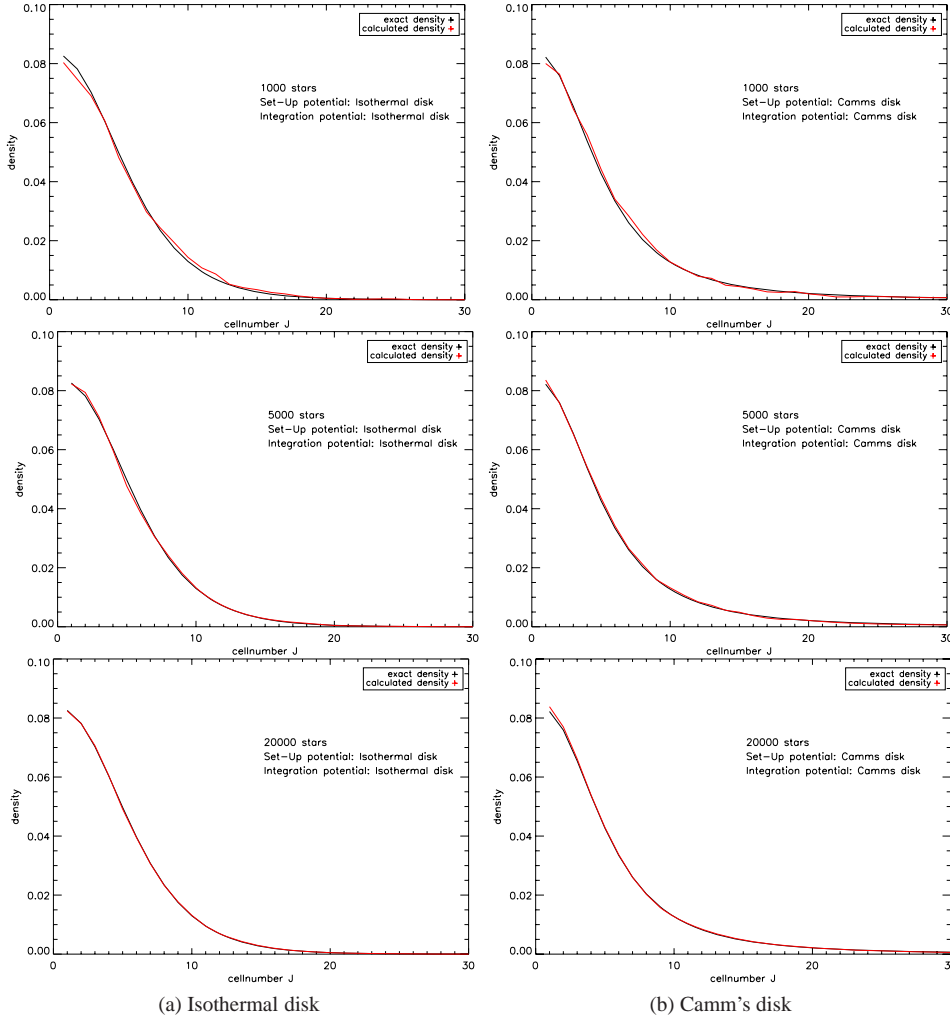


Figure 9.4: Comparison between orbital densities $\rho_A[j]$ and analytical densities $\rho_{obs}[j]$ if the test potential is equal to the set-up potential. The thickness of each cell is 50 pc and the cell number increases with increasing vertical distance z .

It seems that the number of stars in the small sample is not large enough to fully represent an equilibrium distribution corresponding to the chosen disk model after the set-up of initial conditions. This is also supported by Figure 9.2.2, where we show two density comparisons for Camm’s disk which were obtained using the same number of stars and same potential parameters. The only difference was the choice of the seed for the random number generator that is used to set up the initial conditions. This shows that poor statistics can cause discrepancies between the orbital and analytical density distribution and a large number of stars is important. Finally, we show in Figure 9.6 that a variation of the parameters of the test

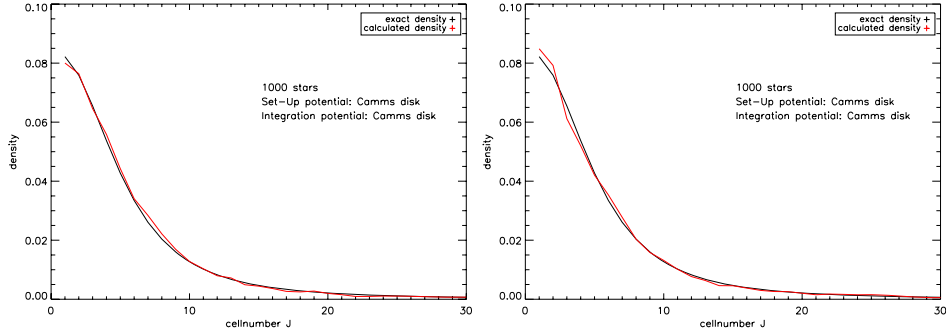


Figure 9.5: The two plots compare the orbital and analytical densities for 1000 stars each and the same potential parameters respectively, but different seeds to initialize the random number generator. 1000 stars might be too few to create an equilibrium distribution according to the chosen disk model.

potential compared to the set-up potential leads to an aggravation of the density fit. The left column shows the results when the set-up and test parameters are chosen as before as $(z_0, k_z) = (0.3 \text{ kpc}, 1500 \text{ kpc/Gyr}^2)$, while for the right column the test parameters were changed to $(0.4 \text{ kpc}, 1400 \text{ kpc/Gyr}^2)$. The upper and lower panels are valid for the isothermal and Camm’s disk potential, respectively (Equations 9.4a and 9.5a). The number of stars in all cases was 5000, and the set-up of initial conditions was performed using the same seed number. It is obvious that integration of the stars in the potential that not correlates to their dynamical equilibrium state leads to sub-optimal results. A least squares algorithm can be used to find out the best fitting parameters.

9.2.3 Least Squares Fitting in a Grid of Parameter Space

For only two test potential parameters it is possible to calculate the χ^2 for each pair of $(z_{\text{fit}}, k_{\text{fit}})$ on a grid in parameter space. Regions in this space where the χ^2 has a minimum give the combination of parameters that best resemble the potential in which stars have settled.

In Table 9.2.3 we show the χ^2 values that have been obtained using an isothermal disk potential for both the set-up and integration of 10,000 stars. The parameters of the set-up potential have been chosen as $(z_0, k_z) = (0.3 \text{ kpc}, 1500$

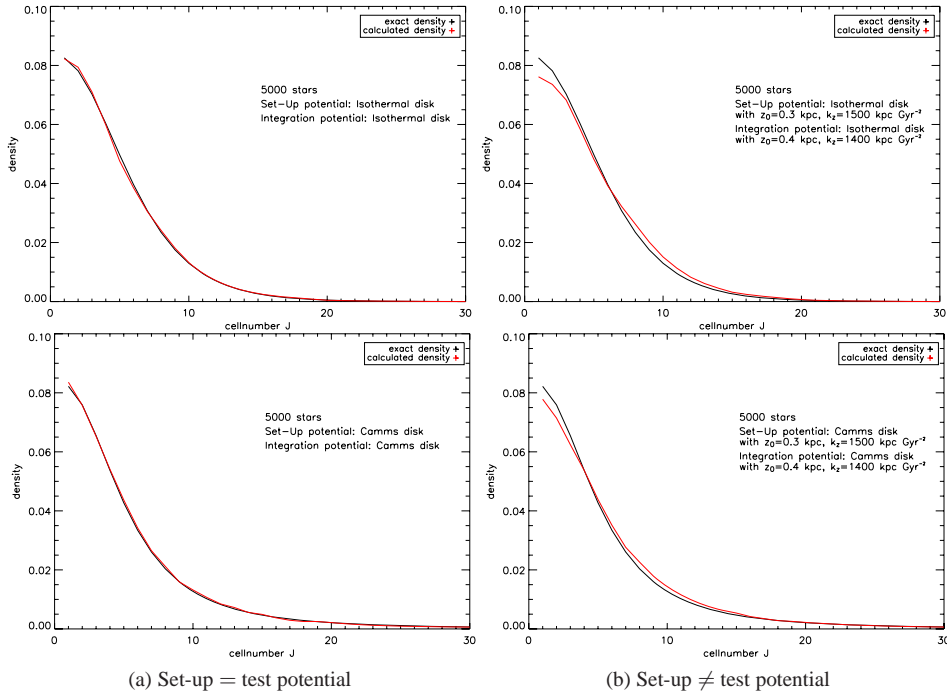


Figure 9.6: Comparison of orbital densities $\rho_A[j]$ with analytical densities $\rho_{obs}[j]$. *Left panels:* Test potential and set-up potential are equal. *Right panels:* Test potential and set-up potential belong to the same disk model, but have different potential parameters.

kpc/Gyr²) and the stars have been integrated in isothermal disk potentials

$$\Phi(z) = k_{\text{fit}} z_{\text{fit}} \ln\left(\cosh\left(\frac{z}{z_{\text{fit}}}\right)\right)$$

with various values for $(z_{\text{fit}}, k_{\text{fit}})$ and a cell thickness of 25 pc. We plot contours of the χ^2 values from Table 9.2.3 in the left panel of Figure 9.7.

Similarly, we have set up 10,000 stars in Camm's disk potential with parameters $(z_0, k_z) = (0.3 \text{ kpc}, 1500 \text{ kpc/Gyr}^2)$ and integrated them in Camm's disk potentials

$$\Phi(z) = k_{\text{fit}} \sqrt{z_{\text{fit}}^2 + z^2}$$

with various values for $(z_{\text{fit}}, k_{\text{fit}})$. The results are plotted in the right panel of Figure 9.7.

From Figure 9.7 it seems that there is a big difference between the two models: While for the isothermal disk the potential underlying the stellar distribution gets recovered to high accuracy, in case of Camm's disk a wrong potential is predicted. We have already checked that the set-up of initial positions and velocities is correct (Figures 9.1 and 9.2) using 100,000 stars. On the other hand we have seen that 1000 stars in Camm's disk were not enough to create an equilibrium distribution according to the chosen disk model (Figure 9.2.2). The results we will obtain in the next section strongly argue that the set-up of the stars in Camm's disk does not produce an equilibrium distribution, even for 100,000 stars.

$k_{\text{fit}}/z_{\text{fit}}$	1000	1100	1200	1300	1400	1500	1600	1700	1800	1900	2000	2100
0.1	735	407	317	357	466	622	804	1000	1200	1407	1610	1810
0.15	754	343	189	177	243	362	512	681	857	1040	1227	1414
0.2	920	397	157	81	93	169	280	415	564	720	884	1049
0.255	1240	581	239	80	30	53	119	217	332	462	603	745
0.3	1727	890	430	178	57	19	37	91	170	270	379	499
0.35	2367	1328	730	370	166	64	28	36	76	139	221	313
0.40	3141	1885	1135	660	360	183	87	48	46	73	121	187
0.45	4075	2570	1635	1035	634	377	214	119	74	64	78	113
0.5	5162	3373	2239	1500	987	641	406	251	157	105	85	90
0.55	6395	4298	2952	2037	1412	974	661	442	292	196	138	111
0.60	7810	5353	3745	2671	1913	1365	977	688	482	335	236	173
0.65	9397	6517	4660	3388	2478	1828	1341	990	718	523	377	275

Table 9.1: Values of $10^4\chi^2$ for different combinations of z_{fit} and k_{fit} after integration of 10000 stars in an isothermal disk potential. The initial density distribution of stars was chosen according to an isothermal disk with parameters $(z_0, k_z) = (0.3 \text{ kpc}, 1500 \text{ kpc/Gyr}^2)$.

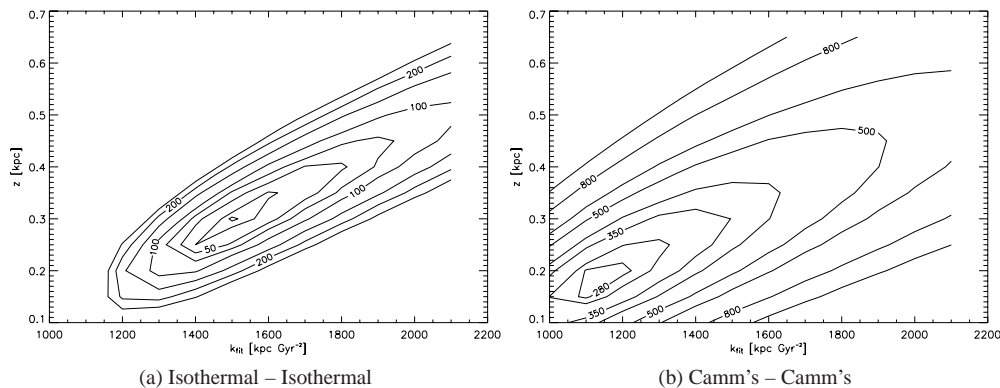


Figure 9.7: Contours of $10^4\chi^2$ values that have been obtained after setting up and integrating 10,000 stars in potentials from the same disk models (*left panel*: isothermal disk, *right panel*: Camm's disk). The χ^2 values from the left panel are also given in Table 9.2.3.

We conclude that our method is able to reproduce the potential that underlies an equilibrium distribution of disk stars. The condition of an equilibrium distribution is vital for the success of the method. For the isothermal disk it seems that $\sim 10,000$ stars are enough to produce an equilibrium distribution, but for Camm's disk still 20,000 (or even 100,000, see next section) stars do not suffice. The detailed reason for this remains unclear.

In the next section we finally progress to a more general routine, in which we use a Levenberg-Marquart algorithm (e.g. Press, 2002) to minimize the χ^2 values.

9.2.4 Least Squares Fitting Using a Levenberg-Marquart Algorithm

We finally test if we are able to recover the set-up potential using the Levenberg-Marquart routine "leasqr" which is implemented in the freely available script language Octave.² This routine uses a function "dfdp" which numerically calculates

²available from <http://www.gnu.org/software/octave/>

partial derivatives of the orbital densities $\rho_A[j]$ with respect to the fitting parameters. These derivatives are used to determine the gradient in the space of the fit parameters and to adjust the increase or decrease of each fit parameter for the next step. Each step consists of assigning the new fit parameters to our C++ routine³, integrating all stars in the corresponding fit potential and evaluating the χ^2 through comparison of the analytical and the orbital densities. The routine "leasqr" stops if convergence of χ^2 to a minimum is achieved.

We used either the isothermal disk or Camm's disk with parameters $(z_0, k_z) = (0.3 \text{ kpc}, 1500 \text{ kpc/Gyr}^2)$ respectively as the set-up potential and the same disk model as the fit potential with a first guess of $(z_{\text{fit}}, k_{\text{fit}}) = (0.5 \text{ kpc}, 1200 \text{ kpc/Gyr}^2)$ for the fitting parameters. The cell thickness has been chosen as 20 pc and we used 0.01 Myr for each time step.

For the case of the isothermal disk the accuracy to which the set-up parameters can be reproduced strongly depends on the number of stars. This is shown in Table 9.2 where we have listed the number of stars that have been set up, the best-fitting parameters and the number of iterations until convergence was achieved. The recovery of the scale-height z_0 is accurate to within 94.6%, 99.5% and 100% for samples of 10000, 50000 and 100,000 stars, respectively. However, even for the sample of 100,000 stars, the routine does not converge towards the "real" slope of the K_z -force, $k_z = 1500 \text{ kpc/Gyr}^2$. Here, the accuracy of the best-fit value is 96.9%. The resulting $K_z(z)$ - and $\rho(z)$ -curves for the sample with 100,000 stars are shown in Figure 9.8 for both disk models.

	No. of stars	Best fit parameters		No. of iterations
		z_{fit}	k_{fit}	
Isothermal disk	1000	0.2513	1341.9	90
	10000	0.3169	1432.1	55
	50000	0.3015	1444.2	68
	100000	0.3000	1454.2	50
Camm's disk	1000	0.1711	1249.3	100
	10000	0.2128	1200.9	50
	50000	0.2000 ^a	1174.4 ^a	22 ^a
	100000	0.1913	1116.8	25

^a Segmentation fault occurred after 22 iterations

Table 9.2: Results of testing the self-consistency of the isothermal disk and Camm's disk models, respectively.

The results for Camm's disk are worse: it is not possible to constrain any of the two potential parameters to an accuracy better than $\sim 75\%$. It is also strange that the largest sample of stars yields best-fit parameters that are even farther away from the true values. One could think of the Levenberg-Marquart routine getting trapped in a local minimum and the step size being too small to get out again.

³kindly adjusted by Robert Schmidt

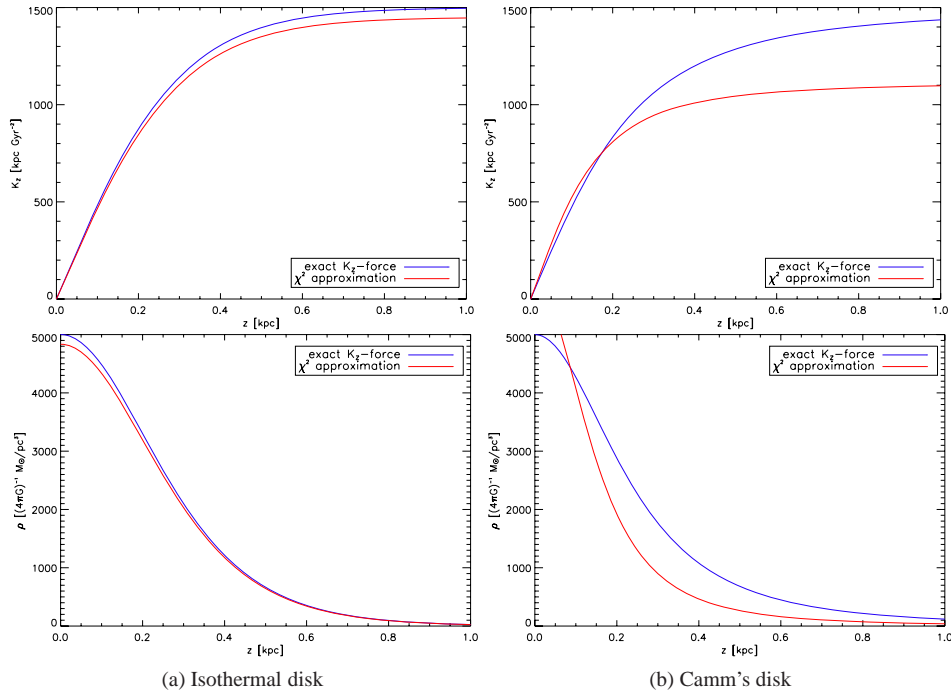


Figure 9.8: Comparison between the forces $K_z(z)$ and densities $\rho(z)$ of the two disk models with parameters $(z_0, k_z) = (0.3 \text{ kpc}, 1500 \text{ kpc/Gyr}^2)$ and those derived from the best-fit parameters that have been obtained by the Levenberg-Marquart routine. The best-fit parameters are those given in Table 9.2 when 100,000 stars are used.

However, the location in $(z_{\text{fit}}, k_{\text{fit}})$ -space where the minimum of χ^2 occurs is comparable to that obtained in the previous section where we computed the χ^2 -values on a discrete $(z_{\text{fit}}, k_{\text{fit}})$ -grid. So the problem seems to be more related to the set-up of the stars, which could not be able to produce a dynamical equilibrium distribution. Also for the isothermal disk the agreement with the contours in Figure 9.7 is good, even though not perfect; the χ^2 -contours suggest the minimum to be located at $k_{\text{fit}} \simeq 1500 \text{ kpc/Gyr}^2$. It is possible that the gradient at $(z_{\text{fit}}, k_{\text{fit}}) \approx (0.3, 1450)$ is not steep enough to cause further changes in the parameters by the routine. In this case it could also be possible that the results would be different, if the minimum is approached from a different direction of parameter space. To test this hypothesis, we could choose different starting parameters for $(z_{\text{fit}}, k_{\text{fit}})$ and see how the results change.

9.3 Approximation of the True K_z -force by a Higher-Parameter Spline Function

9.3.1 The Fourth-order Spline Function

Motivated by the good recovery of the isothermal disk's scale height, we now try to fit a four-parameter spline function to the isothermal disk's potential. We

characterize this spline function through:

$$K_z = k_{\text{fit}} \frac{z + az^3}{1 + b|z| + c|z|^3} \quad (9.9)$$

We first try to get an idea of a realistic choice for $(a, b, c, k_{\text{fit}})$. Therefore we use the data of the vertical force $K_z(z)$ from Flynn and Fuchs (1994) and fit a spline curve to this data using the Gnuplot software.⁴ The result is shown in Figure 9.9. The parameters $(a, b, c, k_{\text{fit}}) = (1.13\text{kpc}^{-2}, 3.96\text{kpc}^{-1}, 3.33\text{kpc}^{-3}, 6441\text{Gyr}^{-2})$ provide a very good fit to the data. This shows that a four-parameter spline function such as that described by equation 9.9 can be used to approximate the vertical K_z -force law.

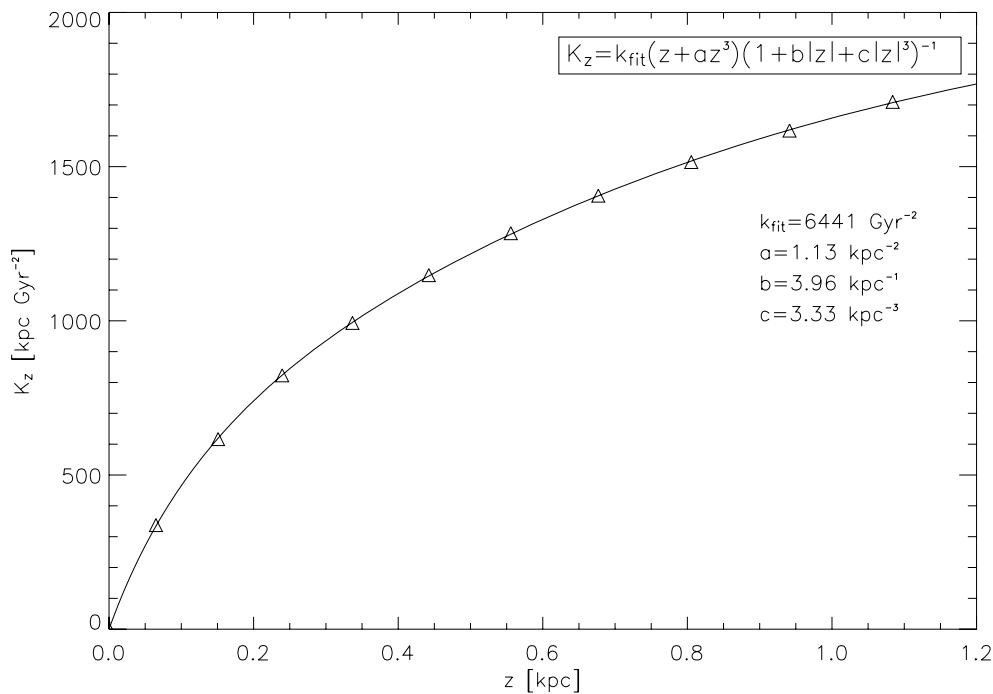


Figure 9.9: Best-fit of a four-parameter spline function to the data points taken from Flynn and Fuchs (1994). The best-fitting parameters are given in the figure; their meaning follows from equation 9.9.

Now we try to obtain the best-fitting spline function to an isothermal disk with parameters $(z_0, k_z) = (0.3 \text{ kpc}, 1500 \text{ kpc/Gyr}^2)$. On the basis of the spline-parameters that yield good fits to realistic observations, we start with a first guess of $(a, b, c, k_{\text{fit}}) = (1.0\text{kpc}^{-2}, 5.0\text{kpc}^{-1}, 5.0\text{kpc}^{-3}, 7000\text{Gyr}^{-2})$. We use 5000 stars representing an isothermal disk in dynamical equilibrium and change the Levenberg-Marquart algorithm to fit four parameters simultaneously. The routine converges to the parameters $(a, b, c, k_{\text{fit}}) = (0.99\text{kpc}^{-2}, 3.84\text{kpc}^{-1}, 6.09\text{kpc}^{-3}, 7432\text{Gyr}^{-2})$, which yield the K_z -force shown as the red solid curve in Figure 9.3.1.

⁴available from <http://www.gnuplot.info/>

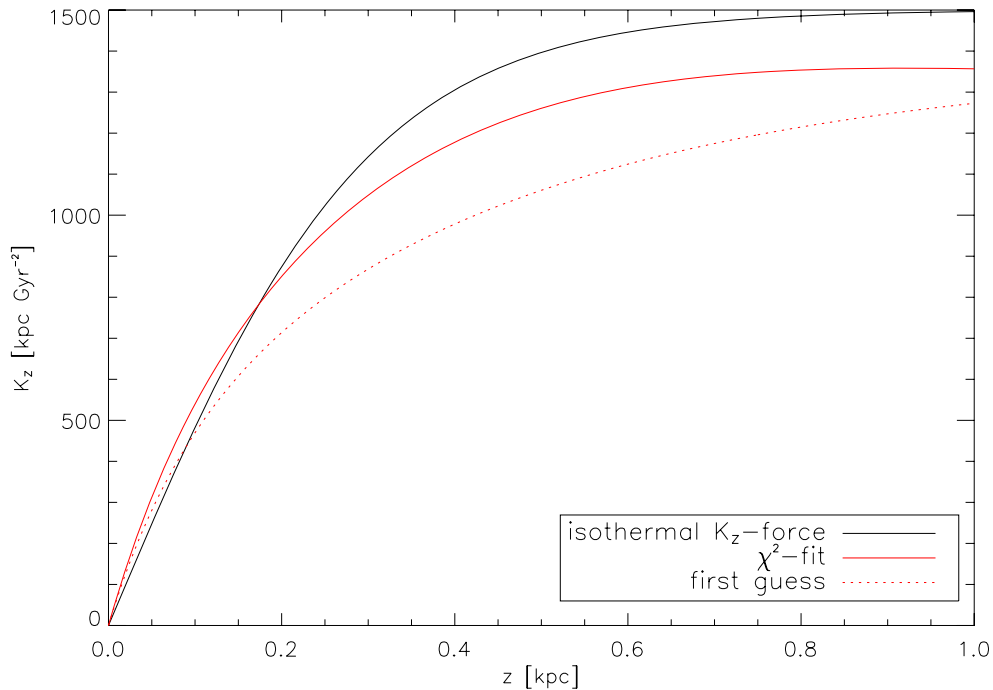


Figure 9.10: K_z -force of the isothermal disk with $(z_0, k_z) = (0.3 \text{ kpc}, 1500 \text{ kpc/Gyr}^2)$ (*black line*), and the input (*red dotted line*) and output (*red solid line*) spline functions of the Levenberg-Marquart routine.

The routine fails in reproducing the K_z -force law of the isothermal disk (*black line*), although the best-fit curve stays closer to the requested trend for $z \gtrsim 0.15$ kpc than the first guess (*red dotted line*). However, it is a general question whether there exists a set of spline parameters that is able to reproduce the trend of the isothermal K_z -force. The isothermal disk is a theoretical construct which is not able to describe the data shown in Figure 9.9, in contrast to the spline function.⁵ Then the problem would not be a fundamental problem of our method per se, nor the Levenberg-Marquart routine, but the fact that we try to fit two functions that have no intersection in their parameter space.

9.4 Conclusions

We described a new method which tries to reproduce an observed density distribution through integration of stellar orbits in a test potential. The underlying assumption is that the density distribution that is generated through the star's orbits matches the observed distribution, if the test potential represents the true one. As the observed density distribution we created Monte Carlo samples of stars that represent the dynamical equilibrium of two theoretical disk models: Spitzer's isothermal (Spitzer, 1942) and Camm's disk (Camm, 1950). These have the advantage that their density distribution and potential are analytically known.

⁵We tried to fit an isothermal disk to the data points with Gnuplot, but no solution exists.

First tests showed that a large sample of randomly drawn stars ($N = 100,000$) is able to fully reproduce the underlying density distribution (Figures 9.1 and 9.2). The idea for testing the validity of our method was to take a sample of stars of which we know the underlying disk model potential and use the same disk model, but with different parameters, as the test potential. Iterative χ^2 -fitting should then lead to the original disk parameters. The outcomes of this test can be summarized as follows:

1. A large sample size ($N \gtrsim 10,000$) is required in order to create an equilibrium distribution according to the chosen disk model. For example, different seeds that initialize the random number generator can have a strong effect on the outcome of the fitting procedure (Figure 9.2.2).
2. If the test potential is equal to the set-up potential, the orbital and analytical densities match well for a large enough sample size (Figure 9.4).
3. If the test potential is not equal to the set-up potential, the orbital and analytical densities do not match, irrespective of the sample size (Figure 9.6).
4. The outcome of a direct comparison between the χ^2 -values that are obtained when the test potential parameters run through a grid in $(z_{\text{fit}}, k_{\text{fit}})$ -space depends on the chosen disk model (Figure 9.7): in case of the isothermal disk, the minimum occurs at the position of the set-up parameters (z_0, k_z) , as expected. For Camm's disk the location of the minimum predicts a wrong potential.
5. Instead of comparing the χ^2 -values in a grid of $(z_{\text{fit}}, k_{\text{fit}})$ -space, we used a Levenberg-Marquart algorithm to minimize the χ^2 by simultaneously altering the test potential parameters. The results were similar to those obtained from the discrete χ^2 -values and showed again a strong dependence on the chosen disk model: for the isothermal disk, the accuracy to which the set-up parameters could be reproduced increases with the number of stars and reaches a 100% match of the scale height z_{fit} for $N = 100,000$ stars. However, the accuracy to which the slope k_{fit} could be reproduced was not better than 96.9%. For Camm's disk the predicted potential again was completely wrong. We currently don't know what the reason for this problem is, but most likely the initial set-up of the stars does not create an equilibrium distribution, like also suggested by the results described in the previous point.
6. We also obtained a negative result in trying to use a four-parameter spline function as the test potential and reproduce the K_z -curve of the isothermal disk. However, the isothermal disk model was not able to fit the K_z -data points from Flynn and Fuchs (1994), while the four-parameter spline function yielded a very good fit. It is therefore possible that there exists no set of spline parameters that is able to yield a fit to the isothermal disk model.

In summary, we have reason to believe that our new method works in principle, but before it can be applied to real data the following questions have to be answered: Why does Camm's disk fail any self-consistency test? Is it because the set-up of stars does not produce an equilibrium distribution? Does such an equilibrium even exist for Camm's disk? Is the Levenberg-Marquart-routine working reliably, or does it stop too early if the χ^2 -gradient in parameter space gets too shallow? What is the influence of the "first guess" parameters on the outcome of the χ^2 minimization? Can we test the performance of another spline function that is able to fit the isothermal disk model? We will aim at answering these questions in future studies to have a reliable method available for the large data sets of future surveys, in particular that of the GAIA mission (Lindegren and Perryman, 1996).

Part IV

Summary and Outlook



The phase-space distribution of Milky Way stars encodes enormous amounts of information on the dynamical state and pre-history of the Milky Way. Motivated by the presently available and future large datasets that provide 6D phase space information for an increasing fraction of the Milky Way's stellar populations, we explored practical ways to find substructure (streams, or moving groups) in the Solar neighborhood. Moving groups emerge for one of the following reasons: the simplest case is an agglomeration of stars that have been born in the same molecular cloud and only recently dissolved. In this case the stars keep on moving in the direction of the once bound cluster, until phase-mixing washes out their common signature. The other scenario is a tidally disrupting cluster or satellite galaxy which places its debris on similar orbits. Such stellar streams can appear as moving groups in the phase-space distribution of nearby stars even several Gyr after their disruption. The third possibility are stars that have been trapped around resonant orbits in the rest frame of periodic perturbations of the otherwise axi-symmetric potential. Such perturbations include the Galactic bar and spiral waves and will group together field stars in (U, V) -space.

It follows that stellar streams are detectable as moving groups in velocity space, independent of their origin. An even better approach to find stellar streams would be in the space of integrals of motion, which are immune to phase-mixing. In practice, however, the integrals of motion are not uniquely defined, because the potential is not known exactly. Further, the error bars on 6D measurements are drastically "anisotropic". We therefore want to develop search strategies in a modified integrals-of-motion-space that match the data and error bars.

We found that the orbits of stars can be described by the effective integrals of motion angular momentum, eccentricity and orbital inclination. For nearby stars ($d \lesssim 2$ kpc) we approximate these integrals by $V_{\text{az}} = \sqrt{(V + V_{\text{LSR}})^2 + W^2}$, $V_{\Delta E} = \sqrt{U^2 + 2(V_{\text{az}} - V_{\text{LSR}})^2}$ and $\nu = \arctan \frac{V}{W}$, respectively. We confirmed through basic tidal stream simulations that – even if there is no spatial coherence left – streams form clumps in this projection of phase-space. This is also the case for eccentricities $e > 0.5$, where the approximation of e through $V_{\Delta E}$ formally breaks down. Our procedure consists of sorting the stars into different ν -slices and in each slice search for overdensities in the $(V_{\text{az}}, V_{\Delta E})$ -distribution of stars. To make such overdensities more identifiable, we apply a wavelet transform with a modified two-dimensional Mexican-hat kernel as the analyzing wavelet. We estimate the statistical significance of the overdensities through Monte Carlo simulations drawn from a three-component Schwarzschild distribution. These three components represent the halo, thin disk and thick disk, and their fraction depends on the metallicity range we consider.

As a first application, we searched for stellar streams in a set of 7015 stars from the first RAVE public data release. Assuming that the stars move on disk-like orbits under the influence of an axisymmetric potential, we detected three already known stellar streams and one candidate for a newly discovered stream as overdensities in $(V, \sqrt{U^2 + 2V^2})$ -space. The latter is present as a broad feature centered at $V \approx 60$ km s⁻¹, and has $(V_{\text{az}}, V_{\Delta E}, \nu) \approx (135$ km s⁻¹, 122 km s⁻¹, 30°).

The other moving groups are the Sirius stream at $V \approx +4 \text{ km s}^{-1}$, the Hercules stream, centered at $V \approx -65 \text{ km s}^{-1}$, and the stream discovered by Arifyanto and Fuchs (2006) and Helmi et al. (2006) at $V \approx -100 \text{ km s}^{-1}$. Although for disk stars there is no one-to-one projection of features from $(V, \sqrt{U^2 + 2V^2})$ -space into (L_z, L_\perp) -space, we found that the dynamical thin/thick-disk streams and the presumable halo streams also form clumps in (L_z, L_\perp) -space.

This justifies the approach to more generally assume a spherical potential and to use $(V_{\text{az}}, V_{\Delta E}, \nu)$ for orbits with arbitrary inclination angles. Using this generalization, we searched for stellar halo streams in a sample of 22,321 SEGUE stars from the seventh SDSS data release. We derived distances to all stars by using the photometric parallax relation and its [Fe/H]-correction term given in Ivezić et al. (2008). Through a comparison with 15 cluster fiducial sequences from An et al. (2008) and Clem et al. (2008), we derived that the distances get systematically under-estimated by a factor below 5%, less than half of the average statistical error. We also showed that the systematic distance errors have no influential effect on our results. To use the available kinematic and chemical informations in the best way, we binned the stars into twelve overlapping ν -slices of 30° width, and made use of the [Fe/H]-estimates by dividing the sample into four metallicity sub-samples in the ranges [Fe/H] = $-0.5 \dots -1.0$, $-1.0 \dots -1.5$, $-1.5 \dots -2.0$ and [Fe/H] ≤ -2.0 . The metallicities provide a new "dimension" in parameter space that is suited well to distinguish tidal streams from those of dynamical origin, or even overdensities that have emerged through Poisson noise. In each metallicity sub-sample and all ν -slices we independently search for overdensities in $(V_{\text{az}}, V_{\Delta E})$ -space. Besides the smooth component of the thick disk, the fraction of which remains constant below [Fe/H] ~ -1.5 , we find a richly sub-structured phase-space distribution of stars. The amount of sub-structure increases with decreasing metallicity. At least three previously detected halo streams are also present in the SDSS sample: first, the new stream found in the RAVE data, which has a metallicity distribution broadly peaked around [Fe/H] ≈ -1.4 . Second, the stream 'S₃' found by Dettbarn et al. (2007), which peaks around [Fe/H] ≈ -1.5 . Third, we find as a highly significant ($\sigma > 10$) feature the stream which has been originally detected by Helmi et al. (1999). Besides these already known features, we find at least four new genuine halo streams (judged by their kinematics and [Fe/H]), to which we can assign unambiguously peaked [Fe/H]-distributions.

In summary, we have demonstrated the practical power of our method to detect substructure in the phase-space distribution of nearby stars belonging to all three stellar components. Our method is a very practical way to use the observables of stars (contained in U, V, W) and account for their errors. Therefore, we do not need to make a priori assumptions about the form of the gravitational potential. Through only one data set of 22,321 stars we have increased the number of genuine halo streams in the Solar vicinity by five. Further detections are expected as new data samples become available. Recently, for example, the second data release of RAVE became available (Zwitter et al., 2008), containing radial velocities and stellar parameters for 49,327 and 21,121 stars, respectively. The goal of

this ambitious project is to increase these numbers up to one million and to make available the most detailed phase-space map of the stellar populations in the Milky Way. We are now at a transition, where data and tools are in place and "many" new substructures are being found and discussed individually. In this context the next step would be to also incorporate age determinations into search strategies. In the future, these search techniques must then be applied in the same way to artificial data from dynamical and/or hierarchical models in order to compare the observations statistically to model expectations.

Future data sets will also provide large enough samples to study the local gravitational potential of the disk to higher accuracy and to larger distances than previous samples allowed. An important assumption in this context is that there exists an effective integral of motion depending only on z and W , because the phase-space density depends on the integrals of motion under the assumption of a dynamical equilibrium. We have shown that such an integral exists in the form of the adiabatic integral of the vertical motion (equation 4.78). We have conducted a preparatory study in the context of GAIA to reproduce an observed density distribution of disk stars through integration of the stellar orbits in a test potential. The validation on two theoretical disk models, Spitzer's isothermal disk (Spitzer, 1942) and Camm's disk (Camm, 1950), resulted in two main problems that still have to be fixed: first, it is not clear if we can create Monte Carlo samples of stars that represent a dynamical equilibrium distribution in Camm's disk. Second, we have to check whether the "first guess" of the potential parameters in the χ^2 -minimization routine (a Levenberg-Marquard algorithm) can have an influence on the results. Third, we need a spline function that is flexible enough to match the isothermal disk potential. For the latter we were able to reproduce the scale height and slope parameter to 100% and 96.9%, respectively, for a sample of $N_{100,000}$ stars. This shows, in principle, that our method is able to derive the potential from the motion of stars.

We will address the problems that still exist in future work and hopefully apply this method to the large data sets that currently are available (RAVE, SDSS). The long-term goal is to extend it towards the 2D case, that is, we try to reproduce the observed two-dimensional density distribution of stars by integrating them in a two-dimensional test potential with various parameters that will be constrained by iterative χ^2 -fitting. Ultimately, GAIA will provide the ideal sample of relaxed (late-type) stars to measure the two-dimensional potential on kpc scale.

All these strands of research show, that the 'fine-grain' phase-space structure of the Milky Way stars is now emerging as a promising and productive research field.



Appendix A

Bibliography

Bibliography

- M. G. Abadi, J. F. Navarro, M. Steinmetz, and V. R. Eke. Simulations of Galaxy Formation in a Λ Cold Dark Matter Universe. I. Dynamical and Photometric Properties of a Simulated Disk Galaxy. *ApJ*, 591:499–514, July 2003a. doi: 10.1086/375512.
- M. G. Abadi, J. F. Navarro, M. Steinmetz, and V. R. Eke. Simulations of Galaxy Formation in a Λ Cold Dark Matter Universe. II. The Fine Structure of Simulated Galactic Disks. *ApJ*, 597:21–34, November 2003b. doi: 10.1086/378316.
- K. Abazajian, J. K. Adelman-McCarthy, M. A. Agüeros, S. S. Allam, S. F. Anderson, J. Annis, N. A. Bahcall, I. K. Baldry, S. Bastian, A. Berlind, M. Bernardi, M. R. Blanton, N. Blythe, J. J. Bochanski, Jr., W. N. Boroski, H. Brewington, J. W. Briggs, J. Brinkmann, R. J. Brunner, T. Budavári, L. N. Carey, M. A. Carr, F. J. Castander, K. Chiu, M. J. Collinge, A. J. Connolly, K. R. Covey, I. Csabai, J. J. Dalcanton, S. Dodelson, M. Doi, F. Dong, D. J. Eisenstein, M. L. Evans, X. Fan, P. D. Feldman, D. P. Finkbeiner, S. D. Friedman, J. A. Frieman, M. Fukugita, R. R. Gal, B. Gillespie, K. Glazebrook, C. F. Gonzalez, J. Gray, E. K. Grebel, L. Grodnicki, J. E. Gunn, V. K. Gurbani, P. B. Hall, L. Hao, D. Harbeck, F. H. Harris, H. C. Harris, M. Harvanek, S. L. Hawley, T. M. Heckman, J. F. Helmboldt, J. S. Hendry, G. S. Hennessy, R. B. Hindsley, D. W. Hogg, D. J. Holmgren, J. A. Holtzman, L. Homer, L. Hui, S.-i. Ichikawa, T. Ichikawa, J. P. Inkmann, Ž. Ivezić, S. Jester, D. E. Johnston, B. Jordan, W. P. Jordan, A. M. Jorgensen, M. Jurić, G. Kauffmann, S. M. Kent, S. J. Kleinman, G. R. Knapp, A. Y. Kniazev, R. G. Kron, J. Krzesiński, P. Z. Kunszt, N. Kuropatkin, D. Q. Lamb, H. Lampeitl, B. E. Laubscher, B. C. Lee, R. F. Leger, N. Li, A. Lidz, H. Lin, Y.-S. Loh, D. C. Long, J. Loveday, R. H. Lupton, T. Malik, B. Margon, P. M. McGehee, T. A. McKay, A. Meiksin, G. A. Miknaitis, B. K. Moorthy, J. A. Munn, T. Murphy, R. Nakajima, V. K. Narayanan, T. Nash, E. H. Neilsen, Jr., H. J. Newberg, P. R. Newman, R. C. Nichol, T. Nicinski, M. Nieto-Santisteban, A. Nitta, M. Odenkirchen, S. Okamura, J. P. Ostriker, R. Owen, N. Padmanabhan, J. Peoples, J. R. Pier, B. Pindor, A. C. Pope, T. R. Quinn, R. R. Rafikov, S. N. Raymond, G. T. Richards, M. W. Richmond, H.-W. Rix, C. M. Rockosi, J. Schaye, D. J. Schlegel, D. P. Schneider, J. Schroeder, R. Scranton, M. Sekiguchi, U. Seljak, G. Sergey, B. Sesar, E. Sheldon, K. Shimasaku, W. A. Siegmund, N. M. Silvestri, A. J. Sinisgalli, E. Sirko, J. A. Smith, V. Smolčić, S. A. Snedden, A. Stebbins, C. Steinhardt,

- G. Stinson, C. Stoughton, I. V. Strateva, M. A. Strauss, M. SubbaRao, A. S. Szalay, I. Szapudi, P. Szkody, L. Tasca, M. Tegmark, A. R. Thakar, C. Tremonti, D. L. Tucker, A. Uomoto, D. E. Vanden Berk, J. Vandenberg, M. S. Vogeley, W. Voges, N. P. Vogt, L. M. Walkowicz, D. H. Weinberg, A. A. West, S. D. M. White, B. C. Wilhite, B. Willman, Y. Xu, B. Yanny, J. Yarger, N. Yasuda, C.-W. Yip, D. R. Yocum, D. G. York, N. L. Zakamska, I. Zehavi, W. Zheng, S. Zibetti, and D. B. Zucker. The First Data Release of the Sloan Digital Sky Survey. *AJ*, 126:2081–2086, October 2003. doi: 10.1086/378165.
- K. Abazajian, J. K. Adelman-McCarthy, M. A. Agüeros, S. S. Allam, K. Anderson, S. F. Anderson, J. Annis, N. A. Bahcall, I. K. Baldry, S. Bastian, A. Berlind, M. Bernardi, M. R. Blanton, J. J. Bochanski, Jr., W. N. Boroski, J. W. Briggs, J. Brinkmann, R. J. Brunner, T. Budavári, L. N. Carey, S. Carliles, F. J. Castander, A. J. Connolly, I. Csabai, M. Doi, F. Dong, D. J. Eisenstein, M. L. Evans, X. Fan, D. P. Finkbeiner, S. D. Friedman, J. A. Frieman, M. Fukugita, R. R. Gal, B. Gillespie, K. Glazebrook, J. Gray, E. K. Grebel, J. E. Gunn, V. K. Gurbani, P. B. Hall, M. Hamabe, F. H. Harris, H. C. Harris, M. Harvanek, T. M. Heckman, J. S. Hendry, G. S. Hennessy, R. B. Hindsley, C. J. Hogan, D. W. Hogg, D. J. Holmgren, S.-i. Ichikawa, T. Ichikawa, Ž. Ivezić, S. Jester, D. E. Johnston, A. M. Jorgensen, S. M. Kent, S. J. Kleinman, G. R. Knapp, A. Y. Kniazev, R. G. Kron, J. Krzesinski, P. Z. Kunszt, N. Kuropatkin, D. Q. Lamb, H. Lampeitl, B. C. Lee, R. F. Leger, N. Li, H. Lin, Y.-S. Loh, D. C. Long, J. Loveday, R. H. Lupton, T. Malik, B. Margon, T. Matsubara, P. M. McGehee, T. A. McKay, A. Meiksin, J. A. Munn, R. Nakajima, T. Nash, E. H. Nielsen, Jr., H. J. Newberg, P. R. Newman, R. C. Nichol, T. Nicinski, M. Nieto-Santisteban, A. Nitta, S. Okamura, W. O’Mullane, J. P. Ostriker, R. Owen, N. Padmanabhan, J. Peoples, J. R. Pier, A. C. Pope, T. R. Quinn, G. T. Richards, M. W. Richmond, H.-W. Rix, C. M. Rockosi, D. J. Schlegel, D. P. Schneider, R. Scranton, M. Sekiguchi, U. Seljak, G. Sergey, B. Sesar, E. Sheldon, K. Shimasaku, W. A. Siegmund, N. M. Silvestri, J. A. Smith, V. Smolčić, S. A. Snedden, A. Stebbins, C. Stoughton, M. A. Strauss, M. SubbaRao, A. S. Szalay, I. Szapudi, P. Szkody, G. P. Szokoly, M. Tegmark, L. Teodoro, A. R. Thakar, C. Tremonti, D. L. Tucker, A. Uomoto, D. E. Vanden Berk, J. Vandenberg, M. S. Vogeley, W. Voges, N. P. Vogt, L. M. Walkowicz, S.-i. Wang, D. H. Weinberg, A. A. West, S. D. M. White, B. C. Wilhite, Y. Xu, B. Yanny, N. Yasuda, C.-W. Yip, D. R. Yocum, D. G. York, I. Zehavi, S. Zibetti, and D. B. Zucker. The Second Data Release of the Sloan Digital Sky Survey. *AJ*, 128: 502–512, July 2004. doi: 10.1086/421365.
- K. Abazajian, J. K. Adelman-McCarthy, M. A. Agüeros, S. S. Allam, K. S. J. Anderson, S. F. Anderson, J. Annis, N. A. Bahcall, I. K. Baldry, S. Bastian, A. Berlind, M. Bernardi, M. R. Blanton, J. J. Bochanski, Jr., W. N. Boroski, H. J. Brewington, J. W. Briggs, J. Brinkmann, R. J. Brunner, T. Budavári, L. N. Carey, F. J. Castander, A. J. Connolly, K. R. Covey, I. Csabai, J. J. Dalcanton, M. Doi, F. Dong, D. J. Eisenstein, M. L. Evans, X. Fan, D. P. Finkbeiner, S. D.

- Friedman, J. A. Frieman, M. Fukugita, B. Gillespie, K. Glazebrook, J. Gray, E. K. Grebel, J. E. Gunn, V. K. Gurbani, P. B. Hall, M. Hamabe, D. Harbeck, F. H. Harris, H. C. Harris, M. Harvanek, S. L. Hawley, J. Hayes, T. M. Heckman, J. S. Hendry, G. S. Hennessy, R. B. Hindsley, C. J. Hogan, D. W. Hogg, D. J. Holmgren, J. A. Holtzman, S.-i. Ichikawa, T. Ichikawa, Ž. Ivezić, S. Jester, D. E. Johnston, A. M. Jorgensen, M. Jurić, S. M. Kent, S. J. Kleinman, G. R. Knapp, A. Y. Kniazev, R. G. Kron, J. Krzesinski, D. Q. Lamb, H. Lampeitl, B. C. Lee, H. Lin, D. C. Long, J. Loveday, R. H. Lupton, E. Mannery, B. Margon, D. Martínez-Delgado, T. Matsubara, P. M. McGehee, T. A. McKay, A. Meiksin, B. Ménard, J. A. Munn, T. Nash, E. H. Neilsen, Jr., H. J. Newberg, P. R. Newman, R. C. Nichol, T. Nicinski, M. Nieto-Santisteban, A. Nitta, S. Okamura, W. O'Mullane, R. Owen, N. Padmanabhan, G. Pauls, J. Peoples, J. R. Pier, A. C. Pope, D. Pourbaix, T. R. Quinn, M. J. Raddick, G. T. Richards, M. W. Richmond, H.-W. Rix, C. M. Rockosi, D. J. Schlegel, D. P. Schneider, J. Schroeder, R. Scranton, M. Sekiguchi, E. Sheldon, K. Shimasaku, N. M. Silvestri, J. A. Smith, V. Smolčić, S. A. Snedden, A. Stebbins, C. Stoughton, M. A. Strauss, M. SubbaRao, A. S. Szalay, I. Szapudi, P. Szkody, G. P. Szokoly, M. Tegmark, L. Teodoro, A. R. Thakar, C. Tremonti, D. L. Tucker, A. Uomoto, D. E. Vanden Berk, J. Vandenberg, M. S. Vogeley, W. Voges, N. P. Vogt, L. M. Walkowicz, S.-i. Wang, D. H. Weinberg, A. A. West, S. D. M. White, B. C. Wilhite, Y. Xu, B. Yanny, N. Yasuda, C.-W. Yip, D. R. Yocum, D. G. York, I. Zehavi, S. Zibetti, and D. B. Zucker. The Third Data Release of the Sloan Digital Sky Survey. *AJ*, 129:1755–1759, March 2005. doi: 10.1086/427544.
- J. K. Adelman-McCarthy, M. A. Agüeros, S. S. Allam, K. S. J. Anderson, S. F. Anderson, J. Annis, N. A. Bahcall, I. K. Baldry, J. C. Barentine, A. Berlind, M. Bernardi, M. R. Blanton, W. N. Boroski, H. J. Brewington, J. Brinchmann, J. Brinkmann, R. J. Brunner, T. Budavári, L. N. Carey, M. A. Carr, F. J. Castander, A. J. Connolly, I. Csabai, P. C. Czarapata, J. J. Dalcanton, M. Doi, F. Dong, D. J. Eisenstein, M. L. Evans, X. Fan, D. P. Finkbeiner, S. D. Friedman, J. A. Frieman, M. Fukugita, B. Gillespie, K. Glazebrook, J. Gray, E. K. Grebel, J. E. Gunn, V. K. Gurbani, E. de Haas, P. B. Hall, F. H. Harris, M. Harvanek, S. L. Hawley, J. Hayes, J. S. Hendry, G. S. Hennessy, R. B. Hindsley, C. M. Hirata, C. J. Hogan, D. W. Hogg, D. J. Holmgren, J. A. Holtzman, S.-i. Ichikawa, Ž. Ivezić, S. Jester, D. E. Johnston, A. M. Jorgensen, M. Jurić, S. M. Kent, S. J. Kleinman, G. R. Knapp, A. Y. Kniazev, R. G. Kron, J. Krzesinski, N. Kuropatkin, D. Q. Lamb, H. Lampeitl, B. C. Lee, R. F. Leger, H. Lin, D. C. Long, J. Loveday, R. H. Lupton, B. Margon, D. Martínez-Delgado, R. Mandelbaum, T. Matsubara, P. M. McGehee, T. A. McKay, A. Meiksin, J. A. Munn, R. Nakajima, T. Nash, E. H. Neilsen, Jr., H. J. Newberg, P. R. Newman, R. C. Nichol, T. Nicinski, M. Nieto-Santisteban, A. Nitta, W. O'Mullane, S. Okamura, R. Owen, N. Padmanabhan, G. Pauls, J. J. Peoples, J. R. Pier, A. C. Pope, D. Pourbaix, T. R. Quinn, G. T. Richards, M. W. Richmond, C. M. Rockosi, D. J. Schlegel, D. P. Schneider, J. Schroeder, R. Scranton, U. Seljak, E. Sheldon, K. Shimasaku, J. A. Smith, V. Smolčić, S. A. Snedden, C. Stoughton,

- M. A. Strauss, M. SubbaRao, A. S. Szalay, I. Szapudi, P. Szkody, M. Tegmark, A. R. Thakar, D. L. Tucker, A. Uomoto, D. E. Vanden Berk, J. Vandenberg, M. S. Vogeley, W. Voges, N. P. Vogt, L. M. Walkowicz, D. H. Weinberg, A. A. West, S. D. M. White, Y. Xu, B. Yanny, D. R. Yocum, D. G. York, I. Zehavi, S. Zibetti, and D. B. Zucker. The Fourth Data Release of the Sloan Digital Sky Survey. *ApJS*, 162:38–48, January 2006. doi: 10.1086/497917.
- J. K. Adelman-McCarthy, M. A. Agüeros, S. S. Allam, K. S. J. Anderson, S. F. Anderson, J. Annis, N. A. Bahcall, C. A. L. Bailer-Jones, I. K. Baldry, J. C. Barentine, T. C. Beers, V. Belokurov, A. Berlind, M. Bernardi, M. R. Blanton, J. J. Bochanski, W. N. Boroski, D. M. Bramich, H. J. Brewington, J. Brinchmann, J. Brinkmann, R. J. Brunner, T. Budavári, L. N. Carey, S. Carliles, M. A. Carr, F. J. Castander, A. J. Connolly, R. J. Cool, C. E. Cunha, I. Csabai, J. J. Dalcanton, M. Doi, D. J. Eisenstein, M. L. Evans, N. W. Evans, X. Fan, D. P. Finkbeiner, S. D. Friedman, J. A. Frieman, M. Fukugita, B. Gillespie, G. Gilmore, K. Glazebrook, J. Gray, E. K. Grebel, J. E. Gunn, E. de Haas, P. B. Hall, M. Harvanek, S. L. Hawley, J. Hayes, T. M. Heckman, J. S. Hendry, G. S. Hennessy, R. B. Hindsley, C. M. Hirata, C. J. Hogan, D. W. Hogg, J. A. Holtzman, S.-i. Ichikawa, T. Ichikawa, Ž. Ivezić, S. Jester, D. E. Johnston, A. M. Jorgensen, M. Jurić, G. Kauffmann, S. M. Kent, S. J. Kleinman, G. R. Knapp, A. Y. Kniazev, R. G. Kron, J. Krzesinski, N. Kuropatkin, D. Q. Lamb, H. Lampeitl, B. C. Lee, R. F. Leger, M. Lima, H. Lin, D. C. Long, J. Loveday, R. H. Lupton, R. Mandelbaum, B. Margon, D. Martínez-Delgado, T. Matsubara, P. M. McGehee, T. A. McKay, A. Meiksin, J. A. Munn, R. Nakajima, T. Nash, E. H. Neilsen, Jr., H. J. Newberg, R. C. Nichol, M. Nieto-Santisteban, A. Nitta, H. Oyaizu, S. Okamura, J. P. Ostriker, N. Padmanabhan, C. Park, J. J. Peoples, J. R. Pier, A. C. Pope, D. Pourbaix, T. R. Quinn, M. J. Raddick, P. Re Fiorentin, G. T. Richards, M. W. Richmond, H.-W. Rix, C. M. Rockosi, D. J. Schlegel, D. P. Schneider, R. Scranton, U. Seljak, E. Sheldon, K. Shimasaku, N. M. Silvestri, J. A. Smith, V. Smolčić, S. A. Snedden, A. Stebbins, C. Stoughton, M. A. Strauss, M. SubbaRao, Y. Suto, A. S. Szalay, I. Szapudi, P. Szkody, M. Tegmark, A. R. Thakar, C. A. Tremonti, D. L. Tucker, A. Uomoto, D. E. Vanden Berk, J. Vandenberg, S. Vidrih, M. S. Vogeley, W. Voges, N. P. Vogt, D. H. Weinberg, A. A. West, S. D. M. White, B. Wilhite, B. Yanny, D. R. Yocum, D. G. York, I. Zehavi, S. Zibetti, and D. B. Zucker. The Fifth Data Release of the Sloan Digital Sky Survey. *ApJS*, 172:634–644, October 2007. doi: 10.1086/518864.
- J. K. Adelman-McCarthy, M. A. Agüeros, S. S. Allam, C. Allende Prieto, K. S. J. Anderson, S. F. Anderson, J. Annis, N. A. Bahcall, C. A. L. Bailer-Jones, I. K. Baldry, J. C. Barentine, B. A. Bassett, A. C. Becker, T. C. Beers, E. F. Bell, A. A. Berlind, M. Bernardi, M. R. Blanton, J. J. Bochanski, W. N. Boroski, J. Brinchmann, J. Brinkmann, R. J. Brunner, T. Budavári, S. Carliles, M. A. Carr, F. J. Castander, D. Cinabro, R. J. Cool, K. R. Covey, I. Csabai, C. E. Cunha, J. R. A. Davenport, B. Dilday, M. Doi, D. J. Eisenstein, M. L. Evans,

- X. Fan, D. P. Finkbeiner, S. D. Friedman, J. A. Frieman, M. Fukugita, B. T. Gänsicke, E. Gates, B. Gillespie, K. Glazebrook, J. Gray, E. K. Grebel, J. E. Gunn, V. K. Gurbani, P. B. Hall, P. Harding, M. Harvanek, S. L. Hawley, J. Hayes, T. M. Heckman, J. S. Hendry, R. B. Hindsley, C. M. Hirata, C. J. Hogan, D. W. Hogg, J. B. Hyde, S.-i. Ichikawa, Ž. Ivezić, S. Jester, J. A. Johnson, A. M. Jorgensen, M. Jurić, S. M. Kent, R. Kessler, S. J. Kleinman, G. R. Knapp, R. G. Kron, J. Krzesinski, N. Kuropatkin, D. Q. Lamb, H. Lampeitl, S. Lebedeva, Y. S. Lee, R. F. Leger, S. Lépine, M. Lima, H. Lin, D. C. Long, C. P. Loomis, J. Loveday, R. H. Lupton, O. Malanushenko, V. Malanushenko, R. Mandelbaum, B. Margon, J. P. Marriner, D. Martínez-Delgado, T. Matsubara, P. M. McGehee, T. A. McKay, A. Meiksin, H. L. Morrison, J. A. Munn, R. Nakajima, E. H. Neilsen, Jr., H. J. Newberg, R. C. Nichol, T. Nicinski, M. Nieto-Santisteban, A. Nitta, S. Okamura, R. Owen, H. Oyaizu, N. Padmanabhan, K. Pan, C. Park, J. J. Peoples, J. R. Pier, A. C. Pope, N. Purger, M. J. Raddick, P. Re Fiorentin, G. T. Richards, M. W. Richmond, A. G. Riess, H.-W. Rix, C. M. Rockosi, M. Sako, D. J. Schlegel, D. P. Schneider, M. R. Schreiber, A. D. Schwobe, U. Seljak, B. Sesar, E. Sheldon, K. Shimasaku, T. Sivarani, J. A. Smith, S. A. Snedden, M. Steinmetz, M. A. Strauss, M. SubbaRao, Y. Suto, A. S. Szalay, I. Szapudi, P. Szkody, M. Tegmark, A. R. Thakar, C. A. Tremonti, D. L. Tucker, A. Uomoto, D. E. Vanden Berk, J. Vandenberg, S. Vidrih, M. S. Vogeley, W. Voges, N. P. Vogt, Y. Wadadekar, D. H. Weinberg, A. A. West, S. D. M. White, B. C. Wilhite, B. Yanny, D. R. Yocum, D. G. York, I. Zehavi, and D. B. Zucker. The Sixth Data Release of the Sloan Digital Sky Survey. *ApJS*, 175:297–313, April 2008. doi: 10.1086/524984.
- C. Allende Prieto, T. Sivarani, T. C. Beers, Y. S. Lee, L. Koesterke, M. Shetrone, C. Sneden, D. L. Lambert, R. Wilhelm, C. M. Rockosi, D. Lai, B. Yanny, I. I. Ivans, J. A. Johnson, W. Aoki, C. A. L. Bailer-Jones, and P. Re Fiorentin. The SEGUE Stellar Parameter Pipeline. III. Comparison with High-Resolution Spectroscopy of SDSS/SEGUE Field Stars. *ArXiv e-prints*, 710, October 2007.
- D. An, J. A. Johnson, J.L. Clem, B. Yanny, C. M. Rockosi, H. L. Morrison, P. Harding, J. E. Gunn, C. Allende Prieto, T. C. Beers, K. M. Cudworth, I. I. Ivans, Z. Ivezić, Y. S. Lee, R. H. Lupton, D. Bizyaev, H. Brewington, E. Malanushenko, V. Malanushenko, D. Oravetz, K. Pan, A. Simmons, S. Snedden, S. Watters, and D. G. York. Galactic Globular and Open Clusters in the Sloan Digital Sky Survey. I. Crowded Field Photometry and Cluster Fiducial Sequences in ugriz. *ApJS*, 2008. in press.
- M. I. Arifyanto and B. Fuchs. Fine structure in the phase space distribution of nearby subdwarfs. *A&A*, 449:533–538, April 2006. doi: 10.1051/0004-6361:20054355.
- M. I. Arifyanto, B. Fuchs, H. Jahreiß, and R. Wielen. Kinematics of nearby subdwarf stars. *A&A*, 433:911–916, April 2005. doi: 10.1051/0004-6361:20035829.

- J. N. Bahcall. Self-consistent determinations of the total amount of matter near the sun. *ApJ*, 276:169–181, January 1984. doi: 10.1086/161601.
- J. N. Bahcall, C. Flynn, and A. Gould. Local dark matter from a carefully selected sample. *ApJ*, 389:234–250, April 1992. doi: 10.1086/171201.
- N. P. Bannister and R. F. Jameson. L and T dwarfs in the Hyades and Ursa Major moving groups. *MNRAS*, 378:L24–L28, June 2007. doi: 10.1111/j.1745-3933.2007.00312.x.
- T. C. Beers and J. Sommer-Larsen. Kinematics of metal-poor stars in the galaxy. *ApJS*, 96:175–221, January 1995. doi: 10.1086/192117.
- K. Bekki and M. Chiba. Formation of the Galactic Stellar Halo. I. Structure and Kinematics. *ApJ*, 558:666–686, September 2001. doi: 10.1086/322300.
- V. Belokurov, D. B. Zucker, N. W. Evans, G. Gilmore, S. Vidrih, D. M. Bramich, H. J. Newberg, R. F. G. Wyse, M. J. Irwin, M. Fellhauer, P. C. Hewett, N. A. Walton, M. I. Wilkinson, N. Cole, B. Yanny, C. M. Rockosi, T. C. Beers, E. F. Bell, J. Brinkmann, Ž. Ivezić, and R. Lupton. The Field of Streams: Sagittarius and Its Siblings. *ApJL*, 642:L137–L140, May 2006. doi: 10.1086/504797.
- O. Bienaymé, C. Soubiran, T. V. Mishenina, V. V. Kovtyukh, and A. Siebert. Vertical distribution of Galactic disk stars. *A&A*, 446:933–942, February 2006. doi: 10.1051/0004-6361:20053538.
- J. Binney and S. Tremaine. *Galactic dynamics*. Princeton, NJ, Princeton University Press, 1987, 747 p., 1987.
- A. Blaauw, C. S. Gum, J. L. Pawsey, and G. Westerhout. The new I. A. U. system of galactic coordinates (1958 revision). *MNRAS*, 121:123–+, 1960.
- P. Bode, J. P. Ostriker, and N. Turok. Halo Formation in Warm Dark Matter Models. *ApJ*, 556:93–107, July 2001. doi: 10.1086/321541.
- C. B. Brook, D. Kawata, and B. K. Gibson. Phase Space Plots of Streams in the Halo and Their Chemical Tags. In F. Prada, D. Martinez Delgado, and T. J. Mahoney, editors, *Satellites and Tidal Streams*, volume 327 of *Astronomical Society of the Pacific Conference Series*, pages 100–+, December 2004a.
- C. B. Brook, D. Kawata, B. K. Gibson, and K. C. Freeman. The Emergence of the Thick Disk in a Cold Dark Matter Universe. *ApJ*, 612:894–899, September 2004b. doi: 10.1086/422709.
- J. S. Bullock and K. V. Johnston. Tracing Galaxy Formation with Stellar Halos. I. Methods. *ApJ*, 635:931–949, December 2005. doi: 10.1086/497422.
- G. L. Camm. Self-gravitating star systems. *MNRAS*, 110:305–+, 1950.

- B. W. Carney. Subdwarf ultraviolet excesses and metal abundances. *ApJ*, 233: 211–225, October 1979. doi: 10.1086/157383.
- B. W. Carney, D. W. Latham, and J. B. Laird. A survey of proper-motion stars. VIII - On the Galaxy's third population. *AJ*, 97:423–430, February 1989. doi: 10.1086/114992.
- D. Carollo, T. C. Beers, Y. S. Lee, M. Chiba, J. E. Norris, R. Wilhelm, T. Sivarani, B. Marsteller, J. A. Munn, C. A. L. Bailer-Jones, P. R. Fiorentin, and D. G. York. Two stellar components in the halo of the Milky Way. *Nature*, 450: 1020–1025, December 2007. doi: 10.1038/nature06460.
- B. Chen, C. Stoughton, J. A. Smith, A. Uomoto, J. R. Pier, B. Yanny, Ž. Ivezić, D. G. York, J. E. Anderson, J. Annis, J. Brinkmann, I. Csabai, M. Fukugita, R. Hindsley, R. Lupton, J. A. Munn, and the SDSS Collaboration. Stellar Population Studies with the SDSS. I. The Vertical Distribution of Stars in the Milky Way. *ApJ*, 553:184–197, May 2001. doi: 10.1086/320647.
- E. Chereul and M. Grenon. The Age Heterogeneity of the Hyades Supercluster. In S. Deiters, B. Fuchs, A. Just, R. Spurzem, and R. Wielen, editors, *Dynamics of Star Clusters and the Milky Way*, volume 228 of *Astronomical Society of the Pacific Conference Series*, pages 398–+, 2001.
- M. Chiba and T. C. Beers. Kinematics of Metal-poor Stars in the Galaxy. III. Formation of the Stellar Halo and Thick Disk as Revealed from a Large Sample of Nonkinematically Selected Stars. *AJ*, 119:2843–2865, June 2000. doi: 10.1086/301409.
- J.-H. Choi, M. D. Weinberg, and N. Katz. The dynamics of tidal tails from massive satellites. *MNRAS*, 381:987–1000, November 2007. doi: 10.1111/j.1365-2966.2007.12313.x.
- J. L. Clem, D. A. Vanden Berg, and P. B. Stetson. Fiducial Stellar Population Sequences for the u'g'r'i'z' System. *AJ*, 135:682–692, February 2008. doi: 10.1088/0004-6256/135/2/682.
- S. Cole, A. Aragon-Salamanca, C. S. Frenk, J. F. Navarro, and S. E. Zepf. A Recipe for Galaxy Formation. *MNRAS*, 271:781–+, December 1994.
- M. Creze, E. Chereul, O. Bienayme, and C. Pichon. The distribution of nearby stars in phase space mapped by Hipparcos. I. The potential well and local dynamical mass. *A&A*, 329:920–936, January 1998.
- J. J. Dalcanton and C. J. Hogan. Halo Cores and Phase-Space Densities: Observational Constraints on Dark Matter Physics and Structure Formation. *ApJ*, 561: 35–45, November 2001. doi: 10.1086/323207.

- G. M. De Silva, K. C. Freeman, J. Bland-Hawthorn, M. Asplund, and M. S. Bessell. Chemically Tagging the HR 1614 Moving Group. *AJ*, 133:694–704, February 2007. doi: 10.1086/510131.
- R. De Simone, X. Wu, and S. Tremaine. The stellar velocity distribution in the solar neighbourhood. *MNRAS*, 350:627–643, May 2004. doi: 10.1111/j.1365-2966.2004.07675.x.
- W. Dehnen. The Effect of the Outer Lindblad Resonance of the Galactic Bar on the Local Stellar Velocity Distribution. *AJ*, 119:800–812, February 2000. doi: 10.1086/301226.
- W. Dehnen. The Distribution of Nearby Stars in Velocity Space Inferred from HIPPARCOS Data. *AJ*, 115:2384–2396, June 1998. doi: 10.1086/300364.
- W. Dehnen and J. J. Binney. Local stellar kinematics from HIPPARCOS data. *MNRAS*, 298:387–394, August 1998.
- E. Dekker. Spiral structure and the dynamics of galaxies. *PhysRep*, 24:315–389, 1976.
- C. Dettbarn, B. Fuchs, C. Flynn, and M. Williams. Signatures of star streams in the phase space distribution of nearby halo stars. *A&A*, 474:857–861, November 2007. doi: 10.1051/0004-6361:20077463.
- J. Diemand, M. Kuhlen, and P. Madau. Formation and Evolution of Galaxy Dark Matter Halos and Their Substructure. *ApJ*, 667:859–877, October 2007. doi: 10.1086/520573.
- D. I. Dinescu. A Solar Neighborhood Search for Tidal Debris from ω Centauri’s Hypothetical Parent Galaxy. In F. van Leeuwen, J. D. Hughes, and G. Piotto, editors, *Omega Centauri, A Unique Window into Astrophysics*, volume 265 of *Astronomical Society of the Pacific Conference Series*, pages 365–+, 2002.
- O. J. Eggen. Star Streams and Galactic Structure. *AJ*, 112:1595–+, October 1996. doi: 10.1086/118126.
- O. J. Eggen, D. Lynden-Bell, and A. R. Sandage. Evidence from the motions of old stars that the Galaxy collapsed. *ApJ*, 136:748–+, November 1962.
- B. Famaey, A. Jorissen, X. Luri, M. Mayor, S. Udry, H. Dejonghe, and C. Turon. Dynamical Streams in the Solar Neighbourhood. In C. Turon, K. S. O’Flaherty, and M. A. C. Perryman, editors, *The Three-Dimensional Universe with Gaia*, volume 576 of *ESA Special Publication*, pages 129–+, January 2005.
- M. Fellhauer, V. Belokurov, N. W. Evans, M. I. Wilkinson, D. B. Zucker, G. Gilmore, M. J. Irwin, D. M. Bramich, S. Vidrih, R. F. G. Wyse, T. C. Beers, and J. Brinkmann. The Origin of the Bifurcation in the Sagittarius Stream. *ApJ*, 651:167–173, November 2006. doi: 10.1086/507128.

- M. Fellhauer, N. W. Evans, V. Belokurov, D. B. Zucker, B. Yanny, M. I. Wilkinson, G. Gilmore, M. J. Irwin, D. M. Bramich, S. Vidrih, P. Hewett, and T. Beers. Is Ursa Major II the progenitor of the Orphan Stream? *MNRAS*, 375:1171–1179, March 2007. doi: 10.1111/j.1365-2966.2006.11404.x.
- K. Finlator, Ž. Ivezić, X. Fan, M. A. Strauss, G. R. Knapp, R. H. Lupton, J. E. Gunn, C. M. Rockosi, J. E. Anderson, I. Csabai, G. S. Hennessy, R. B. Hindsley, T. A. McKay, R. C. Nichol, D. P. Schneider, J. A. Smith, D. G. York, and the SDSS Collaboration. Optical and Infrared Colors of Stars Observed by the Two Micron All Sky Survey and the Sloan Digital Sky Survey. *AJ*, 120:2615–2626, November 2000. doi: 10.1086/316824.
- C. Flynn and B. Fuchs. Density of dark matter in the Galactic disk. *MNRAS*, 270:471–+, October 1994.
- K. C. Freeman. The Galactic spheroid and old disk. *Annu.Rev.Astron.Astrophys.*, 25:603–632, 1987. doi: 10.1146/annurev.aa.25.090187.003131.
- B. Fuchs and R. Wielen. Kinematical Constraints on the Dynamically Determined Local Mass Density of the Galaxy. In S. S. Holt and F. Verter, editors, *Back to the Galaxy*, volume 278 of *American Institute of Physics Conference Series*, pages 580–+, 1993.
- M. Fukugita, T. Ichikawa, J. E. Gunn, M. Doi, K. Shimasaku, and D. P. Schneider. The Sloan Digital Sky Survey Photometric System. *AJ*, 111:1748–+, April 1996. doi: 10.1086/117915.
- R. Fux. Order and chaos in the local disc stellar kinematics induced by the Galactic bar. *A&A*, 373:511–535, July 2001. doi: 10.1051/0004-6361:20010561.
- L. Gao and T. Theuns. Lighting the Universe with Filaments. *Science*, 317:1527–, September 2007. doi: 10.1126/science.1146676.
- L. Girardi, A. Bressan, G. Bertelli, and C. Chiosi. Evolutionary tracks and isochrones for low- and intermediate-mass stars: From 0.15 to $7 M_{sun}$, and from $Z=0.0004$ to 0.03. *A&AS*, 141:371–383, February 2000.
- L. Girardi, E. K. Grebel, M. Odenkirchen, and C. Chiosi. Theoretical isochrones in several photometric systems. II. The Sloan Digital Sky Survey ugriz system. *A&A*, 422:205–215, July 2004. doi: 10.1051/0004-6361:20040250.
- A. Gould. An Upper Limit on the Granularity of the Local Stellar Halo. *ApJL*, 592:L63–L66, August 2003. doi: 10.1086/377525.
- C. J. Grillmair and O. Dionatos. A 22° Tidal Tail for Palomar 5. *ApJL*, 641:L37–L39, April 2006. doi: 10.1086/503744.

- J. E. Gunn, M. Carr, C. Rockosi, M. Sekiguchi, K. Berry, B. Elms, E. de Haas, Ž. Ivezić, G. Knapp, R. Lupton, G. Pauls, R. Simcoe, R. Hirsch, D. Sanford, S. Wang, D. York, F. Harris, J. Annis, L. Bartozek, W. Boroski, J. Bakken, M. Haldeman, S. Kent, S. Holm, D. Holmgren, D. Petravick, A. Protopopescu, R. Rechenmacher, M. Doi, M. Fukugita, K. Shimasaku, N. Okada, C. Hull, W. Siegmund, E. Mannery, M. Blouke, D. Heidtman, D. Schneider, R. Lucinio, and J. Brinkman. The Sloan Digital Sky Survey Photometric Camera. *AJ*, 116: 3040–3081, December 1998. doi: 10.1086/300645.
- N. C. Hambly, H. T. MacGillivray, M. A. Read, S. B. Tritton, E. B. Thomson, B. D. Kelly, D. H. Morgan, R. E. Smith, S. P. Driver, J. Williamson, Q. A. Parker, M. R. S. Hawkins, P. M. Williams, and A. Lawrence. The SuperCOSMOS Sky Survey - I. Introduction and description. *MNRAS*, 326:1279–1294, October 2001. doi: 10.1046/j.1365-8711.2001.04660.x.
- W. E. Harris. A Catalog of Parameters for Globular Clusters in the Milky Way. *AJ*, 112:1487–+, October 1996. doi: 10.1086/118116.
- A. Helmi. Is the dark halo of our Galaxy spherical? *MNRAS*, 351:643–648, June 2004a. doi: 10.1111/j.1365-2966.2004.07812.x.
- A. Helmi. Velocity Trends in the Debris of Sagittarius and the Shape of the Dark Matter Halo of Our Galaxy. *ApJL*, 610:L97–L100, August 2004b. doi: 10.1086/423340.
- A. Helmi and P. T. de Zeeuw. Mapping the substructure in the Galactic halo with the next generation of astrometric satellites. *MNRAS*, 319:657–665, December 2000.
- A. Helmi and S. D. M. White. Building up the stellar halo of the Galaxy. *MNRAS*, 307:495–517, August 1999.
- A. Helmi, S. D. M. White, P. T. de Zeeuw, and H. Zhao. Debris streams in the solar neighbourhood as relicts from the formation of the Milky Way. *Nature*, 402:53–55, November 1999. doi: 10.1038/46980.
- A. Helmi, J. F. Navarro, A. Meza, M. Steinmetz, and V. R. Eke. On the Nature of the Ringlike Structure in the Outer Galactic Disk. *ApJL*, 592:L25–L28, July 2003. doi: 10.1086/377364.
- A. Helmi, J. F. Navarro, B. Nordström, J. Holmberg, M. G. Abadi, and M. Steinmetz. Pieces of the puzzle: ancient substructure in the Galactic disc. *MNRAS*, 365:1309–1323, February 2006. doi: 10.1111/j.1365-2966.2005.09818.x.
- M. Hénon and C. Heiles. The applicability of the third integral of motion: Some numerical experiments. *AJ*, 69:73–+, February 1964.

- E. Høg, C. Fabricius, V. V. Makarov, S. Urban, T. Corbin, G. Wycoff, U. Bastian, P. Schwekendiek, and A. Wicenec. The Tycho-2 catalogue of the 2.5 million brightest stars. *A&A*, 355:L27–L30, March 2000.
- D. W. Hogg, D. P. Finkbeiner, D. J. Schlegel, and J. E. Gunn. A Photometricity and Extinction Monitor at the Apache Point Observatory. *AJ*, 122:2129–2138, October 2001. doi: 10.1086/323103.
- J. Holmberg and C. Flynn. The local density of matter mapped by Hipparcos. *MNRAS*, 313:209–216, April 2000.
- R. Ibata, G. F. Lewis, M. Irwin, E. Totten, and T. Quinn. Great Circle Tidal Streams: Evidence for a Nearly Spherical Massive Dark Halo around the Milky Way. *ApJ*, 551:294–311, April 2001. doi: 10.1086/320060.
- R. A. Ibata, G. Gilmore, and M. J. Irwin. A Dwarf Satellite Galaxy in Sagittarius. *Nature*, 370:194–+, July 1994. doi: 10.1038/370194a0.
- R. A. Ibata, M. J. Irwin, G. F. Lewis, A. M. N. Ferguson, and N. Tanvir. One ring to encompass them all: a giant stellar structure that surrounds the Galaxy. *MNRAS*, 340:L21–L27, April 2003. doi: 10.1046/j.1365-8711.2003.06545.x.
- Ž. Ivezić, S. Tabachnik, R. Rafikov, R. H. Lupton, T. Quinn, M. Hammergren, L. Eyer, J. Chu, J. C. Armstrong, X. Fan, K. Finlator, T. R. Geballe, J. E. Gunn, G. S. Hennessy, G. R. Knapp, S. K. Leggett, J. A. Munn, J. R. Pier, C. M. Rockosi, D. P. Schneider, M. A. Strauss, B. Yanny, J. Brinkmann, I. Csabai, R. B. Hindsley, S. Kent, D. Q. Lamb, B. Margon, T. A. McKay, J. A. Smith, P. Waddel, D. G. York, and the SDSS Collaboration. Solar System Objects Observed in the Sloan Digital Sky Survey Commissioning Data. *AJ*, 122:2749–2784, November 2001. doi: 10.1086/323452.
- Ž. Ivezić, R. H. Lupton, S. Anderson, L. Eyer, J. E. Gunn, M. Jurić, G. R. Knapp, G. Miknaitis, J. E. Gunn, C. M. Rockosi, D. Schlegel, M. A. Strauss, C. Stubbs, and D. E. Vanden Berk. Variability Studies with SDSS. *Memorie della Societa Astronomica Italiana*, 74:978–+, 2003.
- Ž. Ivezić, R. H. Lupton, D. Schlegel, B. Boroski, J. Adelman-McCarthy, B. Yanny, S. Kent, C. Stoughton, D. Finkbeiner, N. Padmanabhan, C. M. Rockosi, J. E. Gunn, G. R. Knapp, M. A. Strauss, G. T. Richards, D. Eisenstein, T. Nicinski, S. J. Kleinman, J. Krzesinski, P. R. Newman, S. Snedden, A. R. Thakar, A. Szalay, J. A. Munn, J. A. Smith, D. Tucker, and B. C. Lee. SDSS data management and photometric quality assessment. *Astronomische Nachrichten*, 325:583–589, October 2004. doi: 10.1002/ansa.200410285.
- Ž. Ivezić, J. A. Smith, G. Miknaitis, H. Lin, D. L. Tucker, R. Lupton, G. R. Knapp, J. E. Gunn, M. Strauss, J. Holtzman, S. Kent, B. Yanny, D. Schlegel, D. Finkbeiner, N. Padmanabhan, C. Rockosi, M. Jurić, N. Bond, B. Lee, S. Jester, H. Harris, P. Harding, J. Brinkmann, and D. York. A Comparison

- of SDSS Standard Star Catalog for Stripe 82 with Stetson's Photometric Standards. In C. Sterken, editor, *The Future of Photometric, Spectrophotometric and Polarimetric Standardization*, volume 364 of *Astronomical Society of the Pacific Conference Series*, pages 165–+, April 2007.
- Z. Ivezić, B. Sesar, M. Juric, N. Bond, J. Dalcanton, C. M. Rockosi, B. Yanny, H. J. Newberg, T. C. Beers, C. Allende Prieto, R. Wilhelm, Y. S. Lee, T. Sivarani, J. E. Norris, C. A. L. Bailer-Jones, P. Re Fiorentin, D. Schlegel, A. Uomoto, R. H. Lupton, G. R. Knapp, J. E. Gunn, K. R. Covey, J. Allyn Smith, G. Miknaitis, M. Doi, M. Tanaka, M. Fukugita, S. Kent, D. Finkbeiner, J. A. Munn, J. R. Pier, T. Quinn, S. Hawley, S. Anderson, F. Kiuchi, A. Chen, J. Bushong, H. Sohi, D. Haggard, A. Kimball, J. Barentine, H. Brewington, M. Harvanek, S. Kleinman, J. Krzesinski, D. Long, A. Nitta, S. Snedden, B. Lee, H. Harris, J. Brinkmann, D. P. Schneider, and D. G. York. The Milky Way Tomography with SDSS: II. Stellar Metallicity. *ArXiv e-prints*, 804, April 2008.
- D. R. H. Johnson and D. R. Soderblom. Calculating galactic space velocities and their uncertainties, with an application to the Ursa Major group. *AJ*, 93: 864–867, April 1987. doi: 10.1086/114370.
- K. V. Johnston. A Prescription for Building the Milky Way's Halo from Disrupted Satellites. *ApJ*, 495:297–+, March 1998. doi: 10.1086/305273.
- K. V. Johnston, L. Hernquist, and M. Bolte. Fossil Signatures of Ancient Accretion Events in the Halo. *ApJ*, 465:278–+, July 1996. doi: 10.1086/177418.
- K. V. Johnston, H. Zhao, D. N. Spergel, and L. Hernquist. Tidal Streams as Probes of the Galactic Potential. *ApJL*, 512:L109–L112, February 1999. doi: 10.1086/311876.
- M. Jurić, Ž. Ivezić, A. Brooks, R. H. Lupton, D. Schlegel, D. Finkbeiner, N. Padmanabhan, N. Bond, B. Sesar, C. M. Rockosi, G. R. Knapp, J. E. Gunn, T. Sumi, D. P. Schneider, J. C. Barentine, H. J. Brewington, J. Brinkmann, M. Fukugita, M. Harvanek, S. J. Kleinman, J. Krzesinski, D. Long, E. H. Nielsen, Jr., A. Nitta, S. A. Snedden, and D. G. York. The Milky Way Tomography with SDSS. I. Stellar Number Density Distribution. *ApJ*, 673:864–914, February 2008. doi: 10.1086/523619.
- A. J. Kalnajs. Pattern Speeds of Density Waves. In B. Sundelius, editor, *Dynamics of Disc Galaxies*, pages 323–+, 1991.
- S. Karaali, Y. Karataş, S. Bilir, S. G. Ak, and E. Hamzaoglu. A New Procedure for the Photometric Parallax Estimation. *Publications of the Astronomical Society of Australia*, 20:270–278, 2003. doi: 10.1071/AS03022.
- S. Karaali, S. Bilir, and S. Tunçel. New Colour Transformations for the Sloan Photometry, and Revised Metallicity Calibration and Equations for Photometric

- Parallax Estimation. *Publications of the Astronomical Society of Australia*, 22: 24–28, 2005. doi: 10.1071/AS04034.
- N. Katz. Dissipational galaxy formation. II - Effects of star formation. *ApJ*, 391: 502–517, June 1992. doi: 10.1086/171366.
- V. I. Korchagin, T. M. Girard, T. V. Borkova, D. I. Dinescu, and W. F. van Altena. Local Surface Density of the Galactic Disk from a Three-Dimensional Stellar Velocity Sample. *AJ*, 126:2896–2909, December 2003. doi: 10.1086/379138.
- K. Kuijken and G. Gilmore. The mass distribution in the galactic disc. I - A technique to determine the integral surface mass density of the disc near the sun. . *MNRAS*, 239:571–603, August 1989a.
- K. Kuijken and G. Gilmore. The Mass Distribution in the Galactic Disc - II - Determination of the Surface Mass Density of the Galactic Disc Near the Sun. *MNRAS*, 239:605–649, August 1989b.
- K. Kuijken and G. Gilmore. The Mass Distribution in the Galactic Disc - Part III - the Local Volume Mass Density. *MNRAS*, 239:651–664, August 1989c.
- K. Kuijken and G. Gilmore. The galactic disk surface mass density and the Galactic force $K(z)$ at $Z = 1.1$ kiloparsecs. *ApJL*, 367:L9–L13, January 1991. doi: 10.1086/185920.
- J. B. Laird, B. W. Carney, and D. W. Latham. A survey of proper-motion stars. III - Reddenings, distances, and metallicities. *AJ*, 95:1843–1875, June 1988. doi: 10.1086/114782.
- R. B. Larson. Dynamical models for the formation and evolution of spherical galaxies. *MNRAS*, 166:585–616, March 1974.
- D. R. Law, K. V. Johnston, and S. R. Majewski. A Two Micron All-Sky Survey View of the Sagittarius Dwarf Galaxy. IV. Modeling the Sagittarius Tidal Tails. *ApJ*, 619:807–823, February 2005. doi: 10.1086/426779.
- Y. S. Lee, T. C. Beers, T. Sivarani, C. Allende Prieto, L. Koesterke, R. Wilhelm, J. E. Norris, C. A. L. Bailer-Jones, P. Re Fiorentin, C. M. Rockosi, B. Yanny, H. Newberg, and K. R. Covey. The SEGUE Stellar Parameter Pipeline. I. Description and Initial Validation Tests. *ArXiv e-prints*, 710, October 2007a.
- Y. S. Lee, T. C. Beers, T. Sivarani, J. A. Johnson, D. An, R. Wilhelm, C. Allende Prieto, L. Koesterke, P. Re Fiorentin, C. A. L. Bailer-Jones, J. E. Norris, B. Yanny, C. M. Rockosi, H. J. Newberg, K. M. Cudworth, and K. Pan. The SEGUE Stellar Parameter Pipeline. II. Validation with Galactic Globular and Open Clusters. *ArXiv e-prints*, 710, October 2007b.
- B. Lindblad. On the Cause of Star-Streaming. *ApJ*, 62:191–+, October 1925. doi: 10.1086/142924.

- L. Lindegren and M. A. C. Perryman. GAIA: Global astrometric interferometer for astrophysics. *A&AS*, 116:579–595, May 1996.
- R. H. Lupton, Z. Ivezić, J. E. Gunn, G. Knapp, M. A. Strauss, and N. Yasuda. SDSS Imaging Pipelines. In J. A. Tyson and S. Wolff, editors, *Survey and Other Telescope Technologies and Discoveries. Edited by Tyson, J. Anthony; Wolff, Sidney. Proceedings of the SPIE, Volume 4836, pp. 350-356 (2002).*, volume 4836 of *Presented at the Society of Photo-Optical Instrumentation Engineers (SPIE) Conference*, pages 350–356, December 2002.
- S. R. Majewski, M. F. Skrutskie, M. D. Weinberg, and J. C. Ostheimer. A Two Micron All Sky Survey View of the Sagittarius Dwarf Galaxy. I. Morphology of the Sagittarius Core and Tidal Arms. *ApJ*, 599:1082–1115, December 2003. doi: 10.1086/379504.
- M. Mayor. On the Vertex Deviation. *A&A*, 18:97–+, April 1972.
- H. J. Mo, S. Mao, and S. D. M. White. The formation of galactic discs. *MNRAS*, 295:319–336, April 1998.
- B. Moore, S. Ghigna, F. Governato, G. Lake, T. Quinn, J. Stadel, and P. Tozzi. Dark Matter Substructure within Galactic Halos. *ApJL*, 524:L19–L22, October 1999. doi: 10.1086/312287.
- H. L. Morrison, C. Flynn, and K. C. Freeman. Where does the disk stop and the halo begin? Kinematics in a rotation field. *AJ*, 100:1191–1222, October 1990. doi: 10.1086/115587.
- J. E. Morrison, S. Röser, B. McLean, B. Bucciarelli, and B. Lasker. The Guide Star Catalog, Version 1.2: An Astrometric Recalibration and Other Refinements. *AJ*, 121:1752–1763, March 2001. doi: 10.1086/319383.
- U. Munari, R. Sordo, F. Castelli, and T. Zwitter. An extensive library of 2500 10 500 Å synthetic spectra. *A&A*, 442:1127–1134, November 2005. doi: 10.1051/0004-6361:20042490.
- J. A. Munn, D. G. Monet, S. E. Levine, B. Canzian, J. R. Pier, H. C. Harris, R. H. Lupton, Ž. Ivezić, R. B. Hindsley, G. S. Hennessy, D. P. Schneider, and J. Brinkmann. An Improved Proper-Motion Catalog Combining USNO-B and the Sloan Digital Sky Survey. *AJ*, 127:3034–3042, May 2004. doi: 10.1086/383292.
- J. F. Navarro, A. Helmi, and K. C. Freeman. The Extragalactic Origin of the Arcturus Group. *ApJL*, 601:L43–L46, January 2004. doi: 10.1086/381751.
- B. Nordstrom, M. Mayor, J. Andersen, J. Holmberg, F. Pont, B. R. Jorgensen, E. H. Olsen, S. Udry, and N. Mowlavi. Geneva-Copenhagen Survey of Solar neighbourhood (Nordstrom+, 2004). *VizieR Online Data Catalog*, 5117:0–+, May 2004.

- M. Odenkirchen, E. K. Grebel, C. M. Rockosi, W. Dehnen, R. Ibata, H.-W. Rix, A. Stolte, C. Wolf, J. E. Anderson, Jr., N. A. Bahcall, J. Brinkmann, I. Csabai, G. Hennessy, R. B. Hindsley, Ž. Ivezić, R. H. Lupton, J. A. Munn, J. R. Pier, C. Stoughton, and D. G. York. Detection of Massive Tidal Tails around the Globular Cluster Palomar 5 with Sloan Digital Sky Survey Commissioning Data. *ApJL*, 548:L165–L169, February 2001. doi: 10.1086/319095.
- A. Ollongren. Three-dimensional galactic stellar orbits. *Bull. Astron. Inst. Neth.*, 16:241–+, October 1962.
- J. H. Oort. The force exerted by the stellar system in the direction perpendicular to the galactic plane and some related problems. *Bulletin of the Astronomical Institutes of the Netherlands*, 6:249–+, August 1932.
- J. H. Oort. Note on the determination of K_z and on the mass density near the Sun. *Bulletin of the Astronomical Institutes of the Netherlands*, 15:45–+, February 1960.
- J. Peñarrubia, D. Martínez-Delgado, H. W. Rix, M. A. Gómez-Flechoso, J. Munn, H. Newberg, E. F. Bell, B. Yanny, D. Zucker, and E. K. Grebel. A Comprehensive Model for the Monoceros Tidal Stream. *ApJ*, 626:128–144, June 2005. doi: 10.1086/429903.
- J. Peñarrubia, A. J. Benson, D. Martínez-Delgado, and H. W. Rix. Modeling Tidal Streams in Evolving Dark Matter Halos. *ApJ*, 645:240–255, July 2006. doi: 10.1086/504316.
- S. Perlmutter, G. Aldering, G. Goldhaber, R. A. Knop, P. Nugent, P. G. Castro, S. Deustua, S. Fabbro, A. Goobar, D. E. Groom, I. M. Hook, A. G. Kim, M. Y. Kim, J. C. Lee, N. J. Nunes, R. Pain, C. R. Pennypacker, R. Quimby, C. Lidman, R. S. Ellis, M. Irwin, R. G. McMahon, P. Ruiz-Lapuente, N. Walton, B. Schaefer, B. J. Boyle, A. V. Filippenko, T. Matheson, A. S. Fruchter, N. Panagia, H. J. M. Newberg, W. J. Couch, and The Supernova Cosmology Project. Measurements of Omega and Lambda from 42 High-Redshift Supernovae. *ApJ*, 517:565–586, June 1999. doi: 10.1086/307221.
- M. A. C. Perryman and ESA, editors. *The HIPPARCOS and TYCHO catalogues. Astrometric and photometric star catalogues derived from the ESA HIPPARCOS Space Astrometry Mission*, volume 1200 of *ESA Special Publication*, 1997.
- M. A. C. Perryman, L. Lindegren, J. Kovalevsky, E. Hoeg, U. Bastian, P. L. Bernacca, M. Crézé, F. Donati, M. Grenon, F. van Leeuwen, H. van der Marel, F. Mignard, C. A. Murray, R. S. Le Poole, H. Schrijver, C. Turon, F. Arenou, M. Froeschlé, and C. S. Petersen. The HIPPARCOS Catalogue. *A&A*, 323:L49–L52, July 1997.

- J. R. Pier, J. A. Munn, R. B. Hindsley, G. S. Hennessy, S. M. Kent, R. H. Lupton, and Ž. Ivezić. Astrometric Calibration of the Sloan Digital Sky Survey. *AJ*, 125:1559–1579, March 2003. doi: 10.1086/346138.
- H. C. Plummer. On the problem of distribution in globular star clusters. *MNRAS*, 71:460–470, March 1911.
- W. H. Press. *Numerical recipes in C++ : the art of scientific computing*. Numerical recipes in C++ : the art of scientific computing by William H. Press. xxviii, 1,002 p. : ill. ; 26 cm. Includes bibliographical references and index. ISBN : 0521750334, 2002.
- W. H. Press and P. Schechter. Formation of Galaxies and Clusters of Galaxies by Self-Similar Gravitational Condensation. *ApJ*, 187:425–438, February 1974.
- R. A. Proctor. Preliminary Paper on Certain Drifting Motions of the Stars. *Royal Society of London Proceedings Series I*, 18:169–171, 1869.
- P. Prugniel and C. Soubiran. ELODIE archive (Prugniel+, 2001). *VizieR Online Data Catalog*, 3218:0–+, January 2001.
- A. C. Quillen and I. Minchev. The Effect of Spiral Structure on the Stellar Velocity Distribution in the Solar Neighborhood. *AJ*, 130:576–585, August 2005. doi: 10.1086/430885.
- P. J. Quinn and J. Goodman. Sinking satellites of spiral systems. *ApJ*, 309:472–495, October 1986. doi: 10.1086/164619.
- P. J. Quinn, L. Hernquist, and D. P. Fullagar. Heating of galactic disks by mergers. *ApJ*, 403:74–93, January 1993. doi: 10.1086/172184.
- M. J. Reid. The distance to the center of the Galaxy. *Annu.Rev.Astron.Astrophys.*, 31:345–372, 1993. doi: 10.1146/annurev.aa.31.090193.002021.
- A. G. Riess, A. V. Filippenko, P. Challis, A. Clocchiatti, A. Diercks, P. M. Garnavich, R. L. Gilliland, C. J. Hogan, S. Jha, R. P. Kirshner, B. Leibundgut, M. M. Phillips, D. Reiss, B. P. Schmidt, R. A. Schommer, R. C. Smith, J. Spyromilio, C. Stubbs, N. B. Suntzeff, and J. Tonry. Observational Evidence from Supernovae for an Accelerating Universe and a Cosmological Constant. *AJ*, 116:1009–1038, September 1998. doi: 10.1086/300499.
- S. Röser. An updated GSC as the astrometric reference for minor planet observations. In S. Ferraz-Mello, B. Morando, and J.-E. Arlot, editors, *Dynamics, Ephemerides, and Astrometry of the Solar System*, volume 172 of *IAU Symposium*, pages 481–+, 1996.
- M. Samland. A Model for the Formation of the Milky Way. *Publications of the Astronomical Society of Australia*, 21:175–178, 2004. doi: 10.1071/AS04009.

- M. Schwarzschild. A numerical model for a triaxial stellar system in dynamical equilibrium. *ApJ*, 232:236–247, August 1979. doi: 10.1086/157282.
- G. M. Seabroke, G. Gilmore, A. Siebert, O. Bienaymé, J. Binney, J. Bland-Hawthorn, R. Campbell, K. C. Freeman, B. Gibson, E. K. Grebel, A. Helmi, U. Munari, J. F. Navarro, Q. A. Parker, A. Siviero, M. Steinmetz, F. G. Watson, R. F. G. Wyse, T. Zwitter, J. Peñarrubia, M. C. Smith, and M. Williams. Is the sky falling? Searching for stellar streams in the local Milky Way disc in the CORAVEL and RAVE surveys. *MNRAS*, 384:11–32, February 2008. doi: 10.1111/j.1365-2966.2007.12513.x.
- L. Searle and R. Zinn. Compositions of halo clusters and the formation of the galactic halo. *ApJ*, 225:357–379, October 1978. doi: 10.1086/156499.
- J. A. Sellwood and J. J. Binney. Radial mixing in galactic discs. *MNRAS*, 336: 785–796, November 2002.
- M. H. Siegel, S. R. Majewski, I. N. Reid, and I. B. Thompson. Star Counts Redivivus. IV. Density Laws through Photometric Parallaxes. *ApJ*, 578:151–175, October 2002.
- E. Sirko, J. Goodman, G. R. Knapp, J. Brinkmann, Ž. Ivezić, E. J. Knerr, D. Schlegel, D. P. Schneider, and D. G. York. Blue Horizontal-Branch Stars in the Sloan Digital Sky Survey. II. Kinematics of the Galactic Halo. *AJ*, 127: 914–924, February 2004. doi: 10.1086/381486.
- J. Skuljan, J. B. Hearnshaw, and P. L. Cottrell. Velocity distribution of stars in the solar neighbourhood. *MNRAS*, 308:731–740, September 1999.
- C. Soubiran, O. Bienaymé, and A. Siebert. Vertical distribution of Galactic disk stars. I. Kinematics and metallicity. *A&A*, 398:141–151, January 2003. doi: 10.1051/0004-6361:20021615.
- D. N. Spergel, L. Verde, H. V. Peiris, E. Komatsu, M. R. Nolta, C. L. Bennett, M. Halpern, G. Hinshaw, N. Jarosik, A. Kogut, M. Limon, S. S. Meyer, L. Page, G. S. Tucker, J. L. Weiland, E. Wollack, and E. L. Wright. First-Year Wilkinson Microwave Anisotropy Probe (WMAP) Observations: Determination of Cosmological Parameters. *ApJS*, 148:175–194, September 2003. doi: 10.1086/377226.
- D. N. Spergel, R. Bean, O. Doré, M. R. Nolta, C. L. Bennett, J. Dunkley, G. Hinshaw, N. Jarosik, E. Komatsu, L. Page, H. V. Peiris, L. Verde, M. Halpern, R. S. Hill, A. Kogut, M. Limon, S. S. Meyer, N. Odegard, G. S. Tucker, J. L. Weiland, E. Wollack, and E. L. Wright. Three-Year Wilkinson Microwave Anisotropy Probe (WMAP) Observations: Implications for Cosmology. *ApJS*, 170:377–408, June 2007. doi: 10.1086/513700.

- L. J. Spitzer. The Dynamics of the Interstellar Medium. III. Galactic Distribution. *ApJ*, 95:329–+, May 1942.
- V. Springel, S. D. M. White, A. Jenkins, C. S. Frenk, N. Yoshida, L. Gao, J. Navarro, R. Thacker, D. Croton, J. Helly, J. A. Peacock, S. Cole, P. Thomas, H. Couchman, A. Evrard, J. Colberg, and F. Pearce. Simulations of the formation, evolution and clustering of galaxies and quasars. *Nature*, 435:629–636, June 2005. doi: 10.1038/nature03597.
- S. Sridhar and J. Touma. Adiabatic evolution and capture into resonance: vertical heating of a growing stellar disc. *MNRAS*, 279:1263–+, April 1996.
- T. S. Statler. Problems in determining the surface density of the Galactic disk. *ApJ*, 344:217–231, September 1989. doi: 10.1086/167791.
- M. Steinmetz. RAVE: the RAdial Velocity Experiment. In U. Munari, editor, *GAIA Spectroscopy: Science and Technology*, volume 298 of *Astronomical Society of the Pacific Conference Series*, pages 381–+, 2003.
- M. Steinmetz and J. F. Navarro. The hierarchical origin of galaxy morphologies. *New Astronomy*, 7:155–160, June 2002. doi: 10.1016/S1384-1076(02)00102-1.
- M. Steinmetz and J. F. Navarro. The Cosmological Origin of the Tully-Fisher Relation. *ApJ*, 513:555–560, March 1999. doi: 10.1086/306904.
- M. Steinmetz, T. Zwitter, A. Siebert, F. G. Watson, K. C. Freeman, U. Munari, R. Campbell, M. Williams, G. M. Seabroke, R. F. G. Wyse, Q. A. Parker, O. Bienaymé, S. Roeser, B. K. Gibson, G. Gilmore, E. K. Grebel, A. Helmi, J. F. Navarro, D. Burton, C. J. P. Cass, J. A. Dawe, K. Fiegert, M. Hartley, K. S. Russell, W. Saunders, H. Enke, J. Bailin, J. Binney, J. Bland-Hawthorn, C. Boeche, W. Dehnen, D. J. Eisenstein, N. W. Evans, M. Fiorucci, J. P. Fulbright, O. Gerhard, U. Jauregi, A. Kelz, L. Mijović, I. Minchev, G. Parmentier, J. Peñarrubia, A. C. Quillen, M. A. Read, G. Ruchti, R.-D. Scholz, A. Siviero, M. C. Smith, R. Sordo, L. Veltz, S. Vidrih, R. von Berlepsch, B. J. Boyle, and E. Schilbach. The Radial Velocity Experiment (RAVE): First Data Release. *AJ*, 132:1645–1668, October 2006.
- C. Stoughton, R. H. Lupton, M. Bernardi, M. R. Blanton, S. Burles, F. J. Castander, A. J. Connolly, D. J. Eisenstein, J. A. Frieman, G. S. Hennessy, R. B. Hindsley, Ž. Ivezić, S. Kent, P. Z. Kunszt, B. C. Lee, A. Meiksin, J. A. Munn, H. J. Newberg, R. C. Nichol, T. Nicinski, J. R. Pier, G. T. Richards, M. W. Richmond, D. J. Schlegel, J. A. Smith, M. A. Strauss, M. SubbaRao, A. S. Szalay, A. R. Thakar, D. L. Tucker, D. E. Vanden Berk, B. Yanny, J. K. Adelman, J. E. Anderson, Jr., S. F. Anderson, J. Annis, N. A. Bahcall, J. A. Bakken, M. Bartelmann, S. Bastian, A. Bauer, E. Berman, H. Böhringer, W. N. Boroski, S. Bracker, C. Briegel, J. W. Briggs, J. Brinkmann, R. Brunner, L. Carey, M. A. Carr, B. Chen, D. Christian, P. L. Colestock, J. H. Crocker, I. Csabai,

- P. C. Czarapata, J. Dalcanton, A. F. Davidsen, J. E. Davis, W. Dehnen, S. Dodelson, M. Doi, T. Dombeck, M. Donahue, N. Ellman, B. R. Elms, M. L. Evans, L. Eyer, X. Fan, G. R. Federwitz, S. Friedman, M. Fukugita, R. Gal, B. Gillespie, K. Glazebrook, J. Gray, E. K. Grebel, B. Greenawalt, G. Greene, J. E. Gunn, E. de Haas, Z. Haiman, M. Haldeman, P. B. Hall, M. Hamabe, B. Hansen, F. H. Harris, H. Harris, M. Harvanek, S. L. Hawley, J. J. E. Hayes, T. M. Heckman, A. Helmi, A. Henden, C. J. Hogan, D. W. Hogg, D. J. Holmgren, J. Holtzman, C.-H. Huang, C. Hull, S.-I. Ichikawa, T. Ichikawa, D. E. Johnston, G. Kauffmann, R. S. J. Kim, T. Kimball, E. Kinney, M. Klaene, S. J. Kleinman, A. Klypin, G. R. Knapp, J. Korienek, J. Krolik, R. G. Kron, J. Krzesiński, D. Q. Lamb, R. F. Leger, S. Limmongkol, C. Lindenmeyer, D. C. Long, C. Loomis, J. Loveday, B. MacKinnon, E. J. Mannery, P. M. Mantsch, B. Margon, P. McGehee, T. A. McKay, B. McLean, K. Menou, A. Merelli, H. J. Mo, D. G. Monet, O. Nakamura, V. K. Narayanan, T. Nash, E. H. Neilsen, Jr., P. R. Newman, A. Nitta, M. Odenkirchen, N. Okada, S. Okamura, J. P. Ostriker, R. Owen, A. G. Pauls, J. Peoples, R. S. Peterson, D. Petravick, A. Pope, R. Pordes, M. Postman, A. Prosapio, T. R. Quinn, R. Rechenmacher, C. H. Rivetta, H.-W. Rix, C. M. Rockosi, R. Rosner, K. Ruthmanskorfer, D. Sandford, D. P. Schneider, R. Scranton, M. Sekiguchi, G. Sergey, R. Sheth, K. Shimasaku, S. Smee, S. A. Snedden, A. Stebbins, C. Stubbs, I. Szapudi, P. Szkody, G. P. Szokoly, S. Tabachnik, Z. Tsvetanov, A. Uomoto, M. S. Vogeley, W. Voges, P. Waddell, R. Waltherbos, S.-i. Wang, M. Watanabe, D. H. Weinberg, R. L. White, S. D. M. White, B. Wilhite, D. Wolfe, N. Yasuda, D. G. York, I. Zehavi, and W. Zheng. Sloan Digital Sky Survey: Early Data Release. *AJ*, 123: 485–548, January 2002. doi: 10.1086/324741.
- D. L. Tucker, S. Kent, M. W. Richmond, J. Annis, J. A. Smith, S. S. Allam, C. T. Rodgers, J. L. Stute, J. K. Adelman-McCarthy, J. Brinkmann, M. Doi, D. Finkbeiner, M. Fukugita, J. Goldston, B. Greenway, J. E. Gunn, J. S. Hendry, D. W. Hogg, S.-I. Ichikawa, Ž. Ivezić, G. R. Knapp, H. Lampeitl, B. C. Lee, H. Lin, T. A. McKay, A. Merelli, J. A. Munn, E. H. Neilsen, Jr., H. J. Newberg, G. T. Richards, D. J. Schlegel, C. Stoughton, A. Uomoto, and B. Yanny. The Sloan Digital Sky Survey monitor telescope pipeline. *Astronomische Nachrichten*, 327:821–+, 2006. doi: 10.1002/asna.200610655.
- D. A. VandenBerg and J. L. Clem. Empirically Constrained Color-Temperature Relations. I. BV(RI)C. *AJ*, 126:778–802, August 2003. doi: 10.1086/376840.
- L. Veltz, O. Bienaymé, K. C. Freeman, J. Binney, J. Bland-Hawthorn, B. K. Gibson, G. Gilmore, E. K. Grebel, A. Helmi, U. Munari, J. F. Navarro, Q. A. Parker, G. M. Seabroke, A. Siebert, M. Steinmetz, F. G. Watson, M. Williams, R. F. G. Wyse, and T. Zwitter. Galactic kinematics with RAVE data. I. The distribution of stars towards the Galactic poles. *A&A*, 480:753–765, March 2008. doi: 10.1051/0004-6361:20066948.

- S. von Hoerner. Die zeitliche Rate der Sternentstehung. *Fortschritte der Physik*, 8:191–244, 1960.
- G. Wallerstein. Abundances in G. Dwarfs.VI. a Survey of Field Stars. *ApJS*, 6: 407–+, February 1962.
- K. Warnick, A. Knebe, and C. Power. The tidal streams of disrupting subhaloes in cosmological dark matter haloes. *MNRAS*, 385:1859–1883, April 2008. doi: 10.1111/j.1365-2966.2008.12992.x.
- S. D. M. White and M. J. Rees. Core condensation in heavy halos - A two-stage theory for galaxy formation and clustering. *MNRAS*, 183:341–358, May 1978.
- S. D. M. White, J. F. Navarro, A. E. Evrard, and C. S. Frenk. The Baryon Content of Galaxy Clusters - a Challenge to Cosmological Orthodoxy. *Nature*, 366: 429–+, December 1993. doi: 10.1038/366429a0.
- R. Wielen. The Age Distribution and Total Lifetimes of Galactic Clusters. *A&A*, 13:309–322, July 1971.
- M. Williams. PhD thesis, Australian National University, 2008.
- X.-X. Xue, H.-W. Rix, G. Zhao, P. Re Fiorentin, T. Naab, M. Steinmetz, F. C. van den Bosch, T. C. Beers, Y. S. Lee, E. F. Bell, C. Rockosi, B. Yanny, H. Newberg, R. Wilhelm, X. Kang, M. C. Smith, and D. P. Schneider.
- B. Yanny, H. J. Newberg, E. K. Grebel, S. Kent, M. Odenkirchen, C. M. Rockosi, D. Schlegel, M. Subbarao, J. Brinkmann, M. Fukugita, Ž. Ivezić, D. Q. Lamb, D. P. Schneider, and D. G. York. A Low-Latitude Halo Stream around the Milky Way. *ApJ*, 588:824–841, May 2003. doi: 10.1086/374220.
- D. G. York, J. Adelman, J. E. Anderson, Jr., S. F. Anderson, J. Annis, N. A. Bahcall, J. A. Bakken, R. Barkhouser, S. Bastian, E. Berman, W. N. Boroski, S. Bracker, C. Briegel, J. W. Briggs, J. Brinkmann, R. Brunner, S. Burles, L. Carey, M. A. Carr, F. J. Castander, B. Chen, P. L. Colestock, A. J. Connolly, J. H. Crocker, I. Csabai, P. C. Czarapata, J. E. Davis, M. Doi, T. Dombeck, D. Eisenstein, N. Ellman, B. R. Elms, M. L. Evans, X. Fan, G. R. Federwitz, L. Fiscelli, S. Friedman, J. A. Frieman, M. Fukugita, B. Gillespie, J. E. Gunn, V. K. Gurbani, E. de Haas, M. Haldeman, F. H. Harris, J. Hayes, T. M. Heckman, G. S. Hennessy, R. B. Hindsley, S. Holm, D. J. Holmgren, C.-h. Huang, C. Hull, D. Husby, S.-I. Ichikawa, T. Ichikawa, Ž. Ivezić, S. Kent, R. S. J. Kim, E. Kinney, M. Klaene, A. N. Kleinman, S. Kleinman, G. R. Knapp, J. Korienek, R. G. Kron, P. Z. Kunszt, D. Q. Lamb, B. Lee, R. F. Leger, S. Limmongkol, C. Lindenmeyer, D. C. Long, C. Loomis, J. Loveday, R. Lucinio, R. H. Lupton, B. MacKinnon, E. J. Mannery, P. M. Mantsch, B. Margon, P. McGehee, T. A. McKay, A. Meiksin, A. Merelli, D. G. Monet, J. A. Munn, V. K. Narayanan, T. Nash, E. Neilsen, R. Neswold, H. J. Newberg, R. C. Nichol, T. Nicinski,

- M. Nonino, N. Okada, S. Okamura, J. P. Ostriker, R. Owen, A. G. Pauls, J. Peoples, R. L. Peterson, D. Petravick, J. R. Pier, A. Pope, R. Pordes, A. Prosapio, R. Rechenmacher, T. R. Quinn, G. T. Richards, M. W. Richmond, C. H. Rivetta, C. M. Rockosi, K. Ruthmansdorfer, D. Sandford, D. J. Schlegel, D. P. Schneider, M. Sekiguchi, G. Sergey, K. Shimasaku, W. A. Siegmund, S. Smee, J. A. Smith, S. Snedden, R. Stone, C. Stoughton, M. A. Strauss, C. Stubbs, M. SubbaRao, A. S. Szalay, I. Szapudi, G. P. Szokoly, A. R. Thakar, C. Tremonti, D. L. Tucker, A. Uomoto, D. Vanden Berk, M. S. Vogeley, P. Waddell, S.-i. Wang, M. Watanabe, D. H. Weinberg, B. Yanny, and N. Yasuda. The Sloan Digital Sky Survey: Technical Summary. *AJ*, 120:1579–1587, September 2000. doi: 10.1086/301513.
- T. Zwitter, F. Castelli, and U. Munari. An extensive library of synthetic spectra covering the far red, RAVE and GAIA wavelength ranges. *A&A*, 417:1055–1062, April 2004. doi: 10.1051/0004-6361:20034324.
- T. Zwitter, A. Siebert, U. Munari, K. C. Freeman, A. Siviero, F. G. Watson, J. P. Fulbright, R. F. G. Wyse, R. Campbell, G. M. Seabroke, M. Williams, M. Steinmetz, O. Bienaymé, G. Gilmore, E. K. Grebel, A. Helmi, J. F. Navarro, B. Anguiano, C. Boeche, D. Burton, P. Cass, J. Dawe, K. Fiegert, M. Hartley, K. Russell, L. Veltz, J. Bailin, J. Binney, J. Bland-Hawthorn, A. Brown, W. Dehnen, N. W. Evans, P. Re Fiorentin, M. Fiorucci, O. Gerhard, B. Gibson, A. Kelz, K. Kujken, G. Matijevič, I. Minchev, Q. A. Parker, J. Peñarrubia, A. Quillen, M. A. Read, W. Reid, S. Roeser, G. Ruchti, R.-D. Scholz, M. C. Smith, R. Sordo, E. Tolstoi, L. Tomasella, S. Vidrih, and E. Wylie-de Boer. The Radial Velocity Experiment (rave): Second Data Release. *AJ*, 136:421–451, July 2008. doi: 10.1088/0004-6256/136/1/421.

Acknowledgements

In the end I am very happy about saying thanks to all the people that contributed to this work by one means or another.

First of all, I would like to thank Hans-Walter for taking me as his PhD student, although my knowledge of Astronomy has been rather limited. You gave me the possibility to re-discover my interest in probably the most fascinating scientific research field, the original reason I started studying physics. Also, every meeting we had resulted in so many new ideas that sometimes I couldn't even work them out.

Very special thanks to Burkhard Fuchs for becoming my inofficial second supervisor. I think a great deal of this work is due to you. I enjoyed very much working with you, and hopefully our collaboration will still continue for some time.

I am deeply grateful to Chris Flynn, who welcomed me twice in Finland not only as a guest, but nearly as a friend. The weeks at the Tuorla Observatory have been both productive and enjoyable, and if I stay in Astronomy, you can count on my third visit!

Thanks to Josef Fried and Werner Aeschbach-Hertig for being my third and fourth examiners. Thank you, Werner, also for accepting me as your first diploma student four and a half years ago and for taking the chair of my final examination. I want to thank Coryn Bailer-Jones, Jelte de Jong, Xiangxiang Xue as well as Christian Dettbarn and Robert Schmidt from the ARI for helping me with their advice. Thanks to Juliet Datson for reading the thesis and correcting some of my bad english. Thanks to all the people at MPIA for creating such a nice working atmosphere. I can't remember even one day when I did not feel like going up the hill (okay, except during some phases of writing this thesis). I would like to especially thank all the people that shared the same office with me during the last three years: Johny, Jens, Boris, Xiangxiang, Juliet and Markus. Thank you for all the jokes, discussions and help. Thank you, Johny, for providing me with delicious "food for thought" every Wednesday, for showing me the secret behind your famous peanut sauce and for your friendship. Thanks to all the students at MPIA. I think the students community here is special and I enjoyed being part of it. I want to thank Jan for helping me with the organization of the Königstuhl-race (and Hans-Walter for participating – you acted like the role model for the whole institute!).

Thanks to my brothers and all my friends for the good times we had (and still will have), for your support and influence. Although you might not know it, you contributed in making me the person I am. Thanks to my mother for her steady support and for teaching me such a positive way of life. Thanks to my father – I think my choice to study physics is also due to your influence. Even though you're gone now for seven years, I still feel your presence during hard times and know you somehow contributed to this work. Last but not least I want to say thank you to Sina, who is my "oasis of calmness" during stressful times. Thank you for your patience and backup.